

AD-A108 429

HYDRONAUTICS INC LAUREL MD

EXPERIMENTAL AND THEORETICAL INVESTIGATION OF FACTORS AFFECTING--ETC(U)

AUG 80 A GOODMAN

N00167-79-C-0093

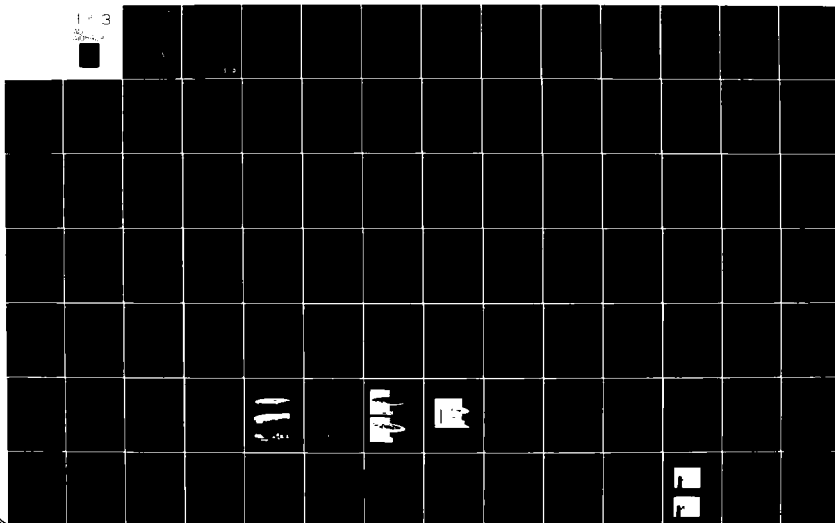
NL

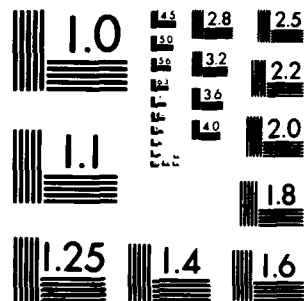
UNCLASSIFIED

TR-7927-1

1 of 3

30-1-2





MICROCOPY RESOLUTION TEST CHART
NATIONAL BUREAU OF STANDARDS-1963-A₁

LEVEL II

①

AD A108429

I

Approved for Public Release: Distribution Unlimited

DTIC
ELECTE
S DEC 10 1981 D

DTIC FILE COPY

D
HYDRONAUTICS, incorporated
research in hydrodynamics

Research, consulting, and advanced engineering in the fields of NAVAL and INDUSTRIAL HYDRODYNAMICS. Offices and Laboratory in the Washington, D. C., area: Pindell School Road, Howard County, Laurel, Md.

81 12 10 002

LEVEL II

(1)

HYDRONAUTICS, Incorporated

TECHNICAL REPORT 7927-1
FINAL

EXPERIMENTAL AND THEORETICAL
INVESTIGATION OF FACTORS
AFFECTING FIN-BODY INTERFERENCE

By
Alex Goodman
August 1980

Accession For	
NTIS GRA&I	<input checked="" type="checkbox"/>
DTIC TAB	<input type="checkbox"/>
Unannounced	<input type="checkbox"/>
Justification	
By	
Distribution/	
Availability Codes	
Dist	Avail and/or Special
A	

Approved for Public Release: Distribution Unlimited

Prepared for
Naval Ship Research and Development Center
Under
Contract N00167-79-C-0093

DTIC
ELECTE
DEC 10 1981
S D
D

SECURITY CLASSIFICATION OF THIS PAGE (When Data Entered)

REPORT DOCUMENTATION PAGE		READ INSTRUCTIONS BEFORE COMPLETING FORM
1. REPORT NUMBER Technical Report 7927-1	2. GOVT ACCESSION NO. AD-A108429	3. RECIPIENT'S CATALOG NUMBER
4. TITLE (and Subtitle) EXPERIMENTAL AND THEORETICAL INVESTIGATION OF FACTORS AFFECTING FIN-BODY INTERFERENCE	5. TYPE OF REPORT & PERIOD COVERED Technical Report Final	
7. AUTHOR(s) Alex Goodman	6. PERFORMING ORG. REPORT NUMBER TR 7927-1	
9. PERFORMING ORGANIZATION NAME AND ADDRESS HYDRONAUTICS, Incorporated 7210 Pindell School Road Laurel, Maryland 20810	8. CONTRACT OR GRANT NUMBER(s) N00167-79-C-0093	
11. CONTROLLING OFFICE NAME AND ADDRESS David Taylor Naval Ship Research and Development Center Bethesda, Maryland 20084	10. PROGRAM ELEMENT, PROJECT, TASK AREA & WORK UNIT NUMBERS 1-257	
14. MONITORING AGENCY NAME & ADDRESS (if different from Controlling Office)	12. REPORT DATE August 1980	
	13. NUMBER OF PAGES 205	
	15. SECURITY CLASS. (of this report) UNCLASSIFIED	
	15a. DECLASSIFICATION/DOWNGRADING SCHEDULE NA	
16. DISTRIBUTION STATEMENT (of this Report) Approved for Public Release: Distribution Unlimited		
17. DISTRIBUTION STATEMENT (of the abstract entered in Block 20, if different from Report)		
18. SUPPLEMENTARY NOTES		
19. KEY WORDS (Continue on reverse side if necessary and identify by block number) Fin-Body Interference Body Sidewash Fin Aspect Ratio Flow Velocity & Angularity Surveys Body-Diameter-Span Ratio Flow-Visualization Fin-Taper Ratio Modified Lifting Surface Method Body-Boundary Layer		
20. ABSTRACT (Continue on reverse side if necessary and identify by block number) A comprehensive series of wind-tunnel experiments were conducted to determine the static-lateral stability characteristics of a systematic series of submarine-type fin-body combinations. The effects of body-boundary layer and sidewash, fin-aspect ratio, fin-taper ratio, and diameter-span ratio on the total forces and moments of the fin-body combinations as well as on the fins in the presence of the bodies were evaluated. Measurements were also made to define the body boundary layer and sidewash in the		

DD FORM 1473 JAN 73

EDITION OF 1 NOV 65 IS OBSOLETE
S/N 0102-014-6001

174500
SECURITY CLASSIFICATION OF THIS PAGE (When Data Entered)

cont
JPC

20. ABSTRACT (continued)

vicinity occupied by the fins. Visualization of the flow behind the body and body-fairwater combination was observed by means of a tuft grid. The results of the investigation are presented in the form of plots and tabulations of the nondimensional force and moment coefficients, static stability derivatives and mutual interference factors. Also, comparisons of the results are made with theory and calculations based on a modified lifting surface method.

A

TABLE OF CONTENTS

	Page
ABSTRACT.....	1
INTRODUCTION.....	2
DESCRIPTION OF MODELS.....	6
DESCRIPTION OF FACILITIES AND TEST APPARATUS.....	10
TEST PROGRAM AND PROCEDURES.....	14
REDUCTION AND PRESENTATION OF DATA.....	18
EFFECTS OF GEOMETRIC PARAMETERS.....	19
FIN-ASPECT RATIO AND DIAMETER-SPAN RATIO.....	25
FIN-TAPER RATIO.....	27
LONGITUDINAL POSITION OF FINS.....	28
FAIRWATER-BODY INTERFERENCE.....	31
FLOW CHARACTERISTICS.....	33
FLOW SURVEY AND VISUALIZATION RESULTS.....	33
CORRELATION WITH THEORY.....	36
CONCLUSIONS AND RECOMMENDATIONS.....	39
ACKNOWLEDGEMENTS.....	42
REFERENCES.....	43
APPENDIX A - GRAPHICAL PRESENTATION OF LATERAL-FORCE, YAWING-MOMENT, ROLLING-MOMENT, FIN-LATERAL FORCE AND FIN-ROOT BENDING MOMENT COEFFICIENTS AS FUNCTIONS OF ANGLE OF SIDESLIP	
APPENDIX B - GRAPHICAL PRESENTATION OF VELOCITY AND ANGULARITY CHARACTERISTICS AT THE STERN OF THE BODY AS A FUNCTION OF ANGLE OF SIDESLIP	

HYDRONAUTICS, Incorporated

-ii-

APPENDIX C - PITOT-STATIC-YAWHEAD RAKE ASSEMBLY DETAILS,
ANALYSIS, AND CALIBRATION

APPENDIX D - DESCRIPTION OF THE MODIFIED-LIFTING SURFACE
METHOD USED IN THEORETICAL CALCULATIONS

HYDRONAUTICS, Incorporated

-iii-

LIST OF FIGURES

- Figure 1 - Sketch of Body and Fin Configurations
- Figure 2 - Photographs of Body and Fin Configurations
- Figure 3 - Sketch Defining Fin-Body Balance Arrangements and Model Support System
- Figure 4 - Photograph of Typical Model Installation in Wind Tunnel
- Figure 5 - Typical Flow-Survey Arrangement Using Pitot-Static-Yaw-Head Rake
- Figure 6 - Sketch Defining Location of Flow-Survey Stations for Bodies B1 and B3
- Figure 7 - General Arrangement for Flow Visualization Tests Using a Tuft-Grid
- Figure 8 - Variation of Lift on Fins in Presence of Body with Aspect Ratio and Diameter-Span Ratio
- Figure 9 - Variation of Average Spanwise Center of Pressure with Aspect Ratio for Several Diameter-Span Ratios
- Figure 10 - Variation of Average Center of Pressure with Diameter-Span Ratio for Various Aspect Ratio Fins
- Figure 11 - Variation of Lift on Fins in Presence of Body with Diameter-Span Ratio for Several Aspect Ratios
- Figure 12 - Variation of Body Induced Lift Parameter with Diameter-Span Ratio
- Figure 13 - Variation of Lift-Curve Slope and Average Spanwise Center of Pressure with Taper Ratio for Several Diameter-Span Ratios. Aspect Ratio = 2.0

HYDRONAUTICS, Incorporated

-iv-

- Figure 14 - Variation of Yawing-Moment Derivative with Lateral-Force Derivative for Several Fin-Body Configurations
- Figure 15 - Variation of Yawing-Moment Interference Factor with Lateral-Force Interference Factor for Several Fin-Body Configurations
- Figure 16 - Variation of Lateral-Flow Angle Parameter with Vertical Distance Parameter for Body B1 and B1+CT
- Figure 17 - Variation of Lateral-Flow Angle Parameter with Vertical Distance Parameter for Body B3
- Figure 18 - Tuft Grid Photographs Taken at Stern of Body B1 and B1+CT. $\beta = 6$ deg.
- Figure 19 - Comparison Between Calculated and Measured Values of Mutual Interference Factor for Several Fin-Body Configurations
- APPENDIX A - GRAPHICAL PRESENTATION OF LATERAL FORCE, YAWING MOMENT, ROLLING MOMENT, FIN-LATERAL FORCE AND FIN-ROOT BENDING MOMENT COEFFICIENTS AS FUNCTIONS OF ANGLE OF SIDESLIP
- Figure A1 - Variation of Lateral Force, Yawing Moment, and Rolling Moment Coefficients with Angle of Sideslip for Bodies B1 and B3
- Figure A2 - Variation of Lateral Force, Yawing Moment, and Rolling Moment Coefficients with Angle of Sideslip for B1 with Fins F_3F_3 to F_6F_6 at Position A
- Figure A3 - Variation of Upper and Lower Fin-Lateral Force and Fin-Root Bending Moment Coefficients with Angle of Sideslip for B1 with Fins F_3F_3 to F_6F_6 at Position A
- Figure A4 - Variation of Lateral Force, Yawing Moment, and Rolling Moment Coefficients with Angle of Sideslip for B1 with Fins F_3F_3 to F_6F_6 at Position B
- Figure A5 - Variation of Upper and Lower Fin-Lateral Force and Fin-Root Bending Moment Coefficients with Angle of Sideslip for B1 with Fins F_3F_3 to F_6F_6 at Position B

HYDRONAUTICS, Incorporated

-v-

- Figure A6 - Variation of Lateral Force, Yawing Moment, and Rolling Moment Coefficients with Angle of Sideslip for B3 with Fins F_3F_3 to F_6F_6 at Position A
- Figure A7 - Variation of Upper and Lower Fin-Lateral Force and Fin-Root Bending Moment Coefficients with Angle of Sideslip for B3 with Fins F_3F_3 to F_6F_6 at Position A
- Figure A8 - Variation of Lateral Force, Yawing Moment, and Rolling Moment Coefficients with Angle of Sideslip for B1 with Fins F_1F_1 , F_2F_2 , and F_4F_4 at Position A
- Figure A9 - Variation of Upper and Lower Fin-Lateral Force and Fin-Root Bending Moment Coefficients with Angle of Sideslip for B1 with Fins F_1F_1 , F_2F_2 , and F_4F_4 at Position A
- Figure A10 - Variation of Lateral Force, Yawing Moment, and Rolling Moment Coefficients with Angle of Sideslip for B1 with Fins F_1F_1 , F_2F_2 , and F_4F_4 at Position B
- Figure A11 - Variation of Upper and Lower Fin-Lateral Force and Fin-Root Bending Moment Coefficients with Angle of Sideslip for B1 with Fins F_1F_1 , F_2F_2 , and F_4F_4 at Position B
- Figure A12 - Variation of Lateral Force, Yawing Moment, and Rolling Moment Coefficients with Angle of Sideslip for B3 with Fins F_1F_1 , F_2F_2 , and F_4F_4 at Position A
- Figure A13 - Variation of Upper and Lower Fin-Lateral Force and Fin-Root Bending Moment Coefficients with Angle of Sideslip for B3 with Fins F_1F_1 , F_2F_2 , and F_4F_4 at Position A
- Figure A14 - Variation of Lateral Force, Yawing Moment, and Rolling Moment Coefficients with Angle of Sideslip for B1 with Fins F_4F_4 , F_7F_7 , and F_8F_8 at Position A

HYDRONAUTICS, Incorporated

-vi-

- Figure A15 - Variation of Upper and Lower Fin-Lateral Force and Fin-Root Bending Moment Coefficients with Angle of Sideslip for B1 with Fins F_4F_4 , F_7F_7 , and F_8F_8 at Position A
- Figure A16 - Variation of Lateral Force, Yawing Moment, and Rolling Moment Coefficients with Angle of Sideslip for B1 with Fins F_4F_4 and F_7F_7 at Position B
- Figure A17 - Variation of Upper and Lower Fin-Lateral Force and Fin-Root Bending Moment Coefficients with Angle of Sideslip for B1 with Fins F_4F_4 and F_7F_7 at Position B
- Figure A18 - Variation of Lateral Force, Yawing Moment, and Rolling Moment Coefficients with Angle of Sideslip for B3 with Fins F_4F_4 and F_7F_7 at Position A
- Figure A19 - Variation of Upper and Lower Fin-Lateral Force and Fin-Root Bending Moment Coefficients with Angle of Sideslip for B3 with Fins F_4F_4 and F_7F_7 at Position A
- Figure A20 - Variation of Lateral Force, Yawing Moment, and Rolling Moment Coefficients with Angle of Sideslip for B1 with Fins F_4F_4 , F_5F_5 , and F_6F_6 with Gap at Position A
- Figure A21 - Variation of Upper and Lower Fin-Lateral Force and Fin-Root Bending Moment Coefficients with Angle of Sideslip for B1 with Fins F_4F_4 , F_5F_5 , and F_6F_6 with Gap at Position A
- Figure A22 - Variation of Lateral Force, Yawing Moment, and Rolling Moment Coefficients with Angle of Sideslip for B1+CT, B1+CT+ F_4F_4 at Positions A and B
- Figure A23 - Variation of Upper and Lower Fin-Lateral Force and Fin-Root Bending Moment Coefficients with Angle of Sideslip for B1+CT+ F_4F_4 at Positions A and B

HYDRONAUTICS, Incorporated

-vii-

- Figure A24 - Variation of Lateral Force, Yawing Moment, and Rolling Moment Coefficients with Angle of Sideslip for $B1+H_4H_4$, $B1+CT+H_4H_4$ at Position A
- Figure A25 - Variation of Upper and Lower Fin-Normal Force and Fin-Root-Bending Moment Coefficients with Angle of Sideslip for $B1+H_4H_4$, $B1+CT+H_4H_4$ at Position A
- Figure A26 - Variation of Lateral Force, Yawing Moment, and Rolling Moment Coefficients with Angle of Sideslip for $B1+F_4$, $B1+F_6$, and $B3+F_4$ at Positions A and B
- Figure A27 - Variation of Upper and Lower Fin-Lateral Force and Fin-Root Bending Moment Coefficients with Angle of Sideslip for $B1+F_4$, $B1+F_6$, and $B3+F_4$ at Positions A and B
- APPENDIX B - GRAPHICAL PRESENTATION OF VELOCITY AND ANGULARITY CHARACTERISTICS AT THE STERN OF THE BODY AS A FUNCTION OF ANGLE OF SIDESLIP
- Figure B1 - Variation of the Vertical and Horizontal Longitudinal Velocity Parameters with Angle of Sideslip for Body B1 at Survey Position A
- Figure B2 - Variation of the Vertical and Horizontal Longitudinal Velocity Parameters with Angle of Sideslip for $B1+CT$ at Survey Position A
- Figure B3 - Variation of the Vertical and Horizontal Longitudinal Velocity Parameters with Angle of Sideslip for Body B1 at Survey Position B
- Figure B4 - Variation of the Vertical and Horizontal Longitudinal Velocity Parameters with Angle of Sideslip for $B1+CT$ at Survey Position B
- Figure B5 - Variation of the Vertical and Horizontal Longitudinal Velocity Parameters with Angle of Sideslip for Body B1 at Survey Position C
- Figure B6 - Variation of the Vertical and Horizontal Longitudinal Velocity Parameters with Angle of Sideslip for $B1+CT$ at Survey Position C

HYDRONAUTICS, Incorporated

-viii-

- Figure B7 - Variation of the Vertical Longitudinal Velocity Parameter with Angle of Sideslip for Body B3 at Survey Position B
- Figure B8 - Variation of the Horizontal Longitudinal Velocity Parameter with Angle of Sideslip for Body B3 at Survey Position B
- Figure B9 - Variation of the Vertical Longitudinal Velocity Parameter with Angle of Sideslip for Body B3 at Survey Position C
- Figure B10 - Variation of the Lateral-Flow Angle with Angle of Sideslip for Body B1 at Survey Position A
- Figure B11 - Variation of the Lateral-Flow Angle with Angle of Sideslip for B1+CT at Survey Position A
- Figure B12 - Variation of the Vertical-Flow Angle with Lateral Distance for Body B1 and B1+CT at Survey Position A
- Figure B13 - Variation of Horizontal-Body-Flow Angle with Lateral Distance for Body B1 and B1+CT at Survey Position A
- Figure B14 - Variation of Vertical-Body-Flow Angle with Vertical Distance for Body B1 at Survey Position A
- Figure B15 - Variation of Vertical-Body-Flow Angle with Vertical Distance for B1+CT at Survey Position A
- Figure B16 - Variation of the Lateral-Flow Angle with Angle of Sideslip for Body B3 at Survey Position B
- Figure B17 - Variation of the Vertical-Flow Angle with Lateral Distance for Body B3 at Survey Position B
- Figure B18 - Variation of Horizontal-Body-Flow Angle with Lateral Distance for Body B3 at Survey Position B
- Figure B19 - Variation of Vertical-Body-Flow Angle with Vertical Distance for Body B3 at Survey Position B

HYDRONAUTICS, Incorporated

-ix-

- APPENDIX C - PITOT-STATIC-YAWHEAD RAKE ASSEMBLY DETAILS, ANALYSIS, AND CALIBRATION
- Figure C1 - Pitot-Static-Yawhead Rake Assembly
- Figure C2 - Sketch Showing Arrangement for Calibration of Pitot-Static-Yawhead Rake Assembly in TMB 24 x 48-inch Low Turbulence Wind Tunnel
- Figure C3 - Inclined Manometer Board Used for Calibration
- Figure C4 - Typical Manometer Board Hookup for One Pitot-Static-Yawhead Tube
- Figure C5 - Sketches Showing Effects of Yawhead Tube Imperfections on Calibration Curves
- Figure C6 - Sketch Defining Angles Measured by Pitot-Static-Yawhead Tube
- Figure C7 - Variation of Yawhead Parameters with Angle of Incidence of the Tube No. 1
- Figure C8 - Variation of Yawhead Parameters with Angle of Incidence of the Tube No. 2
- Figure C9 - Variation of Yawhead Parameters with Angle of Incidence of the Tube No. 3
- Figure C10 - Variation of Yawhead Parameters with Angle of Incidence of the Tube No. 4
- Figure C11 - Variation of Yawhead Parameters with Angle of Incidence of the Tube No. 5
- Figure C12 - Variation of Yawhead Parameters with Angle of Incidence of the Tube No. 6
- Figure C13 - Variation of Dynamic Pressure Ratio with Angle of Incidence of the Tube
- Figure C14 - Charts for Determining the Flow Angles from the Yawhead Parameters

HYDRONAUTICS, Incorporated

-x-

- APPENDIX D - DESCRIPTION OF THE MODIFIED-LIFTING SURFACE METHOD USED IN THEORETICAL CALCULATIONS
- Figure D1 - Variation of Lift Curve Slope with Aspect Ratio for Various Sweep and Taper Ratio
- Figure D2 - Vortex Pattern, System of Axes, and Subscripts Used in Calculation of Span Loadings by Modified-Lifting-Surface Method
- Figure D3 - Analysis of Single Horseshoe Vortex
- Figure D4 - Pictorial Description of the Modified-Lifting Surface Method Used to Calculate Interference Effects of Fins in the Presence of a Body
- Figure D5 - Sketch of Fin-Body Configuration and Vortex-Image System Used in the Calculation of Span Loadings by the Modified-Lifting Surface Method
- Figure D6 - Variation of Theoretical Lift on Fins in Presence of Body with Aspect Ratio for Various Diameter-Span Ratios
- Figure D7 - Variation of Theoretical Lift on Fins in Presence of Body with Diameter-Span Ratio for Several Aspect Ratios
- Figure D8 - Variation of Theoretical Body-Induced Lift Parameter with Diameter-Span Ratio
- Figure D9 - Effect of Gap Size on Fin Lift in Presence of a Reflection Plane
- Figure D10 - Effect of Gap Size on Fin Load Distribution in Presence of a Reflection Plane
- Figure D11 - Effect of Gap Size on Fin Lift in Presence of Body
- Figure D12 - Effect of Gap Size on Fin Load Distribution in Presence of a Body
- Figure D13 - Calculated Values of the Force and Moment Coefficients Due to Rolling for Various Fairwater Span-Body Diameter Ratios

HYDRONAUTICS, Incorporated

-xi-

LIST OF TABLES

	Page
Table 1 - Geometric Characteristics of Body B1 (TMB Model 4439).....	7
Table 2 - Geometric Characteristics of Fins Used in Combination with Bodies B1 and B3.....	8
Table 3 - Outline of Test Program.....	15
Table 4 - Static Stability Derivatives, Inter- ference Factors and Estimated Values for Various Fin-Body Combinations.....	20
Table 5 - Static Stability Derivatives, Inter- ference Factors and Estimated Values for Several B1+CT Configurations.....	23
Table 6 - Horizontal Fin Normal-Forces and Root-Bending- Moments Caused by the Interference of the Body-Fairwater Combination.....	24

NOTATION

The nomenclature defined in DTMB Report 1319 is used herein where applicable. The positive direction of axes, angles, forces, moments, and velocities are shown in the accompany sketch. The coefficients and symbols are defined as follows:

SYMBOL	DIMENSIONLESS FORM	DEFINITION
A_F	$A_F' = \frac{A_F}{l^2}$	Projected area of fin
AP		After perpendicular
a	$\frac{b_F^2}{2A_F}$	Aspect ratio
b_F		Fin span, distance between tip chord and root chord at 50 percent chordline
CB		Center of buoyancy of submarine
CG		Center of mass of submarine
c		Fin chord
d	$d' = \frac{d}{l}$	Diameter of body
FP		Forward perpendicular
I_x	$I_x' = \frac{I_x}{\frac{1}{2}\rho l^5}$	Moment of inertia of the body about x-axis
I_y	$I_y' = \frac{I_y}{\frac{1}{2}\rho l^5}$	Moment of inertia of the body about y-axis
I_z	$I_z' = \frac{I_z}{\frac{1}{2}\rho l^5}$	Moment of inertia of the body about z-axis

HYDRONAUTICS, INCORPORATED

-xiii-

K	$K' = \frac{K}{\frac{1}{2}\rho l^3 U^2}$	Hydrodynamic moment about x -axis through center of gravity
K_p	$K_p' = \frac{K_p}{\frac{1}{2}\rho l^4 U}$	Derivative of moment component with respect to angular velocity component p
$K_{\dot{p}}$	$K_{\dot{p}}' = \frac{K_{\dot{p}}}{\frac{1}{2}\rho l^5}$	Derivative of moment component with respect to angular acceleration component \dot{p}
K_r	$K_r' = \frac{K_r}{\frac{1}{2}\rho l^4 U}$	Derivative of moment component with respect to angular velocity component r
$K_{\dot{r}}$	$K_{\dot{r}}' = \frac{K_{\dot{r}}}{\frac{1}{2}\rho l^5}$	Derivative of moment component with respect to angular acceleration component \dot{r}
K_v	$K_v' = \frac{K_v}{\frac{1}{2}\rho l^3 U}$	Derivative of moment component with respect to velocity component v
$K_{\dot{v}}$	$K_{\dot{v}}' = \frac{K_{\dot{v}}}{\frac{1}{2}\rho l^4}$	Derivative of moment component with respect to acceleration component \dot{v}
K_{δ_r}	$K_{\delta_r}' = \frac{K_{\delta_r}}{\frac{1}{2}\rho l^3 U^2}$	Derivative of moment component with respect to rudder angle component δ_r
k_y	$k_y' = \frac{k_y}{l}$	Radius of gyration of ship and added mass of ship about y -axis
l	$l' = 1$	Characteristic length of submarine
M	$M' = \frac{M}{\frac{1}{2}\rho l^3 U^2}$	Hydrodynamic moment about y -axis through center of gravity

HYDRONAUTICS, INCORPORATED

-xiv-

$$M_q \quad M_q' = \frac{M_q}{\frac{1}{2}\rho l^4 U}$$

Derivative of moment component with respect to angular velocity component q

$$M_{\dot{q}} \quad M_{\dot{q}}' = \frac{M_{\dot{q}}}{\frac{1}{2}\rho l^5}$$

Derivative of moment component with respect to angular acceleration component \dot{q}

$$M_w \quad M_w' = \frac{M_w}{\frac{1}{2}\rho l^3 U}$$

Derivative of moment component with respect to velocity component w

$$M_{\dot{w}} \quad M_{\dot{w}}' = \frac{M_{\dot{w}}}{\frac{1}{2}\rho l^4}$$

Derivative of moment component with respect to acceleration component \dot{w}

$$M_{\delta}, N_{\delta} \quad M_{\delta}' = \frac{M_{\delta}}{\frac{1}{2}\rho l^3 U^2}$$

Derivative of moment component with respect to control surface angle component δ

$$M_{\delta_b} \quad M_{\delta_b}' = \frac{M_{\delta_b}}{\frac{1}{2}\rho l^3 U^2}$$

Derivative of moment component with respect to bow plane angle component δ_b

$$M_{\delta_s} \quad M_{\delta_s}' = \frac{M_{\delta_s}}{\frac{1}{2}\rho l^3 U^2}$$

Derivative of moment component with respect to stern plane angle component δ_s

$$M_{\theta} \quad M_{\theta}' = \frac{M_{\theta}}{\frac{1}{2}\rho l^3 U^2}$$

Derivative of moment component with respect to pitch angle component θ

$$M_0 \quad M_0' = \frac{M_0}{\frac{1}{2}\rho l^3 U^2}$$

Hydrodynamic moment at zero angle of attack

$$m \quad m' = \frac{m}{\frac{1}{2}\rho l^3}$$

Mass of submarine, including water in free-flooding spaces

$$N \quad N' = \frac{N}{\frac{1}{2}\rho l^3 U^2}$$

Hydrodynamic moment about z -axis through center of gravity

$$N_r \quad N_r' = \frac{N_r}{\frac{1}{2}\rho l^4 U}$$

Derivative of moment component with respect to angular velocity component r

HYDRONAUTICS, INCORPORATED

-xv-

N_i	$N_i' = \frac{N_i}{\frac{1}{2} \rho l^5}$	Derivative of moment component with respect to angular acceleration component \dot{i}
N_v	$N_v' = \frac{N_v}{\frac{1}{2} \rho l^3 U}$	Derivative of moment component with respect to velocity component v
$N_{\ddot{v}}$	$N_{\ddot{v}}' = \frac{N_{\ddot{v}}}{\frac{1}{2} \rho l^4}$	Derivative of moment component with respect to acceleration component \ddot{v}
N_{δ_r}	$N_{\delta_r}' = \frac{N_{\delta_r}}{\frac{1}{2} \rho l^3 U^2}$	Derivative of moment component with respect to rudder angle component δ_r
p	$p' = \frac{pl}{U}$	Angular velocity component relative to x -axis
\dot{p}	$\dot{p}' = \frac{\dot{p}l^2}{U^2}$	Angular acceleration component relative to x -axis
q	$q' = \frac{ql}{U}$	Angular velocity component relative to y -axis
\dot{q}	$\dot{q}' = \frac{\dot{q}l^2}{U^2}$	Angular acceleration component relative to y -axis
r	$r' = \frac{rl}{U}$	Angular velocity component relative to z -axis
\dot{r}	$\dot{r}' = \frac{\dot{r}l^2}{U^2}$	Angular acceleration component relative to z -axis
U	$U' = 1$	Velocity of origin of body axes relative to fluid in feet per second
V_k		Velocity of origin of body axes relative to fluid in knots

HYDRONAUTICS, INCORPORATED

-xvi-

v	$v' = \frac{v}{U}$	Component along y -axis of velocity of origin of body relative to fluid
\dot{v}	$\dot{v}' = \frac{\dot{v} l}{U^2}$	Component along y -axis of acceleration of origin of body relative to fluid
w	$w' = \frac{w}{U}$	Component along z -axis of velocity of origin of body axes relative to fluid
\dot{w}	$\dot{w}' = \frac{\dot{w} l}{U^2}$	Component along z -axis of acceleration of origin of body axes relative to fluid
X	$X' = \frac{X}{\frac{1}{2} \rho l^2 U^2}$	Hydrodynamic longitudinal force, positive forward
x		The longitudinal axis, directed from the after to the forward end of the submarine with origin taken at the center of gravity
x_B, z_B	$x_B' = \frac{x_B}{l}$ $z_B' = \frac{z_B}{l}$	Coordinates of center of buoyancy with respect to body axes
Y	$Y' = \frac{Y}{\frac{1}{2} \rho l^2 U^2}$	Hydrodynamic lateral force, positive to star-board
Y_r	$Y_r' = \frac{Y_r}{\frac{1}{2} \rho l^3 U}$	Derivative of lateral force component with respect to angular velocity component r
$Y_{\dot{r}}$	$Y_{\dot{r}}' = \frac{Y_{\dot{r}}}{\frac{1}{2} \rho l^4}$	Derivative of lateral force component with respect to angular acceleration component \dot{r}
Y_v	$Y_v' = \frac{Y_v}{\frac{1}{2} \rho l^2 U}$	Derivative of lateral force component with respect to velocity component v
$Y_{\dot{v}}$	$Y_{\dot{v}}' = \frac{Y_{\dot{v}}}{\frac{1}{2} \rho l^3}$	Derivative of lateral force component with respect to acceleration component \dot{v}

HYDRONAUTICS, INCORPORATED

-xvii-

$$Y_{\delta}, Z_{\delta} \quad Y_{\delta}' = \frac{Y_{\delta}}{\frac{1}{2} \rho l^2 U^2}$$

Derivative of force component with respect to control surface angle component δ

$$Y_{\delta_r} \quad Y_{\delta_r}' = \frac{Y_{\delta_r}}{\frac{1}{2} \rho l^2 U^2}$$

Derivative of lateral force component with respect to rudder angle component δ_r

y

Distance along the transverse axis, directed to starboard with origin taken at center of gravity

$$Z \quad Z' = \frac{Z}{\frac{1}{2} \rho l^2 U^2}$$

Hydrodynamic normal force, positive downward

$$Z_q \quad Z_q' = \frac{Z_q}{\frac{1}{2} \rho l^3 U}$$

Derivative of normal force component with respect to angular velocity component q

$$Z_{\dot{q}} \quad Z_{\dot{q}}' = \frac{Z_{\dot{q}}}{\frac{1}{2} \rho l^4}$$

Derivative of normal force component with respect to angular acceleration component \dot{q}

$$Z_w \quad Z_w' = \frac{Z_w}{\frac{1}{2} \rho l^2 U}$$

Derivative of normal force component with respect to velocity component w

$$Z_{\dot{w}} \quad Z_{\dot{w}}' = \frac{Z_{\dot{w}}}{\frac{1}{2} \rho l^3}$$

Derivative of normal force component with respect to acceleration component \dot{w}

$$Z_{\delta_b} \quad Z_{\delta_b}' = \frac{Z_{\delta_b}}{\frac{1}{2} \rho l^2 U^2}$$

Derivative of normal force component with respect to bow plane angle δ_b

$$Z_{\delta_s} \quad Z_{\delta_s}' = \frac{Z_{\delta_s}}{\frac{1}{2} \rho l^2 U^2}$$

Derivative of normal force component with respect to stern-plane angle component δ_s

$$Z_0 \quad Z_0' = \frac{Z_0}{\frac{1}{2} \rho l^2 U^2}$$

Normal force at zero angle of attack

z

Distance along the normal axis, directed from top to bottom (deck to keel), with origin taken at center of gravity

HYDRONAUTICS, INCORPORATED

-xviii-

α		The angle of attack; the angle to the longitudinal body axis from the projection into the principal plane of symmetry of the velocity of the origin of the body axes relative to the fluid, positive in positive sense of rotation about the y-axis
β		The drift or sideslip angle; the angle to the principal plane of symmetry from the velocity of the origin of the body axes relative to the fluid, positive in the positive sense of rotation about the z-axis
δ		Angular displacement of a control surface
δ_b		Angular displacement of bow planes, positive trailing edge down
δ_r		Angular displacement of rudders, positive trailing edge port
δ_s		Angular displacement of stern planes, positive trailing edge down
θ		The angle of pitch; the angle of elevation of the x-axis positive bow up
ρ	$\rho' = 1$	Mass density of water
σ_i	$\sigma_i' = \sigma_i \frac{l}{U}$	Roots of stability equation, $i = 1, 2, \dots$
ψ		The angle of yaw

SUPPLEMENTARY NOTATION

SYMBOL	DIMENSIONLESS FORM	DEFINITION
a_o		Section lift curve slope of two dimensional wing
\bar{c}		Mean geometric chord
C_L	$\frac{L}{\frac{1}{2}\rho U^2 (2A_F)}$	Lift coefficient of fins
C_{L_α}		Lift curve slope at $\alpha = 0$
L		Lift
N		Number of horseshoe vortices $\left(\frac{b_F}{2s}\right)$
s		Semispans of horseshoe vortex of fin
s'		Semispans of horseshoe vortex image in body
Γ_n	$\Gamma_n' = \frac{2\Gamma_n}{b_F U}$	Circulation strength of a given horseshoe vortex
σ		Sidewash angle
ϵ		Downwash angle
$\Delta 3Y_v', \Delta 3N_v'$		Increments of coefficients caused by fin-body mutual interference; that is, $\Delta 3Y_v' = \left[\left(Y_v' \right)_{B+FF} - Y_v' B \right]$ $= \left[Y_v' FF \right]_B + \left[Y_v' B \right]_F$
$\Delta 4Y_v', \Delta 4N_v'$		Increments of coefficients caused by interference of fin on the body, $\Delta 4Y_v' = \left[\left(Y_v' \right)_{B+FF} - Y_v' B \right] - \left[Y_v' FF \right]_B$ $= \left[Y_v' B \right]_{FF}$

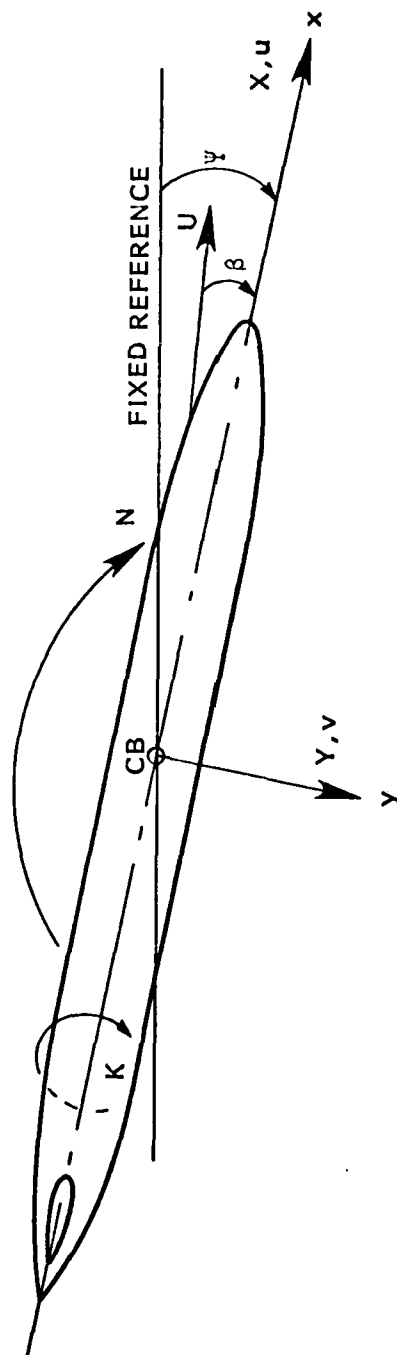
HYDRONAUTICS, Incorporated

-xx-

SUBSCRIPTS

SYMBOL	DIMENSIONLESS FORM	DEFINITION
B		Due to body
B + FF		Body plus fins
C		Calculated
CT		Fairwater or conning tower
F or FF		Due to fin(s)
i		Induced
LF		Lower fin
L		Local
M		Measured
n		Control point number
p		Port side
r		Root
s		Starboard side
UF		Upper fin
t		Tip
FB		Fin balance

HYDRONAUTICS, INCORPORATED



SKETCH SHOWING POSITIVE DIRECTIONS OF AXES,
ANGLES, VELOCITIES, FORCES AND MOMENTS

HYDRONAUTICS, Incorporated

-1-

ABSTRACT

A comprehensive series of wind-tunnel experiments were conducted to determine the static-lateral stability characteristics of a systematic series of submarine-type fin-body combinations. The effects of body-boundary layer and sidewash, fin-aspect ratio, fin-taper ratio, and diameter-span ratio on the total forces and moments of the fin-body combinations as well as on the fins in the presence of the bodies were evaluated. Measurements were also made to define the body boundary layer and sidewash in the vicinity occupied by the fins. Visualization of the flow behind the body and body-fairwater combination was observed by means of a tuft grid. The results of the investigation are presented in the form of plots and tabulations of the nondimensional force and moment coefficients, static stability derivatives and mutual interference factors. Also, comparisons of the results are made with theory and calculations based on a modified lifting surface method.

HYDRONAUTICS, Incorporated

-2-

INTRODUCTION

HYDRONAUTICS, Incorporated was requested by the David W. Taylor Naval Ship Research and Development Center to prepare a technical report summarizing the experimental results obtained from a systematic series of wind-tunnel experiments performed to determine the static-stability characteristics of submarine type fin-body combinations.¹ The primary purpose of the investigation was to determine the effects of body-boundary layer and sidewash, fin-aspect ratio, fin-taper ratio, fin-gap ratio, and body-fin span ratio on the total forces and moments of the fin-body combinations and to present the results in a form useful for predicting the static stability characteristics of submarines, torpedoes, and other submersibles. As an integral part of this study, the forces on the fins in the presence of the body as well as the characteristics of the flow field in which the fins are immersed were also to be evaluated.

The prediction of the stability and control characteristics of submarines, torpedoes, and other submersibles during the preliminary design stage is of primary concern to the U. S. Navy. Prediction of these characteristics requires a knowledge of the stability derivatives which are specified by the equations of motion.^{2,3} Attempts have been made to calculate the required stability derivatives using potential flow and strip-theory methods. In general, these efforts have not been successful due to a lack of understanding of the interference mechanisms existing between submarine type fin-body combinations.⁴ Most of the theoretical and experimental investigations pertaining to fin-body or wing-body interference do not include the effects

HYDRONAUTICS, Incorporated

-3-

of body-boundary layer and sidewash.^{5,6,7,8,9,10,11,12} In general the results and methods presented in the current literature apply to wings and/or fins which extend far beyond the body boundary layer. Therefore, a considerable overestimation of fin effectiveness and fin-body interference is obtained if these results are applied to submarine configurations which are equipped with low-aspect-ratio lifting surfaces that are completely immersed in the body-boundary layer. Another prediction method available to the designer is based on the results of systematic series. Systematic series afford the designer a data base which can be used to predict the stability characteristics of a submarine having physical characteristics encompassed by the series. Results of typical systematic series which provide the static stability characteristics of low-aspect-ratio fins and bodies applicable to submarine design are presented in References 13, 14, and 15, respectively.

In 1953 a fin-body investigation was proposed which was a natural extension of the systematic series investigations presented in References 13 and 14. The systematic program proposed originally was designed to evaluate the mutual interference effects of the fin and body combinations due to fin-aspect ratio, body-tail-taper ratio, body-fineness ratio, and fin-taper ratio. Also, the effects of various forward appendages and modifications to the bow section of the bodies were to be studied. In addition, the determination of the flow-field in the vicinity of the fins as affected by the body and any forward appendages was to be studied. It was proposed that the investigation be conducted in either the NACA Ames 12-foot Variable-Pressure Wind-Tunnel or the NACA Langley 7 x 10-foot Wind Tunnel to achieve

HYDRONAUTICS, Incorporated

-4-

high Reynolds number test conditions. The wind funnel facility was proposed for these studies to simplify the instrumentation requirements and to eliminate the effects of strut interference experience in the tests reported in Reference 14. The Three-Component Dynamometer and Yaw Oscillator Systems used at DTMB in the early 1950's for submerged body static and dynamic stability testing are described in References 4 and 14. In these systems the models were supported by a large vertical-faired single strut and the model drift angles were changed in the plane normal to the faired strut. Forces and moments were measured by an external balance system and as a result the effects of the strut-fairing interference introduced large errors in the lateral force measurements. The introduction of the Planar Motion Mechanism in 1955^{16, 17, 18} eliminated the strut-fairing interference problem, the measurement problems, and the model size reductions associated with the equipment described in References 4 and 14.

Due to funding and scheduling problems associated with the use of the NACA facilities, the scope of the original program was reduced and the tests were conducted in the DTMB 8 x 10-foot Wind Tunnel¹⁹. As part of the program special miniature multi-component strain-gage balances were developed for measurement of the fin lift and bending moments. These balance designs were innovative and stretched the strain-gage state-of-the-art existing in 1953. The development, calibration, and use of a small diameter, multi-tube yawhead rake was also innovative and unique when compared with the single, thirteen-hole spherical probe (0.75-inch diameter) commonly used at DTMB. The tests were conducted during the latter part of 1954. The force data and flow data were reduced to coefficient form using Frieden desk calcu-

HYDRONAUTICS, Incorporated

-5-

lators. All data reduction was independently checked. Theoretical calculations using a Modified Lifting Surface Method were also completed during this period.

This report describes the bodies of revolution and fin configurations; the facilities and special test equipment developed for the program; outlines the program and test procedures used in the investigation; explains the methods used to reduce and analyze the results; presents the basic test results in the form of nondimensional coefficients versus angle of sideslip in Appendices A and B; provides in Appendix C a detailed description of the design and calibration of the pitot-static-yawhead rake used for the flow surveys; describes and illustrates a Modified Lifting Surface Method in Appendix D; summarizes the results using graphs and tables; compares the results with various theories and discusses the results and draws conclusions based on these analyses.

DESCRIPTION OF MODELS

The overall dimensions and other pertinent characteristics of the bodies used in the present investigation are presented in Figure 1(a). As shown in Figure 1(a), the basic body B1 is a streamlined body of revolution having an overall length of 91.20 inches and a maximum diameter of 12.44 inches (TMB Model 4439). The model offsets are based on the Series 58 formulation presented in Reference 20. The model was constructed of mahogany and was equipped with an aluminum tail cone. The offsets and geometric characteristics of Body B1 are presented in Table 1.

Body B3 consists of the same forebody as body B1 and a constant diameter afterbody equal to the maximum diameter. The constant diameter section of Body B3 was obtained by adding a cylindrical mahogany sleeve to body B1. Thus, the fineness ratio for both bodies is 7.33.

The planform chosen for the basic fin series used in the present study was obtained from the unswept series evaluated for free-stream conditions in Reference 13. The geometric characteristics of the fins are presented in Table 2. Fin designations and other definitions are presented in Figure 1(b). As shown in Table 2 and Figure 1(b) the fin series had unswept quarter-chord lines and geometric-aspect ratios (based on one fin) of 0.5, 1.0, 1.5, and 2.0 for a taper ratio of 0.45; a span variation for a constant geometric-aspect ratio of 1.0 and taper ratio of 0.45; and a taper ratio variation of 0.45, 1.0, and 1.5 for a constant geometric-aspect ratio of 1.0. The fins were attached to the bodies at the locations defined in Figure 1(a). The fins were fabricated using both mahogany and a

HYDRONAUTICS, Incorporated

-7-

TABLE 1
GEOMETRIC CHARACTERISTICS OF BODY B1
(TMB MODEL 4439)

Length, ft.	7.60
Maximum diameter, ft.	1.037
Fineness ratio	7.33
Prismatic coefficient	0.60
Volume, cu. ft.	3.84
Wetted surface area, sq. ft.	18.11
Longitudinal distance from FP to CB, ft.	3.382

Body Offsets

x inches	y inches	x inches	y inches
0.0	0.000	47.42	5.989
1.82	1.773	49.25	5.908
3.64	2.522	51.07	5.882
5.47	3.095	52.90	5.720
7.30	3.571	54.72	5.609
9.12	3.977	56.54	5.487
10.94	4.332	58.37	5.350
12.77	4.641	60.19	5.204
14.59	4.913	62.02	5.043
16.42	5.153	63.84	4.871
18.24	5.361	65.66	4.683
20.06	5.538	67.49	4.480
21.89	5.695	69.31	4.262
23.71	5.827	71.14	4.025
25.54	5.933	72.96	3.773
27.36	6.024	74.78	3.501
29.18	6.095	76.61	3.209
31.01	6.146	78.43	2.896
32.83	6.186	80.26	2.560
34.66	6.207	82.08	2.201
36.48	6.219	83.90	1.816
38.30	6.207	85.73	1.406
40.13	6.186	87.55	0.967
41.95	6.156	89.38	0.499
43.78	6.110	91.20	0.000
45.60	6.065		

TABLE 2
GEOMETRIC CHARACTERISTICS OF FINS USED
IN COMBINATION WITH BODIES B1 AND B3

(Values are for one Fin)

Fin	F1	F2	F3	F4	F5	F6	F7	F8
Planform area, sq. in.	8.42	33.61	37.85	18.90	12.62	9.45	18.90	18.90
Span, distance from root to tip chord at 50% chord, in.	2.90	5.80	4.35					
Aspect ratio	1.0	1.0	0.5	1.0	1.5	2.0	1.0	1.0
Root chord, in.	4.0	8.00	12.00	6.0	4.00	3.00	4.35	3.48
Tip chord, in.	1.80	3.60	5.40	2.70	1.80	1.35	4.35	5.22
Mean chord, in.	2.90	5.80	8.20	4.35	2.90	2.18	4.35	4.35
Taper ratio	0.45						1.00	1.50
Sweepback of quarter-chord line, deg.	0							
Section profile (NACA designation)								
Tip	0015							0006
Root	0015							
Span at Fin-Balance, in.	2.90	5.80	4.35					

HYDRONAUTICS, Incorporated

-9-

dental-type casting plastic material. The base of the fins was adapted to either body B1 or B3 by means of filler strips. For Body B1 the filler strips provided a 12-degree slant to fit the average slope of the body at the mounting points. For body B3 the filler strips provided a zero degree base as shown in Figure 2(c). Photographs of bodies B1 and B3 and the fin series are shown in Figure 2.

The fairwater (conning tower) used with TMB model 4439 was adapted to fit body B1 as shown in Figure 1. The overall dimensions for the fairwater (CT) are also presented in Figure 1.

DESCRIPTION OF FACILITIES AND TEST APPARATUS

The experimental investigation was conducted in the 8 x 10-foot Subsonic Wind Tunnel located at the Taylor Model Basin. This tunnel is an atmospheric, closed-throat, return-flow type in which a maximum airspeed of about 160 mph ($q = 60$ psf) can be obtained.¹⁹

The bodies were supported by a sting-wire system shown in Figure 3. This unique type of model-support system was used to avoid the adverse interference effects associated with typical support strut systems.^{4,14} At the model, the tubular sting was attached to an internal-three-component strain-gage balance. The load characteristics for this balance are presented in Figure 3. The sting-balance system was supported in the vertical and horizontal planes by three-piano-wire members which were located at the center of buoyancy of the model. The downstream end of the sting was supported by a strut located about two feet aft of the body. The strut base was attached to a circular slide assembly mounted on the tunnel floor. The body sideslip angle could be varied remotely by positioning the circular slide using a motor driven linear actuator. The circular slide assembly was located relative to the body so that the body rotation took place about the CB. Sideslip angles of ± 10 degrees could be obtained with this system. A digital readout was used to record the angles. A typical model installation showing the sting and piano-wire-support system is presented in Figure 4. Also, the linear actuator motor drive system is shown in Figure 4.

The fins were attached to the bodies by means of strain-

gage balances which could be located at longitudinal positions A or B as shown in Figures 1 and 3. The fins and strain-gage balance were designed to permit quick and easy interchange of the fins. The fin balances were also designed to rotate about the fin quarter chord-line to provide fin deflection angles of ± 10 degrees in two degree increments. The design load characteristics of the fin balances are presented in Figure 3.

A null-balance-servo system was used to provide a digital readout of the forces and moments sensed by the body and fin balances for any given test condition. Briefly, a force applied to the strain-gage balance unbalanced the gage-bridge circuitry. The resulting error signal is amplified and is used to drive a servo motor which positions a potentiometer to restore electrical balance, or null, to the system. The amount that the potentiometer is moved is directly proportional to the forces or moments applied to the balance. The servo motor also drives a decade counter which provides a digital readout proportional to the forces or moments. The system also provides a means to initially balance or zero the gages under no-load conditions and to set the sensitivity of each strain-gage bridge based on deadweight calibrations. A typical servo-balance unit is shown in DTMB Drawing P019006.

Velocity and flow-angularity measurements were made through a range of sideslip angles in a region around each body where the fins would be located. The surveys were made using a specially designed pitot-static-yawhead rake and several small total-head rakes or boundary-layer mice. A detailed description of the pitot-static-yawhead rake design, calibration, and application is presented in Appendix C. A description of the

boundary-layer mouse is presented in Reference 21. A typical arrangement for a flow-survey test using the pitot-static yaw-head rake is shown in Figure 5.

A back-lighted, multitube (48), glass-manometer board was used in conjunction with the yawhead rake and mice for this investigation. Photographs of the manometer board were made for each test condition. The camera used for this purpose was calibrated to account for the errors introduced by parallax.

Velocity and angularity surveys were performed in both the vertical and horizontal planes of bodies B1 and B3 at several longitudinal locations defined in Figure 6.

Qualitative measurements of the flow angularity as affected by variation in the body configuration and sideslip angle were made using the tuft-grid technique described in Reference 22. The general arrangement for flow visualization tests using a tuft grid is shown in Figure 7. The tuft grid employed in this investigation consisted essentially of a rectangular grid of fine piano wire (0.012-inch diameter) having a 2-inch mesh. The grid was supported at the periphery by a rectangular frame and truss-like structure fabricated using thin-wall streamline tubing having a 0.75-inch chord. A preloading system consisting of a spring mounted between one end of each wire and the frame was used to maintain about a 1.5-pound tension in each wire. Also each intersection of a vertical and horizontal wire was soft-soldered to eliminate relative movement between wires. The tufts were 2-inches long and consisted of 4-ply-wool baby yarn. Each tuft was attached to the grid with strong thread. A small loop of thread was provided at the attaching point to

HYDRONAUTICS, Incorporated

-13-

permit the tuft freedom in all directions. The downstream ends of the tufts were singed to prevent fraying. The tufted area of the grid was 104-inches wide and 72-inches high.

The tuft grid was wire-supported to the tunnel walls and located at the stern of the model. The grid was mounted in the tunnel normal to the direction of flow. The still camera used for these tests was a remotely-controlled aerial type camera with a 20-inch-focal-length lens. The camera was placed about 50 feet downstream of the tuft grid for all tests to minimize parallax. Thus, the camera can only record the projections of the tufts and model in a vertical plane. An illustrative example of the type of picture obtained by the still camera is shown in Figure 7(b).

TEST PROGRAM AND PROCEDURES

The test program for the subject investigation is summarized in Table 3. As shown in Table 3, the test program consisted of three phases; namely, force and moment tests; velocity and flow angularity tests; and flow visualization tests. All tests were conducted at a dynamic pressure of 50 pounds per square foot which corresponds to a Mach number of about 0.17 and a Reynolds number of 1.1×10^7 based on the overall body length of 7.60 feet. A sandstrip was installed on the bodies at 4.56-inches aft of the nose (5 percent of length) to fix transition and insure a turbulent boundary layer over the bodies.

For the present investigation the fins were maintained at zero fin deflection with respect to the body axis. For all tests, except as noted, the gap between the fins and body was maintained at a constant 1/32-inch (Gap ratio of 0.007).

Prior to the formal tests, the three-component body balance and the upper and lower fin balances were calibrated using standard weights. A matrix calibration was performed for each balance to account for interactions. After the balances and models were installed in the tunnel, as shown in Figure 4, lateral forces, yawing and rolling moments were applied to establish the sign conventions shown in the NOTATION.

The yawhead rake was completely calibrated in the TMB Low Turbulence Wind Tunnel as described in Appendix C. Tygon tubing was used to connect the rake and mice to the manometer board. The entire system was checked for air leaks prior to each complete survey. The vertical location of the rake and

TABLE 3
OUTLINE OF TEST PROGRAM

A. FORCE AND MOMENT TESTS

Configuration	Fin Position	Sideslip Angle	Measurement
B1 B3	- -	Range Range	Lateral Force, Yawing and Rolling Moments
B1+F1F1 B1+F2F2 B1+F3F3 B1+F4F4 B1+F5F5 B1+F6F6 B1+F7F7 B1+F8F8	A and B ↑ ↓ ↓ ↓ ↓ ↓ A	Range ↑ ↓ ↓ ↓ ↓ ↓ Range	Lateral Force, Yawing and Rolling Moment of Body-Fin Combination. Lateral Forces and Root Bending Moments of Upper and Lower Fins
B3+F1F1 B3+F2F2 B3+F3F3 B3+F4F4 B3+F5F5 B3+F6F6 B3+F7F7	A ↑ ↓ ↓ ↓ ↓ A	Range ↓ ↓ ↓ ↓ ↓ Range	
*B1+F4F4 B1+F5F5 B1+F6F6	A A A	Range Range Range	
B1+CT B1+CT+F4F4	- A and B	Range ↑	
B1+H4H4 B1+CT+H4H4	A A	↑ ↓	
B1+F4 B1+F6 B3+F4	A and B A A	↓ ↓ Range	
*Gap Ratio Changed from 0.007 to 0.042			
Sideslip Angle Range is 0, <u>+1</u> , <u>+2</u> , <u>+3</u> , <u>+4</u> , <u>+6</u> , <u>+8</u> and <u>+10</u> Degrees			

TABLE 3
OUTLINE OF TEST PROGRAM
(concluded)

B. VELOCITY AND ANGULARITY SURVEY TESTS

Configuration	Survey Station	Rake & Mouse Location	Sideslip Angle	Measurement
B1	A, B and C	Upper, Lower and Starboard Positions	Range	Velocity ratios, and flow angularity in vertical and horizontal planes
B1+CT	A, B and C	↓	↓	
B3	B and C	↓	↓	
Sideslip Angle Range is 0, <u>+1</u> , <u>+2</u> , <u>+3</u> , <u>+4</u> and <u>+6</u> Degrees				

C. FLOW VISUALIZATION TESTS

Configuration	Sideslip Angle Degrees	Measurements
B1	6	Still Photographs
B1+CT	6	

HYDRONAUTICS, Incorporated

-17-

mice tubes with respect to the body was measured and recorded for each test. Test photographs were made of the manometer board to check camera focus and parallax.

Prior to the conduct of the formal flow visualization tests, the aerial camera was installed and checked for focus, parallax and remote operation. An illustrative example of the type of picture obtained by the still camera is shown in Figure 7(b). As shown in Figure 7(b), the vertical projection of the B1+CT configuration at an angle of sideslip is shown forward of the grid. The short dark lines (white on photographs) represent the tufts. In the relatively undisturbed region of flow, the tufts appear as short dark lines or dots and in disturbed regions as longer lines. One of the tufts in the sketch has been magnified for purpose of illustration. The vertical and horizontal projections of each tuft together with the tuft length can be used to indicate the magnitude of the downwash and sidewash angles of the flow at a given location.

REDUCTION AND PRESENTATION OF DATA

The force and moment data obtained from the captive-model tests are presented in nondimensional form in Appendix A. These data have been corrected for the effects of blockage and jet boundaries.²³ Corrections for the interference effects of the model-support system were believed to be insignificant. The results of the velocity and flow-angularity survey tests are presented in Appendix B. The test results presented in Appendices A and B have been reduced to coefficient form in accordance with the definitions presented in the NOTATION.

Details of the pitot-static-yawhead rake design, calibration and application are discussed in Appendix C. Appendix D contains a description of the Modified-Lifting-Surface Method used for the theoretical calculations. Notation and references applicable specifically to Appendices C and D are presented in the respective appendices.

The effects of the various geometric parameters investigated and correlation of results with theory are summarized in the body of the report. Also, the results of the flow visualization tests are presented and correlated with the flow angularity measurements. Application of the Modified-Lifting Surface Method to the prediction of roll dependent coefficients is also presented and discussed.

EFFECTS OF GEOMETRIC PARAMETERS

A method used to evaluate the effects of the various geometric parameters on the fin-body interference characteristics is based on a comparison of the static-lateral stability derivatives and the corresponding interference factors.^{8,12} The derivatives Y_v' , N_v' , K_v' , and $(Y_v'_{FF})_B$ are determined for all the configurations by taking the slopes, at β equal to zero degrees, of the Y' , N' , and K' curves versus β curves shown in Appendix A and converting these values to a "per radian" base. The values of the lateral-stability derivatives and the corresponding interference factors for all the configurations associated with bodies B1 and B3 are presented in Table 4. Values associated with the B1+CT configurations are summarized in Tables 5 and 6.

The lateral force and root-bending-moment derivatives determined for the upper and lower fins in the presence of the bodies were also converted to lift-curve slope and average spanwise center of pressure coefficients for direct comparison with aerodynamic data and theories. The lift-curve slope for the fins can be expressed as,

$$(C_{L_{\alpha FF}})_B = -57.3 \frac{l^2}{2A_F} \left[(Y_v'_{UF})_B + (Y_v'_{LF})_B \right] \quad [11]$$

TABLE 4
 STATIC STABILITY DERIVATIVES, INTERFERENCE FACTORS AND
 ESTIMATED VALUES FOR VARIOUS FIN-BODY COMBINATIONS
 (a) Body B1; $(x_F')\bar{c}/4 = -0.45$

Configuration	a	$\frac{I^2}{2A_F}$	$\frac{d_F}{2b_F}$	$\frac{Y_V'}{x10^3}$	$\frac{N_V'}{x10^3}$	$\frac{(Y_V'FF)B}{x10^3}$	$\frac{\bar{z}_F}{b_F}$	$\frac{(\Delta_3 Y_V')M}{x10^3}$	$\frac{(\Delta_3 N_V')M}{x10^3}$	$\frac{(\Delta_3 Y_V')}{x10^3}$	$\frac{\Delta_3 Y_V'}{1+(Y_V'FF)B}$	$\frac{(\Delta_3 Y_V')C}{x10^3}$	$\frac{(\Delta_3 Y_V')C}{x10^3}$
B1	-	-	-	-8.88	-13.29	-	-	-	-	-	-	-	-
B1+F1F1	2.0	493.9	0.78	-13.64	-11.29	-2.86	0.34	-4.76	2.00	-18.96	1.66	-4.99	-9.78
B1+F2F2	2.0	123.7	0.39	-28.65	-4.87	-14.15	0.42	-19.77	8.42	-5.62	1.40	-19.92	-31.10
B1+F3F3	1.0	109.9	0.52	-22.40	-7.79	-8.55	0.49	-13.52	5.50	-4.97	1.58	-13.04	-22.86
B1+F4F4	2.0	220.0	0.41	-19.60	-8.54	-7.28	0.41	-10.72	4.75	-3.44	1.47	-11.20	-19.60
B1+F5F5	3.0	329.5	0.38	-18.51	-9.20	-6.79	0.38	-9.63	4.09	-2.84	1.42	-9.57	-16.40
B1+F6F6	4.0	440.1	0.39	-17.65	-9.86	-6.05	0.39	-8.77	3.43	-2.72	1.45	-8.33	-13.90
B1+F7F7	2.0	220.0	0.52	-19.88	-8.31	-7.81	0.52	-11.00	4.98	-3.19	1.41	-11.20	-19.60
B1+F8F8	2.0	220.0	0.52	-20.80	-7.88	-8.86	0.54	-11.92	5.41	-3.06	1.35	-11.20	-19.60

TABLE 4 (continued)

(b) Body B1; $(x_F')_{C/4} = -0.40$

Configuration	a	$\frac{z^2}{2A_F}$	$\frac{d_F}{2b_F}$	Y_V' $\times 10^3$	N_V' $\times 10^3$	$(Y_V' FF')_B$ $\times 10^3$	$\frac{z_F}{b_F}$	$(\Delta_3 Y_V')_M$ $\times 10^3$	$(\Delta_3 N_V')_M$ $\times 10^3$	$(\Delta_3 Y_V')$ $\times 10^3$	$\frac{\Delta_3 Y_V'}{1 + (Y_V' FF')_B}$	$(\Delta_3 Y_V')_C$ $\times 10^3$	$(\Delta_3 Y_V')_C$ $\times 10^3$
B1	-	-	-	-8.88	-13.29	-	-	-	-	-	-	-	-
B1+F1F1	2.0	493.9	1.09	-17.00	-10.31	-4.24	0.35	-8.12	2.98	-3.88	1.91	-4.99	-10.8
B1+F2F2	2.0	123.7	0.54	-34.95	-3.61	-17.76	0.34	-26.07	9.68	-8.31	1.47	-19.92	-34.50
B1+F3F3	1.0	109.9	0.72	-30.00	-5.99	-12.26	0.46	-21.12	7.30	-8.86	1.72	-13.04	-25.10
B1+F4F4	2.0	220.0		-24.98	-7.48	-9.90	0.38	-16.10	5.81	-6.20	1.63	-11.20	-21.80
B1+F5F5	3.0	329.5		-22.63	-7.74	-8.87	0.35	-13.75	5.55	-4.83	1.55	-9.57	-18.30
B1+F6F6	4.0	440.1		-20.92	-8.31	-7.94	0.36	-12.04	4.38	-4.10	1.52	-8.33	-15.60
B1+F7F7	2.0	220.0	0.72	-25.96	-7.16	-10.40	0.47	-17.08	6.13	-6.68	1.64	-11.20	-21.80

TABLE 4 (concluded)

(c) Body B3; $(x_F')\bar{c}/4 = -0.40$

Configuration	a	$\frac{L^2}{2A_F}$	$\frac{d_F}{2b_F}$	V_V' $\times 10^3$	N_V' $\times 10^3$	$(Y_V'FF)B$ $\times 10^3$	\bar{z}_F $\frac{b_F}{b_F}$	$(\Delta_3 Y_V')M$ $\times 10^3$	$(\Delta_3 N_V')M$ $\times 10^3$	$(\Delta_3 Y_V')C$ $\times 10^3$	$\frac{\Delta_3 Y_V'}{1+(Y_V'FF)B}$	$(\Delta_3 Y_V')C$ $\times 10^3$	$(\Delta_3 Y_V')C$ $\times 10^3$
B3	-	-	-	-39.82	0	-	-	-	-	-	-	-	-
B3-F1F1	2.0	493.9	2.14	-52.14	3.44	-6.96	0.26	-12.32	3.44	-5.36	1.77	-4.99	-13.10
B3-F2F2	2.0	123.7	1.07	-80.22	12.03	-27.66	0.35	-40.40	12.03	-12.74	1.46	-19.92	-43.10
B3-F3F3	1.0	109.9	1.43	-70.76	8.74	-18.77	0.36	-30.94	8.74	-12.17	1.65	-13.04	-32.49
B3-F4F4	2.0	220.0	1.43	-65.03	8.02	-15.60	0.32	-25.21	8.02	-9.61	1.62	-11.20	-27.17
B3-F5F5	3.0	329.5	1.43	-58.45	5.62	-12.53	0.29	-18.63	5.62	-6.10	1.49	-9.57	-22.53
B3-F6F6	4.0	440.1	1.43	-56.15	5.44	-10.94	0.31	-16.33	5.44	-5.39	1.49	-8.33	-18.79
B3-F7F7	2.0	220.0	1.43	-66.64	8.31	-16.67	0.36	-26.82	8.31	-10.15	1.61	-11.20	-27.17

NOTE:

(1) Estimate Based on (C_{L_a}) of Fins Alone

(2) Estimate Based on Modified Lifting Surface Theory Presented in Appendix D

TABLE 5
 STATIC STABILITY DERIVATIVES, INTERFERENCE FACTORS,
 AND ESTIMATED VALUES FOR SEVERAL BI+CT CONFIGURATIONS

Configuration	a	$\frac{\lambda^2}{2A_F}$	$\frac{\lambda^2}{A_{CT}}$	$\frac{d_F}{2b_F}$	Y_V' $\times 10^3$	N_V' $\times 10^3$	K_V' $\times 10^3$	$Y_V' UF$ $\times 10^3$	$Y_V' LF$ $\times 10^3$	$\left(\frac{z}{b_F}\right)_{UF}$	$\left(\frac{z}{b_F}\right)_{LF}$	$\Delta_3 Y_V'$ $\times 10^3$	$\Delta_3 N_V'$ $\times 10^3$	$\Delta_3 K_V'$ $\times 10^3$	(1) $(-3Y_V')_C$ $\times 10^3$
BI	-	-	-	-	-8.88	-13.29	0	-	-	-	-	-	-	-	-
BI+CT	1.22	-	130.3	1.00	-39.02	-16.04	-1.49	-	-	-	-	-30.14	-2.75	-1.49	-31.70
(3I+CT+FF4F4)A	2.0	220.0	-	0.52	-45.32	-12.64	-1.32	-0.40	-4.70	-0.73	0.34	-6.30	3.40	0.17	-
(3I+CT+FF4F4)B	2.0	220.0	-	0.72	-49.39	-11.80	-1.24	-0.60	-5.31	-0.72	0.36	-10.37	4.24	0.25	-

NOTE:

(1) Estimate Based on Modified Lifting Surface Theory Presented in Appendix D.

TABLE 6

HORIZONTAL FIN NORMAL-FORCES AND ROOT-BENDING
MOMENTS CAUSED BY THE INTERFERENCE OF THE
BODY-FAIRWATER COMBINATION

Configuration	a	$\frac{\ell^2}{2A_F}$	$\frac{\ell^2}{A_{CT}}$	$\frac{d_F}{2b_F}$	$Y_V \times 10^{-3}$	$N_V \times 10^{-3}$	$K_V \times 10^{-3}$	$(Z_V')_{SF} \times 10^{-3}$	$(Z_V')_{PF} \times 10^{-3}$	$(K_V' FR)_{SF} \times 10^{-3}$	$(K_V' FR)_{PF} \times 10^{-3}$
B1	-	-	-	-	-8.88	-13.29	0	-	-	-	-
B1+CT	1.22	-	130.3	1.00	-39.02	-16.04	-1.49	-	-	-	-
(B1+H4H4)A	2.0	220.0	-	0.52	-9.00	-13.29	0	-0.008	0	0	0
(B1+CT+H4H4)A	2.0	220.0	-	0.52	-40.11	-16.04	-1.40	-1.88	1.60	0.052	0.047

The average spanwise center of pressure of the fin was determined as follows,

$$\frac{\bar{z}_F}{b_F} = \frac{\ell}{2b_F} \left[\frac{(K_V' FR)_{UF}}{(Y_V' F)_{UF}} - \frac{(K_V' FR)_{LF}}{(Y_V' F)_{LF}} \right] - \frac{1.25}{b_F} \quad [2]$$

The factor $1.25/b_F$ transfers the root bending moment readings, which were measured with respect to the base of the strain-gage balance, to the fin root. See Figure 3. Values of b_F are presented in Table 2.

FIN-ASPECT RATIO AND DIAMETER-SPAN RATIO

The values of the lateral-force coefficient associated with the forces on the fins in the presence of the body, $(Y_V' FF)_B$, are tabulated in Table 4 for each fin configuration associated with bodies B1 and B3. These values have been converted to $(C_{L_{\alpha FF}})_B$ using Equation [1] and are plotted against fin-aspect ratio for various diameter-span ratios in Figure 8. Theoretical values of $C_{L_{\alpha}}$ for the fins alone case ($d_F/2b_F = 0$), obtained from Figure D1, are presented in Figure 8 for comparison.

The results presented in Figure 8, for the various values of $d_F/2b_F$, show the same typical increase in $(C_{L_{\alpha FF}})_B$ with

aspect ratio as for the fins alone case ($d_F/2b_F = 0$). However, for the fins that are completely submerged in the body-boundary layer, ($d_F/2b_F = 0.52$), the values of $(C_{L_{\alpha FF}})_B$ are about 30 to 40 percent lower than the case for the fins alone. Such a decrease in $C_{L_{\alpha}}$ is primarily due to the thick-body boundary in which the fins are completely immersed. See Figure B1. Also, the characteristics of the body sidewash velocity distribution, due to the vortices shed by the body, affects the lift contributed by the fins. The characteristics of the body sidewash velocity distribution will be discussed in a later section. For the fin configurations operating in a flow field which has a minimum body-boundary layer (see Figure B7) and a favorable sidewash due to the body cross-flow velocity, ($d_F/2b_F = 1.43$), the values of $(C_{L_{\alpha FF}})_B$ are about 30 to 40 percent higher than the case for the fins alone. The increase in the effective aspect ratio of the fins due to the reflection of the body is also evident in this case. The values of $(C_{L_{\alpha FF}})_B$ for the fins that are partially immersed in the body-boundary layer, ($d_F/2b_F = 0.72$), are in good agreement with the values for the fins alone. The agreement in these cases would imply that the negative effects of the body-boundary layer are just cancelled by the positive effects of the body reflection.

The aforementioned trends are further illustrated by the variation of the average-spanwise center of pressure with aspect ratio and diameter-span ratio presented in Figures 9 and 10, respectively. As shown by Figures 9 and 10, the spanwise center of pressure moves outboard on the fins as the aspect ratio and diameter-span ratio are decreased. This outboard movement im-

plies a change in the spanwise loading on the fins from approximately elliptical to approximately trapazoidal (see Figure D8).

The variations of $(C_{L_{\alpha FF}})_B$ and the body-induced lift parameter with diameter-span ratio are presented in Figures 11 and 12, respectively, for the fin configurations operating in a flow field having a minimum body-boundary layer (Body B3). Also, the theoretical curves presented in Figures D7 and D8 are reproduced in Figures 11 and 12 for comparison purposes and will be discussed in a later section. The body-induced lift parameter presented in Figure 12 is a direct measure of the induced lift on the body due to the presence of the fins. As shown in Figure 12, the lift induced on the body by the fins increases with an increase in the diameter-span ratio.

FIN-TAPER RATIO

The effects of fin-taper ratio on the fin lift and spanwise center of pressure were investigated for fins having a constant aspect ratio of 2.0 and taper ratios of 0.45, 1.0 and 1.5. The variations of $(C_{L_{\alpha FF}})_B$ and the average spanwise center of pressure with fin-taper ratio, resulting from this phase of the study, are presented in Figure 13 for several diameter-span ratios. The spanwise center of pressure results are also presented in Figure 10 as a function of diameter-span ratio. As expected, the trends presented in Figures 8 and 13 show an increase in $(C_{L_{\alpha FF}})_B$ with an increase in taper ratio for all diameter-span ratios, and an outboard movement of the center of pressure with an increase in fin taper ratio and a decrease in diameter-span ratio. Both of these trends are probably due to the fact that the fin areas located in a higher velocity region

outside the body boundary layer are increased with the increase in taper ratio. The effect on fin-lift caused by an increase in fin-taper ratio is interesting. However, the use of fin-taper ratios greater than 1.0 are not practical, due generally to both structural and operational problems that might be encountered in a given submerged body design.

LONGITUDINAL POSITION OF FINS

The static lateral stability characteristics of the fin-body combinations were determined for two longitudinal positions of the fins on body B1 and one longitudinal position of the fins on body B3. An interesting result is obtained by plotting the values of N_v' versus the values of Y_v' for each configuration as shown in Figure 14. The coefficients for Series 58 bodies, obtained from Reference 15, are also presented in Figures 14(a) and 14(b). In addition, values of $(N_v')_I$ (Ideal or Munk moment) for several fineness ratios and prismatic coefficients corresponding to the Series 58 bodies are presented in Figure 14(a). As shown in Figure 14(a), the results for all the fins located at $(x'_F)_{\bar{c}/4} = -0.45$ on body B1 collapse on a straight line which passes through the bare body values and approximately through the value of $(N_v')_I$ (corresponding to an $\ell/d = 7.33$) and has a slope of 0.44. Similarly, in Figure 14(b), the data for all the fins located at $(x'_F)_{\bar{c}/4} = -0.40$ on body B1 collapse on a straight line which passes through the bare body values and has a slope of 0.37. Straight lines have been drawn through the Series 58 data points, presented in Figures 14(a) and 14(b), which have the same slope as the data curves. It is conjectured that if the present fin series is used in combination with other Series 58 bodies, at the same longitudinal locations, the resulting measurements

would collapse on the lines shown in Figures 14(a) and 14(b), respectively. The results for body B3 are presented in Figure 14(c). The magnitudes of the slopes presented in Figure 14 are related to the effective longitudinal position of the center of pressure of the forces due to the fins with respect to the body center of buoyancy (reference point). However, a more direct measure of the effective longitudinal center of pressure of the forces due to the fins can be obtained by analyzing the mutual interference factors, $\Delta 3Y_v'$ and $\Delta 3N_v'$, presented in Table 4. The interference factors used in the present study can be defined in a manner similar to that presented in References 8 and 24. The total force on the fin-body due to sideslip can be expressed as,

$$(Y_v')_{B+FF} = Y_v'{}_B + (Y_v'{}_{FF})_B + (Y_v'{}_B)_{FF} \quad [3]$$

$$= Y_v'{}_B + \Delta 3Y_v' \quad [4]$$

and the mutual interference increment can be expressed as,

$$\Delta 3Y_v' = [(Y_v')_{B+FF} - Y_v'{}_B] \quad [5]$$

The mutual interference increments of the fin-body combination, that is $\Delta 3Y_v'$, $\Delta 3N_v'$, and $\Delta 3K_v'$ are made up of two separate interference increments. For example, the increment $\Delta 3Y_v'$ consists of the interference of the fins on the body, which can be expressed as,

$$\begin{aligned} \Delta 4Y_v' &= [(Y_v')_{B+FF} - Y_v'{}_B] - (Y_v'{}_{FF})_B \\ &= (Y_v'{}_B)_{FF} \end{aligned} \quad [6]$$

and the interference of the body on the fins,

$$\Delta 5Y_v' = (Y_v'_{FF})_B - Y_v'_{FF} \quad [7]$$

where

$Y_v'_{FF}$ is the lateral-force coefficient for the fins alone.

Values of $Y_v'_{FF}$ were not experimentally determined during the present study and therefore the interference increments $\Delta 5Y_v'$, $\Delta 5N_v'$, and $\Delta 5K_v'$ were not evaluated. Values for the fins alone presented in Figure D1 or in Reference 13 may be used to evaluate these increments.

Equation [5] can be also expressed as,

$$\Delta 3Y_v' = (Y_v'_{FF})_B + (Y_v'_{FF})_B \quad [8]$$

$$= (Y_v'_{FF})_B \left[1 + \frac{(Y_v'_{FF})_B}{(Y_v'_{FF})_B} \right] \quad [9]$$

Substituting $\Delta 4Y_v'$ from Equation [6] for $(Y_v'_{FF})_B$ in Equation [9] we have

$$\Delta 3Y_v' = (Y_v'_{FF})_B \left[1 + \frac{\Delta 4Y_v'}{(Y_v'_{FF})_B} \right] \quad [10]$$

Values of the increment $\Delta 4Y_v'$ are presented in Table 4. The body induced lift parameter,

$$1 + \frac{\Delta 4Y_v'}{(Y_v'_{FF})_B} \quad [11]$$

is also tabulated in Table 4 and is plotted versus diameter-span ratio for all the fins in Figure 12.

The effective longitudinal center of pressure of the forces acting on the fins and induced on the body can be evaluated using the ratio of the increments

$$x_F' = \frac{\Delta 3N_v'}{\Delta 3Y_v'} \quad [12]$$

The average value of x_F' for all the fins can be obtained by plotting the increments $\Delta 3N_v'$ versus $\Delta 3Y_v'$ as shown in Figure 15. It should be noted that the effective values of x_F' determined in this manner agree quite well with the magnitude of the slopes evaluated in Figure 14. Also, the effective values of x_F' are in reasonably good agreement with the values of $(x_F')_{\bar{c}/4}$ for the fins appended to body B1. The disagreement between the effective value of x_F' and $(x_F')_{\bar{c}/4}$ for body B3 might be due to the manner in which the load induced on the body by the fins is distributed longitudinally on body B3.

FAIRWATER-BODY INTERFERENCE

The interference effects of a fairwater (CT), appended to body B1, on the contribution of vertical and horizontal fins having an aspect ratio of 2.0 were evaluated. The static stability derivatives and interference factors for the vertical and horizontal fins are summarized in Tables 5 and 6, respectively.

As shown in Table 5 and Figure A23, for both longitudinal positions of the fins, the lift on the upper fin is about an order of magnitude less than the lift on the lower fins. The total lift contributed by the fins is about 30 to 40 percent less than the case without fairwater interference. (See Table 4.) The mutual interference increments $\Delta 3Y_v'$ also re-

flect the same degradation in the fin-body contribution. The effects on the upper fin are due to the adverse sidewash created by the trailing vortices generated by the lift of the body-fairwater combination. Also, the trailing vortex system and the images in the body tend to provide a favorable sidewash in the plane of the lower fins, thus enhancing the lift contribution of these fins.

The effects of the trailing vortex system due to the lift of the body-fairwater combination also impose an asymmetrical loading on the horizontal fins as shown in Table 6 and Figure A25.

The trends presented in Tables 5 and 6 as well as Figures A23 and A25 can best be explained by analyzing the results of the flow survey and flow visualization tests discussed in the next section.

FLOW CHARACTERISTICS

Velocity and flow angularity measurements were made in both the vertical and horizontal planes of the after sections of bodies B1, B1+CT, and B3 corresponding to the region where the fins are located. These measurements were made over a range of sideslip angles and for various distances from the surface of the bodies. The results of these surveys are presented in Appendix B.

Qualitative measurements of the flow angularity at the stern of bodies B1 and B1+CT were made using the tuft-grid technique. The results obtained from the flow visualization tests compliment the flow survey measurements and provide an overall picture of the flow angularity induced at the fin locations due to the vortices shed by the body and body-fairwater combinations.

FLOW SURVEY AND VISUALIZATION RESULTS

An overall picture of the variation in the spanwise distribution of the local sideslip angles, β_L , to which the fins are subjected can be obtained for bodies B1, B1+CT, and B3 from the slopes of the curves (taken at $\beta = 0$) presented in Figures B10, B11, and B16, respectively. Values of the lateral-flow angle parameter $\partial\beta_L/\partial\beta$, which are proportional to the fin angle of attack, are plotted versus a nondimensional vertical distance parameter, z/R_{\max} , in Figures 16 and 17 for bodies B1 and B3, respectively. The measured spanwise distribution of $\frac{\partial\beta_L}{\partial\beta}$ for body B1 is compared with the potential flow distribution associated with the cross-flow velocity around a cylinder (see Reference D6) in Figure 16. As shown in Figure 16, the

measured values of $\partial\beta_L/\partial\beta$ exceed the potential flow values over a good part of the fin span. However, in a vicinity near the fin root, the measured distribution of $\partial\beta_L/\partial\beta$ is markedly smaller than the potential flow distribution. The character of the $\partial\beta_L/\partial\beta$ distribution can be deduced from the tuft-grid picture presented in Figure 18(a) for body B1. The pair of vortices shed by the lifting body produces positive and negative sidewash velocities; that is, positive velocities above the vortex centers and negative velocities below the vortex centers as illustrated in Figure 18(c). As shown in Figure 17, the $\partial\beta_L/\partial\beta$ distribution for body B3 is in very good agreement with the potential flow distribution associated with the cross-flow velocity around a cylinder. A more extensive discussion of the effects of viscosity on the vortex characteristics associated with bodies of revolution are presented in References 25 and 26.

The interference effects of the body-fairwater combination on the lift of the vertical and horizontal fins are illustrated by the $\partial\beta_L/\partial\beta$ distribution presented in Figure 16, the α_L distribution presented in Figure B12, and the tuft-grid picture presented in Figure 18(b). The strong tip vortex from the fairwater shown in Figure 18(b), in combination with its image in the body, produces a negative sidewash distribution in the plane of the upper vertical fin resulting in the $\partial\beta_L/\partial\beta$ distribution presented in Figure 16. In addition, the body image of the fairwater-tip vortex enhances the strength of the body lower vortex which provides a favorable sidewash distribution in the plane of the lower fin as shown in Figure 16. The enhanced lower body vortex also induces an asymmetrical angle of attack distribution on the horizontal fins as shown in Figure B12. An illustration of the overall induced effects caused

HYDRONAUTICS, Incorporated

-35-

by the body-fairwater interference is presented in Figure 18(d). The fin force and moment data discussed in Tables 5 and 6 can be better understood after studying the aforementioned results.

CORRELATION WITH THEORY

The results of the Modified Lifting Surface Method (MLSM) presented in Figures D6, D7, and D8 of Appendix D are used to calculate theoretical values of $(\Delta 3Y_V')_C$ for comparison with the measured values of $(\Delta 3Y_V')_M$. The measured values of $(\Delta 3Y_V')_M$ are defined by Equations [5] and [8]. The MLSM expression for $(\Delta 3Y_V')_C$ can be written as,

$$(\Delta 3Y_V')_C = -57.3 \frac{2A_F}{l^2} \left[C_{L_{\alpha F} B} + C_{L_{\alpha B} F} \right] \quad [13]$$

$$= -57.3 \frac{2A_F}{l^2} \left[C_{L_{\alpha F} B} \left(1 + \frac{C_{L_{\alpha B} F}}{C_{L_{\alpha F} B}} \right) \right] \quad [14]$$

It should be noted that Equation [14] has the same form as Equation [9].

The comparisons between measured and theoretical values of $\Delta 3Y_V'$ for the configurations associated with bodies B1 and B3 are presented in Figure 19. For the case of the fins located at $(x_F')_{\bar{c}/4} = -0.45$ on body B1, presented in Figure 19(a), the measured values of $(\Delta 3Y_V')_M$ are compared with several results obtained with the MLSM by varying the boundary conditions. See Appendix D. The calculations were made for the following boundary conditions:

MLSM-1. Uniform axial velocity (no boundary layer) and potential cross-flow velocity distribution (results presented in Figures D6, D7, and D8),

MLSM-2. Measured values of axial velocity and cross-flow velocity from Figures 16 and B1

$$\left[\frac{v_n}{U\beta} = \left(\frac{u_n}{U} \right) \frac{\partial \beta_L}{\partial \beta} \right], \text{ and}$$

MLSM-3. Measured values of axial velocity and cross-flow velocity but neglecting load induced on body by fins.

In addition, the measured values of $(\Delta 3Y_v')_M$ are compared with the values based on the lift-curve slope of the fins alone presented in Figure D1. For this case, the fin aspect ratio is defined as $2b_F^2/A_F$ and

$$(\Delta 3Y_v')_C = -57.3 \frac{2A_F}{\ell^2} C_{L_{\alpha FF}} \quad [15]$$

As shown in Figure 19(a), the values of $(\Delta 3Y_v')_C$ obtained using MLSM-1 are about 70 percent larger than the measured values. Including the effects of boundary layer and cross-flow velocity, MLSM-2 produces values of $(\Delta 3Y_v')_C$ which are about 50 percent larger than the measured values. The calculated results obtained with MLSM-3 are only about 10 percent larger than the measured values. Excellent correlation is obtained using the values calculated by Equation [15]. It would appear that the MLSM overestimates the loading induced on the body by the fins.

For the case of the fins located at $(x_F')_{\bar{c}/4} = -0.40$ on body B1 presented in Figure 19(b), the values of $(\Delta 3Y_v')_C$ calculated using the MLSM-1 are about 30 percent larger than the measured values. Values calculated using Equation [15] are about 30 percent lower than the measured values. However, the calculated results obtained with MLSM-3 are only about 10 percent lower than the measured values. This comparison also indicates that the MLSM overestimates the loading induced on the body by the fins.

For the case of the fins located at $(x_F')_{\bar{c}/4} = -0.45$ on body B3 presented in Figure 19(c), the values of $(\Delta 3Y_v')_C$ calculated using the MLSM-1 are in very good agreement with the measured values (about 6 percent higher). However, values calculated using Equation [15] are about 200 percent lower than the measured values. The excellent agreement obtained using MLSM-1 is probably due to the fact that the axial boundary layer for B3 is small and the cross-flow velocity distribution shown in Figure 17 is in good agreement with the potential-flow values. It is expected, therefore, that MLSM-1 can be used successfully in the calculation of the fairwater contribution to the static-lateral stability derivatives because the fairwater is generally located in a thin-boundary-layer regime on the body. Also, as shown in Appendix D, MLSM-1 can be used to calculate the rolling-stability derivatives Y_p' and K_p' which are primarily contributed to by the body-fairwater. The value of N_p' can also be calculated using Y_p' and the appropriate moment arm.

CONCLUSIONS AND RECOMMENDATIONS

Based on the results of a comprehensive series of wind-tunnel experiments conducted to determine the effects of body-boundary layer and sidewash, fin-aspect ratio, fin-taper ratio, and diameter-span ratio on the static-lateral forces and moments of a systematic series of submarine-type fin-body combinations the following conclusions and recommendations are indicated:

1. The fins that are completely submerged in the body-boundary layer, $d_F/2b_F = 0.52$, have lift-curve slopes that are 30 to 40 percent lower than the values for the fins alone. The fin-body configurations which are subjected to a minimum body-boundary layer, $d_F/2b_F = 1.43$, have lift-curve slopes that are 30 to 40 percent higher than the values for the fins alone.
2. The average-spanwise center of pressure of the fins moves outboard as the fin-aspect ratio and diameter-span ratio are decreased.
3. The lift induced on the body by the fins increases with an increase in the diameter-span ratio.
4. The lift-curve slope of the fins increase with an increase in taper ratio for all diameter-span ratios. Also, the average-spanwise center of pressure moves outboard with an increase in fin-taper ratio and a decrease in diameter-span ratio.
5. The static lateral force and yawing moment coefficients results for all the fins located at a given longitudinal position on each body collapse on a straight line which

passes through the bare body values and has a slope equal to the effective longitudinal center of pressure of the forces acting on the fins and induced on the bodies.

6. The effective longitudinal center of pressure of the forces acting on the fins and induced on the body are in reasonable good agreement with the longitudinal distance from the CB to the quarter-chord line of the fins for the Series 58 body.

7. The adverse sidewash created by the trailing vortices generated by the lift of body-fairwater combination decreases the lift on the upper fins and increases the lift on the lower fins. As a result the total fin lift is about 30 to 40 percent less than the cases without the fairwater.

8. The flow survey and visualization techniques provide a physical picture of the flow fields in which the fins operate and a better understanding of the factors affecting the fin contributions.

9. The Modified Lifting Surface Method overpredicts the fin-lateral force and lateral force induced on the body for the thick-boundary layer cases ($d_F/2b_F = 0.52$). However, it accurately predicts the forces for the minimum boundary layer cases ($d_F/2b_F = 1.43$).

10. An accurate prediction of the fin-lateral force and lateral force induced on the body for the thick-boundary layer ($d_F/2b_F = 0.52$) cases was obtained by using values of the lift-curve slopes for the fins alone.

HYDRONAUTICS, Incorporated

-41-

It is recommended that the present study be expanded to include other fin geometries in combination with Series 58 bodies having various fineness ratios. Also, the interference effects of fairwaters on the stern appendages should be systematically studied. The introduction of the Planar Motion Mechanism System as a research tool can now be used to efficiently carry out such investigations using large models. In addition, the PMM can be used to evaluate the rotary and acceleration derivatives for the systematic series. The results of such systematic studies can provide the designer with a powerful "data base" which is presently nonexistent. These results can also be used to check and/or develop close-form expressions for prediction of the stability coefficients.

HYDRONAUTICS, Incorporated

-42-

ACKNOWLEDGEMENTS

The author wishes to express his appreciation to Miss Elizabeth Dempsey of the Hydromechanics Laboratory for her assistance in the carrying out of the theoretical calculations and presentation of test results; to Mr. E. H. Dittrich for his assistance in the preparation of the models and the conduct of the experimental program; to Mr. Leon Money of the Aerodynamics Laboratory for his assistance in the performance of the wind tunnel test program; to Messrs. Meredith Wilson and Jessie Stern for assistance in the design of the strain-gage balances; to Mr. Mills Dean for the excellent job of strain gaging the fin balances; and to Mr. J. Luistro for his help in the calibration of the pitot-static yawhead rake in the Low Turbulence Wind Tunnel.

Also, the author wishes to thank Mr. M. Martin of the Hydromechanics Laboratory for his support and guidance, and Mr. Jerome Feldman for his calculations of the roll dependent coefficients using the Modified Lifting Surface Method presented herein.

HYDRONAUTICS, Incorporated

-43-

REFERENCES

1. Naval Ship Research and Development Center Contract N00167-79-C-0093 dated May 8, 1979.
2. "Nomenclature for Treating the Motion of a Submerged Body Through a Fluid," Technical and Research Bulletin 1-5 of the Society of Naval Architects and Marine Engineers, New York, 1950.
3. Gertler, Morton and Hagen, Grant R., "Standard Equations of Motion for Submarine Simulation," NSRDC Report 2510, June 1967.
4. Landweber, L. and Johnson, J. L., "Prediction of Dynamic Stability Derivatives of an Elongated Body of Revolution," DTMB Report C-359, May 1951.
5. Lennertz, J., "Influence of the Airplane Body on the Wings," Aerodynamic Theory, W. F. Durand, Editor, Durand Reprinting Committee, Vol. IV, 1943, pp. 152-158.
6. Spreiter, John R., "The Aerodynamic Forces on Slender Plane- and Cruciform-Wing and Body Combinations," NACA Report 962, 1950. (Formerly NACA TN's 1662 and 1897.)
7. Pitts, W. C., Nielsen, J. N., and Kaattari, G. E., "Lift and Center of Pressure of Wing-Body-Tail Combinations at Subsonic, Transonic, and Supersonic Speeds," NACA Report 1307, 1957.
8. Goodman, A., "Effects of Wing Position and Horizontal-Tail Position on Static Stability Characteristics of Models with Unswept and 45° Sweptback Surfaces with some Reference to Mutual Interference," NACA TN 2504, October 1951.
9. Lawrence, H. R. and Flax, A. H., "Wing-Body Interference at Subsonic and Supersonic Speeds - Survey and New Developments," Journal of Aeronautical Sciences, Vol. 21, May 1954.
10. Low, L. and Stone, H. N., "The Subsonic Aerodynamic Characteristics of Wings in Combination with Slender Bodies of Revolution," Cornell Aeronautical Laboratory, Bumblebee Report No. CAL/CM-679, July 1951.

HYDRONAUTICS, Incorporated

-44-

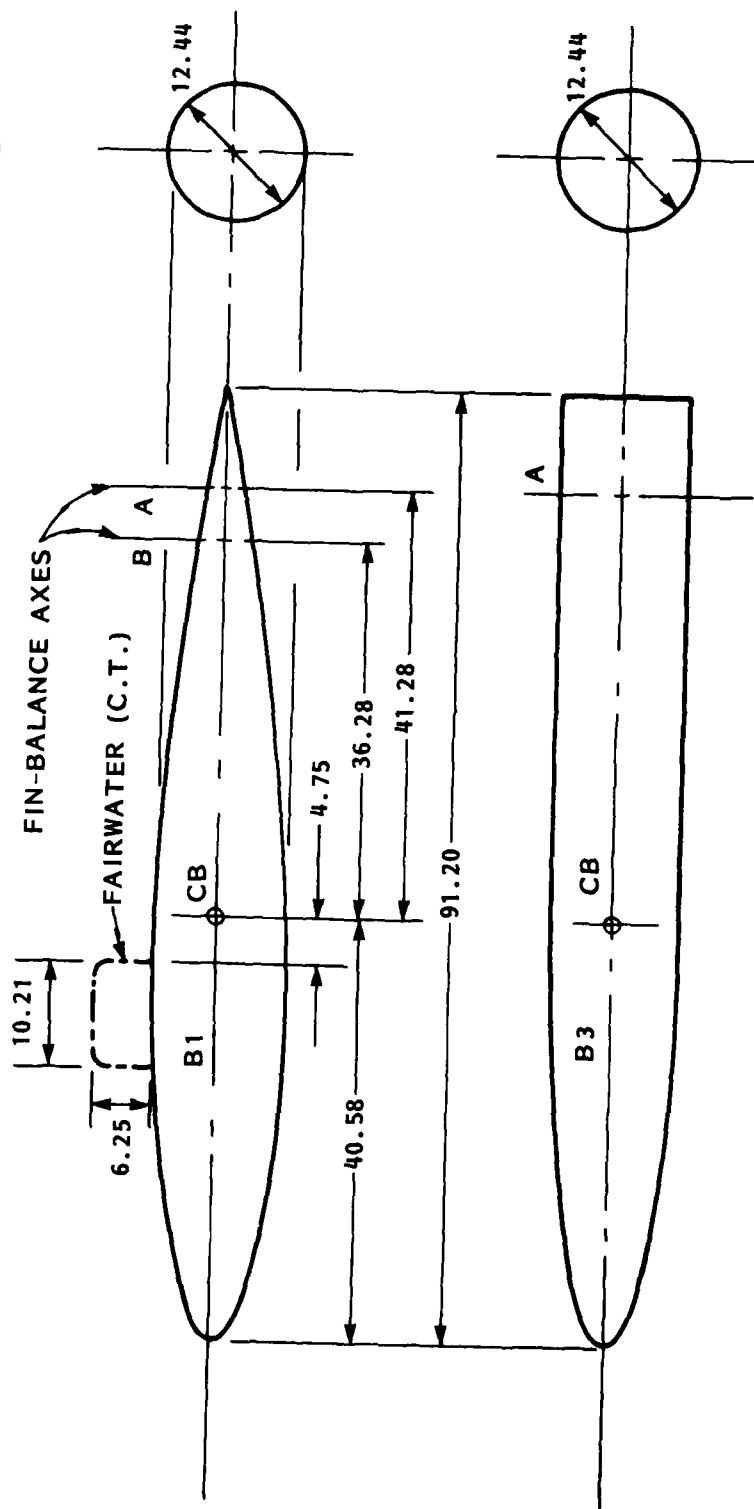
11. Lawrence, H. R., "The Aerodynamic Characteristics of Low-Aspect-Ratio Wing-Body Combinations in Steady Subsonic Flow," Cornell Aeronautical Laboratory Report, No. AF-743-A-6, November 1952.
12. Michael, William H., Jr., "Investigation of Mutual Interference Effects of Several Vertical-Tail-Fuselage Configurations in Sideslip," NACA TN 3135, 1954.
13. Whicker, L. Folger and Fehlner, Leo F., "Free-Stream Characteristics of a Family of Low-Aspect-Ratio, All-Movable Control Surfaces for Application to Ship Design," DTMB Report 933 Revised Edition, December 1958.
14. Johnson, J. L., "The Static Stability Derivatives of a Series of Related Bodies of Revolution," TMB Report C-383, 1951.
15. Johnson, J. L., "PMM Tests to Determine the Static and Dynamic Stability Derivatives of a Systematic Series of Related Bodies of Revolution," DTMB Report (Unpublished).
16. Gertler, M., "The DTMB Planar-Motion-Mechanism-System," paper presented at the Symposium on the Towing Tank Facilities, Instrumentation and Measuring Technique on September 22-25, 1959.
17. Goodman, A., "Experimental Techniques and Methods of Analysis Used in Submerged Body Research," prepared for Third Symposium on Naval Hydrodynamics, held in Scheveningen (The Hague), 19-21 September 1960.
18. Goodman, A. and Gertler, M., "U. S. Patent No. 3,052,120, September 4, 1962 for Planar Motion Mechanism System."
19. "Subsonic Wind Tunnel Facilities," David Taylor Naval R&D Report 3782, January 1972.
20. Gertler, M., "Resistance Measurements on a Systematic Series of Streamlined Bodies of Revolution for Application to the Design of High-Speed Submarines," TMB Report C-297, April 1950.
21. Pope, Alan, "Wind Tunnel Testing," John Wiley and Sons, New York.

HYDRONAUTICS, Incorporated

-45-

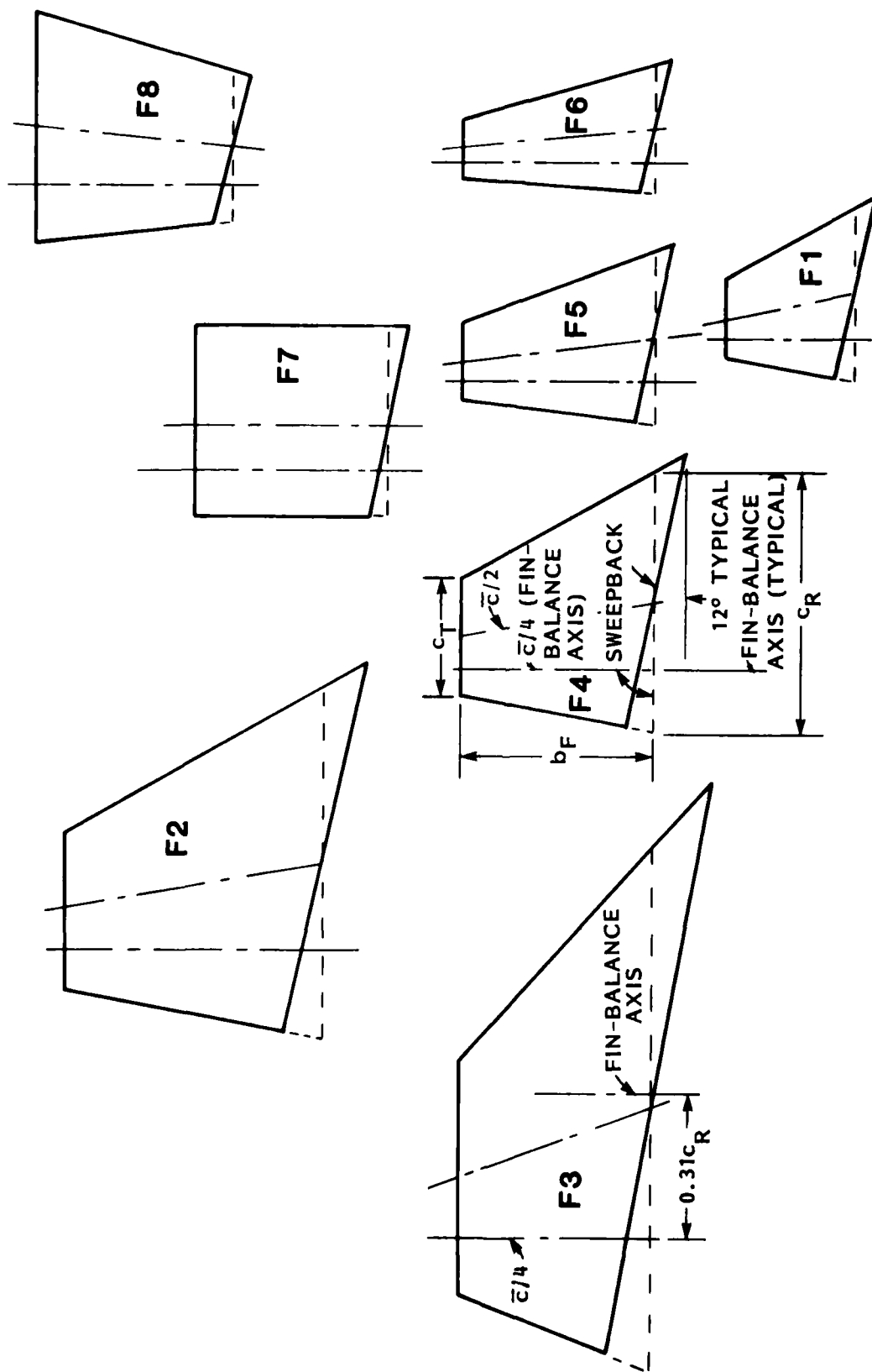
22. Bird, John D. and Riley, Donald R., "Some Experiments on Visualization of Flow Fields Behind Low-Aspect Ratio Wings by Means of a Tuft Grid," NACA TN 2674, 1952.
23. Herriot, John G., "Blockage Corrections for Three-Dimensional-Flow Closed-Throat Wind Tunnels, with Consideration of the Effect of Compressibility," NACA Report 995, 1950. (Formerly NACA RM A7B28.)
24. Goodman, Alex and Thomas, David F. Jr., "Effects of Wing Position and Fuselage Size on the Low-Speed Static and Rolling Stability Characteristics of a Delta-Wing Model," NACA Report 1224, 1955.
25. Harrington, R. P., "An Attack on the Origin of Lift of an Elongated Body," Daniel Guggenheim Airship Institute Publication 2, 1935.
26. Allen, Julian H. and Perkins, Edward W., "A Study of Effects of Viscosity on Flow Over Slender Inclined Bodies of Revolution," NACA Report 1048, 1951.

LONGITUDINAL POSITION OF FIN-BALANCE AXIS, in.	B1		B3
	POSITION B	POSITION A	POSITION A
x' FB	36.28	41.28	41.28
	0.398	0.453	0.453
LOCAL BODY DIAMETER, in.	6.30	4.52	12.44



a. BODY CONFIGURATIONS

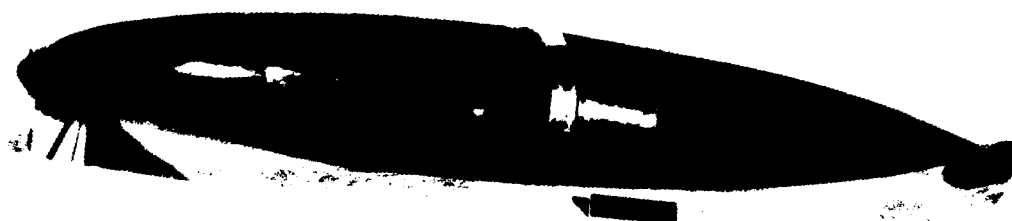
FIGURE 1 - SKETCH OF BODY AND FIN CONFIGURATIONS
(ALL DIMENSIONS IN INCHES)



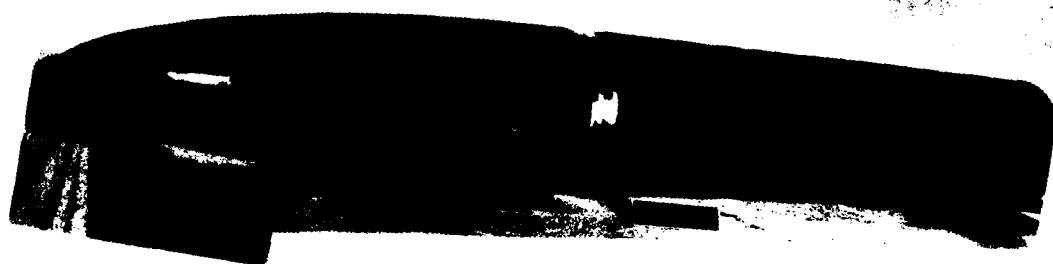
b. FIN CONFIGURATIONS

FIGURE 1 - CONCLUDED

HYDRONAUTICS, INCORPORATED



a. B1



b. B3



c. FINS

FIGURE 2 - PHOTOGRAPHS OF BODY AND FIN CONFIGURATIONS

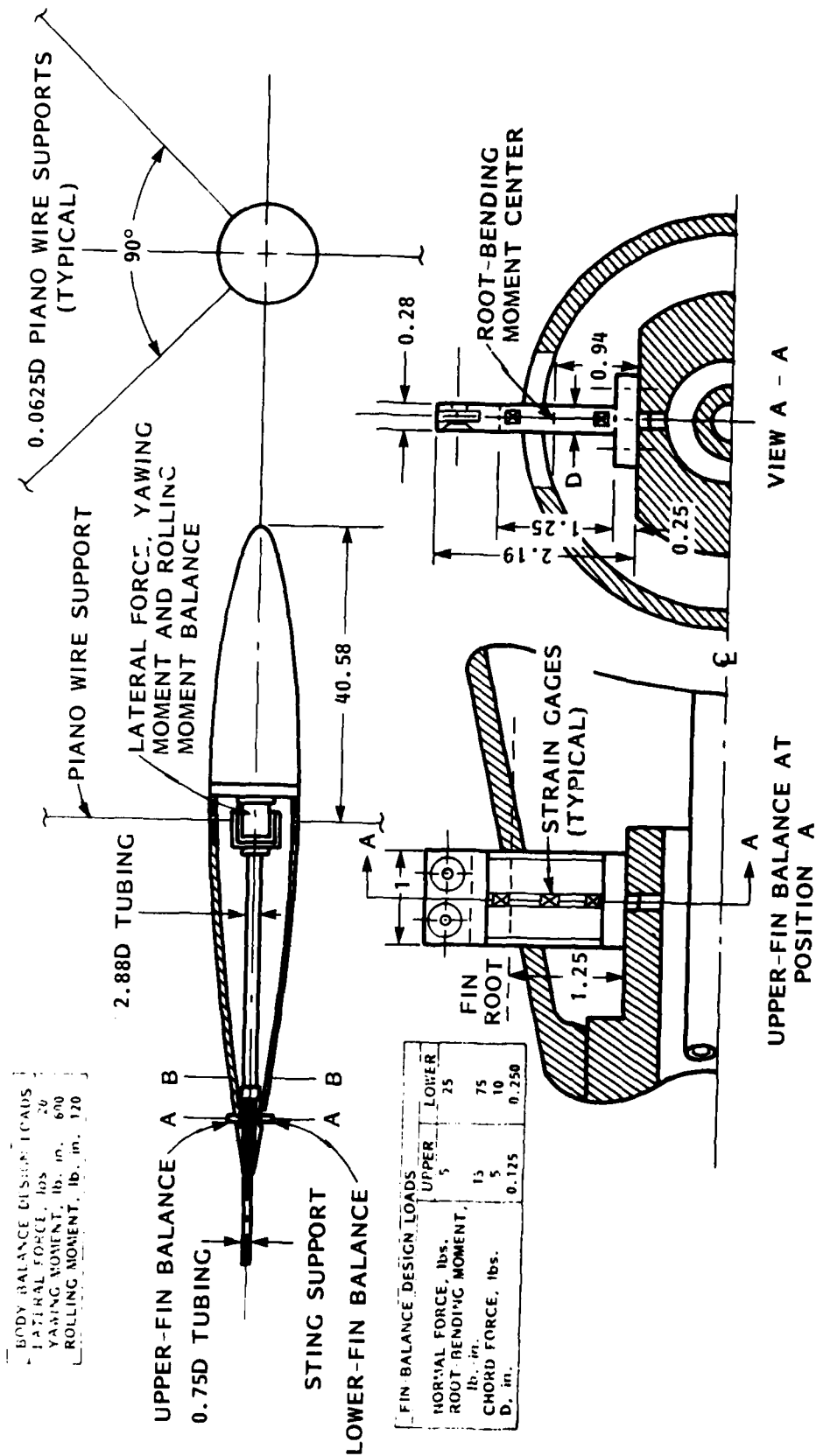
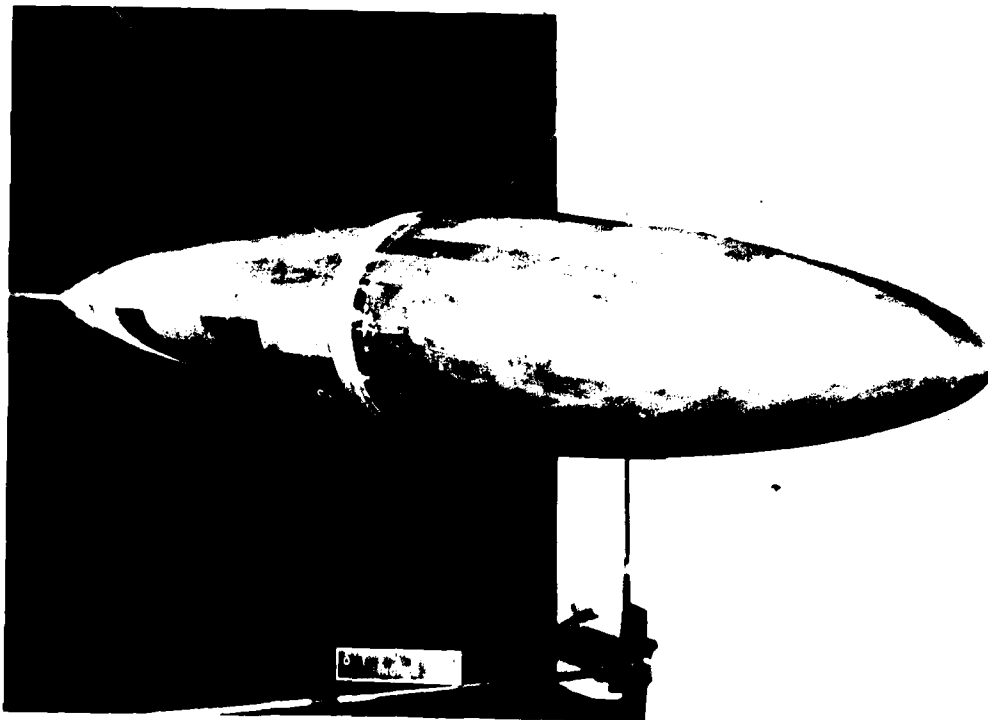
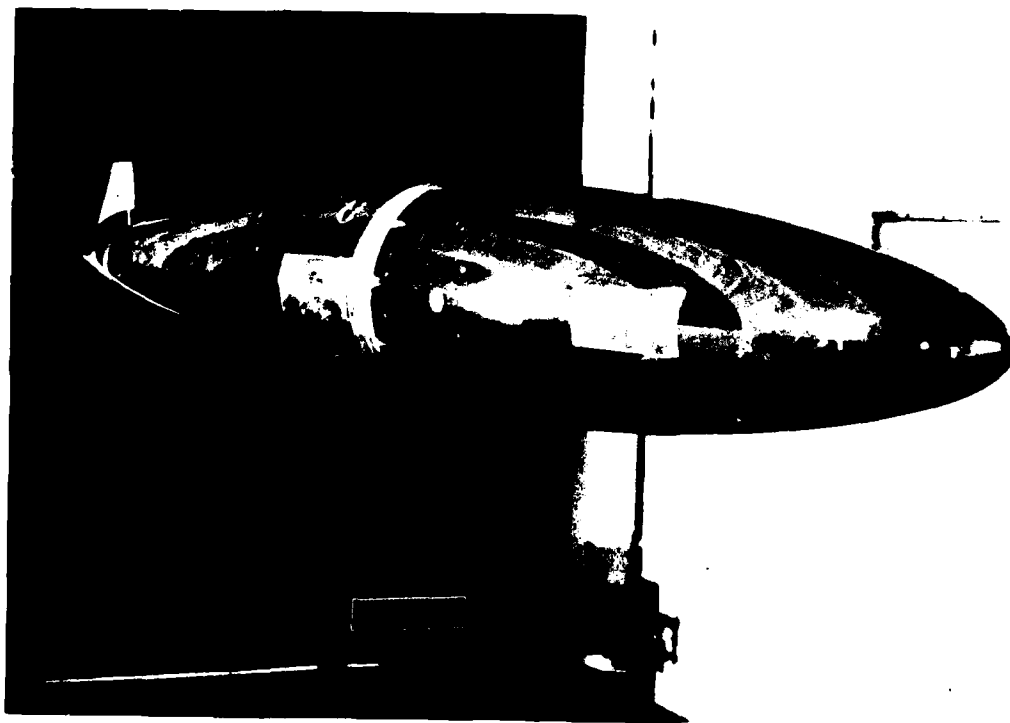


FIGURE 3 - SKETCH DEFINING FIN-BODY BALANCE ARRANGEMENTS AND MODEL SUPPORT SYSTEM (ALL DIMENSIONS IN INCHES)

HYDRONAUTICS, INCORPORATED



a. B1 ALONE



b. B1 + F₄

FIGURE 4 - PHOTOGRAPH OF TYPICAL MODEL INSTALLATION
IN WIND TUNNEL

HYDRONAUTICS, INCORPORATED

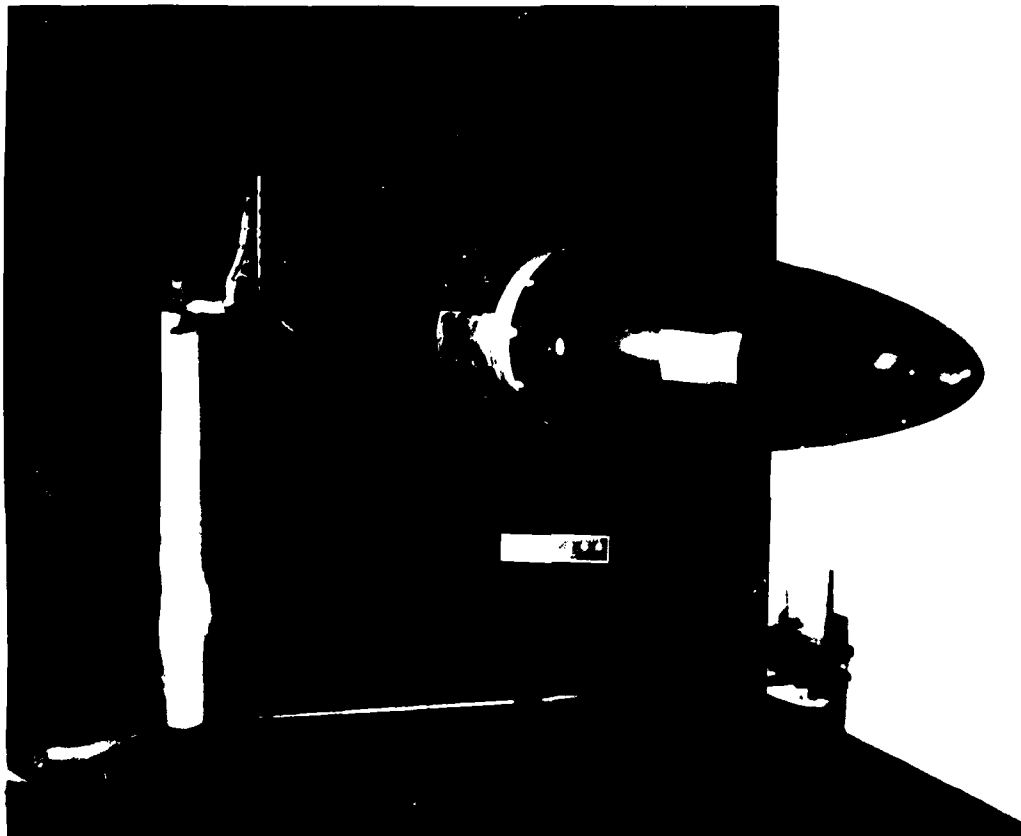
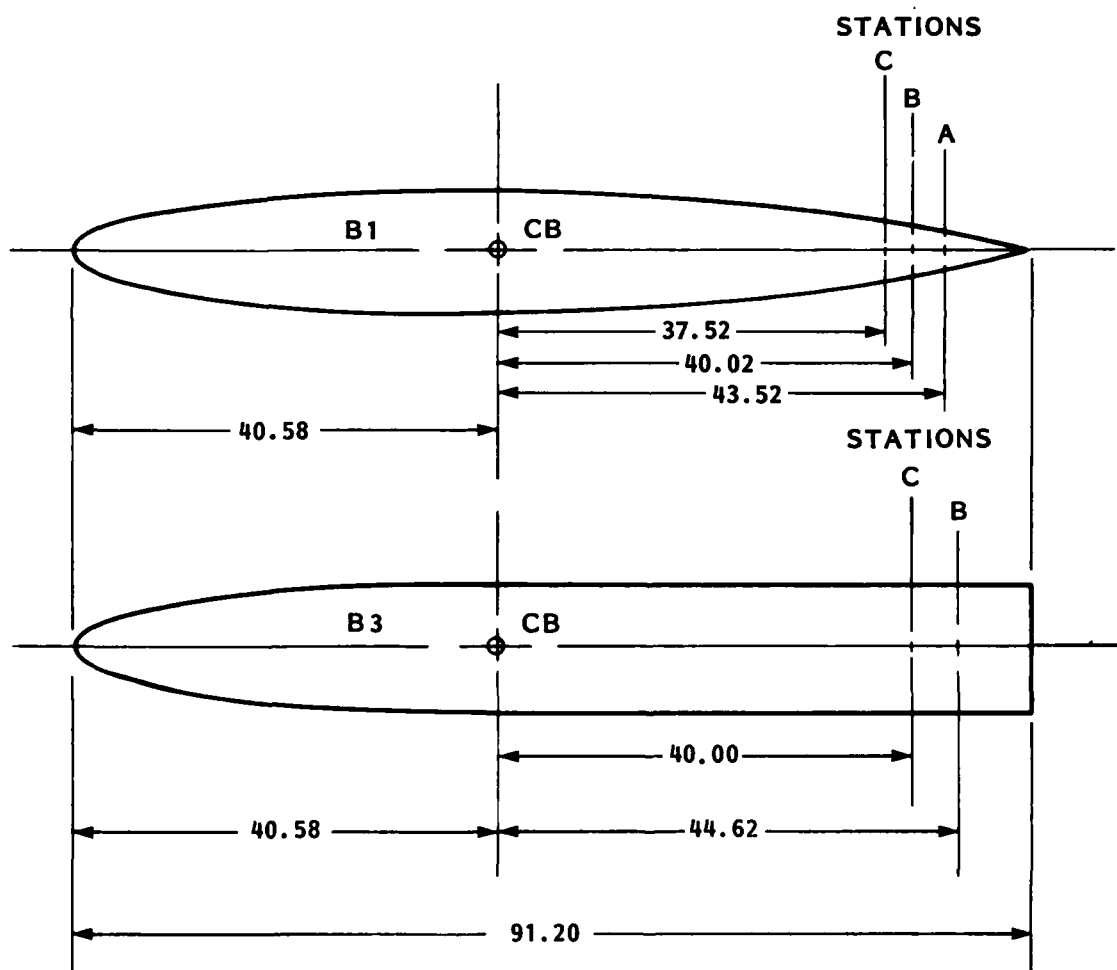


FIGURE 5 - TYPICAL FLOW-SURVEY ARRANGEMENT USING
PITOT-STATIC-YAW-HEAD RAKE

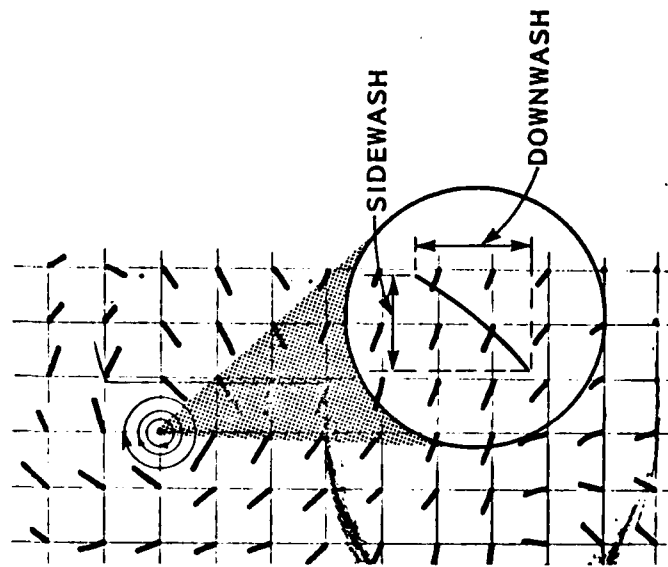
HYDRONAUTICS, INCORPORATED

BODY	SURVEY POSITION	LONGITUDINAL DISTANCE FROM CB		BODY DIAMETER, in.
		in.	x'_{sp}	
B1	A	43.52	0.477	3.50
	B	40.02	0.439	5.00
	C	37.52	0.411	5.90
B3	B	40.00	0.439	12.44
	C	44.62	0.489	12.44

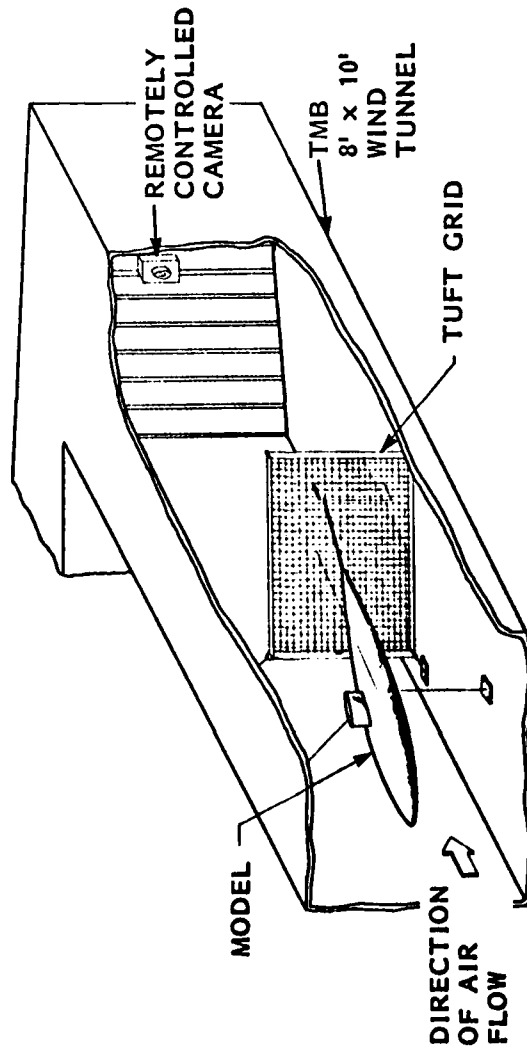


(ALL DIMENSIONS IN INCHES)

FIGURE 6 - SKETCH DEFINING LOCATION OF FLOW-SURVEY STATIONS FOR BODIES B1 AND B3



b. TYPICAL TUFT PATTERN
BEHIND GRID



a. TUFT-GRID TEST SETUP

FIGURE 7 - GENERAL ARRANGEMENT FOR FLOW VISUALIZATION
TESTS USING A TUFT-GRID

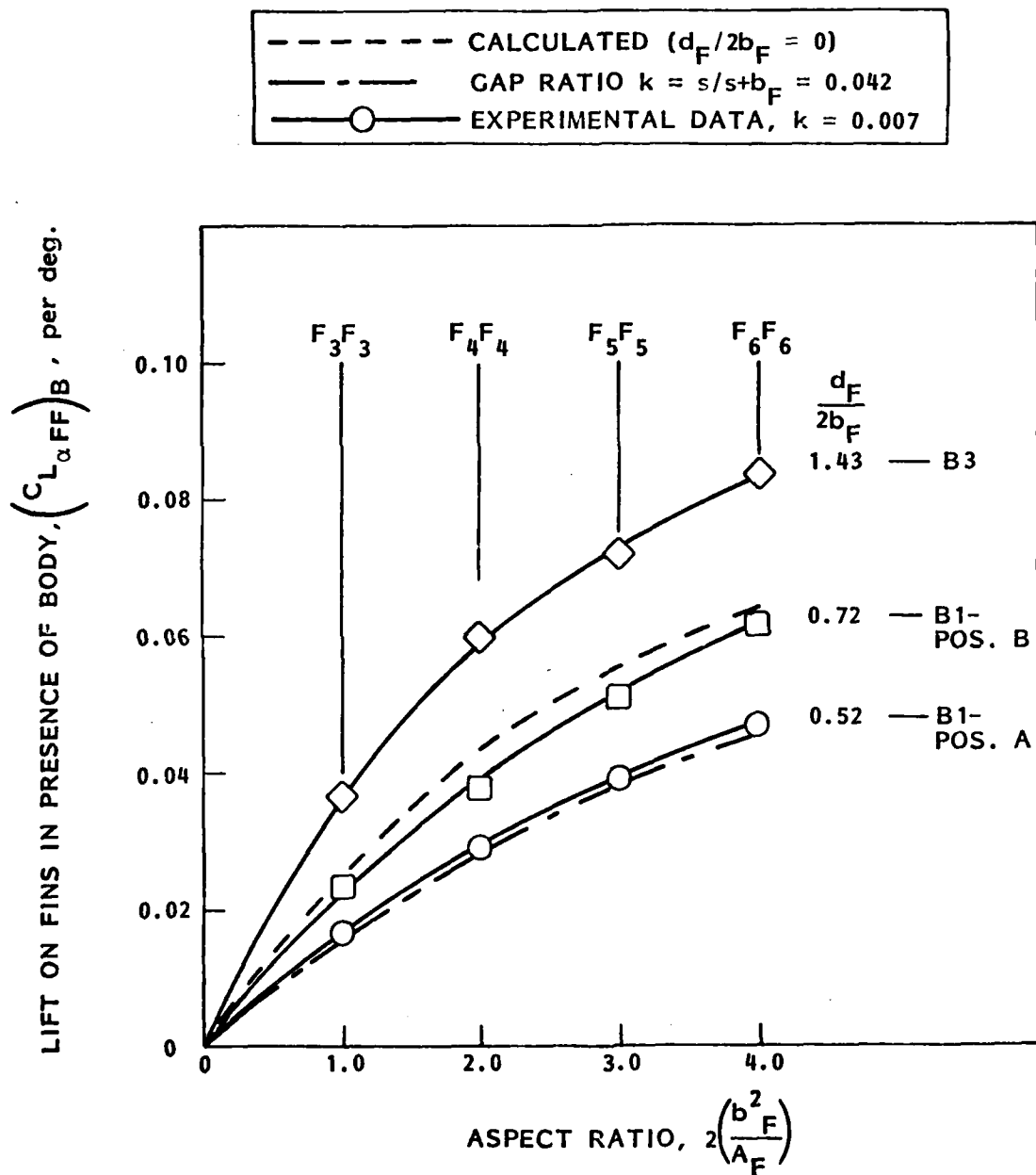


FIGURE 8 - VARIATION OF LIFT ON FINS IN PRESENCE OF BODY WITH ASPECT RATIO AND DIAMETER-SPAN RATIO

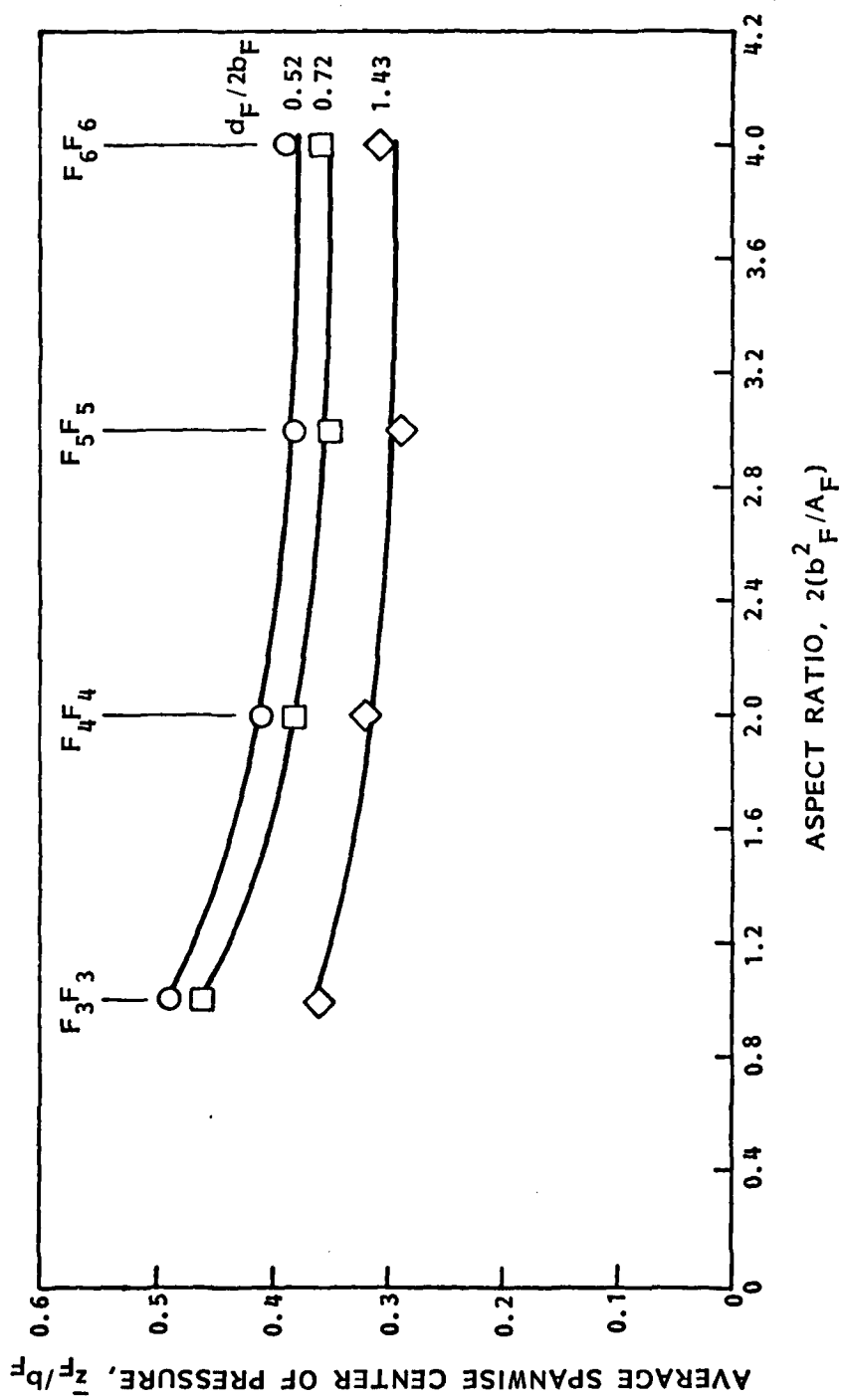


FIGURE 9 - VARIATION OF AVERAGE SPANWISE CENTER OF PRESSURE WITH ASPECT RATIO FOR SEVERAL DIAMETER - SPAN RATIOS

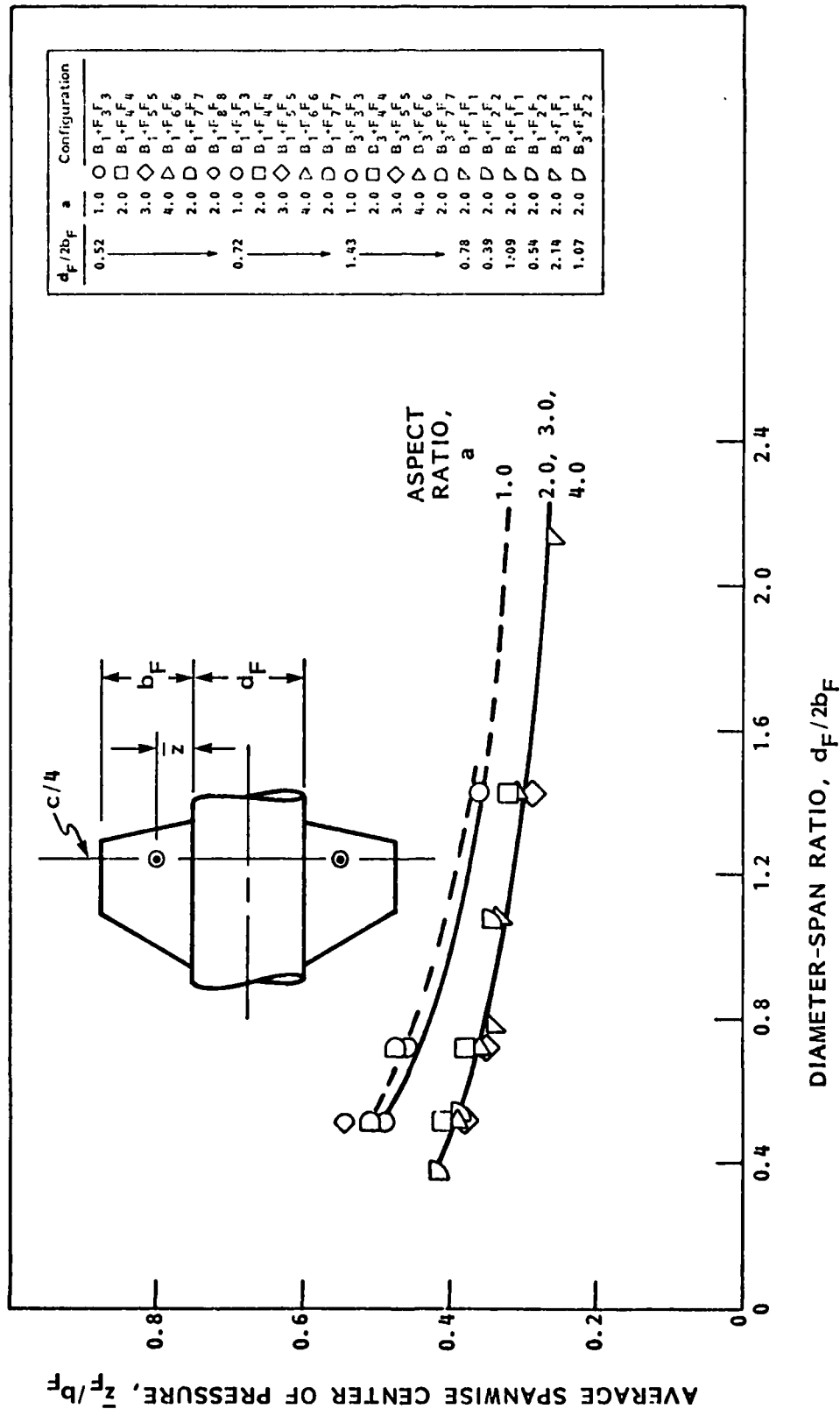


FIGURE 10 - VARIATION OF AVERAGE SPANWISE CENTER OF PRESSURE WITH DIAMETER-SPAN RATIO FOR VARIOUS ASPECT RATIO FINS

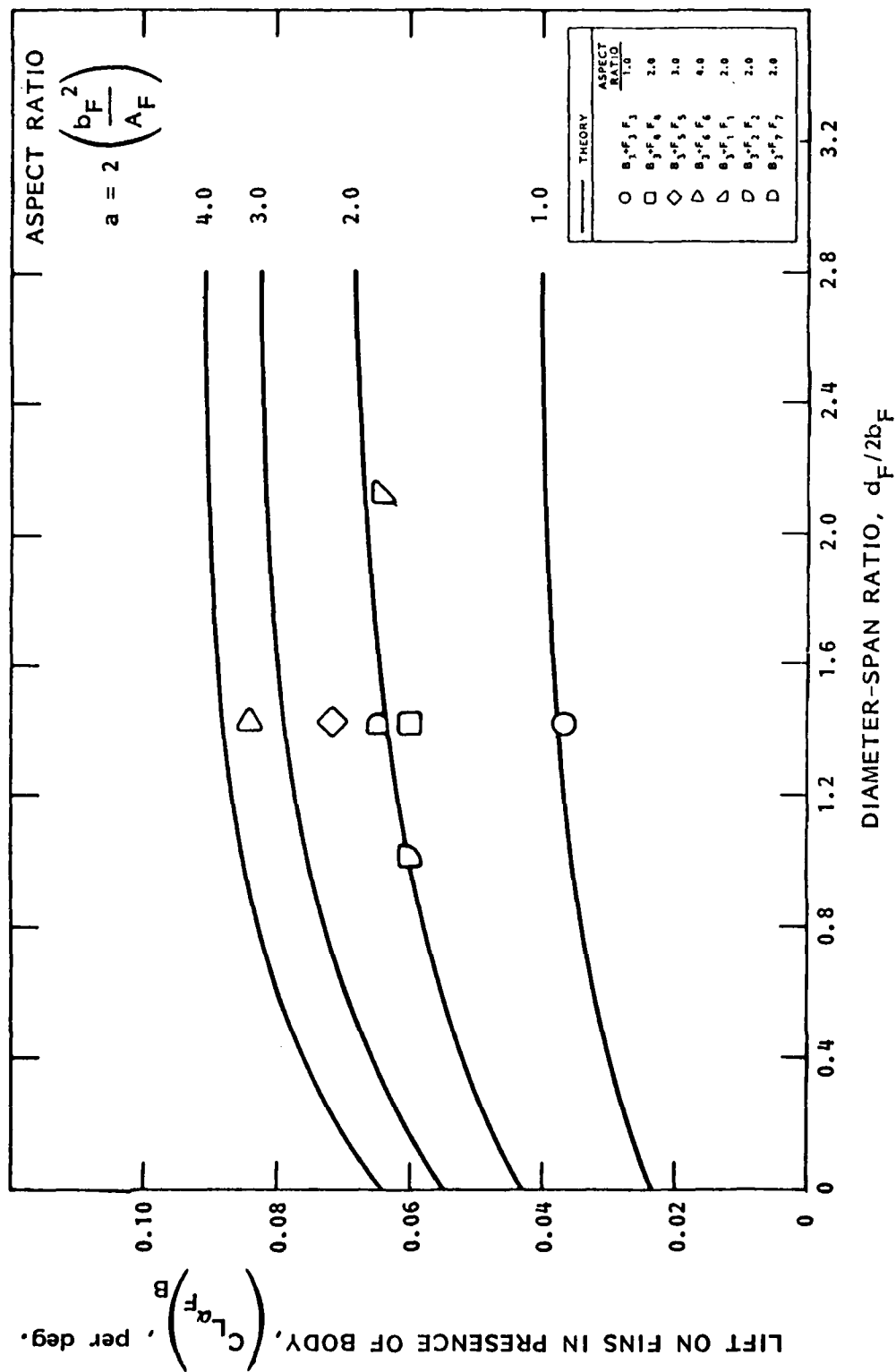


FIGURE 11 - VARIATION OF LIFT ON FINS IN PRESENCE OF BODY WITH DIAMETER-SPAN RATIO FOR SEVERAL ASPECT RATIOS

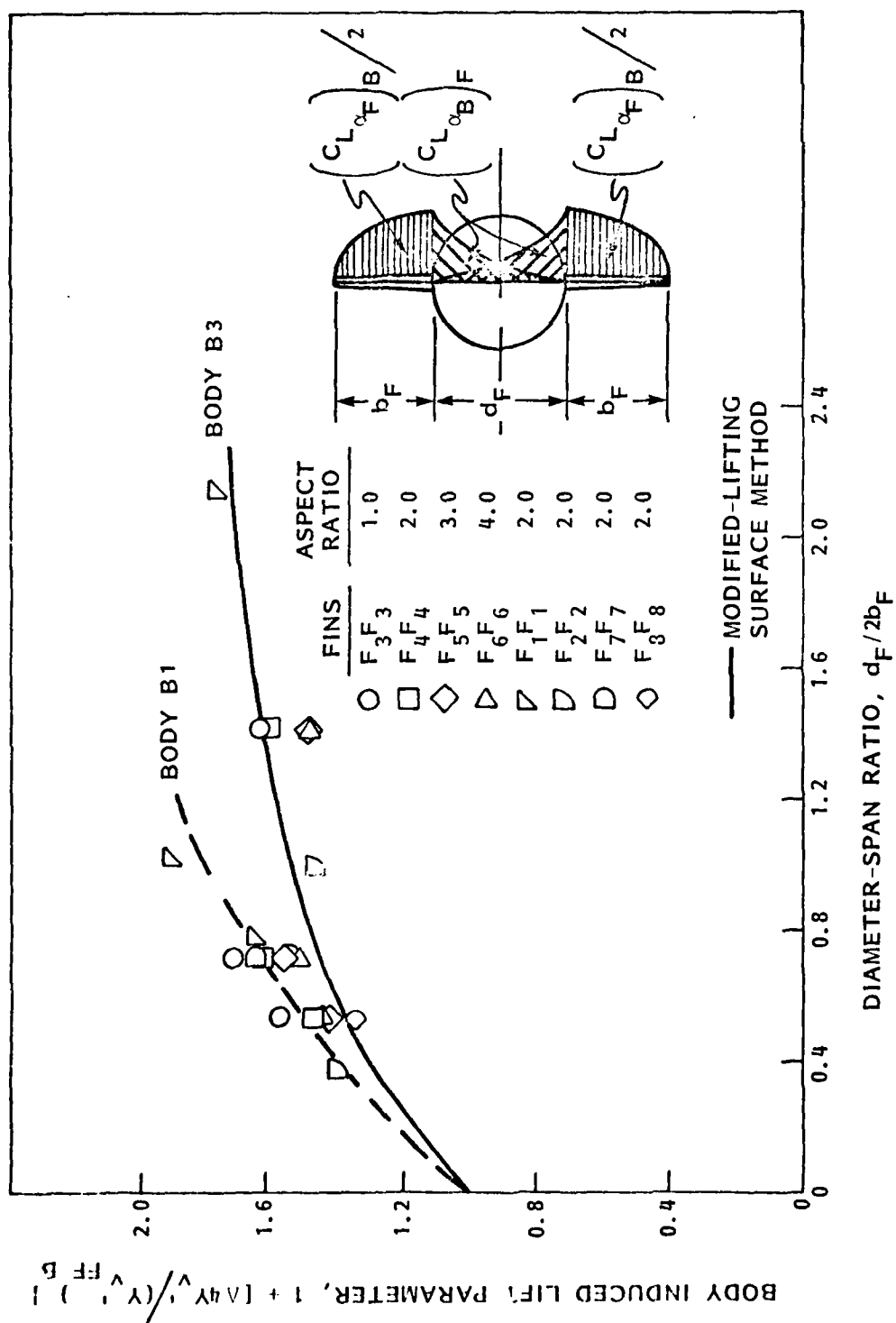


FIGURE 12 - VARIATION OF BODY-INDUCED LIFT PARAMETER WITH DIAMETER-SPAN RATIO

HYDRONAUTICS, INCORPORATED

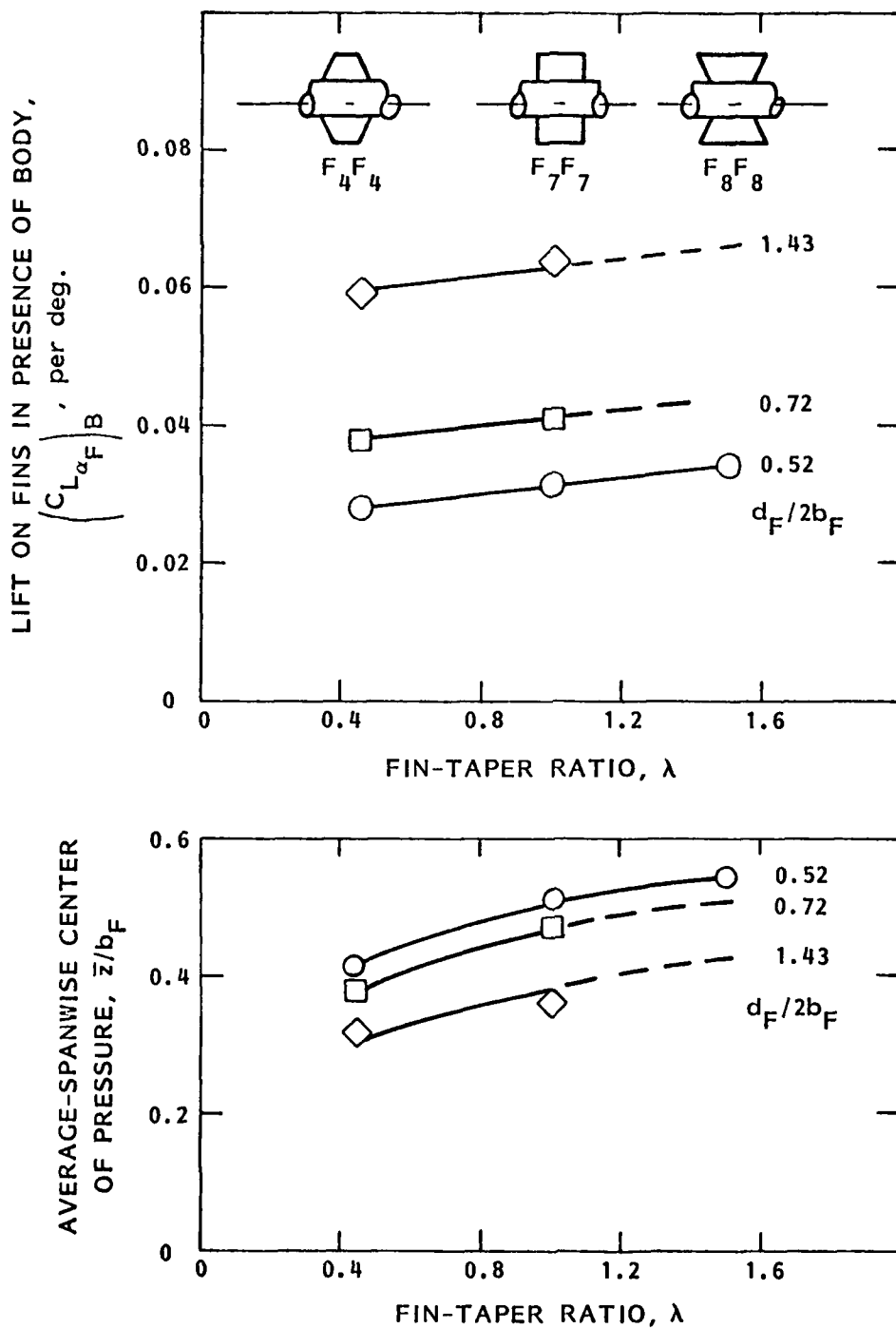


FIGURE 13 - VARIATION OF LIFT-CURVE SLOPE AND AVERAGE-SPANWISE CENTER OF PRESSURE WITH TAPER RATIO FOR SEVERAL DIAMETER-SPAN RATIOS. ASPECT RATIO = 2.0

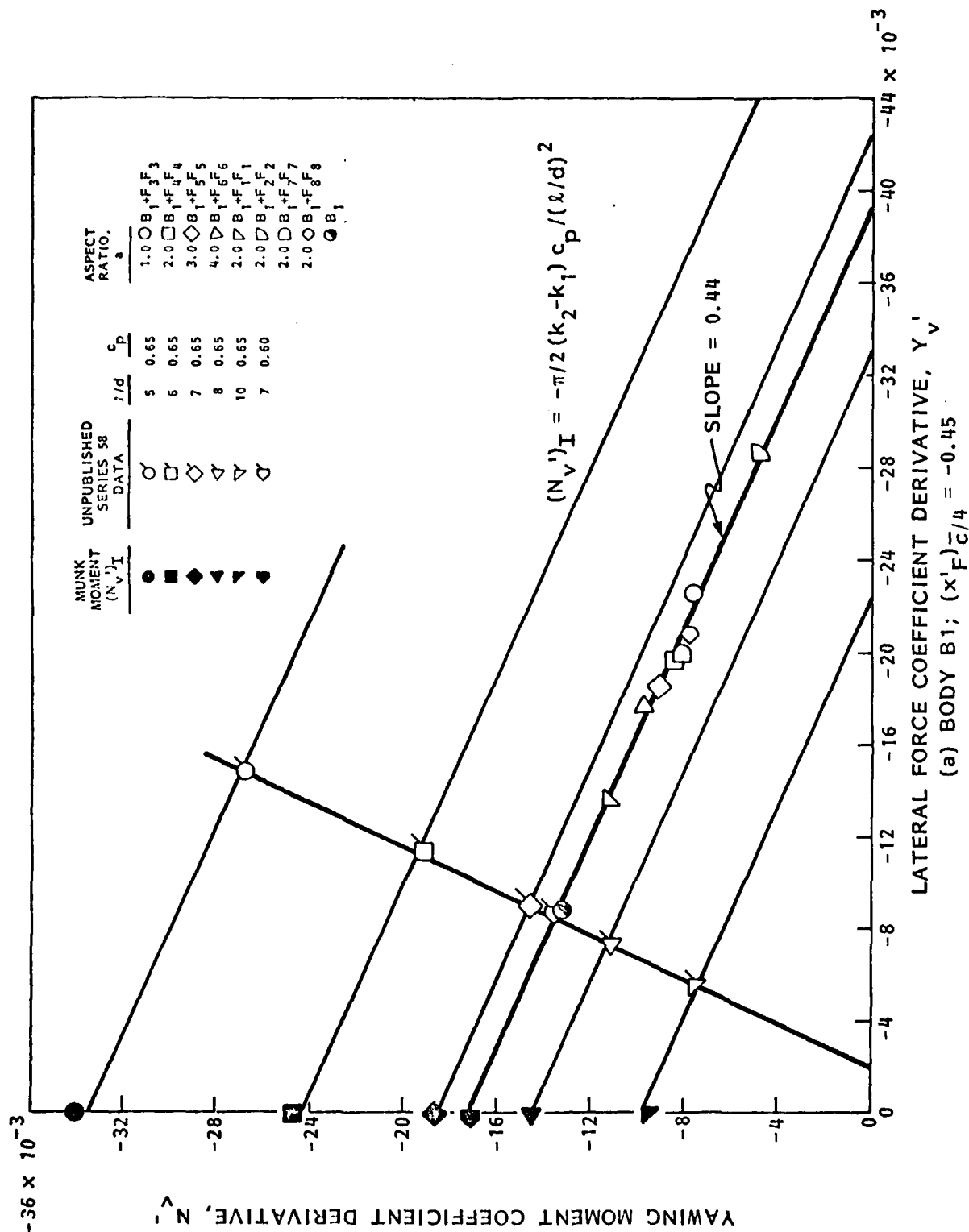


FIGURE 14 - VARIATION OF YAWING-MOMENT DERIVATIVE WITH LATERAL-FORCE DERIVATIVE FOR SEVERAL FIN-BODY CONFIGURATIONS

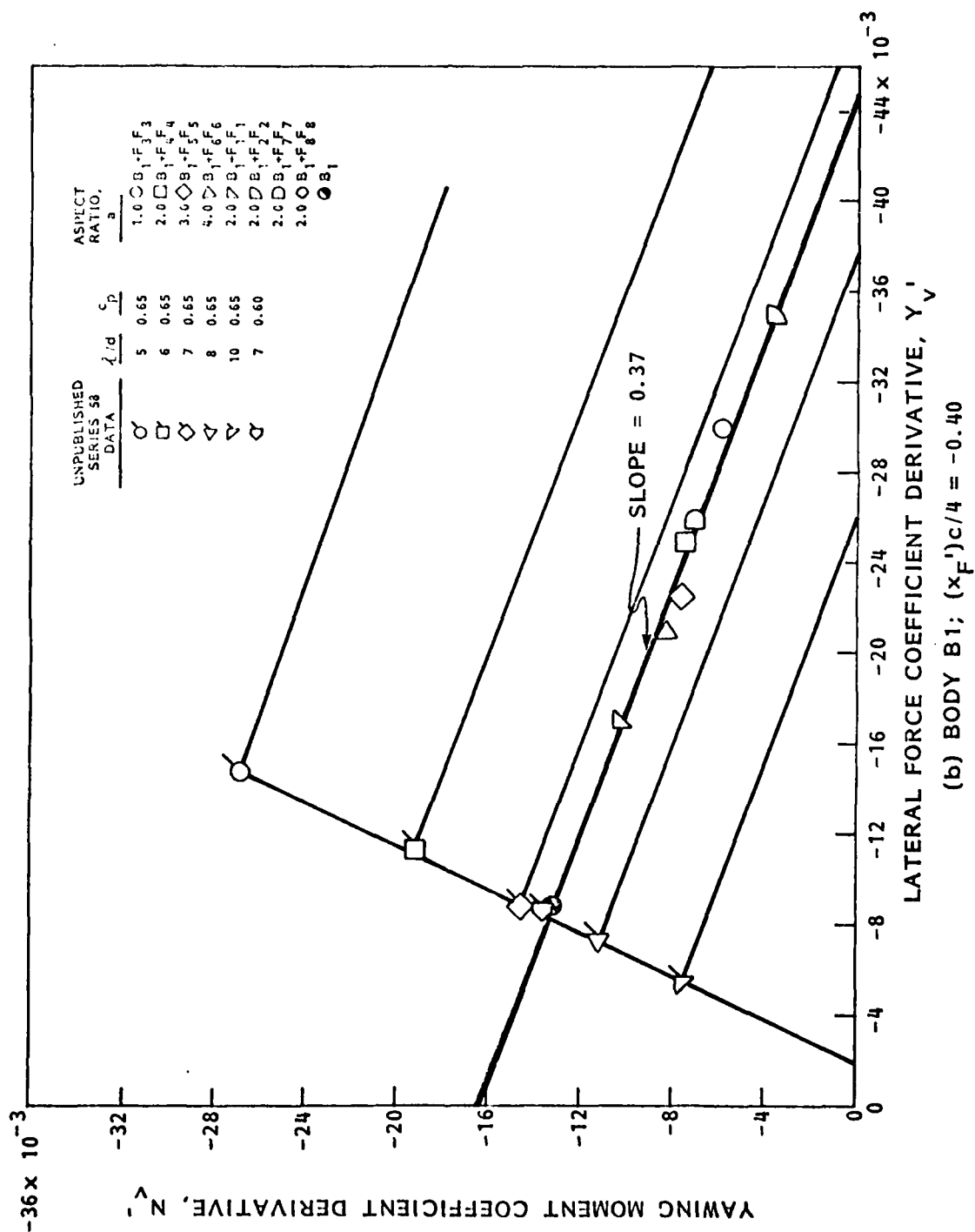
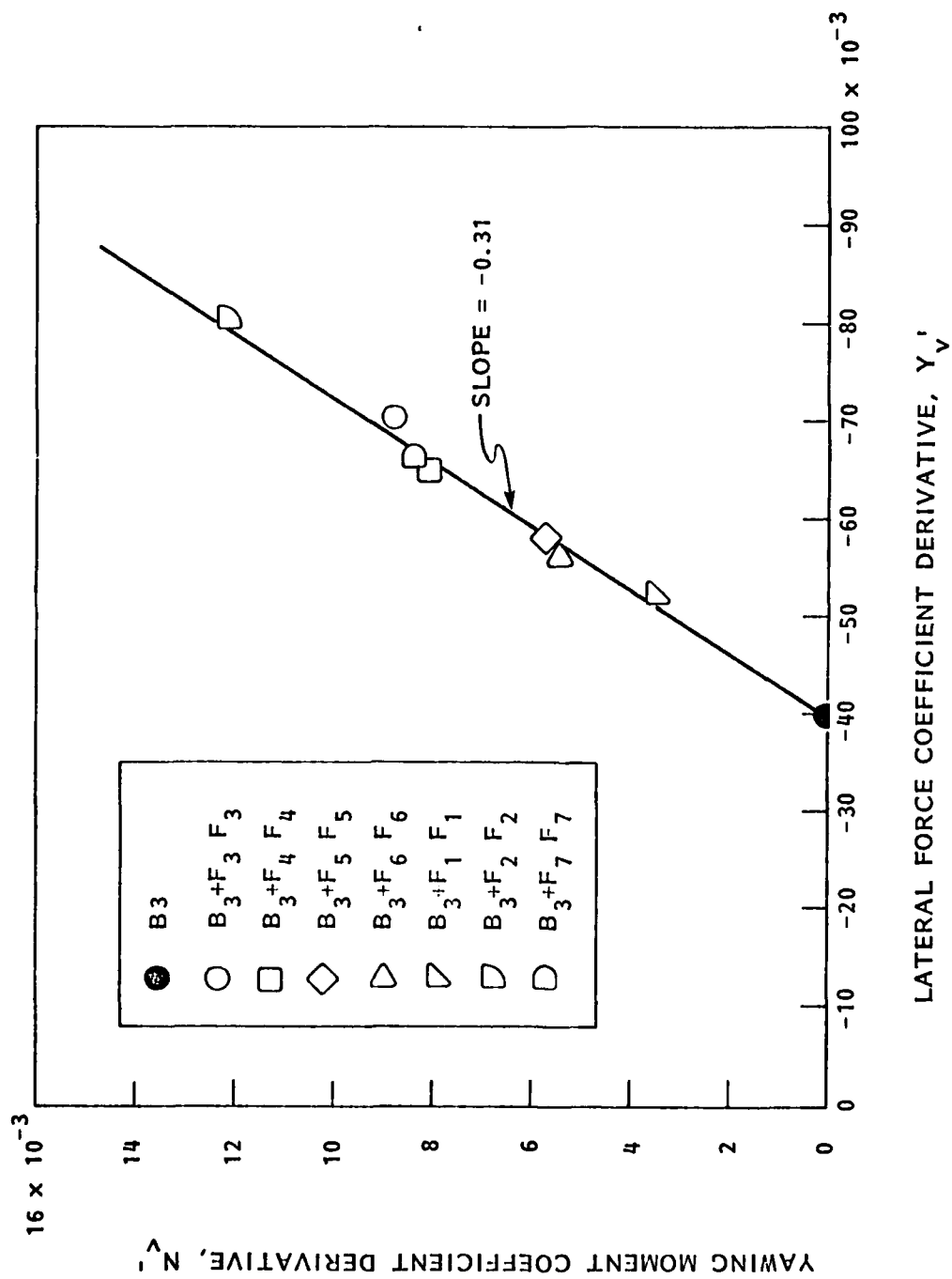


FIGURE 14 - CONTINUED



(c) B3 CONFIGURATIONS

FIGURE 14 - CONCLUDED

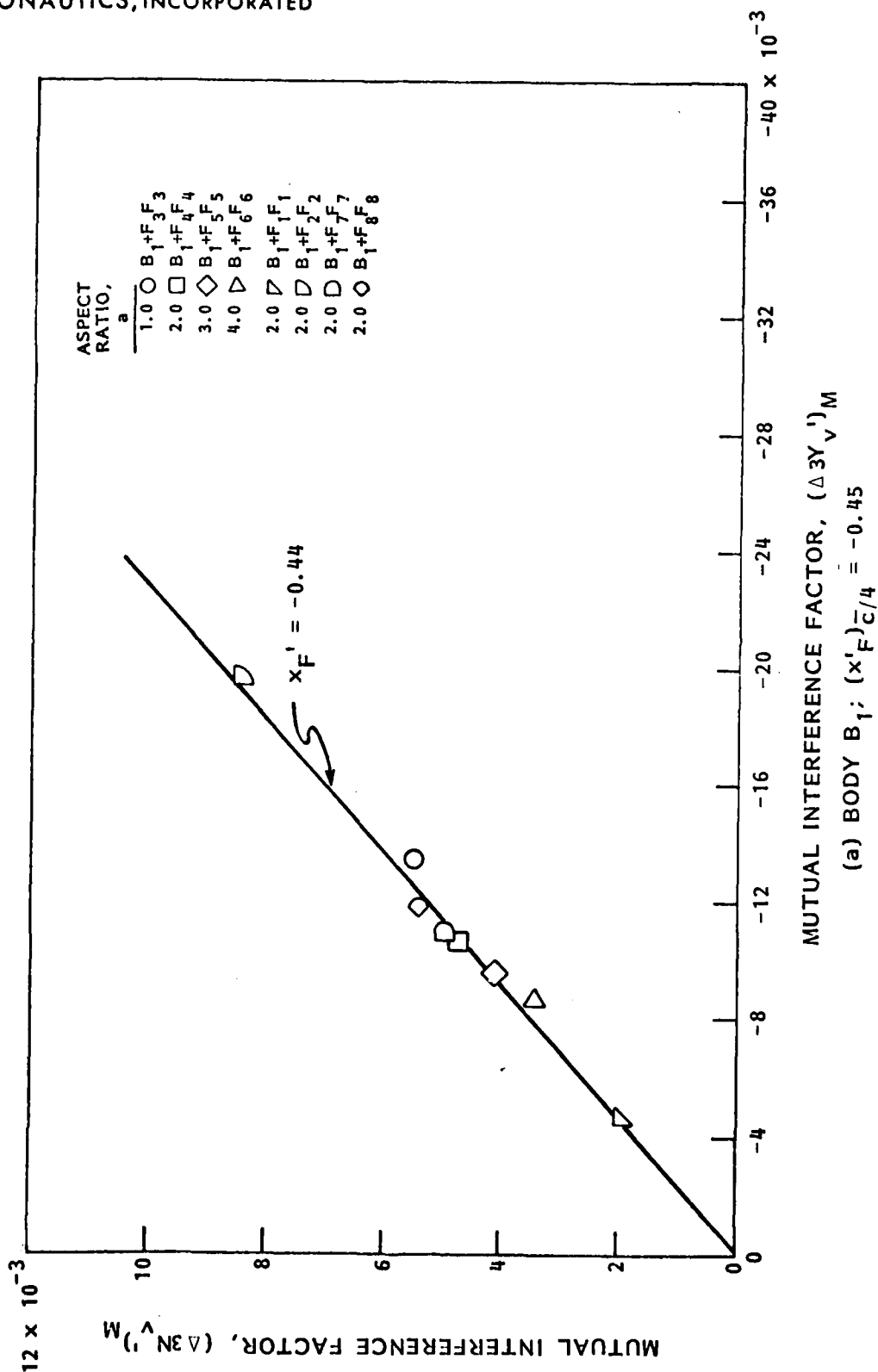
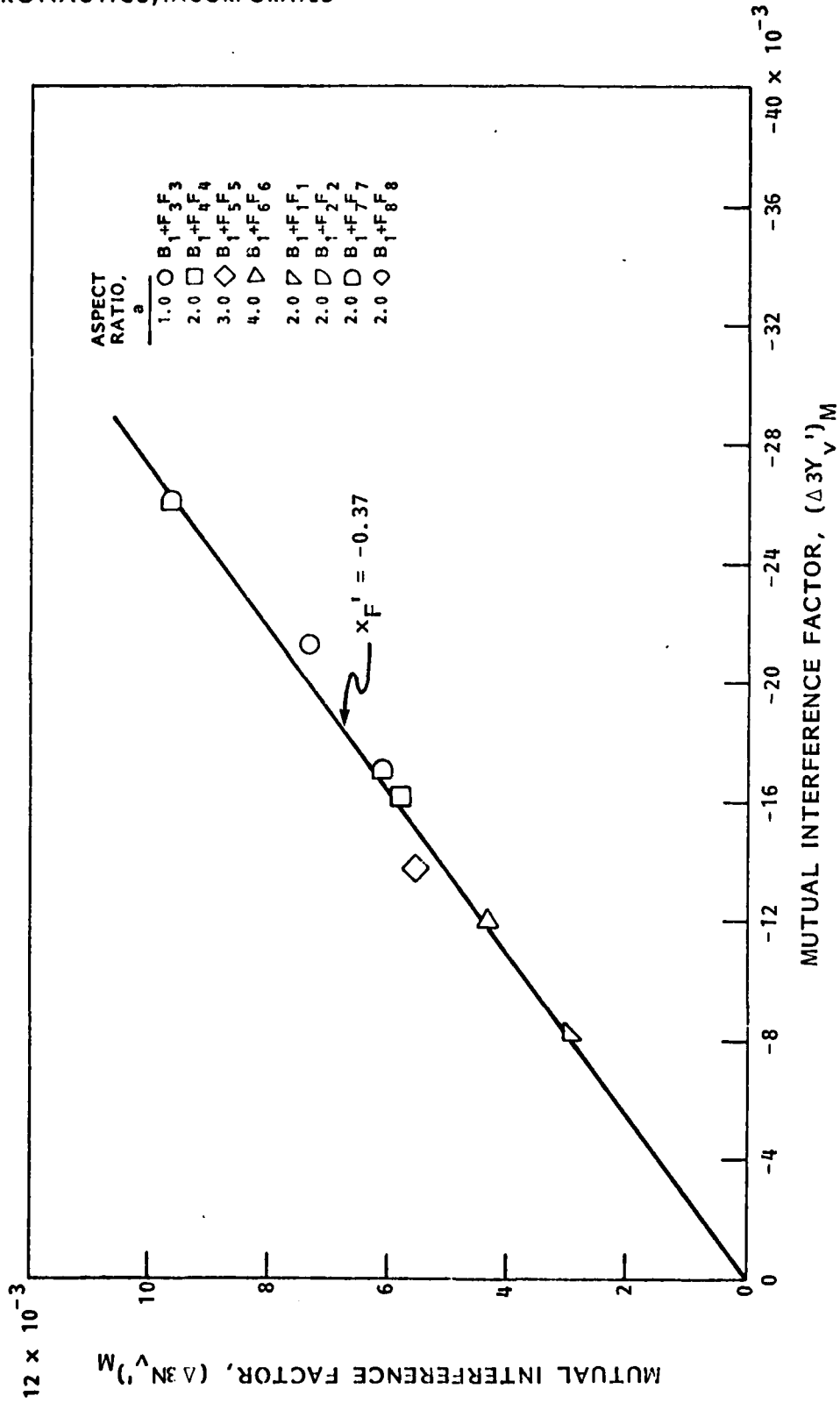
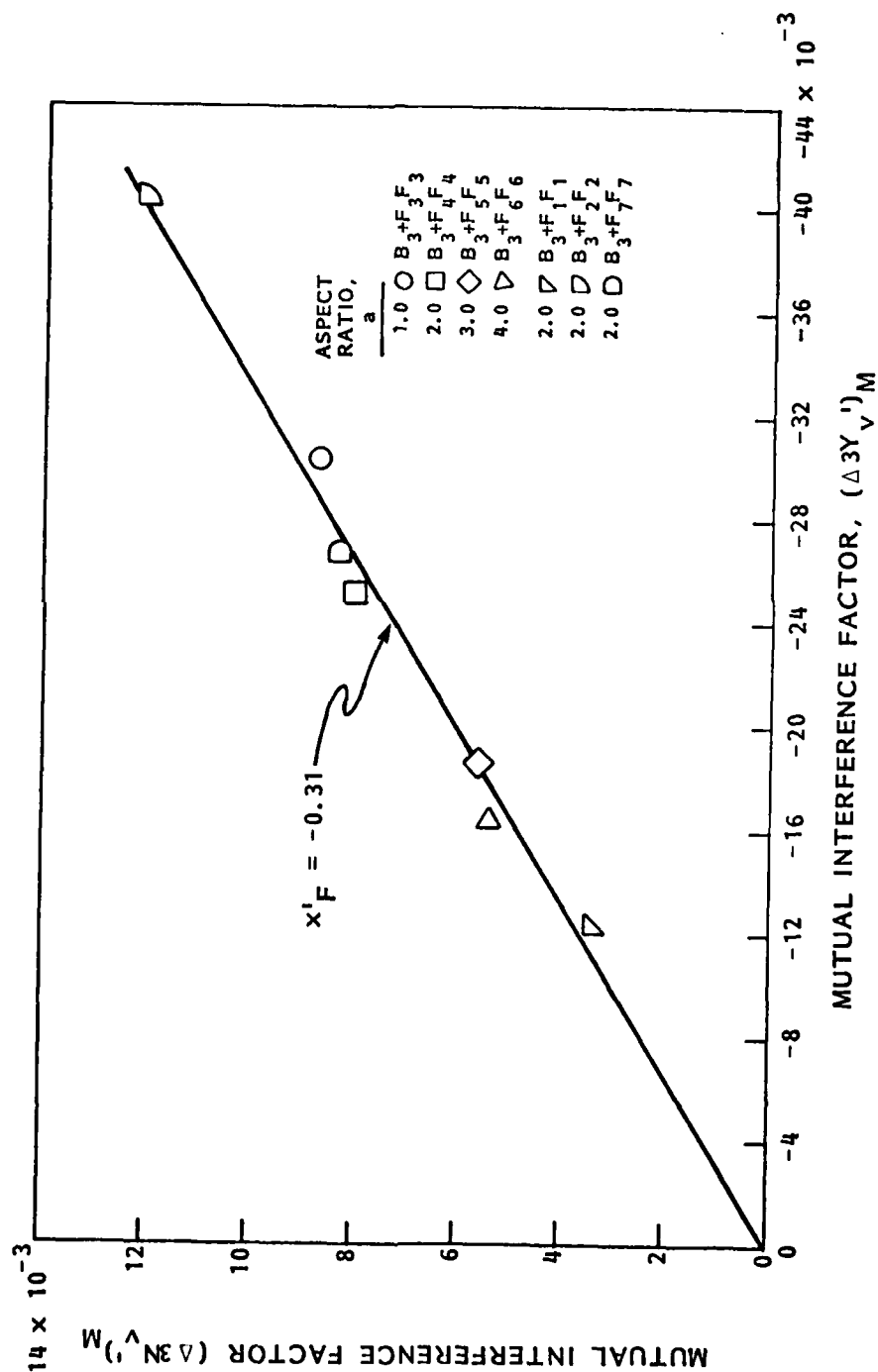


FIGURE 15 - VARIATION OF YAWING MOMENT INTERFERENCE FACTOR WITH LATERAL FORCE INTERFERENCE FACTOR FOR SEVERAL FIN BODY CONFIGURATIONS



(b) BODY B1; $(x_F')_{c/4} = -0.40$

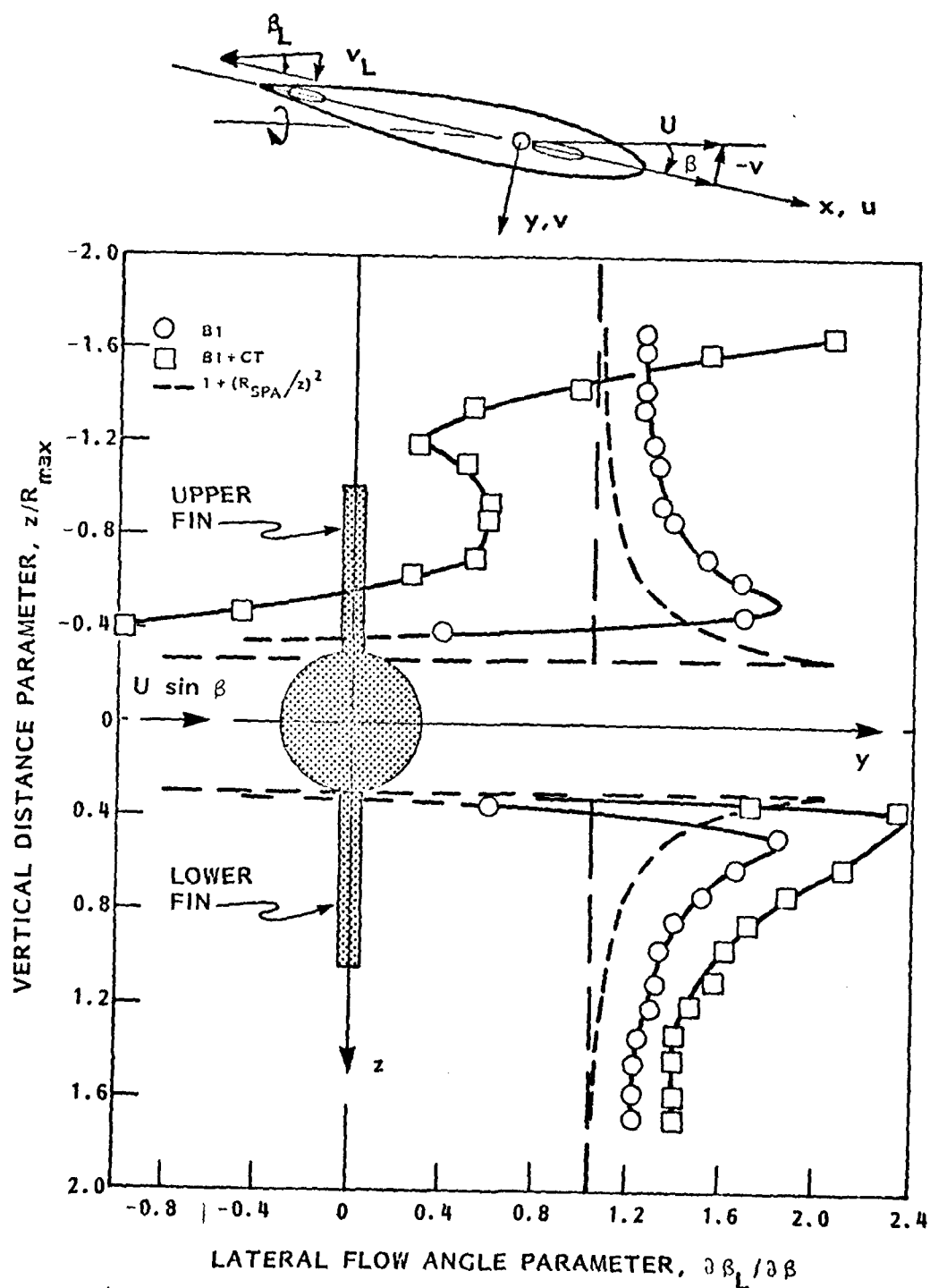
FIGURE 15 - CONTINUED



(c) BODY B3; $(x_F^I)_{C/4} = -0.45$

FIGURE 15 - CONCLUDED

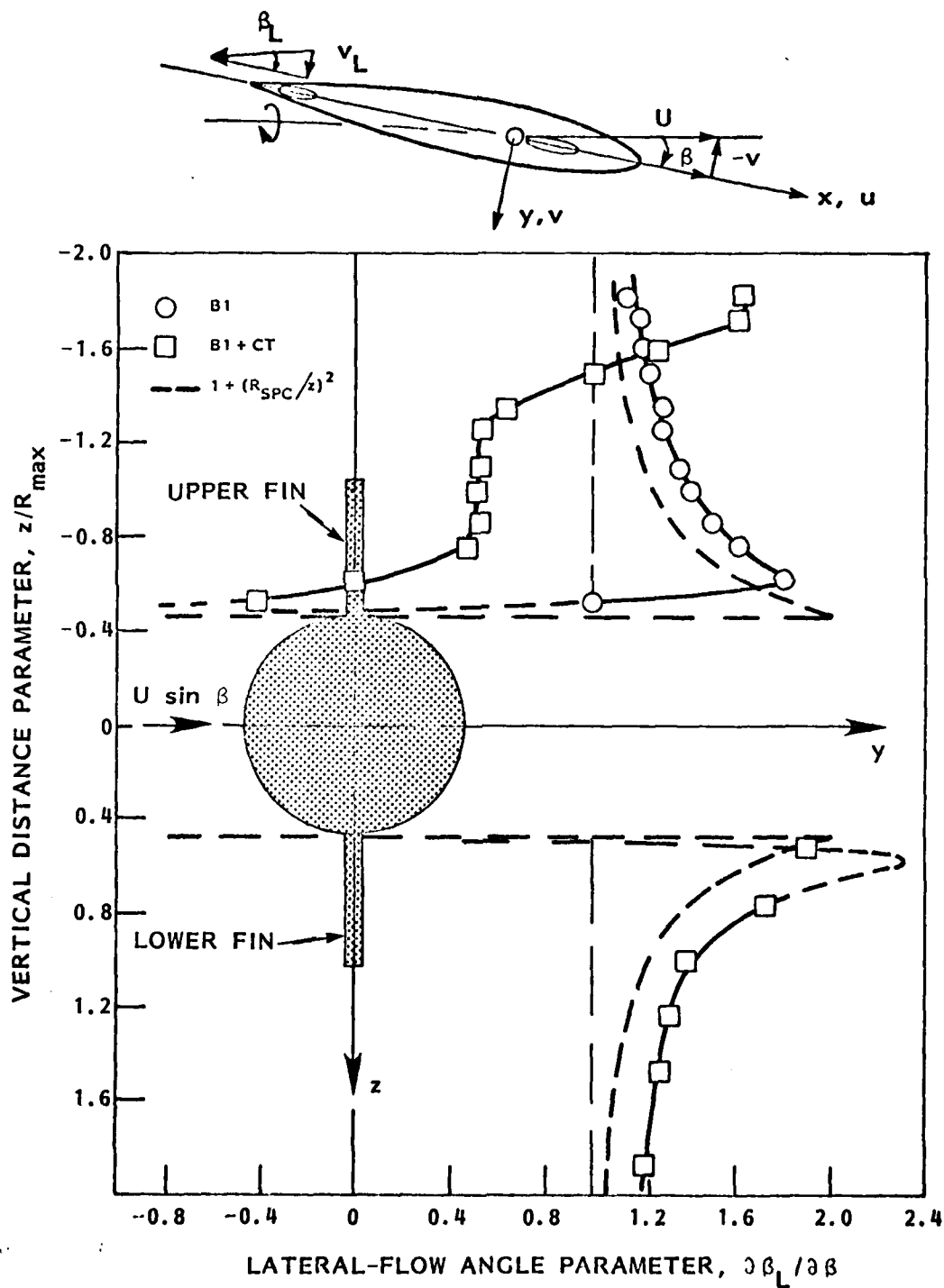
HYDRONAUTICS, INCORPORATED



(a) SURVEY POSITION A

FIGURE 16 - VARIATION OF LATERAL-FLOW ANGLE PARAMTER WITH VERTICAL DISTANCE PARAMETER FOR BODY B1 AND B1 + CT

HYDRONAUTICS, INCORPORATED



(b) SURVEY POSITION C

FIGURE 16 - CONCLUDED

HYDRONAUTICS, INCORPORATED

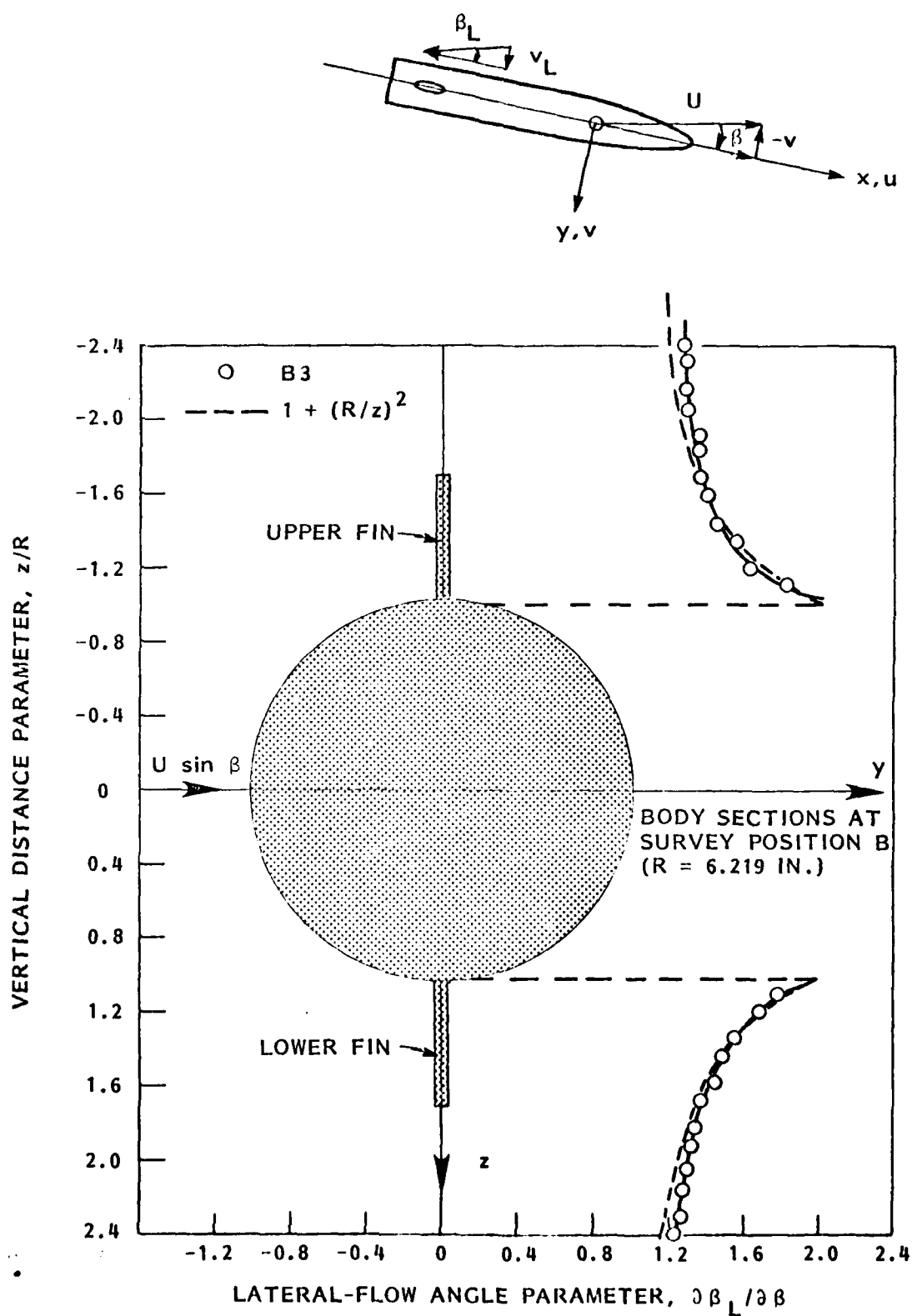
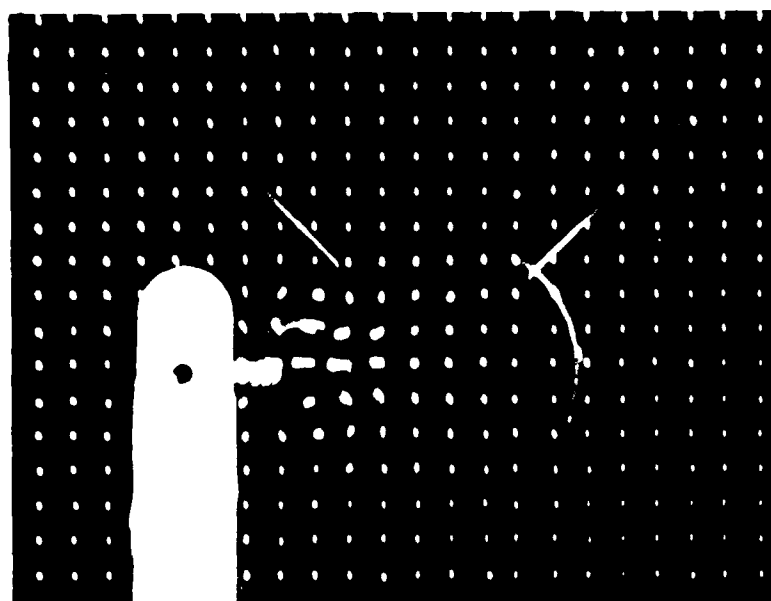
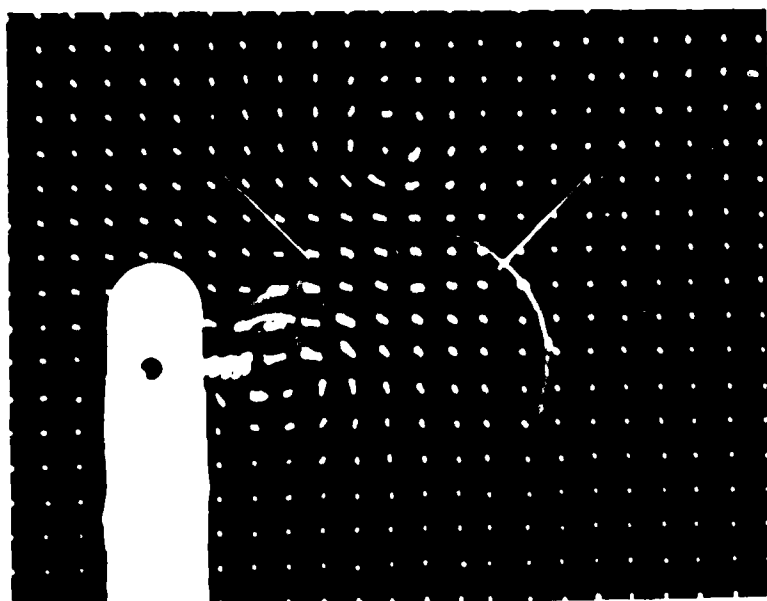
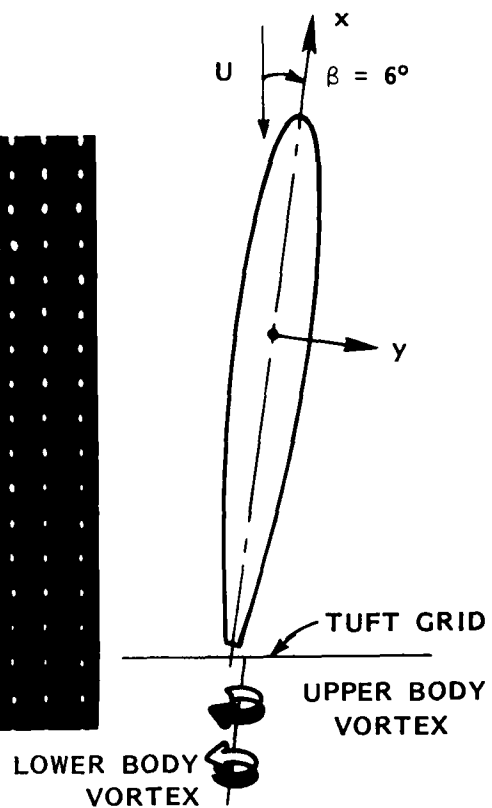


FIGURE 17 - VARIATION OF LATERAL-FLOW ANGLE PARAMETER WITH VERTICAL DISTANCE PARAMETER FOR BODY B3



a. B1



b. B1+CT

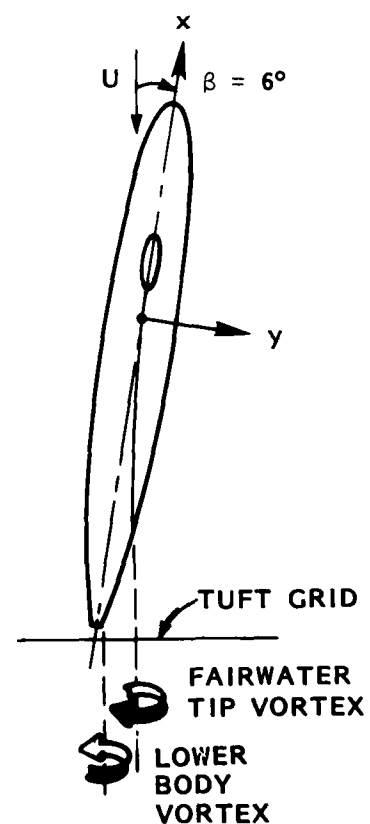
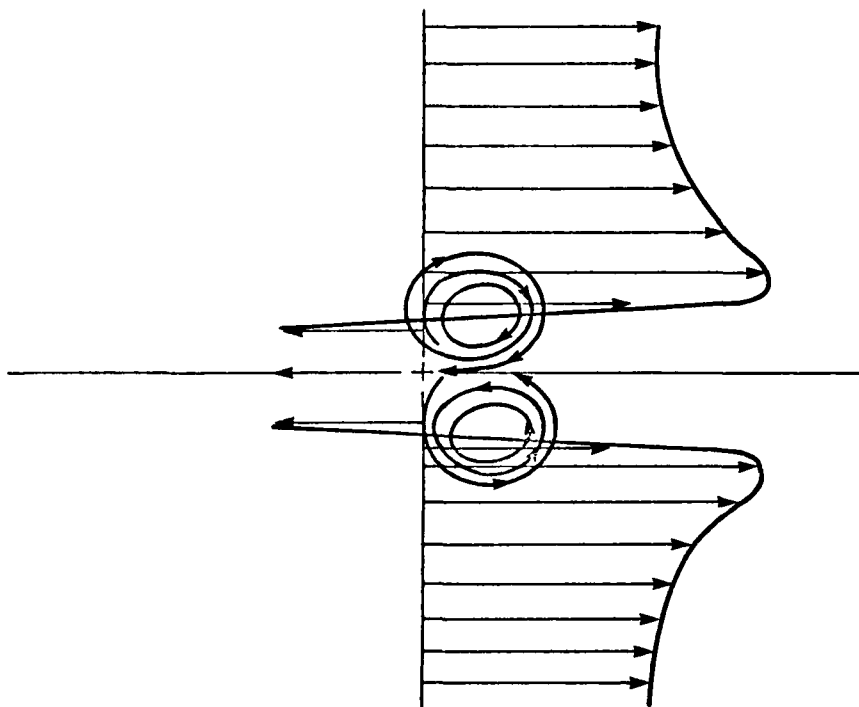
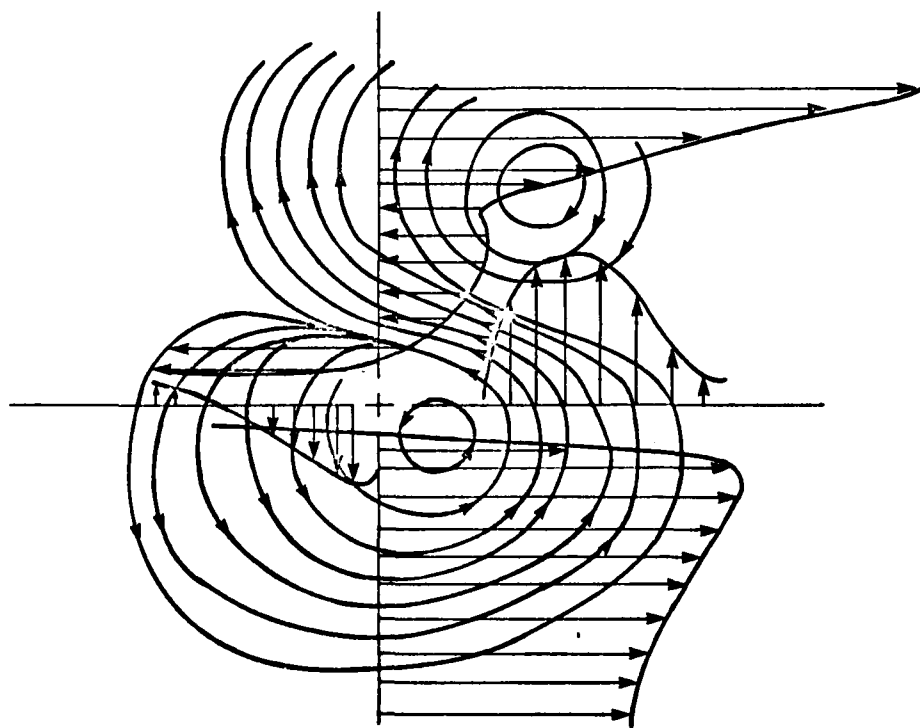


FIGURE 18 - TUFT GRID PHOTOGRAPHS TAKEN AT STERN OF BODY B1 AND B1+CT. $\beta = 6$ DEG.

HYDRONAUTICS, INCORPORATED



(c) SKETCH OF VORTEX AND INDUCED VELOCITY PATTERNS FOR BODY B1



(d) SKETCH OF VORTEX AND INDUCED VELOCITY PATTERNS FOR BODY B1+CT

FIGURE 18 - CONCLUDED

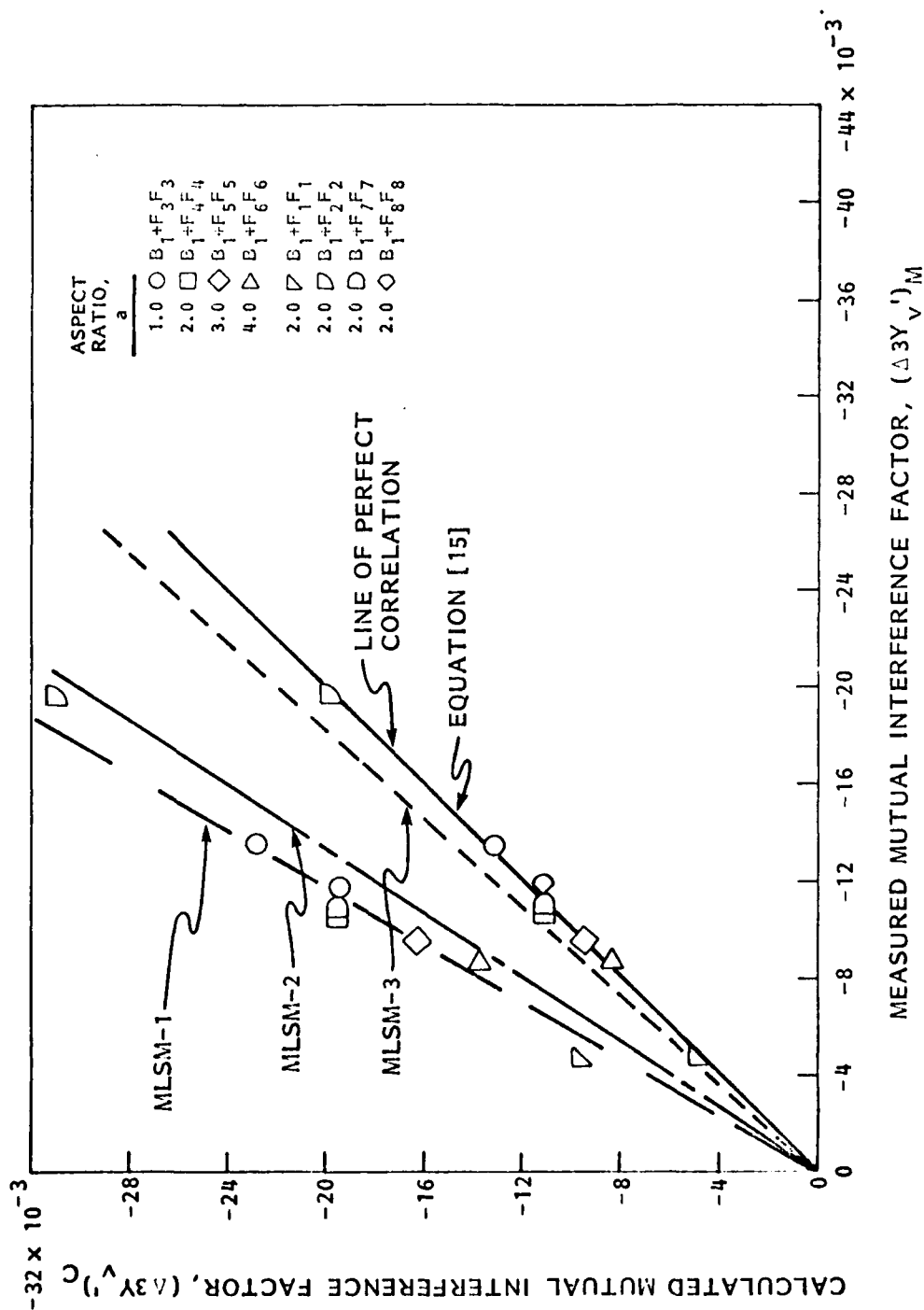


FIGURE 19 - COMPARISON BETWEEN CALCULATED AND MEASURED VALUES OF MUTUAL INTERFERENCE FACTOR FOR SEVERAL FIN-BODY CONFIGURATIONS

AD-A108 429

HYDRONAUTICS INC LAUREL MD

EXPERIMENTAL AND THEORETICAL INVESTIGATION OF FACTORS AFFECTING--ETC (U)

AUG 80 A GOODMAN

TR-7927-1

F/G 20/4

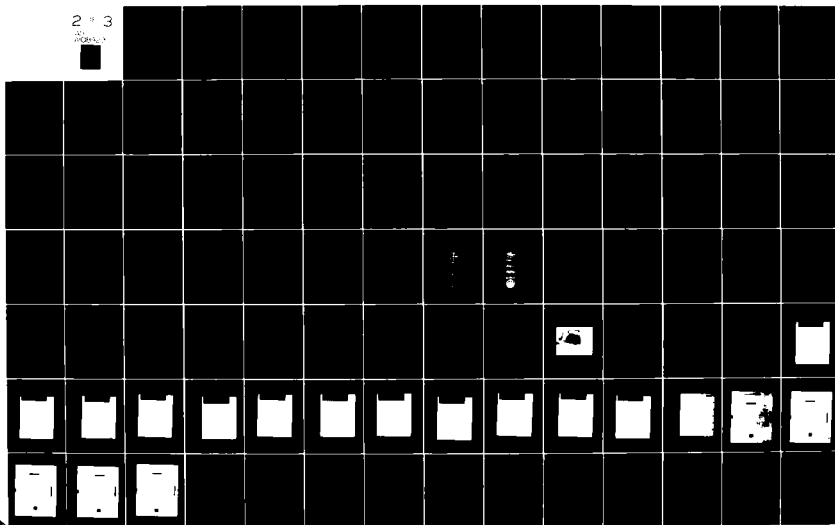
N00167-79-C-0093

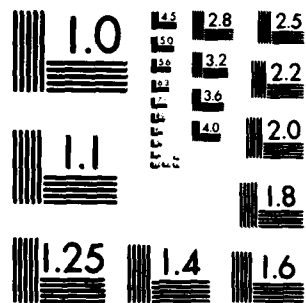
NL

UNCLASSIFIED

2 * 3

2000000





MICROCOPY RESOLUTION TEST CHART
NATIONAL BUREAU OF STANDARDS-1963-A

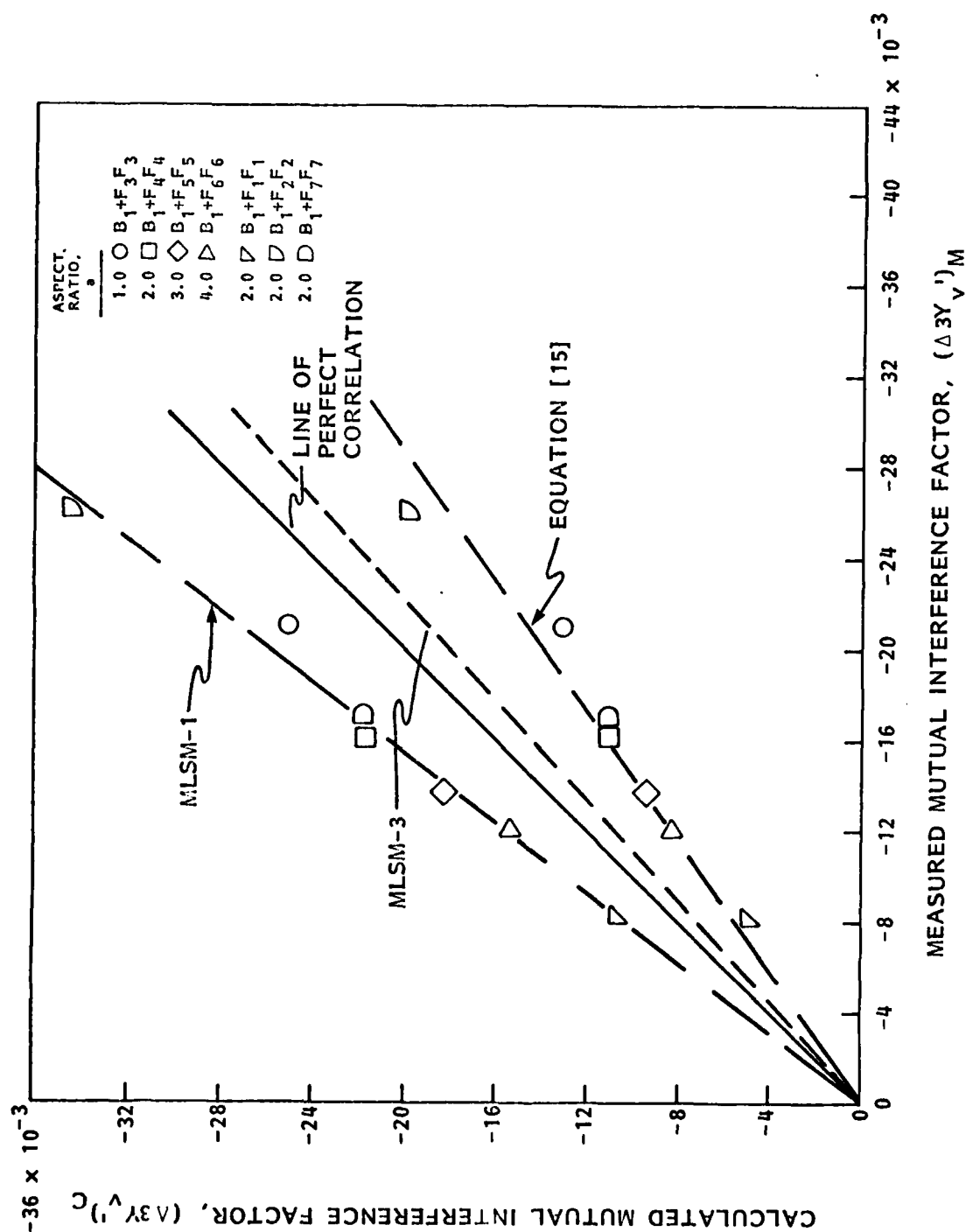
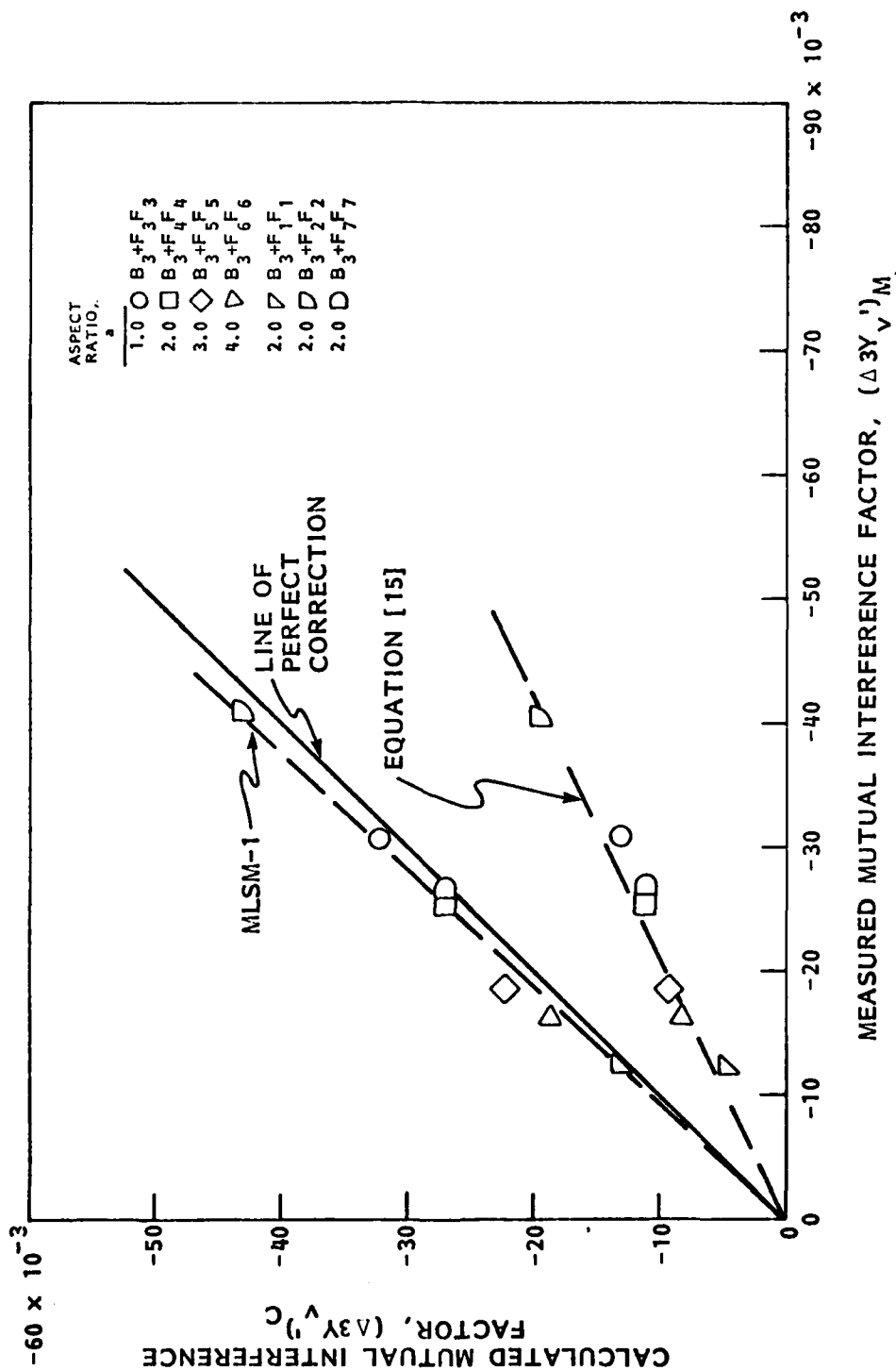


FIGURE 19 - CONTINUED



(c) BODY B3; $(x_F')_{C/4} = -0.45$

FIGURE 19 - CONCLUDED

HYDRONAUTICS, Incorporated

APPENDIX A

GRAPHICAL PRESENTATION OF LATERAL FORCE,
YAWING MOMENT, ROLLING MOMENT, FIN-LATERAL
FORCE AND FIN-ROOT BENDING MOMENT
COEFFICIENTS AS FUNCTIONS OF ANGLE
OF SIDESLIP

Configuration	Fin-Balance Position	Body Dia. In.	Longitudinal Distance from CB, x'_{FB}
B1 and B1+CT	A	4.52	0.453
	B	6.30	0.398
B3	A	12.44	0.453

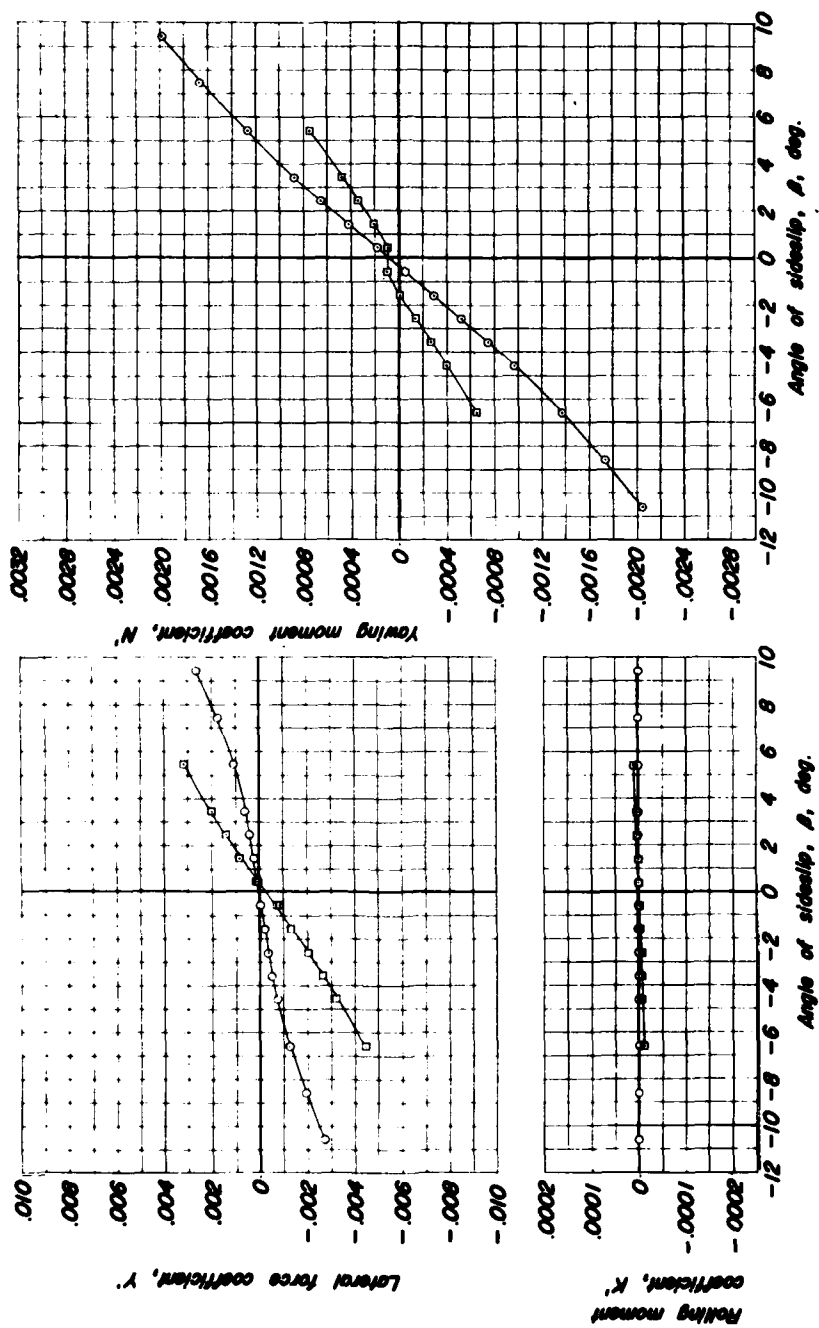


FIGURE A1 - VARIATION OF LATERAL FORCE, YAWING MOMENT, AND ROLLING MOMENT COEFFICIENTS WITH ANGLE OF SIDE-SLIP FOR BODIES B1 AND B3

HYDRONAUTICS, INCORPORATED

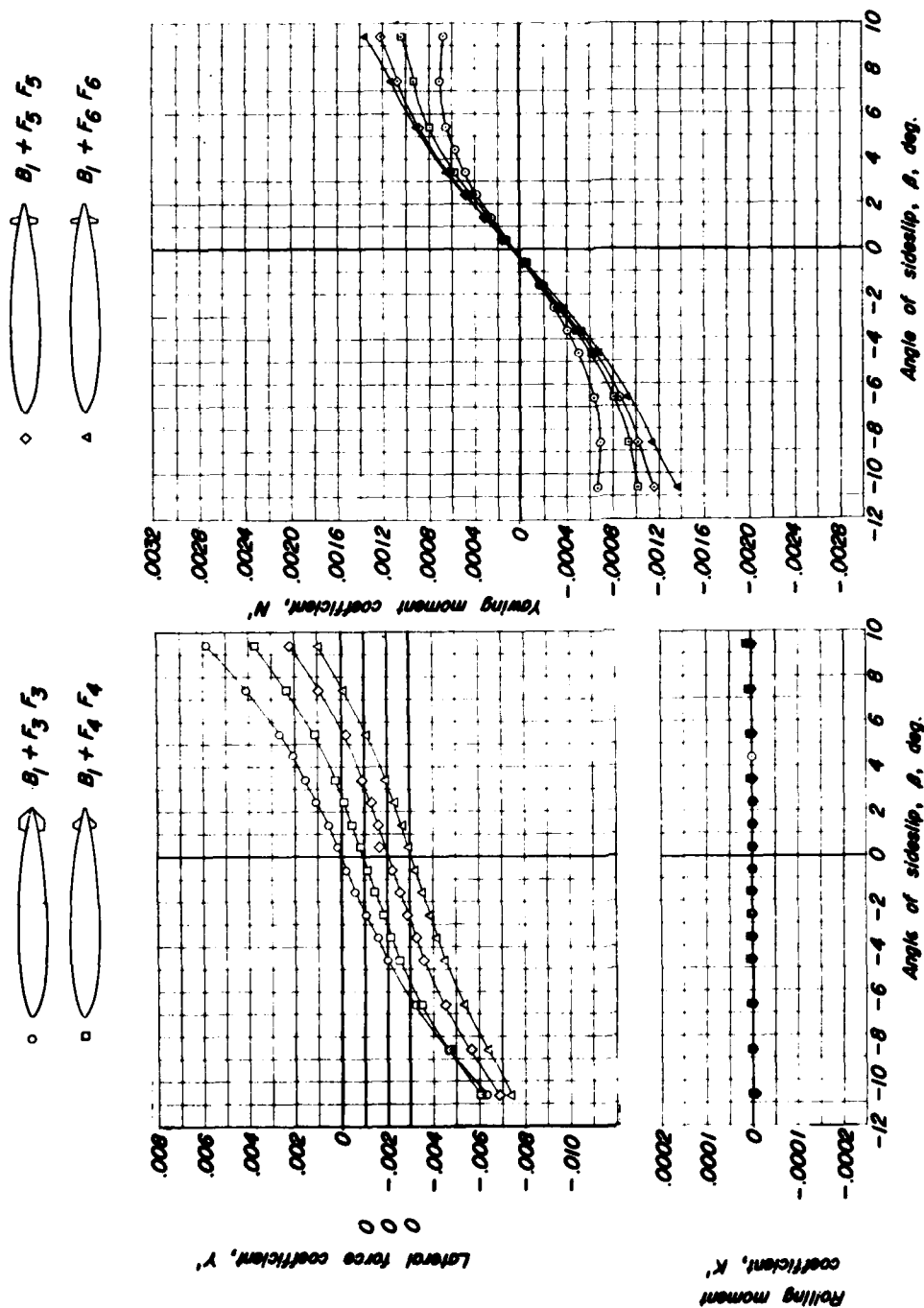


FIGURE A2 - VARIATION OF LATERAL FORCE, YAWING MOMENT, AND ROLLING MOMENT COEFFICIENTS WITH ANGLE OF SIDESLIP FOR B1 WITH FINS $F_3 F_3$ TO $F_6 F_6$ AT POSITION A

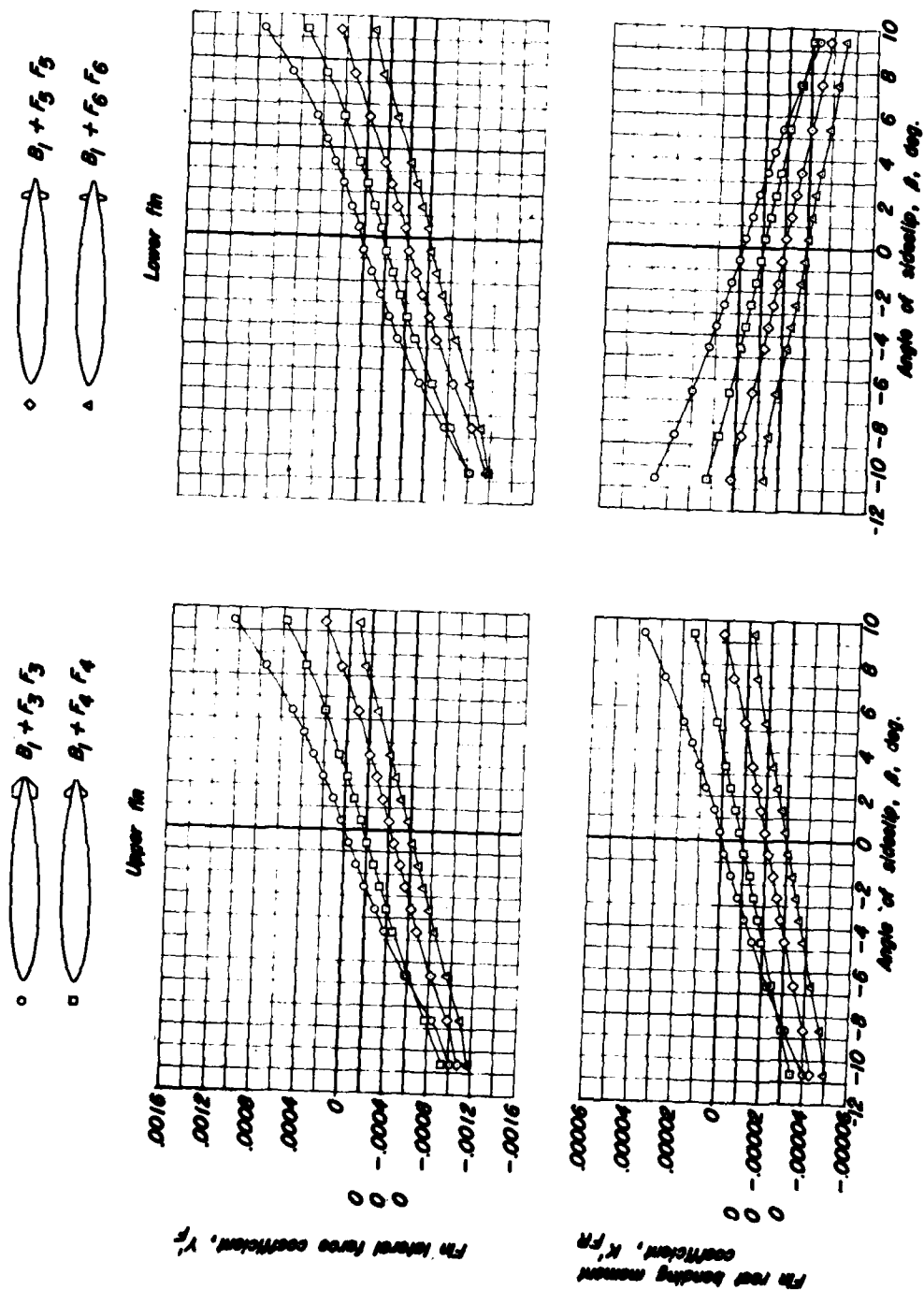


FIGURE A3 - VARIATION OF UPPER AND LOWER FIN-LATERAL FORCE AND FIN-ROOT BENDING MOMENT COEFFICIENTS WITH ANGLE OF SIDESLIP FOR B1 WITH FINS F_3 TO F_6 AT POSITION A

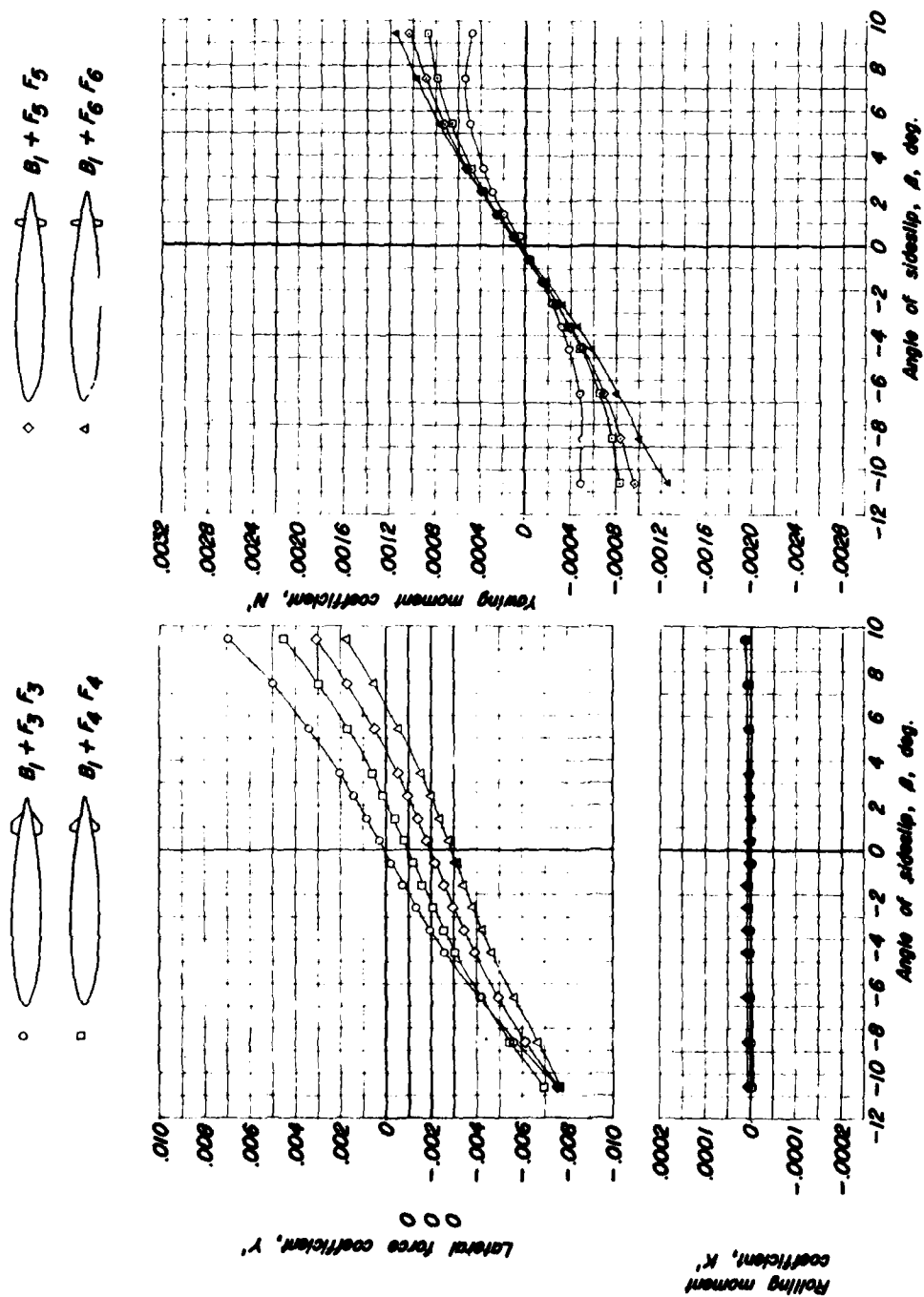


FIGURE A4 - VARIATION OF LATERAL FORCE, YAWING MOMENT, AND ROLLING MOMENT COEFFICIENTS WITH ANGLE OF SIDESLIP FOR B1 WITH FINS F_3 TO F_6 AT POSITION B

HYDRONAUTICS, INCORPORATED

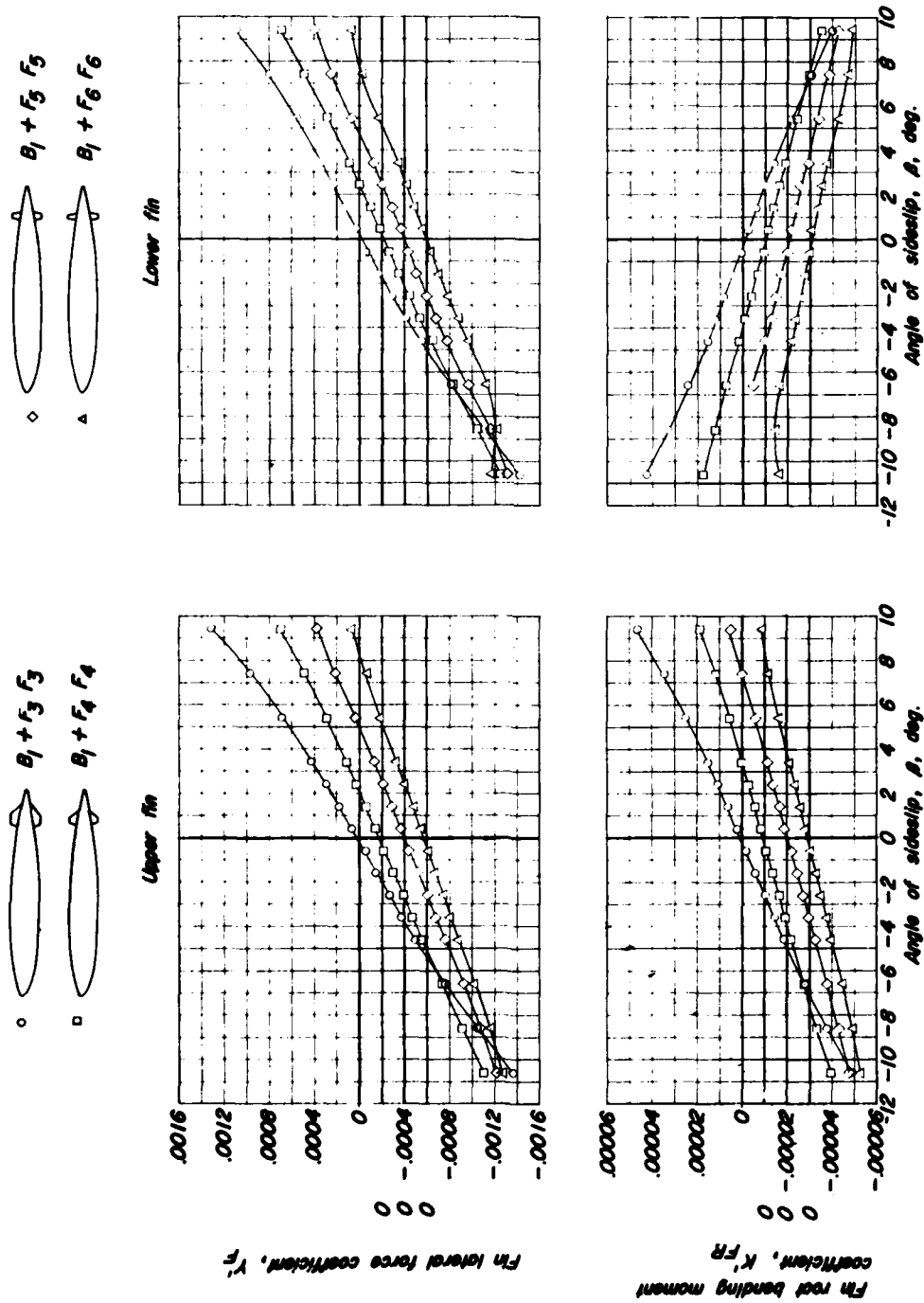


FIGURE A5 - VARIATION OF UPPER AND LOWER FIN-LATERAL FORCE AND FIN-ROOT BENDING MOMENT COEFFICIENTS WITH ANGLE OF SIDESLIP FOR B1 WITH FINS F_3 TO F_6 AT POSITION B

HYDRONAUTICS, INCORPORATED

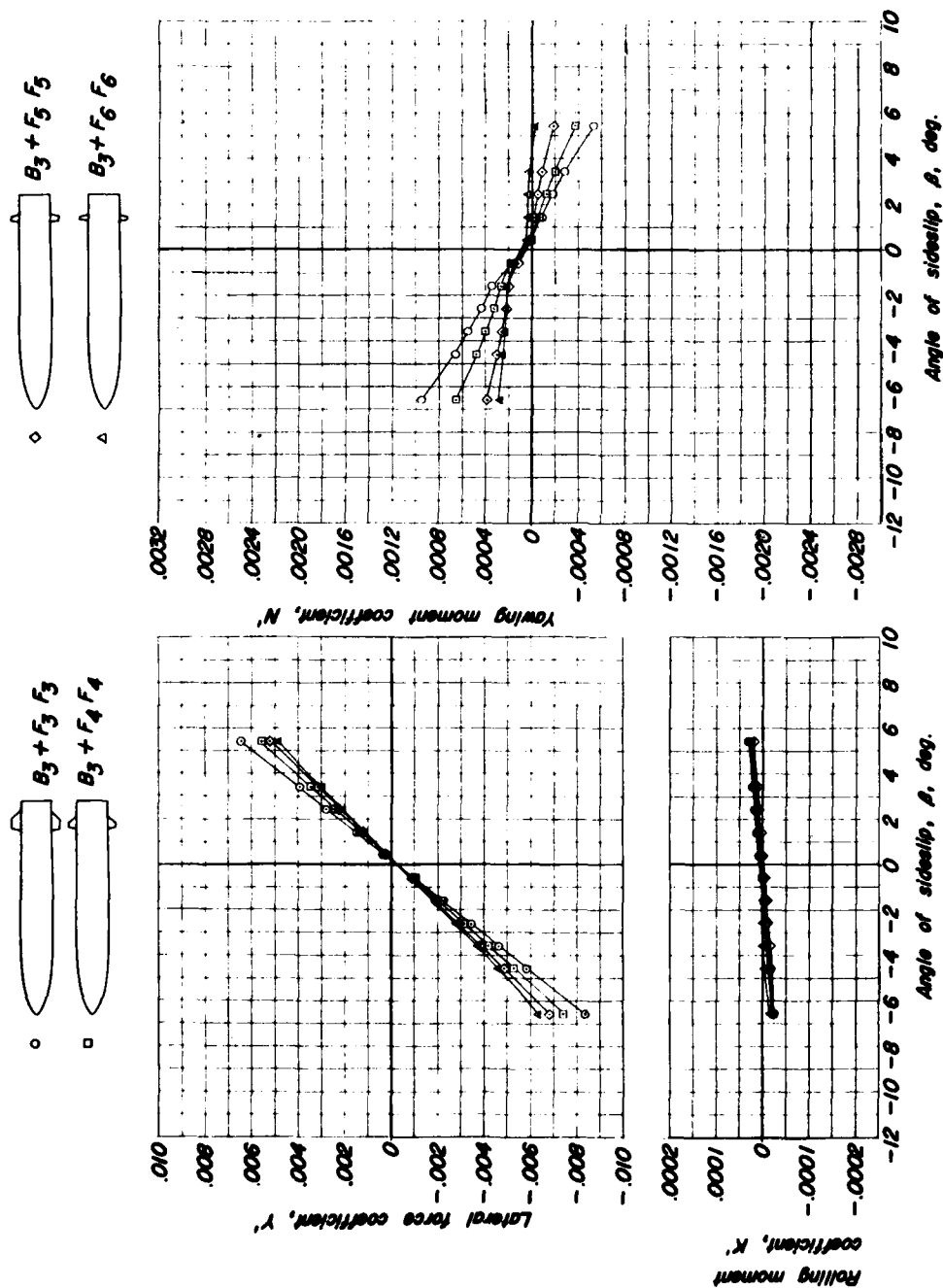


FIGURE A6 - VARIATION OF LATERAL FORCE, YAWING MOMENT, AND ROLLING MOMENT COEFFICIENTS WITH ANGLE OF SIDESLIP FOR B3 WITH FINS F_3 TO F_6 AT POSITION A

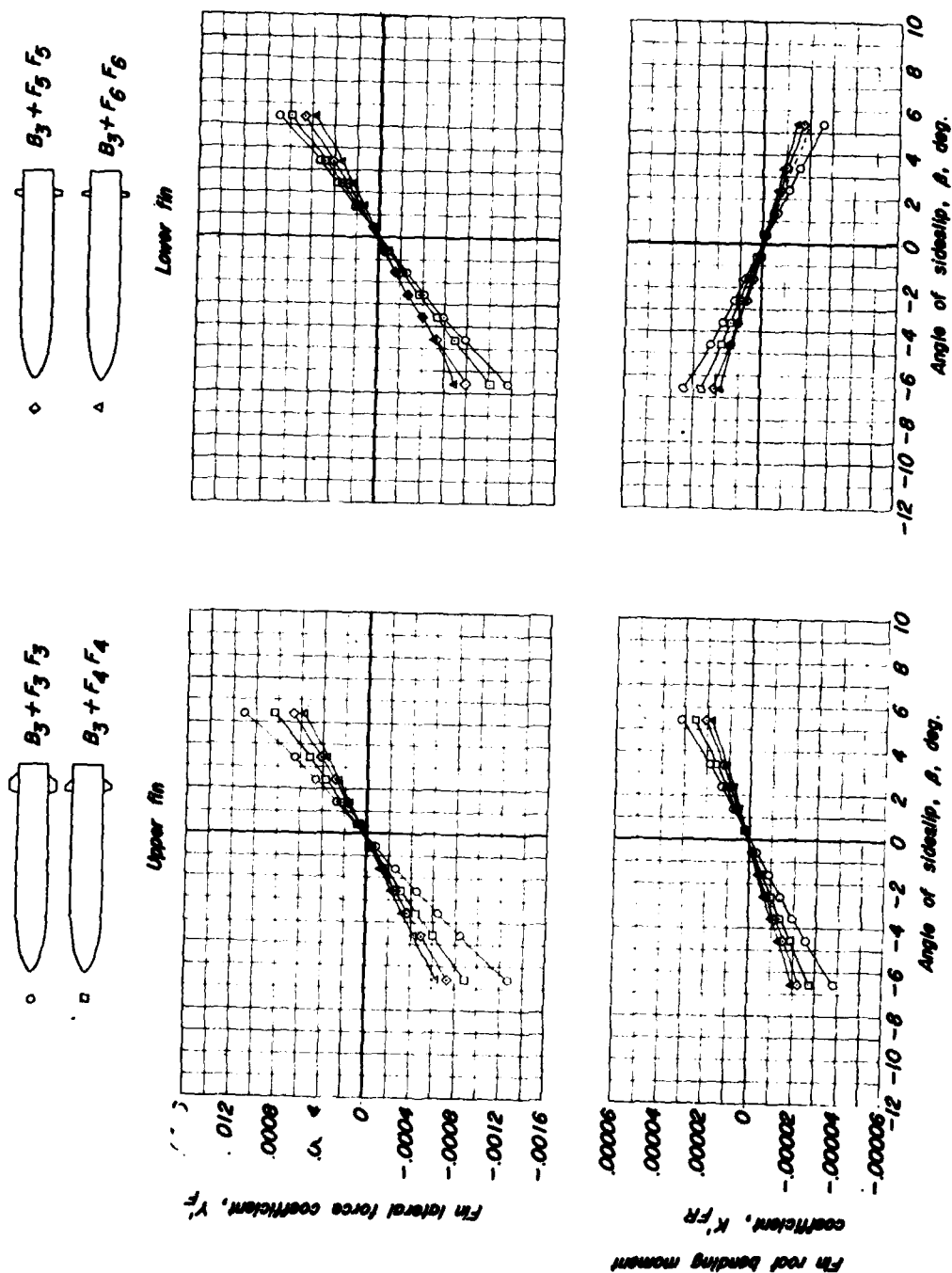


FIGURE A7 - VARIATION OF UPPER AND LOWER FIN-LATERAL FORCE AND FIN-ROOT BENDING MOMENT COEFFICIENTS WITH ANGLE OF SIDESLIP FOR B# WITH FINS F_3 TO F_6 AT POSITION A

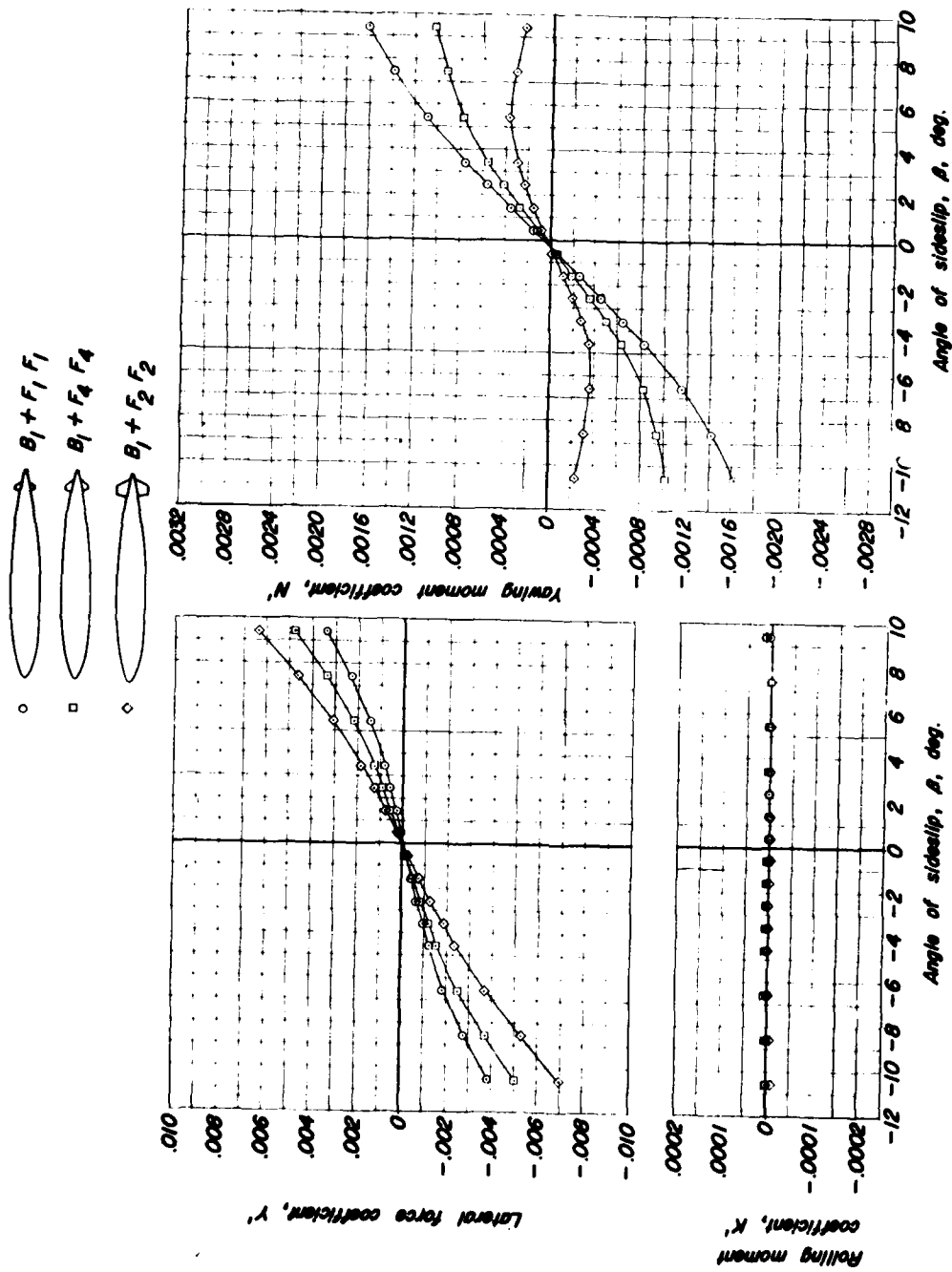


FIGURE A8 - VARIATION OF LATERAL FORCE, YAWING MOMENT, AND ROLLING MOMENT COEFFICIENTS WITH ANGLE OF SIDESLIP FOR B1 WITH FINS F_1 , F_2 , F_4 AND F_4 AT POSITION A

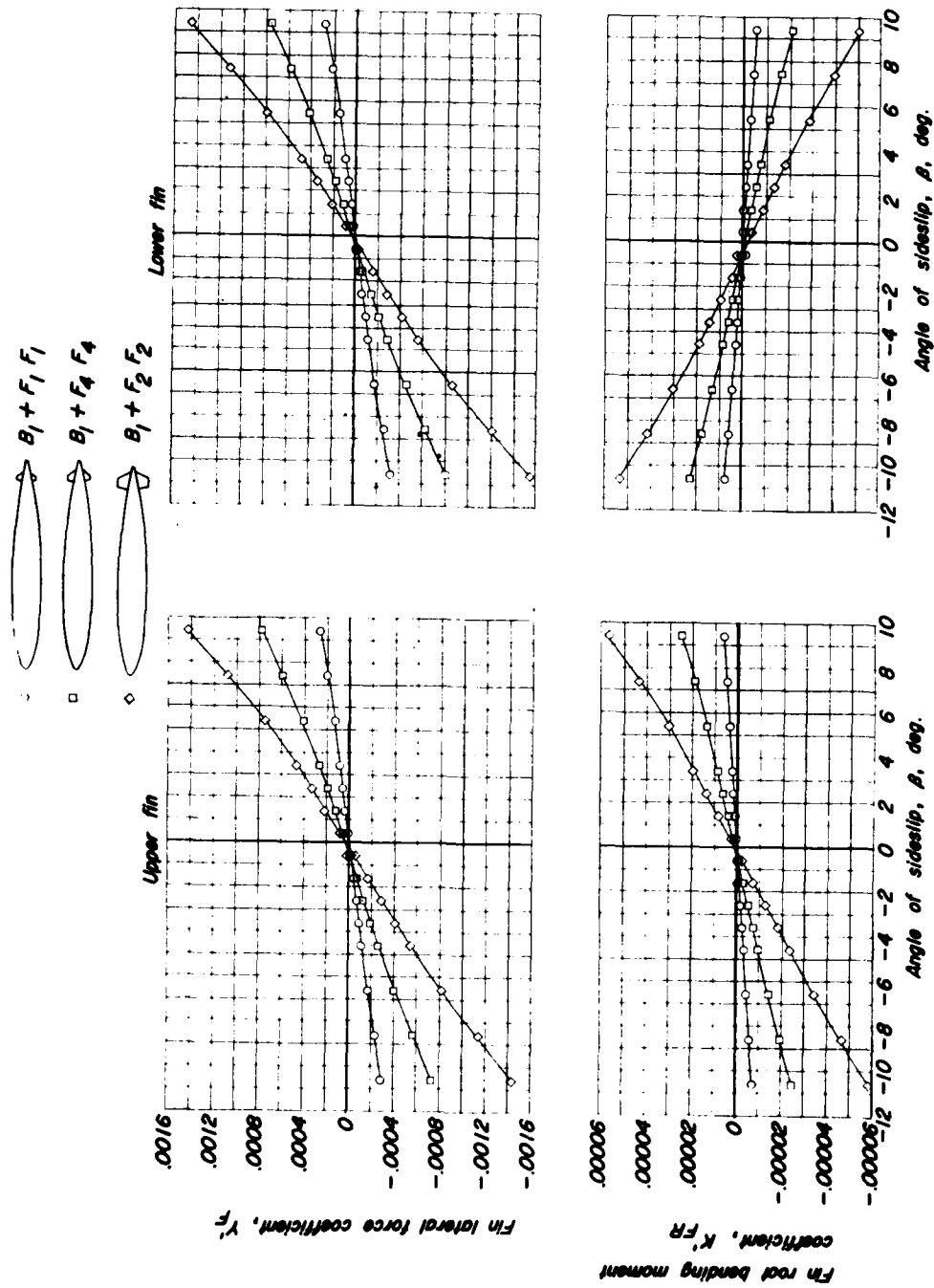


FIGURE A9 - VARIATION OF UPPER AND LOWER FIN-LATERAL FORCE AND FIN-ROOT BENDING MOMENT COEFFICIENTS WITH ANGLE OF SIDESLIP FOR B1 WITH FINS F_1, F_2, F_4 AND F_4' AT POSITION A

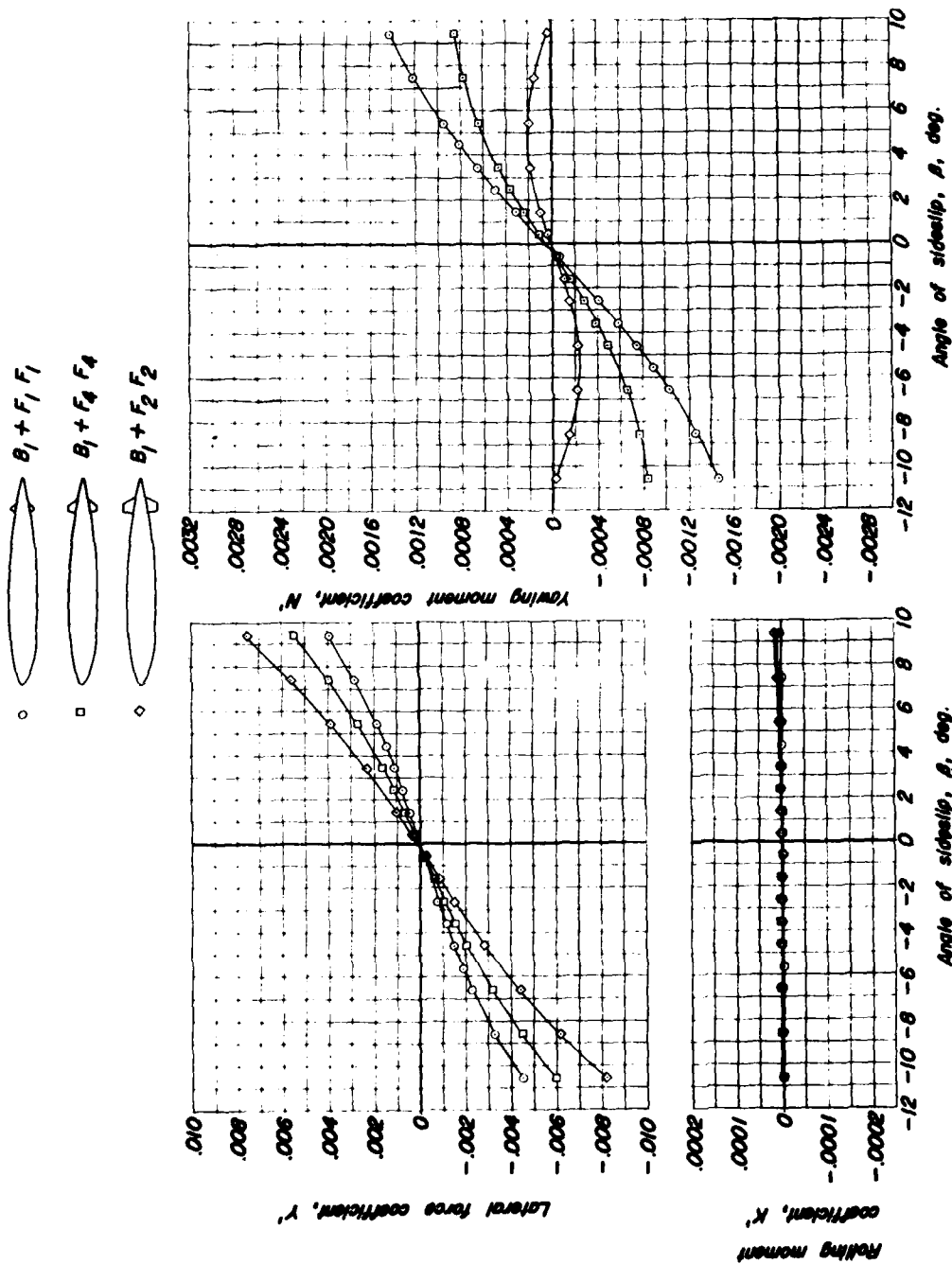


FIGURE A10 - VARIATION OF LATERAL FORCE, YAWING MOMENT, AND ROLLING MOMENT COEFFICIENTS WITH ANGLE OF SIDESLIP FOR B1 WITH FINS $F_1 F_1$, $F_2 F_2$, AND $F_4 F_4$ AT POSITION B

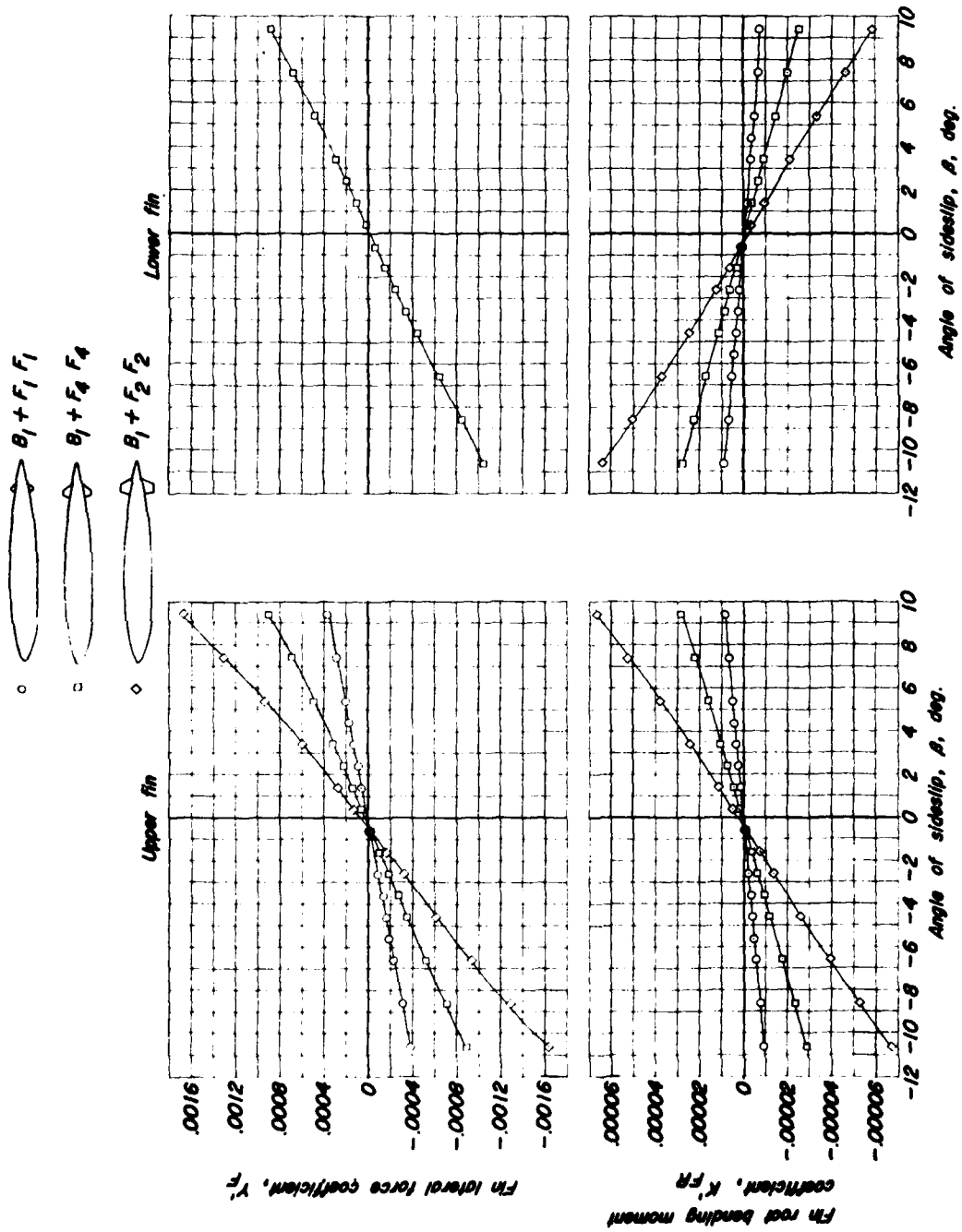


FIGURE A11 - VARIATION OF UPPER AND LOWER FIN LATERAL FORCE AND FIN-ROOT BENDING MOMENT COEFFICIENTS WITH ANGLE OF SIDESLIP FOR B_1 WITH FIN $F_1 F_1$, $F_4 F_4$ AND $F_2 F_2$ AT POSITION B

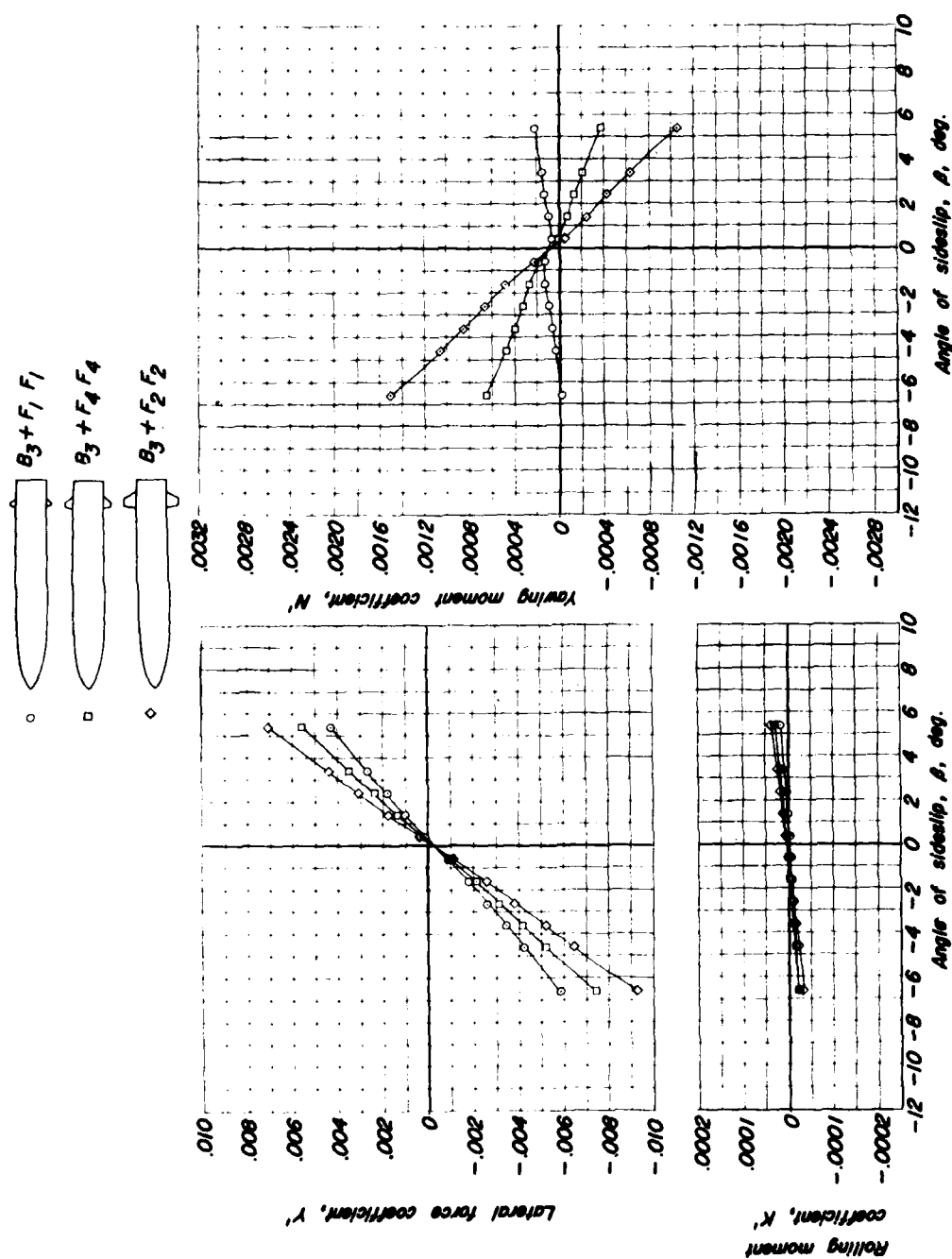


FIGURE A12 - VARIATION OF LATERAL FORCE, YAWING MOMENT, AND ROLLING MOMENT COEFFICIENTS WITH ANGLE OF SIDESLIP FOR B_3 WITH FINS $F_1 F_1$, $F_2 F_2$, AND $F_4 F_4$ AT POSITION A

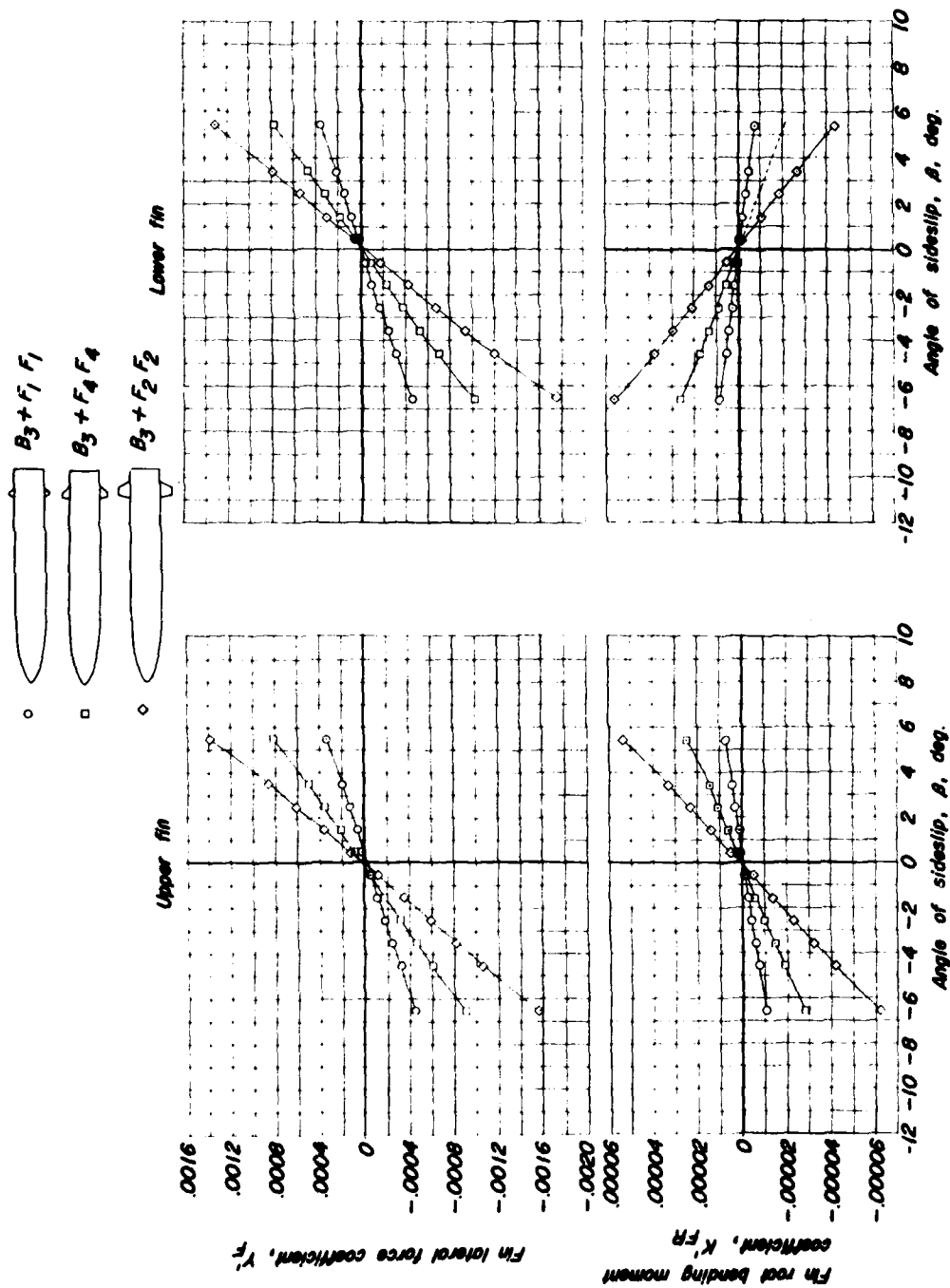


FIGURE A13 - VARIATION OF UPPER AND LOWER FIN-LATERAL FORCE AND FIN-ROOT BENDING MOMENT COEFFICIENTS WITH ANGLE OF SIDESLIP FOR B3 WITH FINS $F_1 F_1$, $F_4 F_4$ AND $F_2 F_2$ AT POSITION A

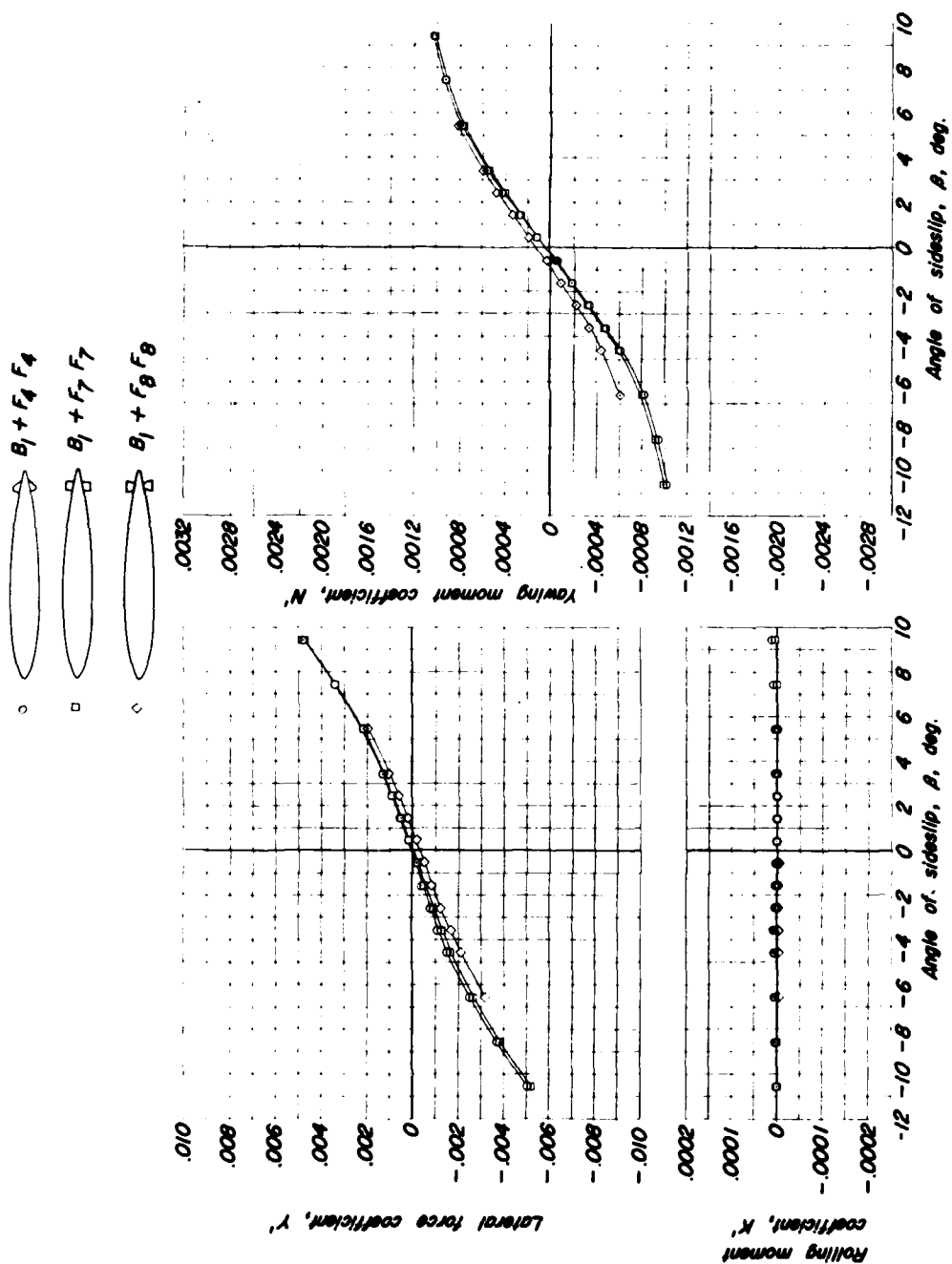


FIGURE A14 - VARIATION OF LATERAL FORCE, YAWING MOMENT, AND ROLLING MOMENT COEFFICIENTS WITH ANGLE OF SIDESLIP FOR B1 WITH FINS $F_4 F_4$, $F_7 F_7$, AND $F_8 F_8$ AT POSITION A

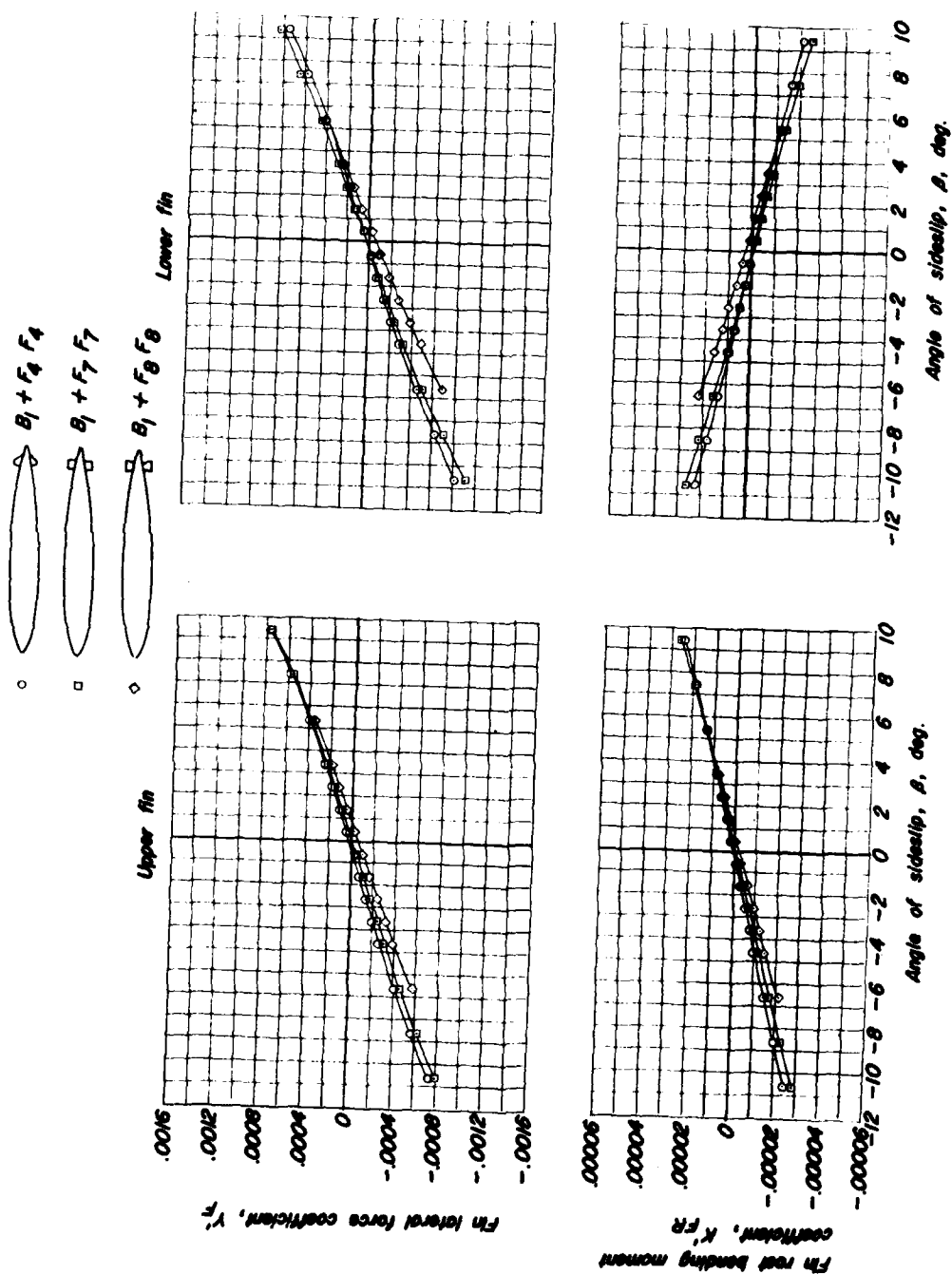


FIGURE A15 - VARIATION OF UPPER AND LOWER FIN-LATERAL FORCE AND FIN-ROOT BENDING MOMENT COEFFICIENTS WITH ANGLE OF SIDESLIP FOR B1 WITH FIN F_4 , F_7 , F_8 AND F_8 AT POSITION A

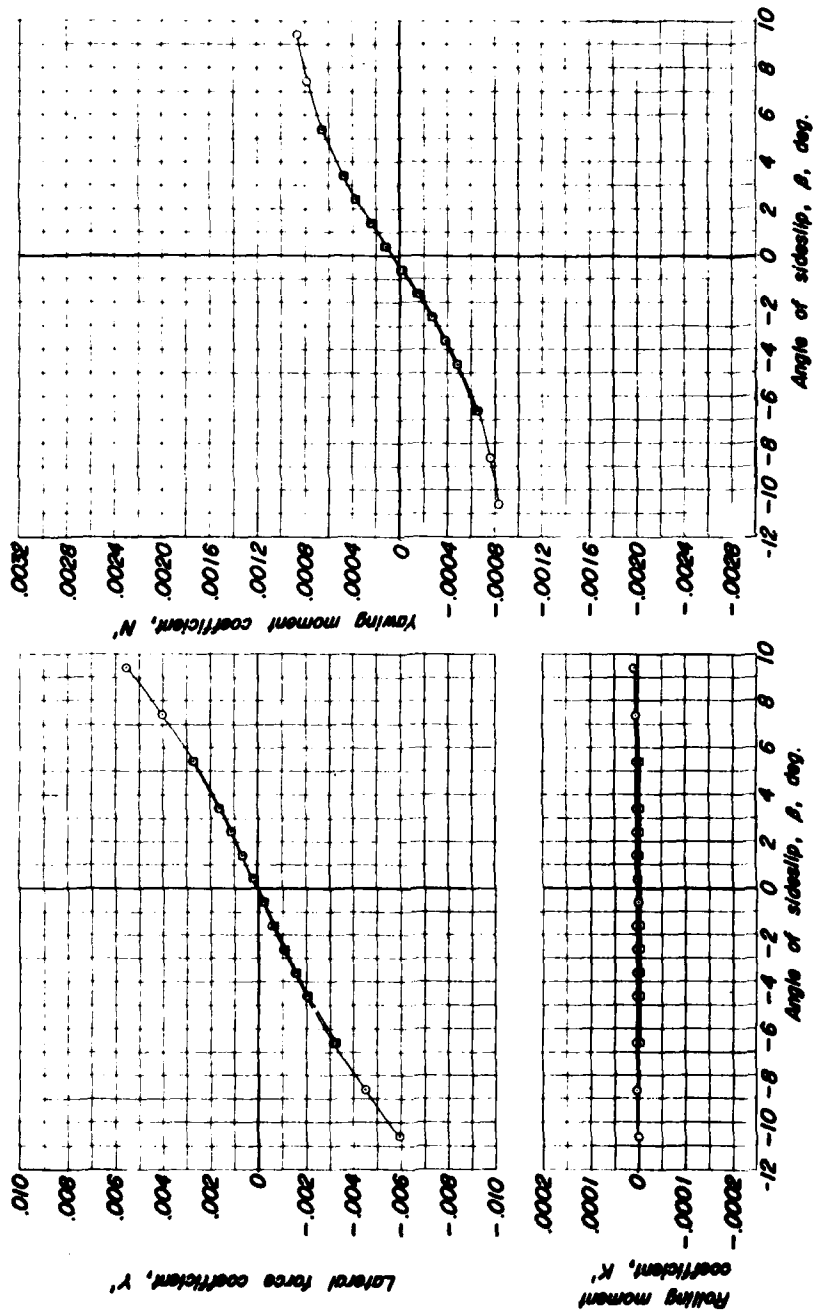
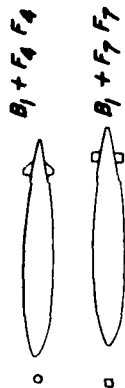


FIGURE A16 - VARIATION OF LATERAL FORCE, YAWING MOMENT, AND ROLLING MOMENT COEFFICIENTS WITH ANGLE OF SIDESLIP FOR B1 WITH FINS F_4 AND F_7 AT POSITION B

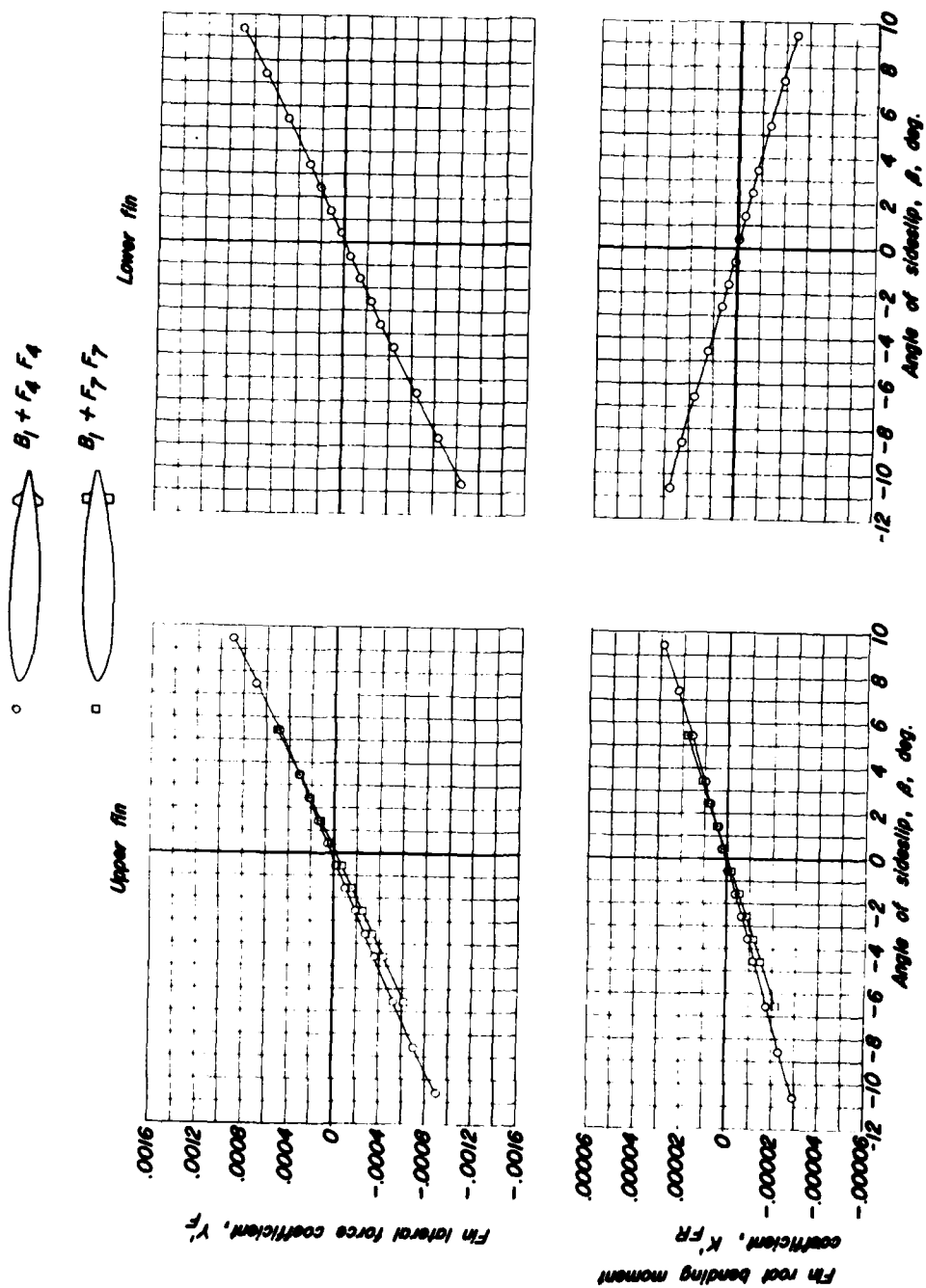


FIGURE A17 - VARIATION OF UPPER AND LOWER FIN-LATERAL FORCE AND FIN-ROOT BENDING MOMENT COEFFICIENTS WITH ANGLE OF SIDESLIP FOR B1 WITH FINs F_4 AND F_7 AT POSITION B

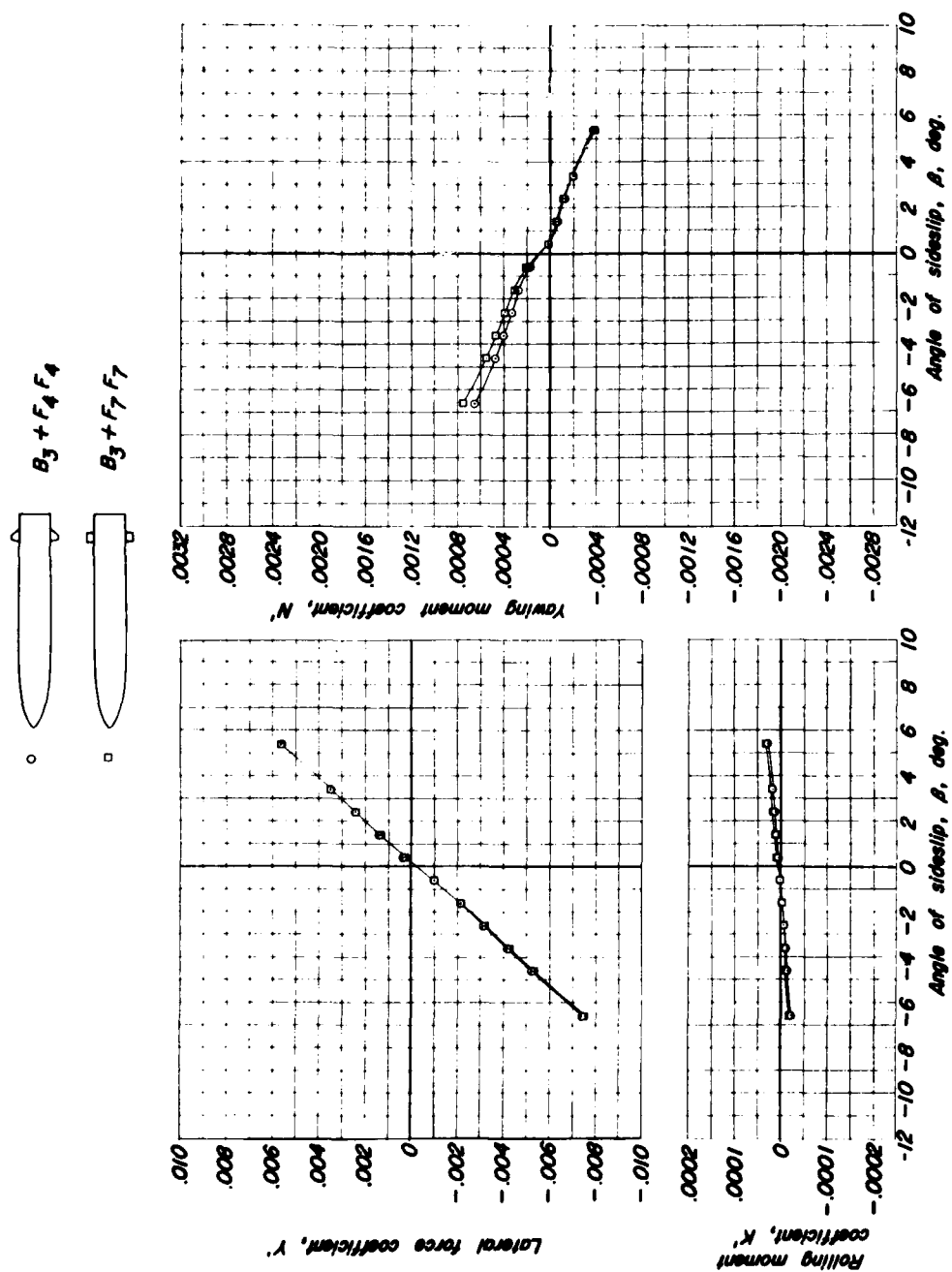


FIGURE A18 - VARIATION OF LATERAL FORCE, YAWING MOMENT, AND ROLLING MOMENT COEFFICIENTS WITH ANGLE OF SIDESLIP FOR B3 WITH FINS F_4 AND F_7 AT POSITION A

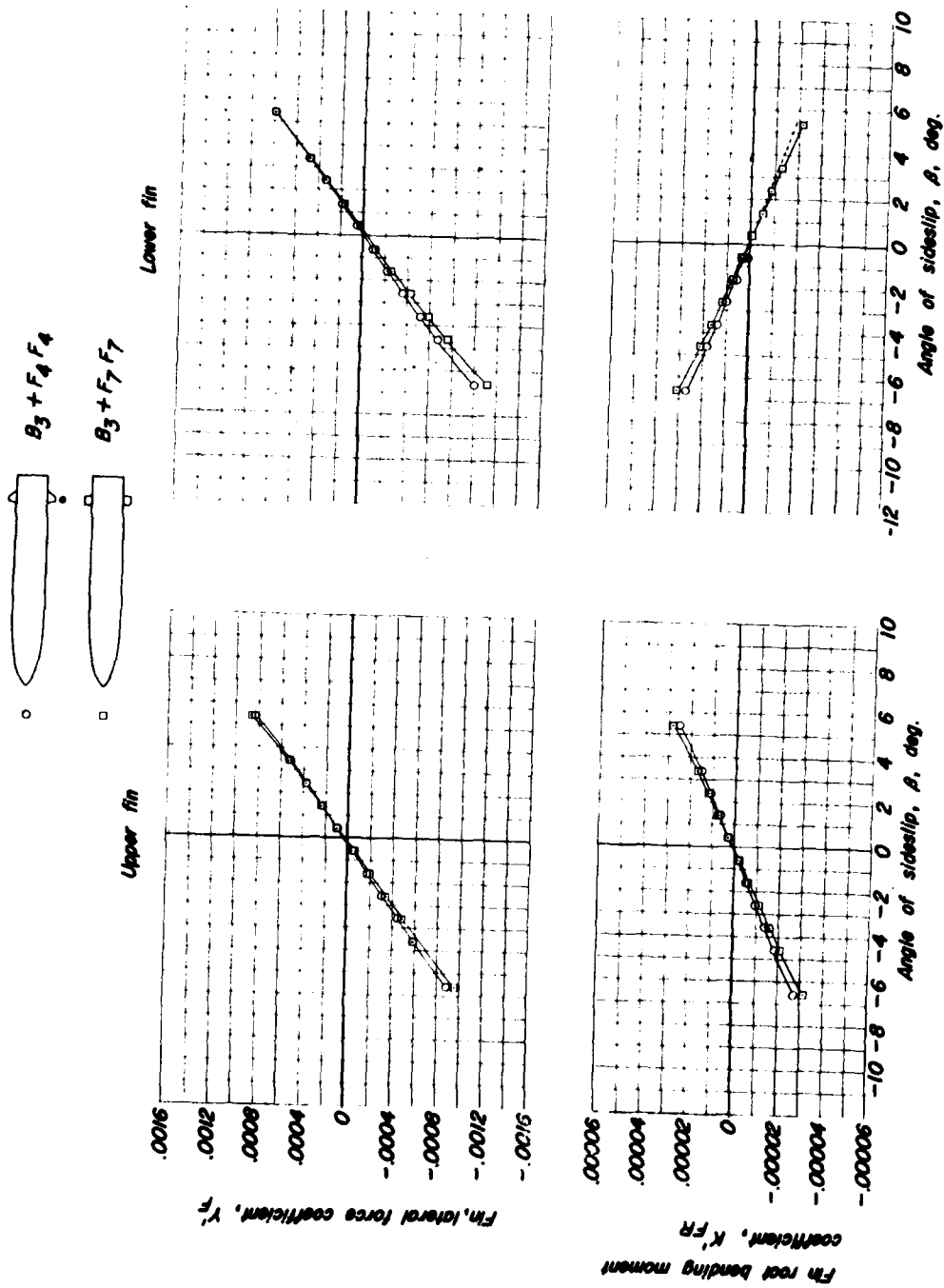


FIGURE A19 - VARIATION OF UPPER AND LOWER FIN-LATERAL FORCE AND FIN-ROOT BENDING MOMENT COEFFICIENTS WITH ANGLE OF SIDESLIP FOR B3 WITH FINS F_4 AND F_7 POSITION A

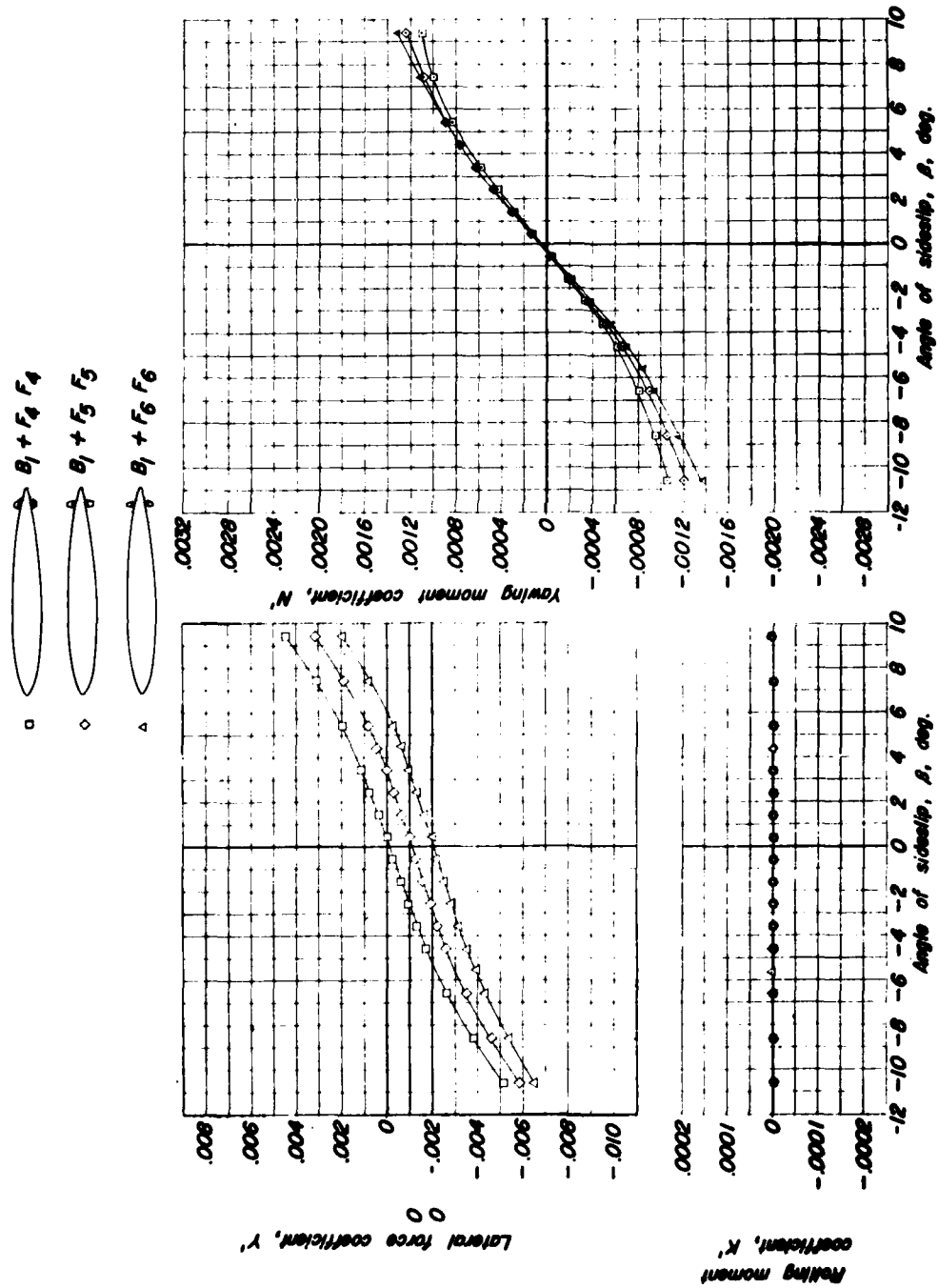


FIGURE A20 - VARIATION OF LATERAL FORCE, YAWING MOMENT, AND ROLLING MOMENT COEFFICIENTS WITH ANGLE OF SIDESLIP FOR B_1 WITH FINS F_4 , F_5 , AND F_6 WITH GAP AT POSITION A

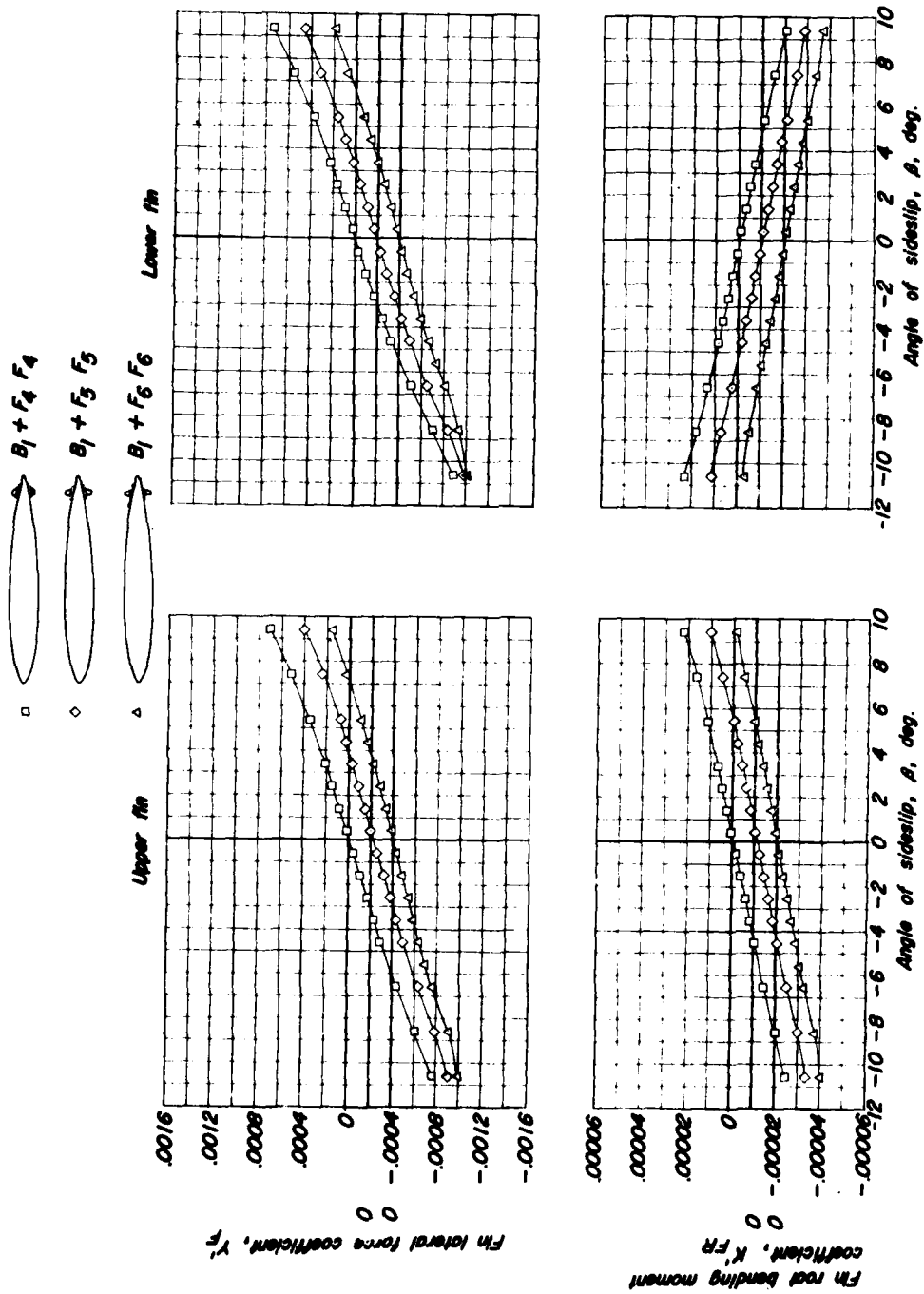


FIGURE A21 - VARIATION OF UPPER AND LOWER FIN-LATERAL FORCE AND FIN-ROOT BENDING MOMENT COEFFICIENTS WITH ANGLE OF SIDESLIP FOR B1 WITH FINS F_4 , F_5 , AND F_6 WITH GAP AT POSITION A

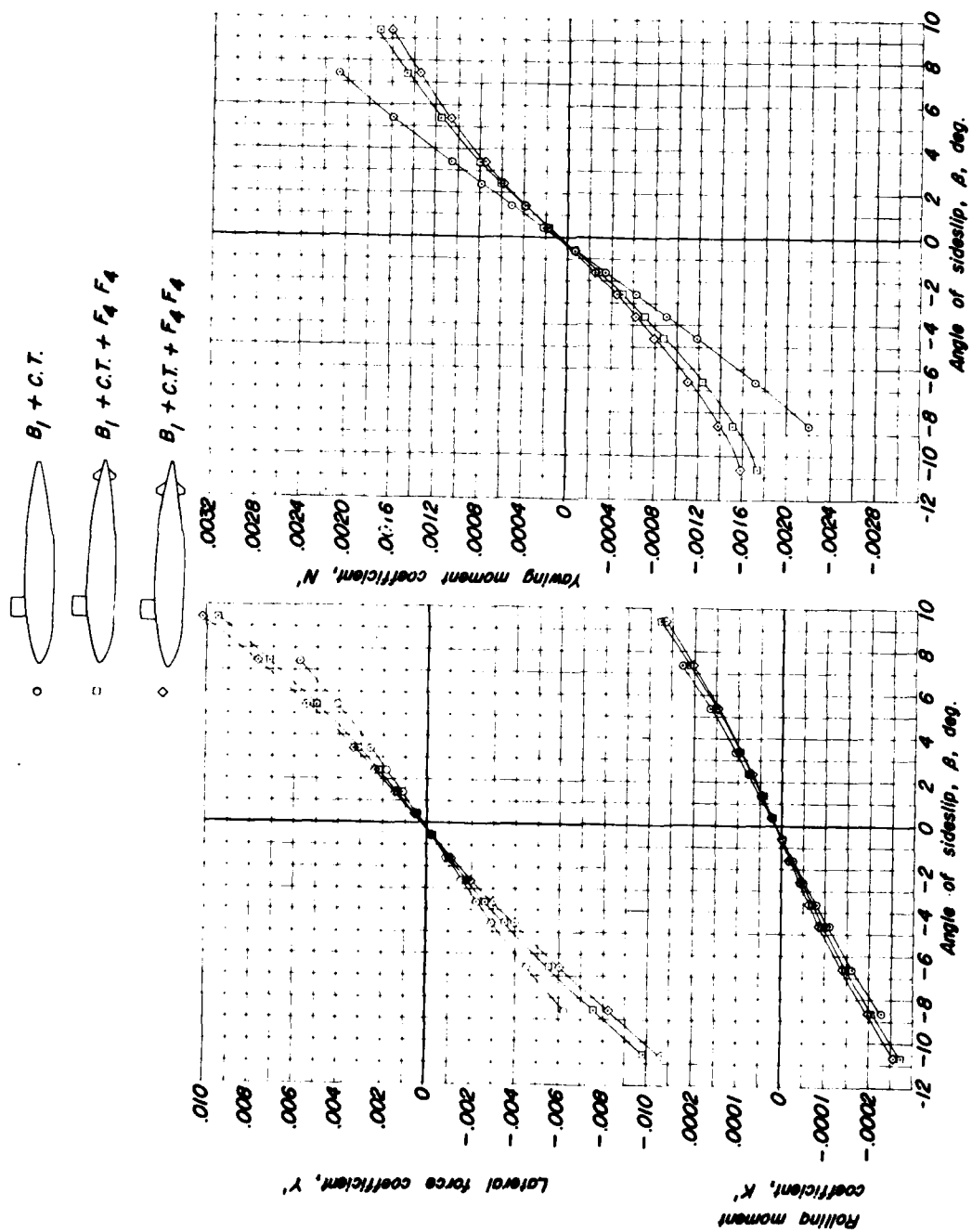


FIGURE A22 - VARIATION OF LATERAL FORCE, YAWING MOMENT, AND ROLLING MOMENT COEFFICIENTS WITH ANGLE OF SIDESLIP FOR $B_1+C.T.$, $B_1+C.T.+F_4 F_4$ AT POSITIONS A AND B

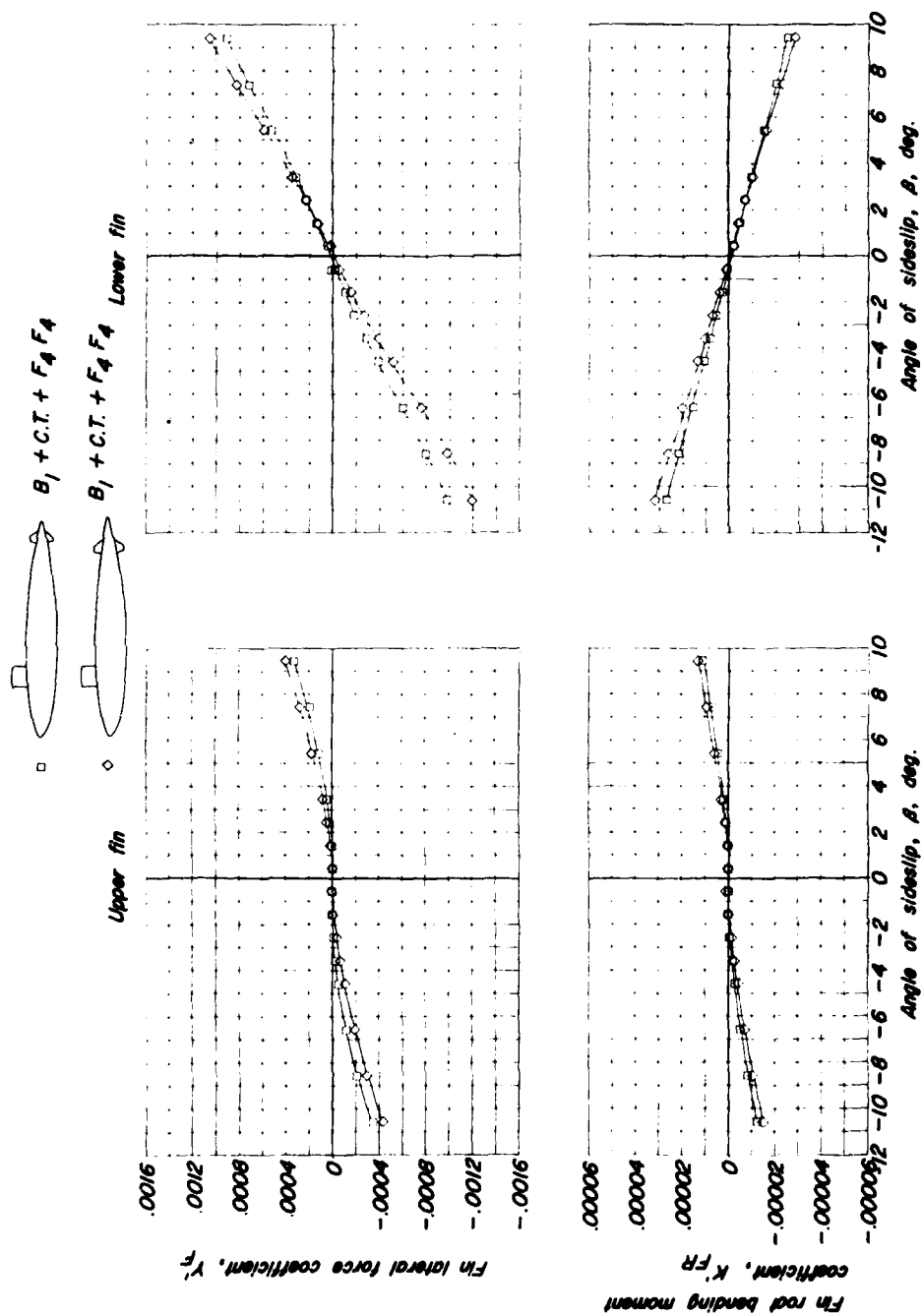


FIGURE A23 - VARIATION OF UPPER AND LOWER FIN-LATERAL FORCE AND FIN-ROOT BENDING MOMENT COEFFICIENTS WITH ANGLE OF SIDESLIP FOR $B_1 + C.T. + F_4 F_4$ AT POSITION A AND B

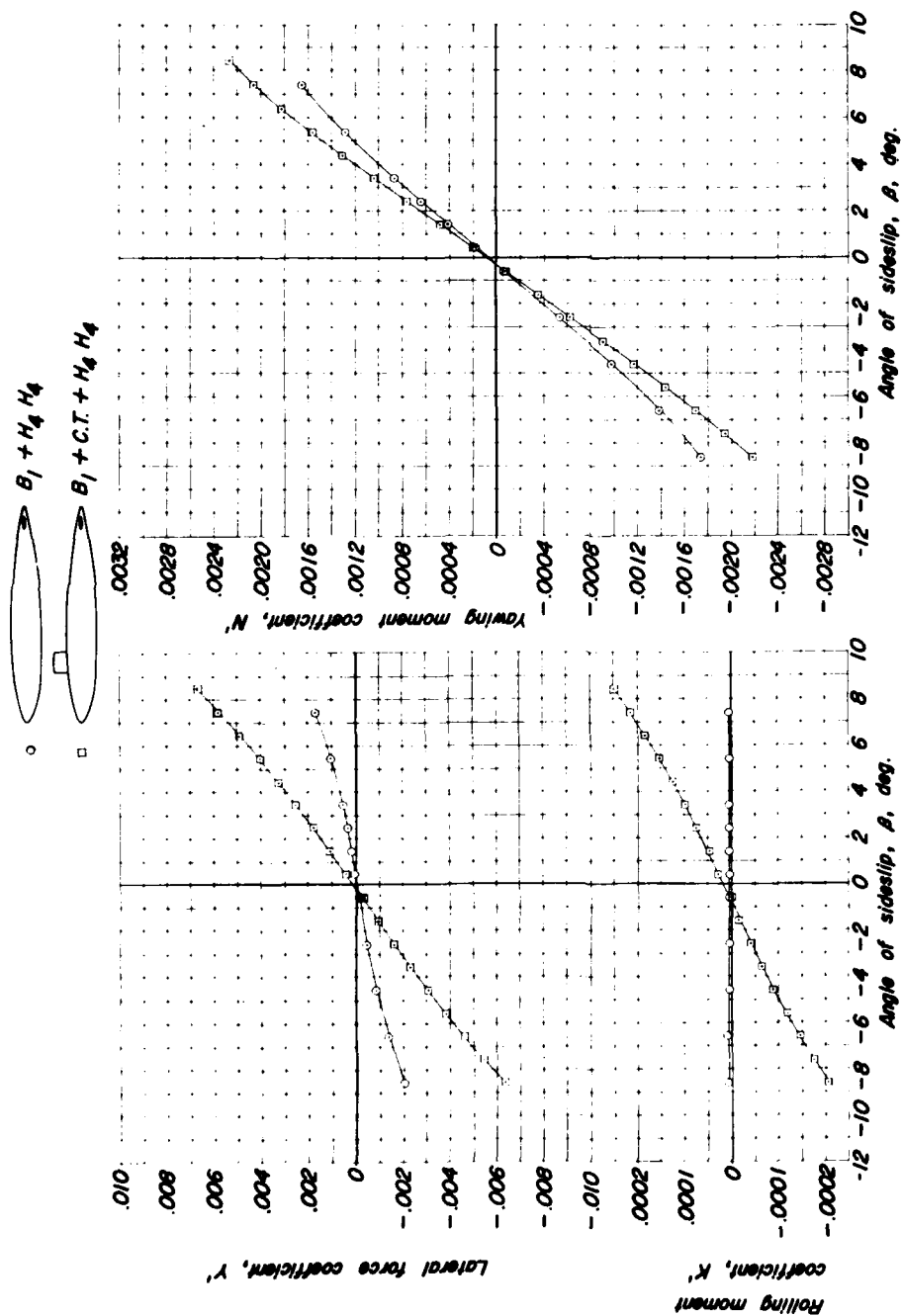


FIGURE A24 - VARIATION OF LATERAL FORCE, YAWING MOMENT, AND ROLLING MOMENT COEFFICIENTS WITH ANGLE OF SIDESLIP FOR $B_1 + H_4 H_4$, $B_1 + C.T. + H_4 H_4$ AT POSITION A

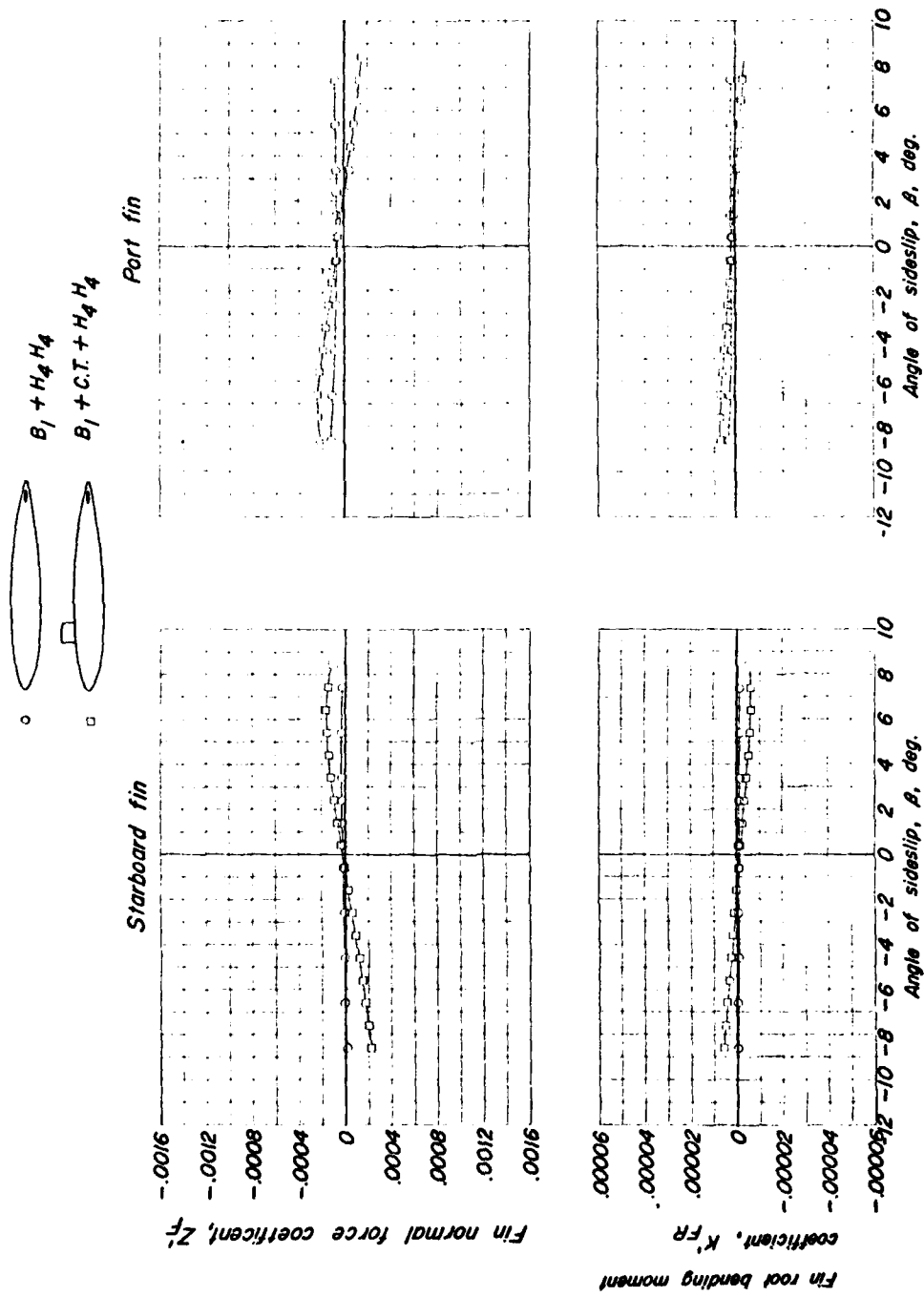


FIGURE A25 - VARIATION OF UPPER AND LOWER FIN-NORMAL FORCE AND FIN-ROOT BENDING MOMENT COEFFICIENTS WITH ANGLE OF SIDESLIP FOR $B_1 + H_4 H_4$, $B_1 + C.T. + H_4 H_4$ AT POSITION A

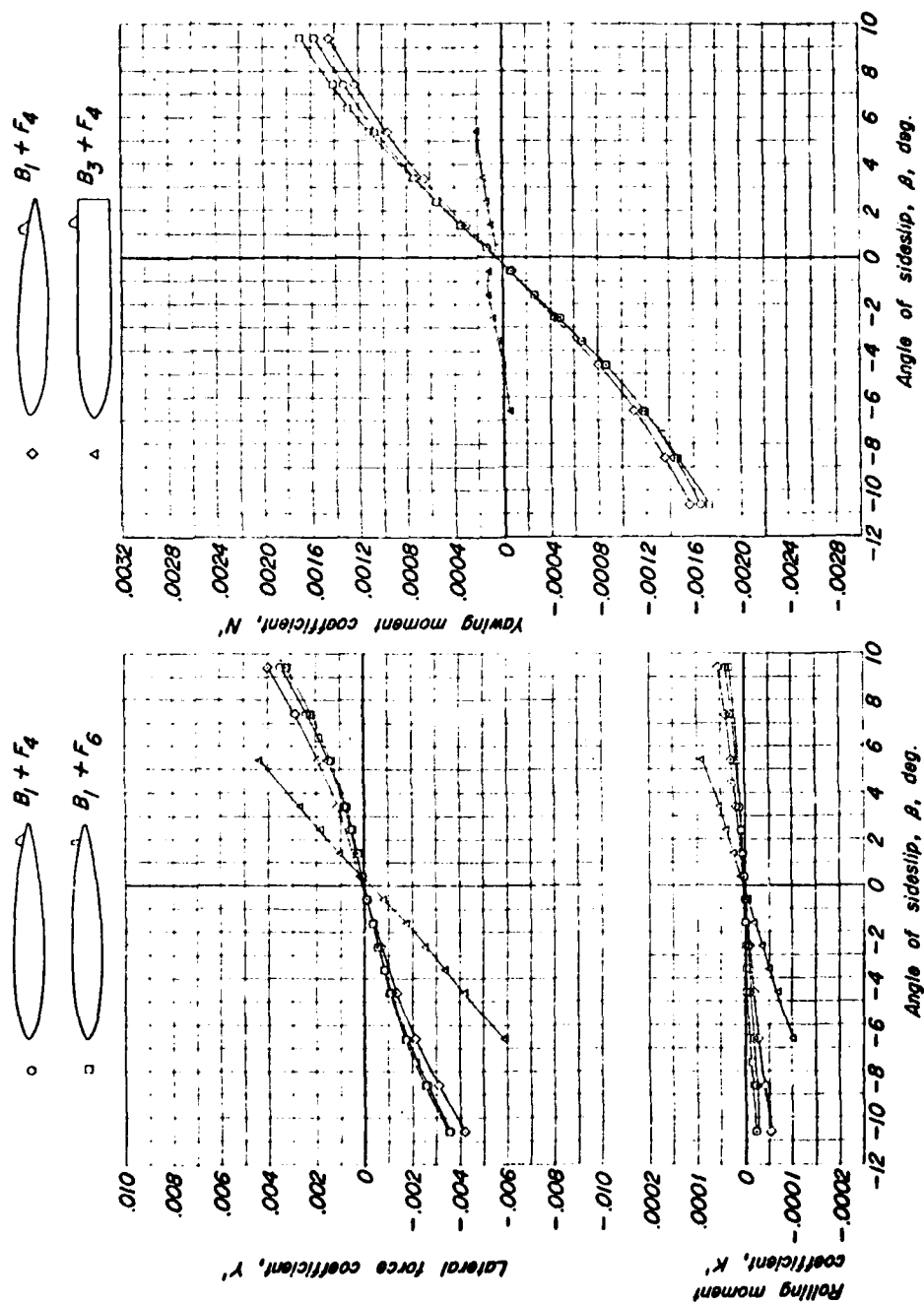


FIGURE A26 - VARIATION OF LATERAL FORCE, YAWING MOMENT, AND ROLLING MOMENT COEFFICIENTS WITH ANGLE OF SIDESLIP FOR $B_1 + F_4$, $B_1 + F_6$, AND $B_3 + F_4$ AT POSITION A AND B

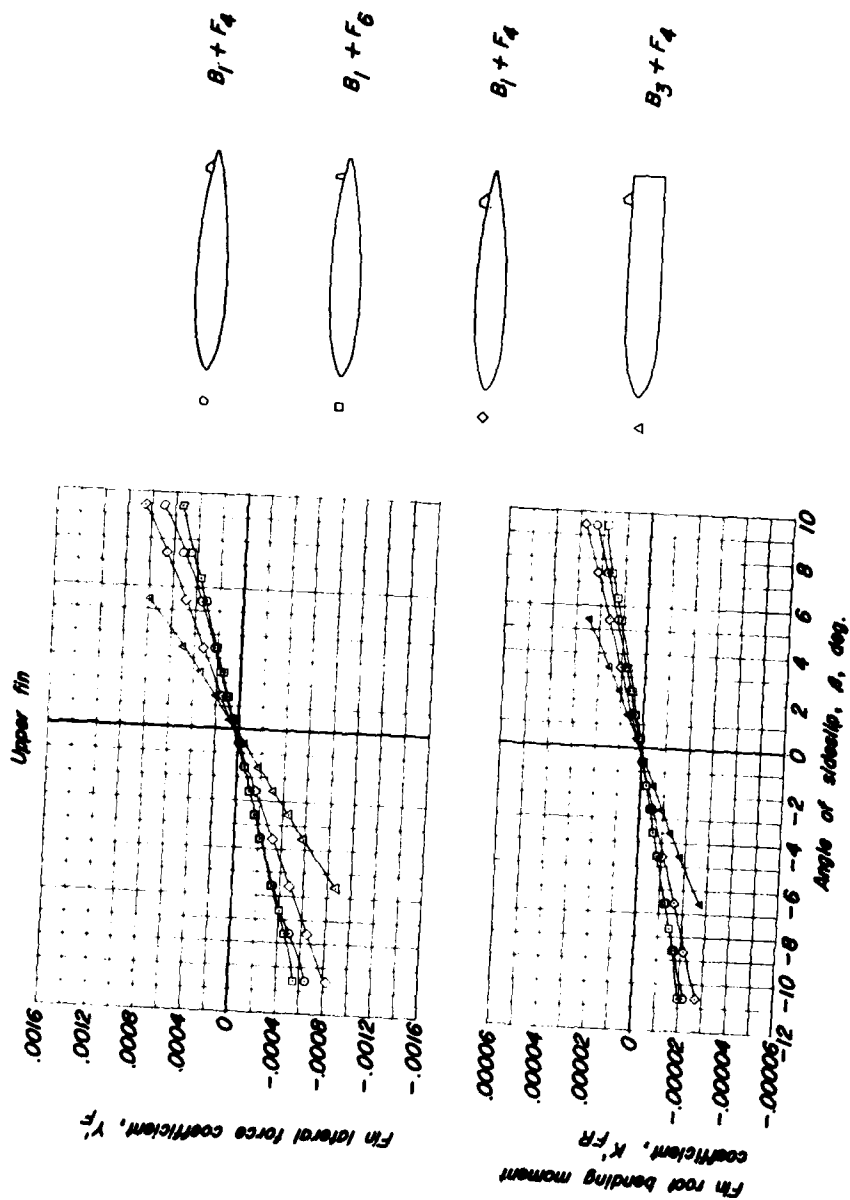


FIGURE A27 - VARIATION OF UPPER AND LOWER FIN-LATERAL FORCE AND FIN-ROOT BENDING MOMENT COEFFICIENTS WITH ANGLE OF SIDESLIP FOR $B_1 + F_4$, $B_1 + F_6$, AND $B_3 + F_4$ AT POSITIONS A AND B

HYDRONAUTICS, Incorporated

APPENDIX B

GRAPHICAL PRESENTATION OF VELOCITY
AND ANGULARITY CHARACTERISTICS AT
THE STERN OF THE BODY AS A FUNCTION
OF ANGLE OF SIDESLIP

Configuration	Survey Position	Body Dia. In.	Longitudinal Distance from CB, x'_{SP}
B1 and B1+CT	A	3.50	0.477
B3	B	12.44	0.439

HYDRONAUTICS, INCORPORATED

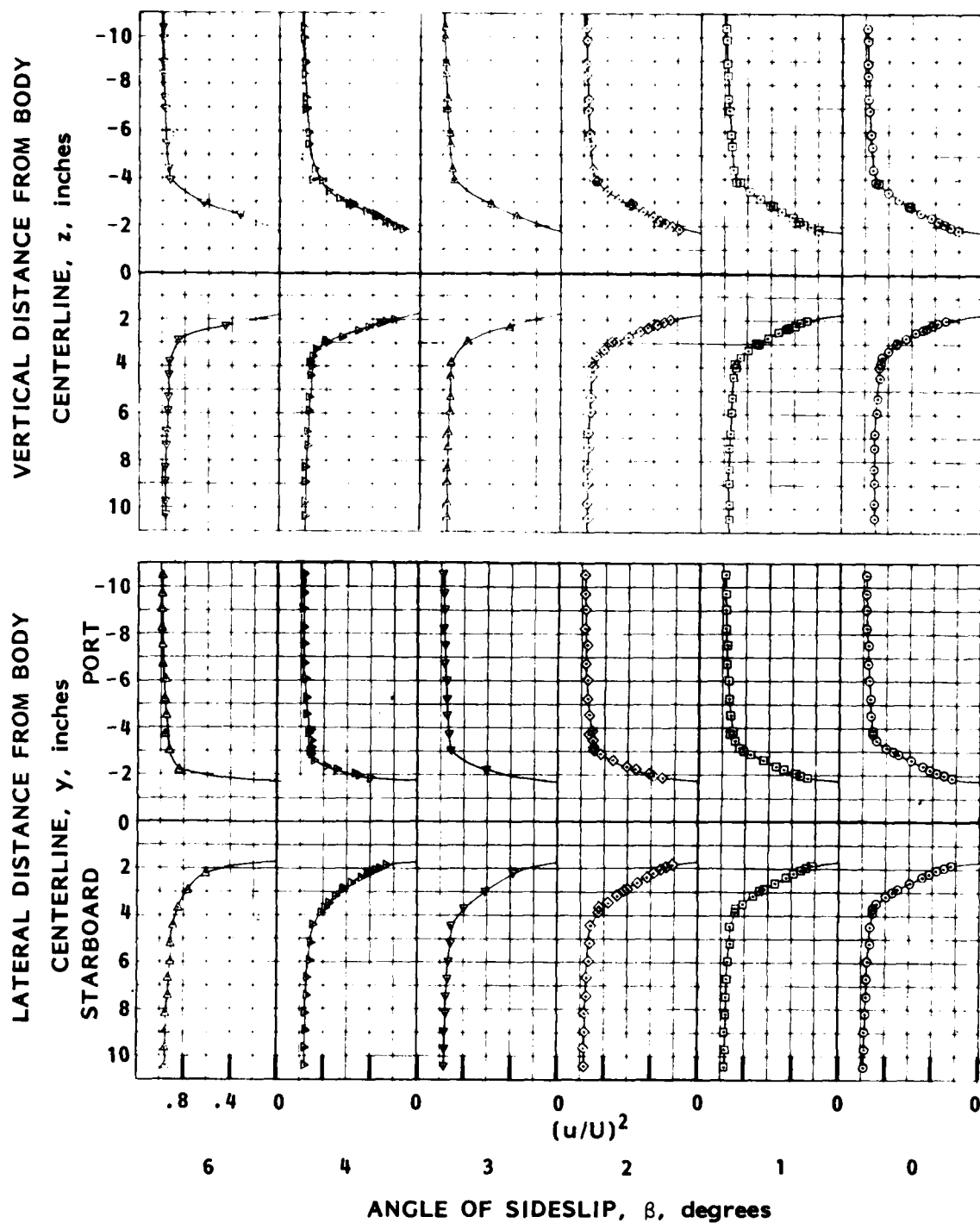


FIGURE B1 - VARIATION OF THE VERTICAL AND HORIZONTAL
LONGITUDINAL VELOCITY PARAMETERS WITH ANGLE
OF SIDESLIP FOR BODY B1 AT SURVEY POSITION A

HYDRONAUTICS, INCORPORATED

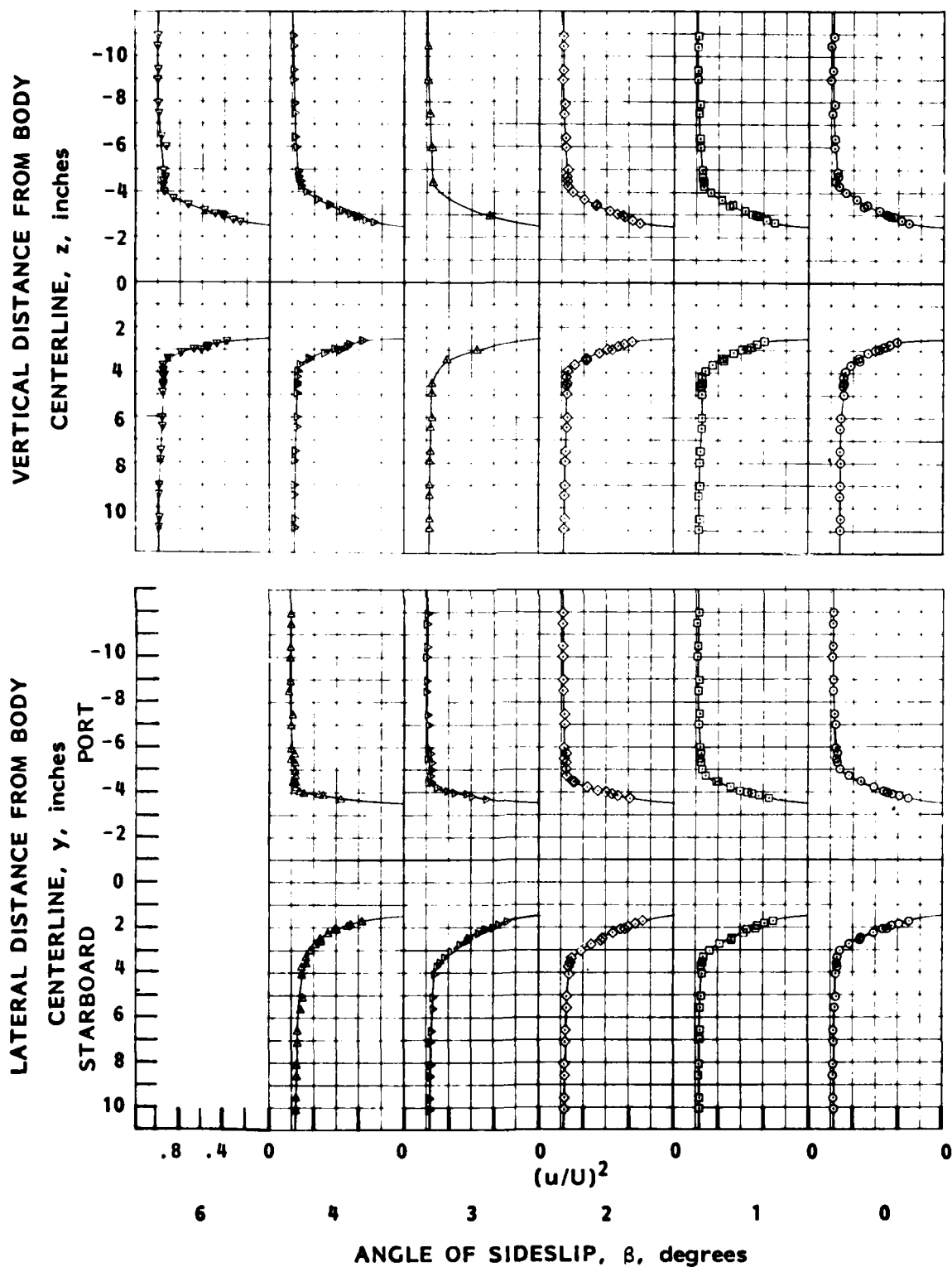


FIGURE B2 - VARIATION OF THE VERTICAL AND HORIZONTAL LONGITUDINAL VELOCITY PARAMETERS WITH ANGLE OF SIDESLIP FOR B1+CT AT SURVEY POSITION A

HYDRONAUTICS, INCORPORATED

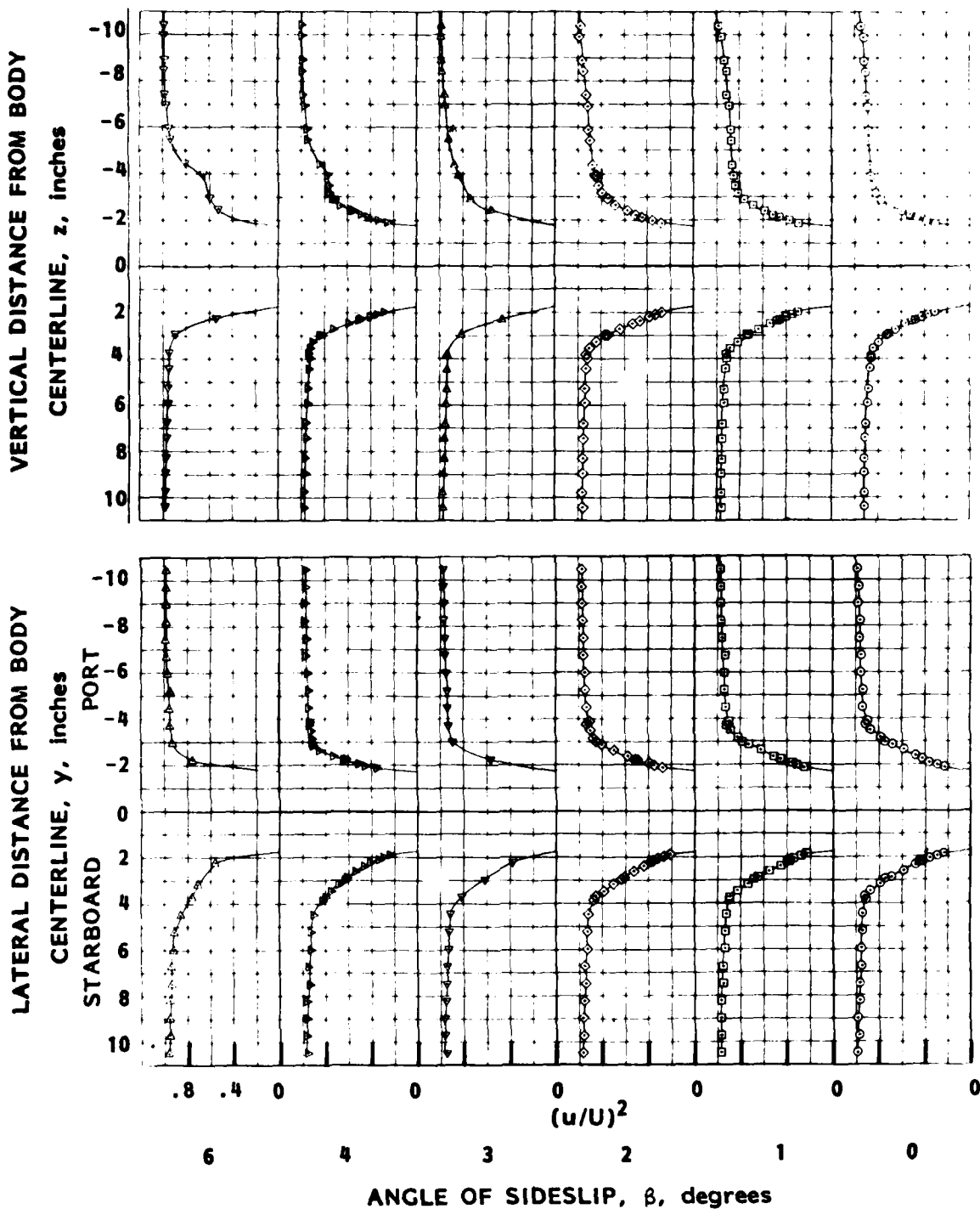


FIGURE B3 - VARIATION OF THE VERTICAL AND HORIZONTAL LONGITUDINAL VELOCITY PARAMETERS WITH ANGLE OF SIDESLIP FOR BODY B1 AT SURVEY POSITION B

HYDRONAUTICS, INCORPORATED

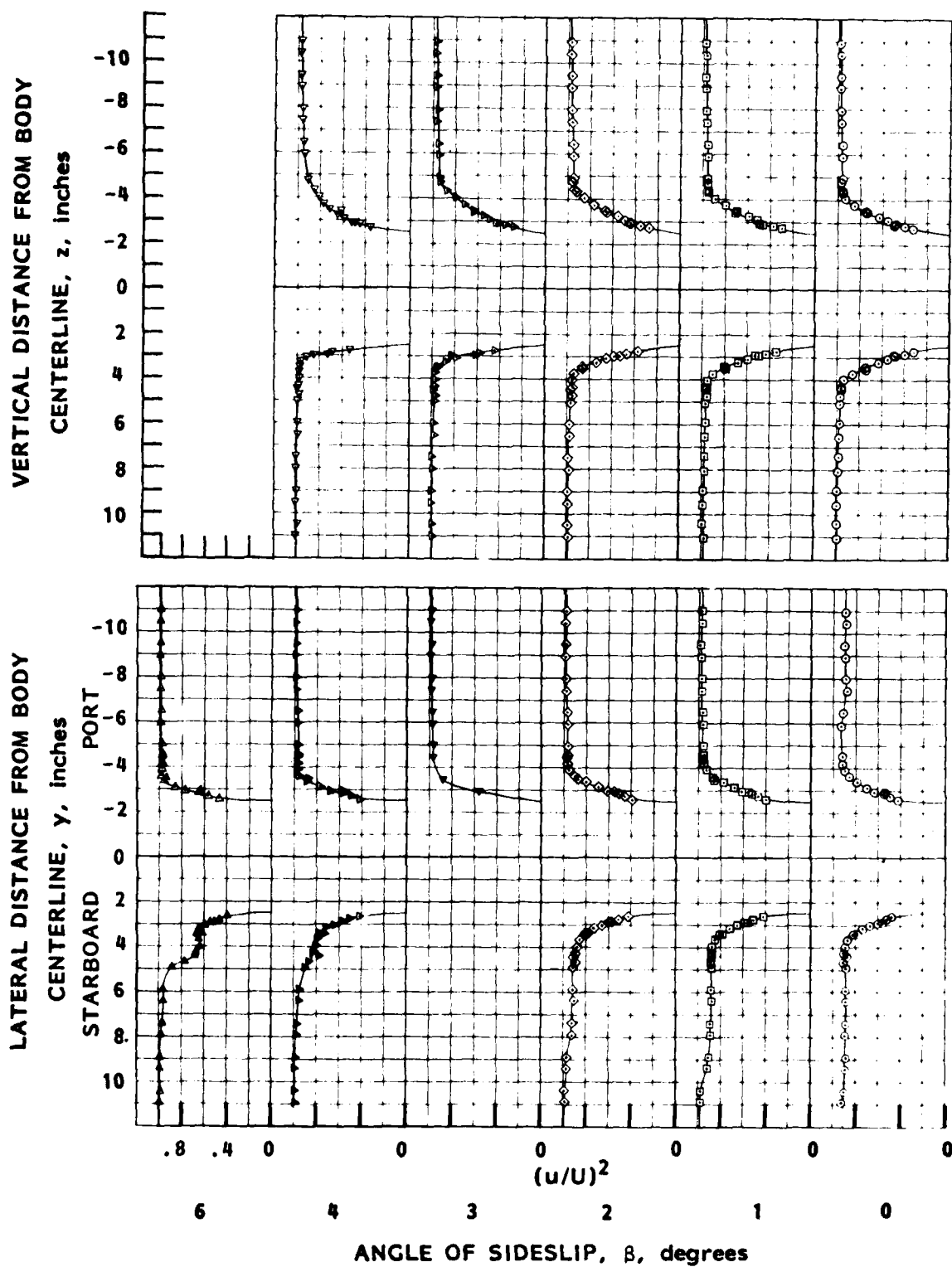


FIGURE B4 - VARIATION OF THE VERTICAL AND HORIZONTAL LONGITUDINAL VELOCITY PARAMETERS WITH ANGLE OF SIDESLIP FOR B1+CT AT SURVEY POSITION B

HYDRONAUTICS, INCORPORATED

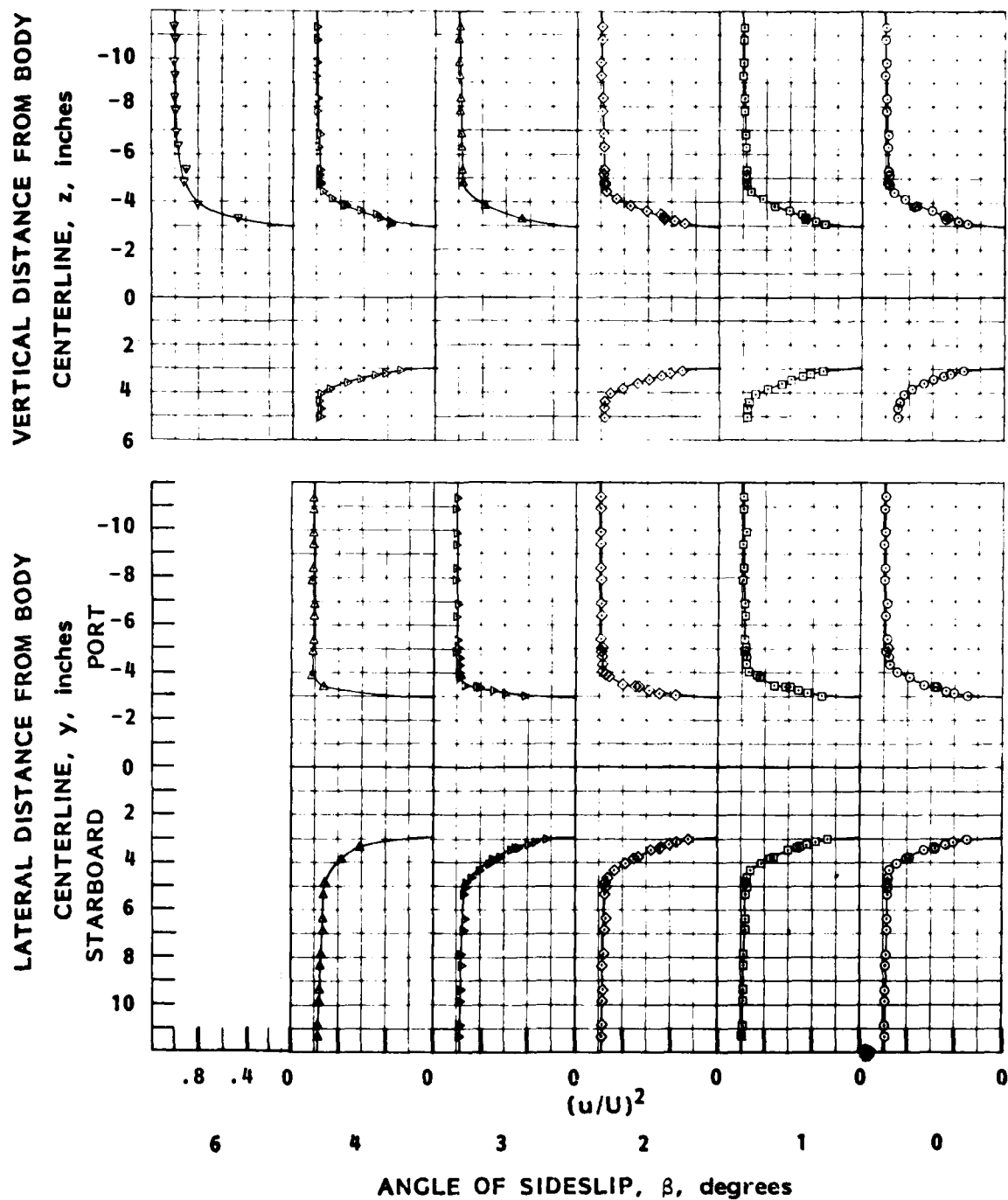


FIGURE B5 - VARIATION OF THE VERTICAL AND HORIZONTAL LONGITUDINAL VELOCITY PARAMETERS WITH ANGLE OF SIDESLIP FOR BODY B1 AT SURVEY POSITION C

HYDRONAUTICS, INCORPORATED

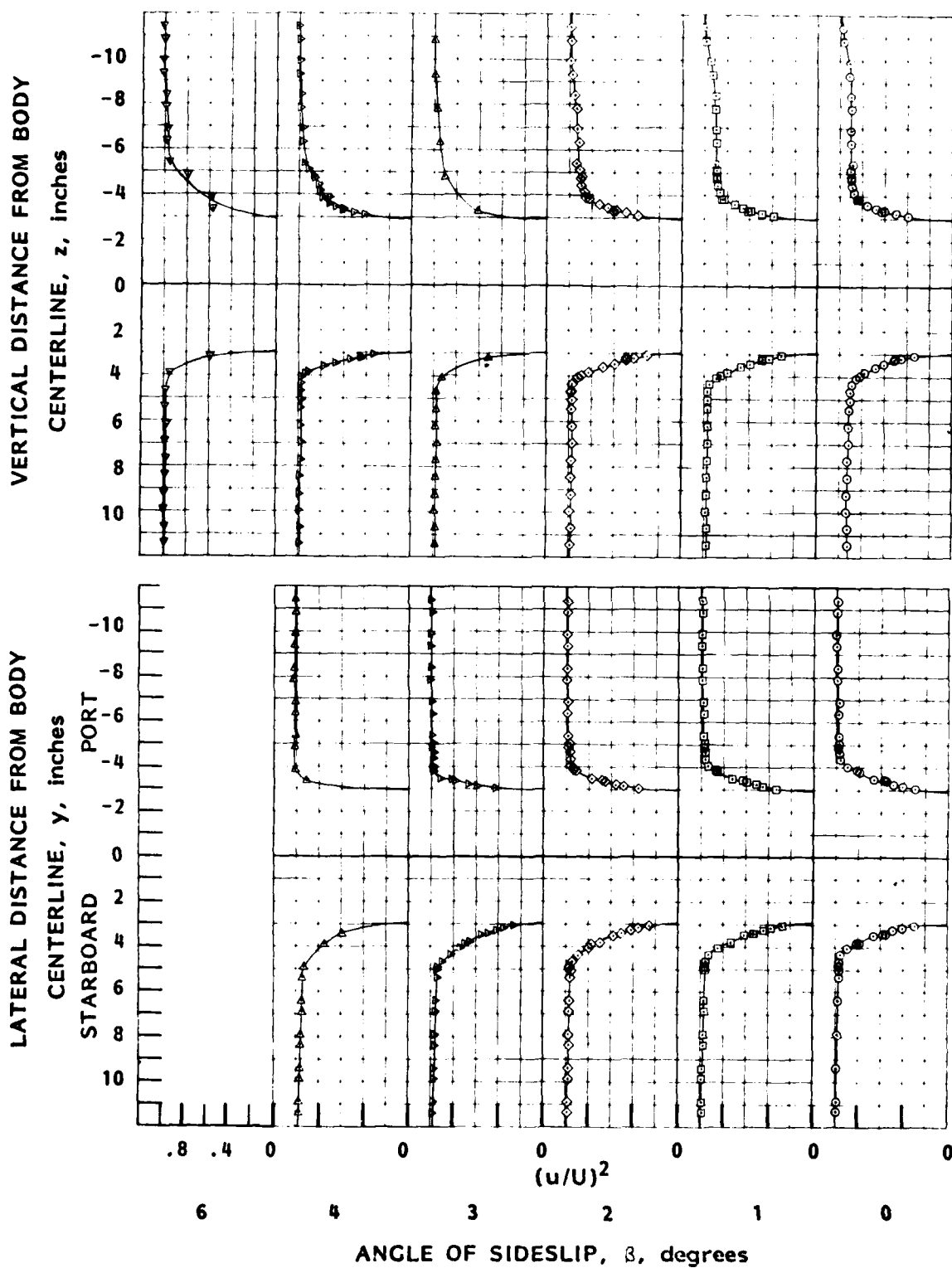


FIGURE B6 - VARIATION OF THE VERTICAL AND HORIZONTAL LONGITUDINAL VELOCITY PARAMETERS WITH ANGLE OF SIDESLIP FOR B1+CT AT SURVEY POSITION C

HYDRONAUTICS, INCORPORATED

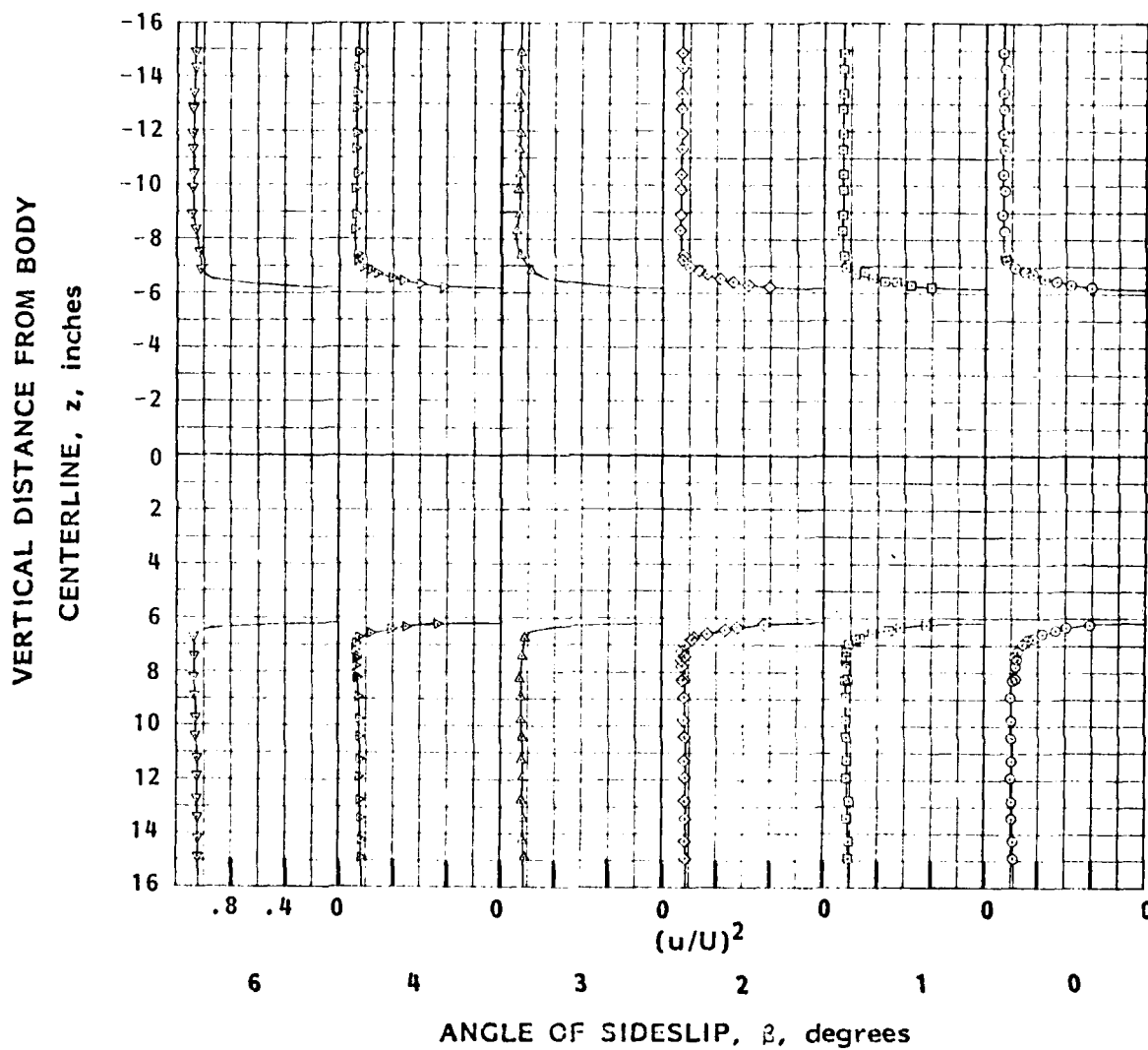


FIGURE B7 - VARIATION OF THE VERTICAL LONGITUDINAL VELOCITY PARAMETER WITH ANGLE OF SIDESLIP FOR BODY B3 AT SURVEY POSITION B

HYDRONAUTICS, INCORPORATED

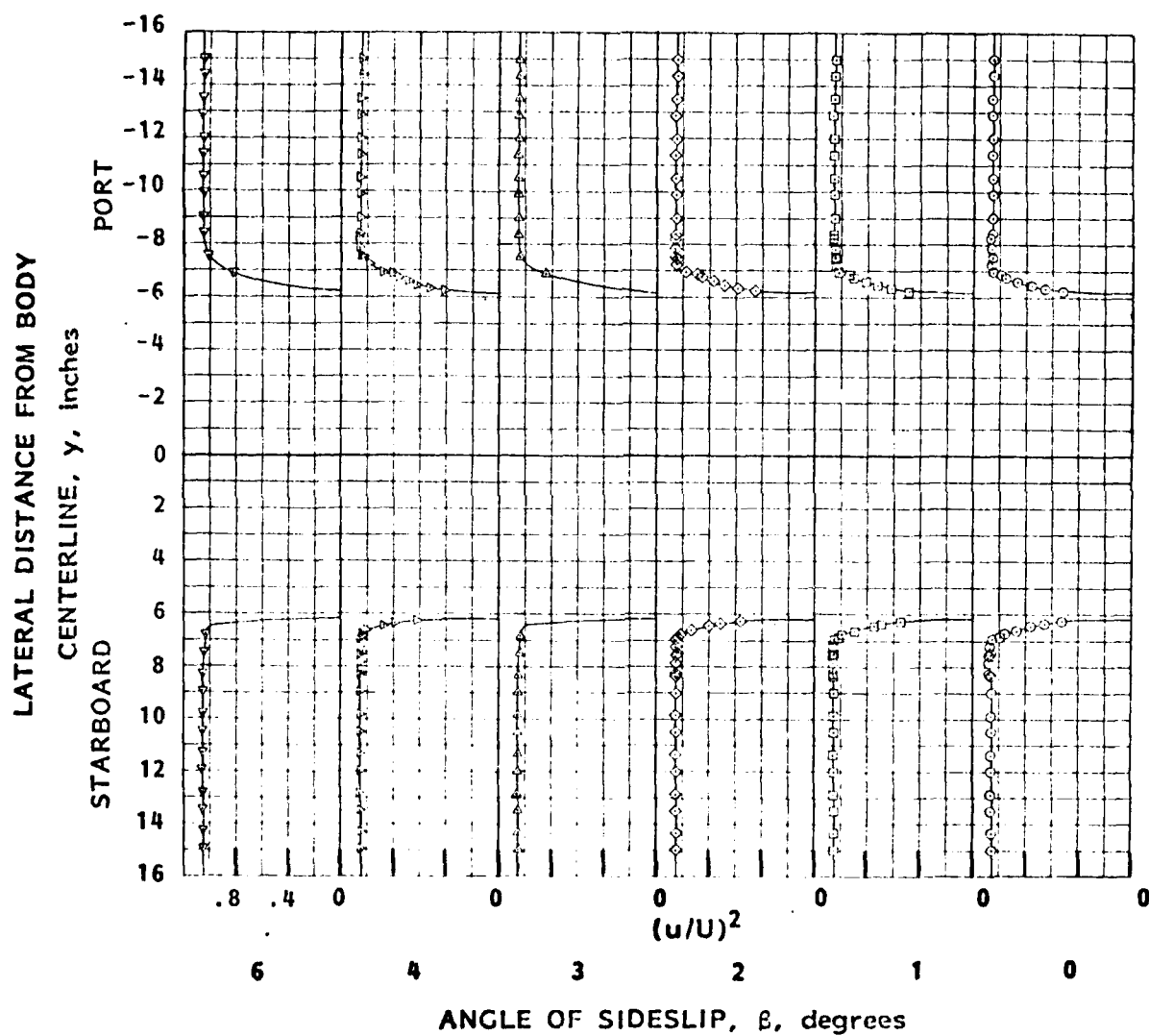


FIGURE B8 - VARIATION OF THE HORIZONTAL LONGITUDINAL VELOCITY PARAMETER WITH ANGLE OF SIDESLIP FOR BODY B3 AT SURVEY POSITION B

HYDRONAUTICS, INCORPORATED

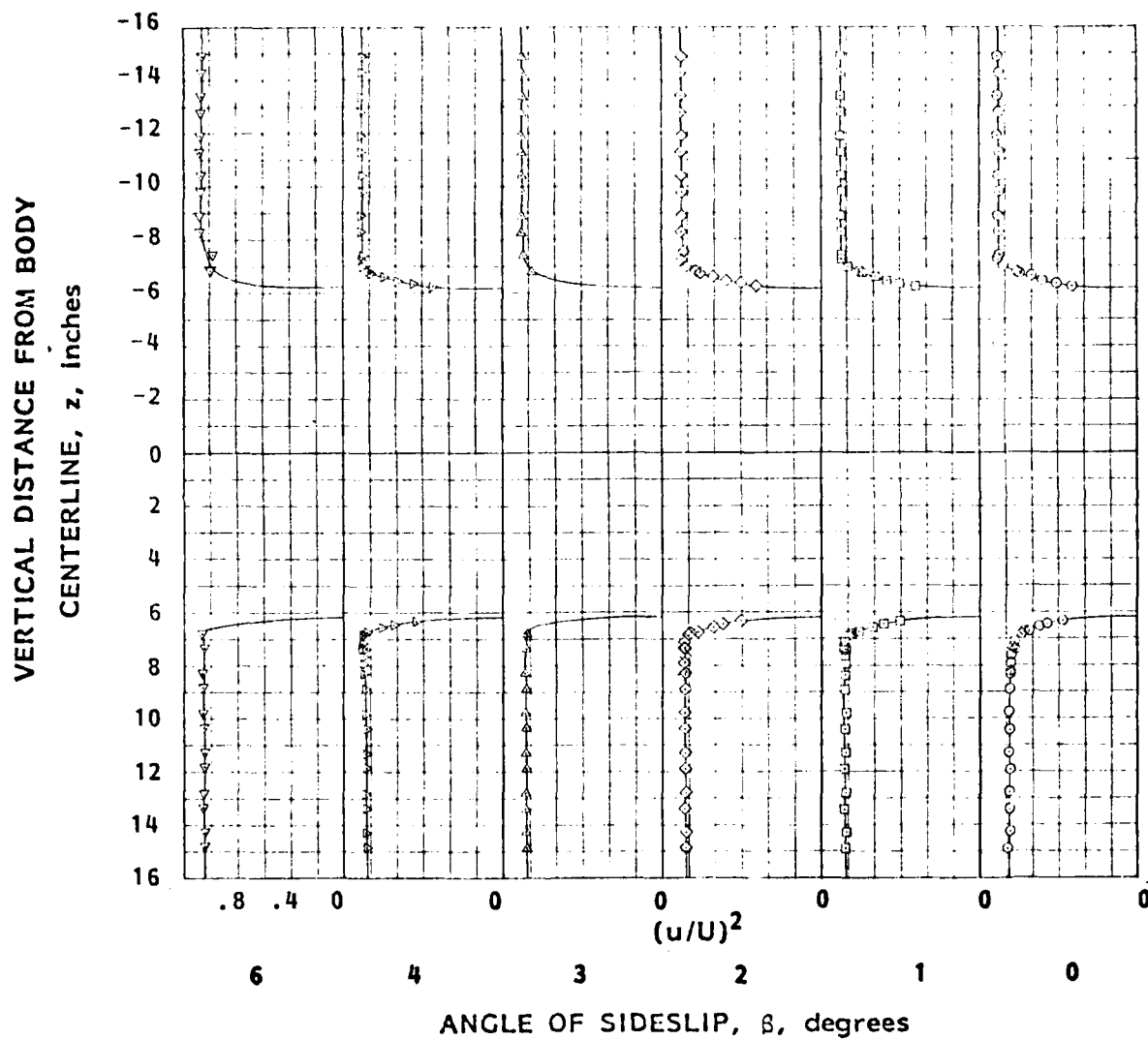


FIGURE B9 - VARIATION OF THE VERTICAL LONGITUDINAL
VELOCITY PARAMETER WITH ANGLE OF SIDESLIP
FOR BODY B3 AT SURVEY POSITION C

HYDRONAUTICS, INCORPORATED

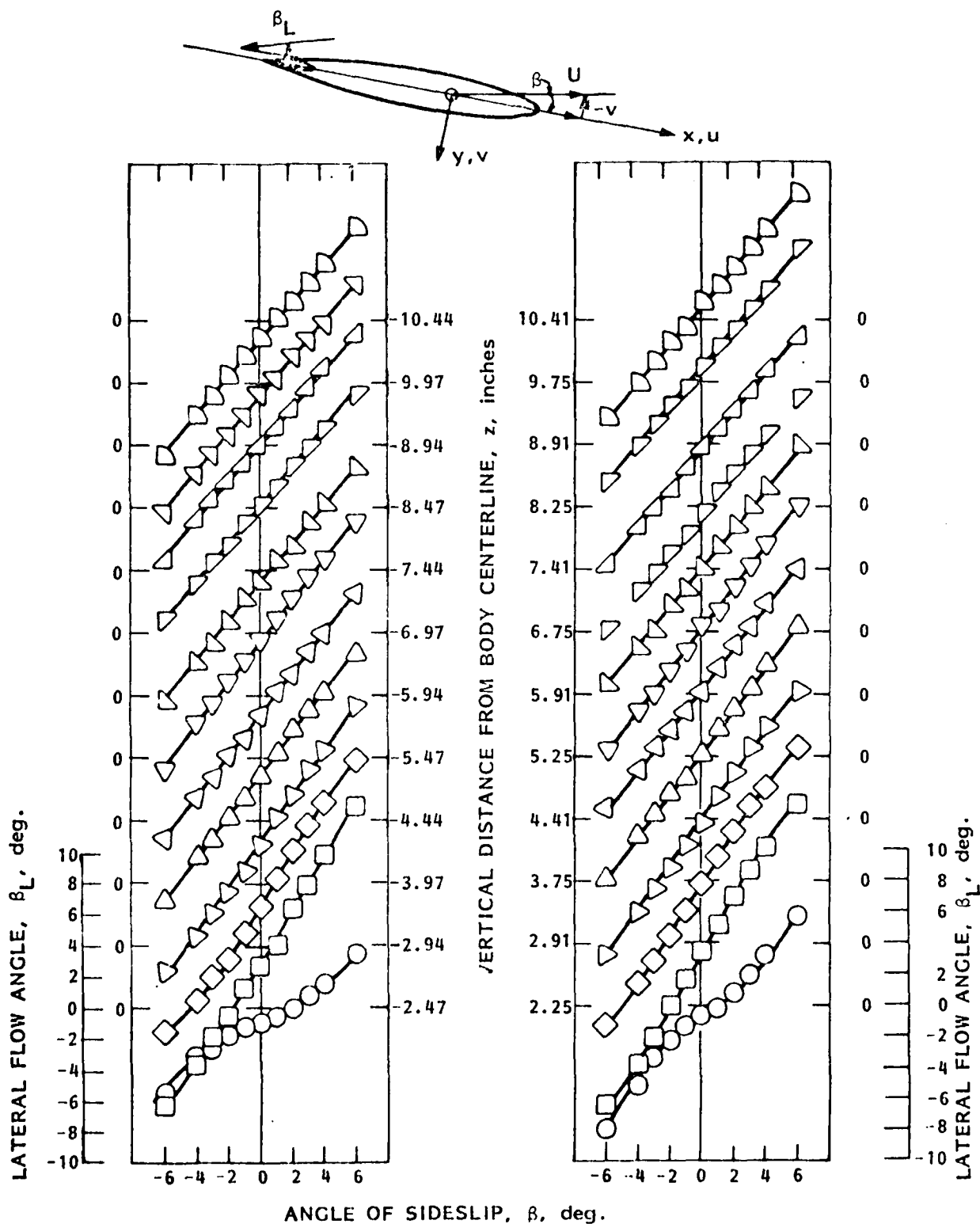


FIGURE B10 - VARIATION OF THE LATERAL-FLOW ANGLE WITH ANGLE OF SIDESLIP FOR BODY B1 AT SURVEY POSITION A

HYDRONAUTICS, INCORPORATED

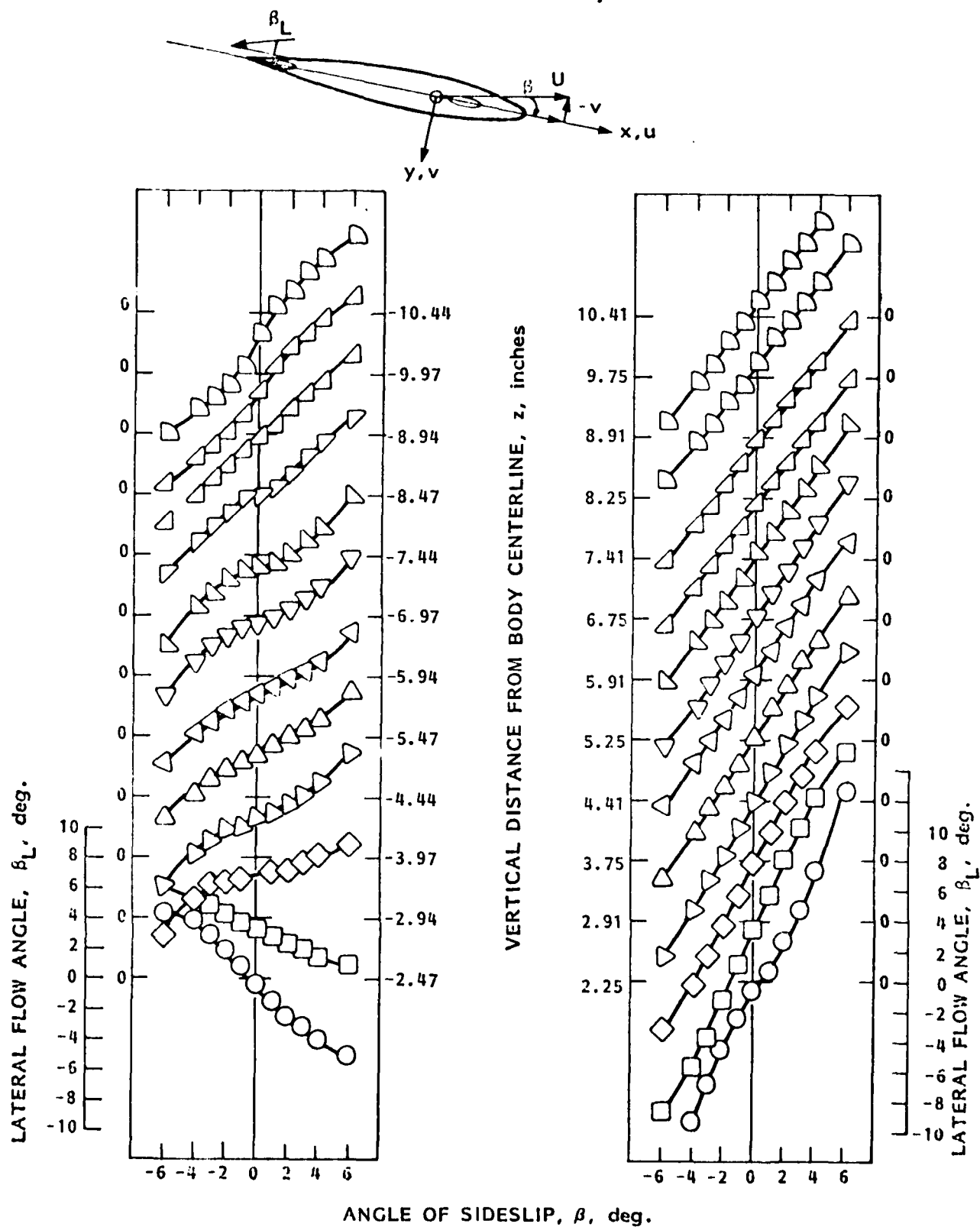
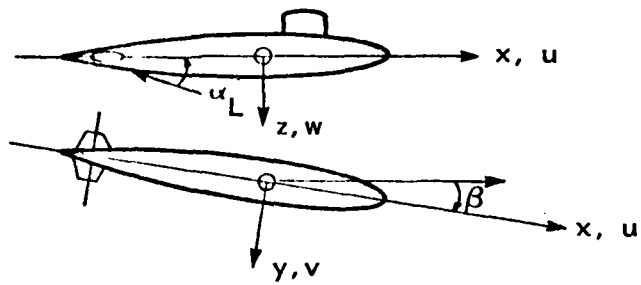


FIGURE B11 - VARIATION OF THE LATERAL-FLOW ANGLE WITH ANGLE OF SIDESLIP FOR B1+CT AT SURVEY POSITION A

HYDRONAUTICS, INCORPORATED



ANGLE OF SIDESLIP, β , deg.

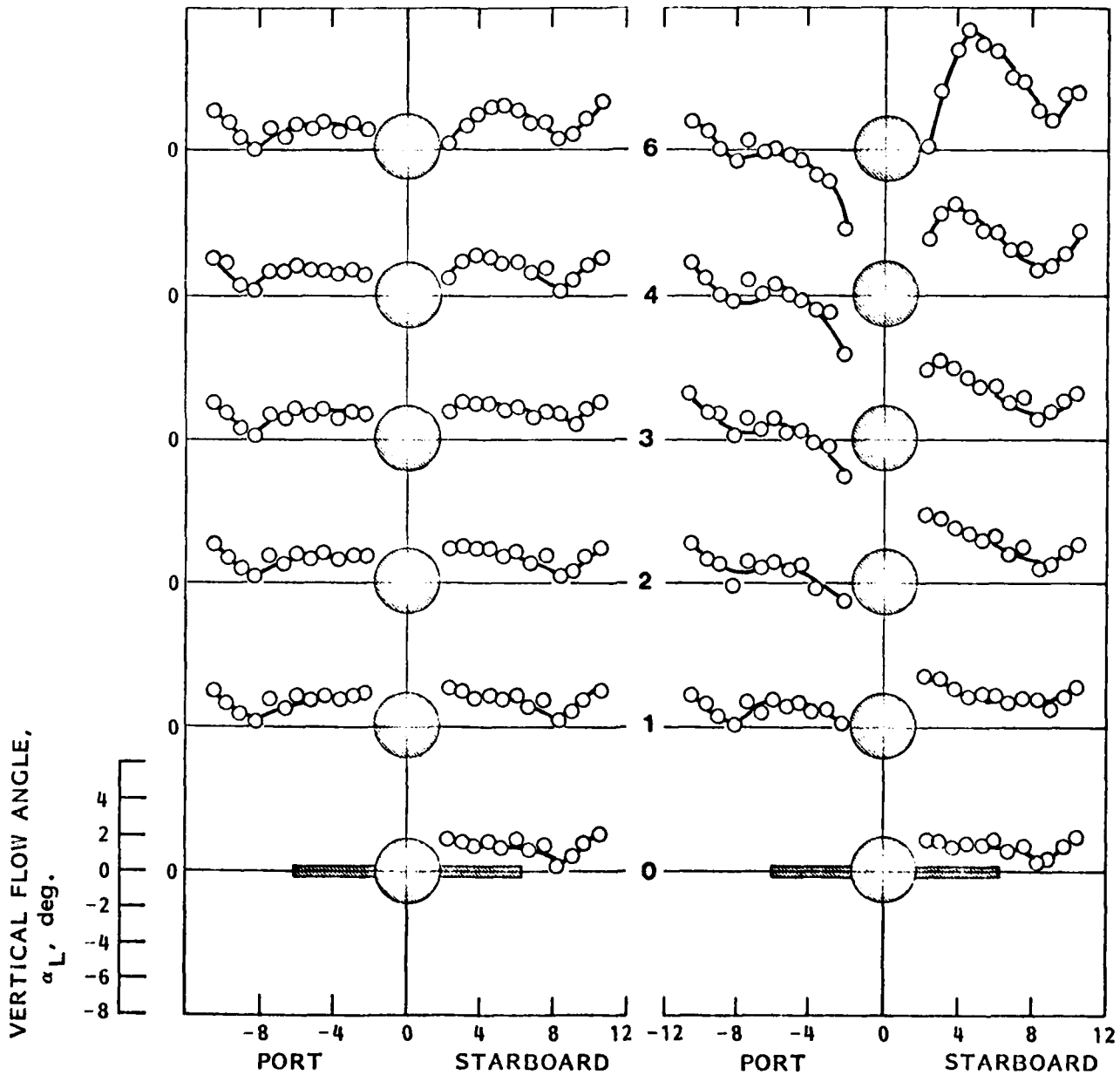
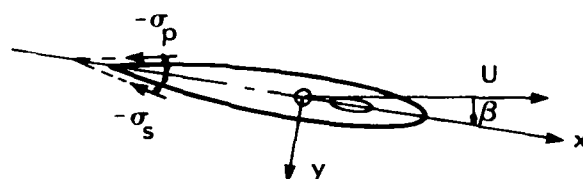
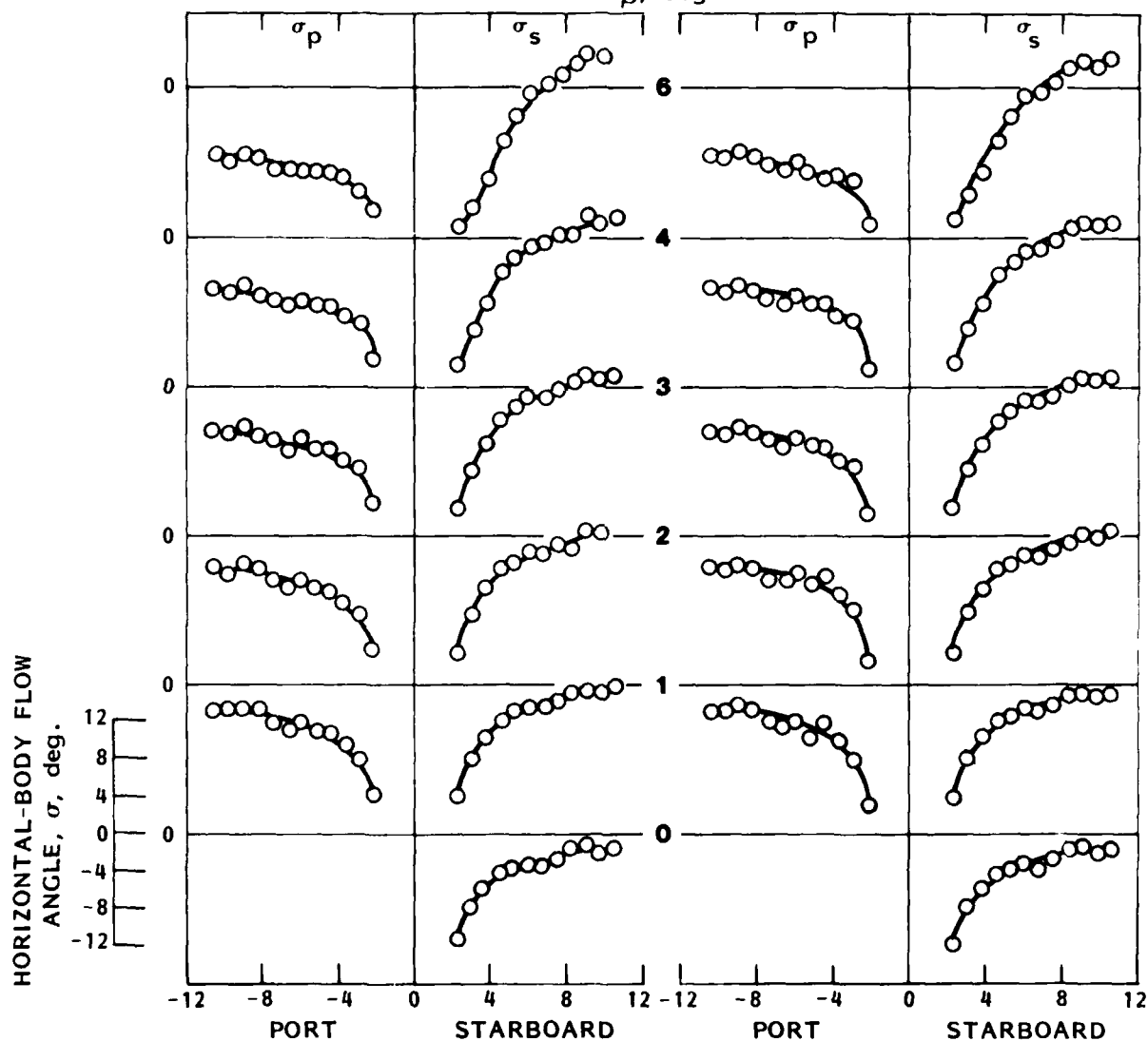


FIGURE B12 - VARIATION OF THE VERTICAL-FLOW ANGLE WITH LATERAL DISTANCE FOR BODY B1 AND B1+CT AT SURVEY POSITION A

HYDRONAUTICS, INCORPORATED



ANGLE OF
SIDESLIP,
 β , deg.



LATERAL DISTANCE FROM BODY CENTERLINE, y , inches

a. B1

b. B1+CT

FIGURE B13 - VARIATION OF HORIZONTAL-BODY-FLOW ANGLE WITH LATERAL DISTANCE FOR BODY B1 AND B1+CT AT SURVEY POSITION A

HYDRONAUTICS, INCORPORATED

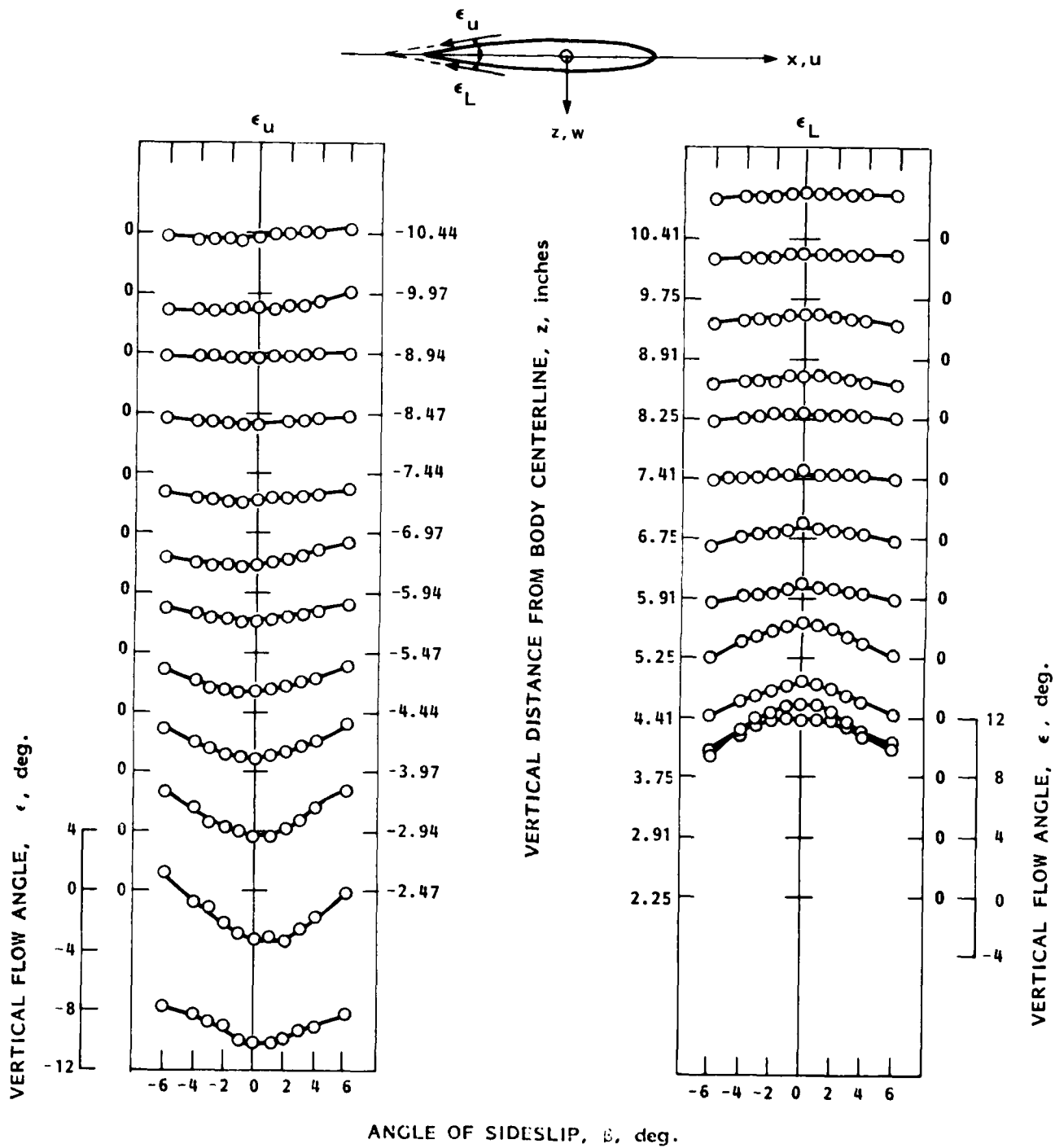


FIGURE B14 - VARIATION OF VERTICAL-BODY-FLOW ANGLE WITH VERTICAL DISTANCE FOR B1 AT SURVEY POSITION A

HYDRONAUTICS, INCORPORATED

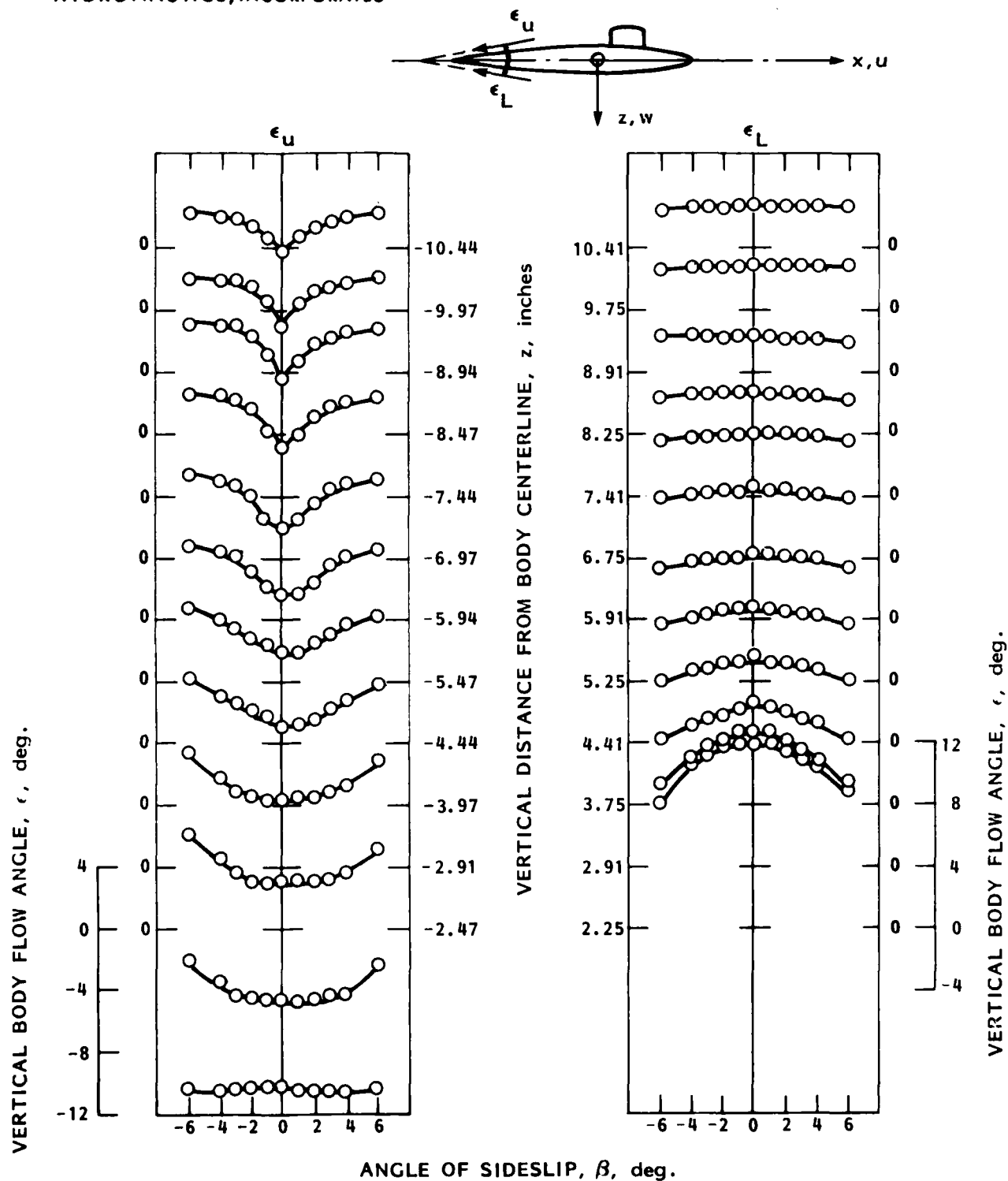


FIGURE B15 - VARIATION OF VERTICAL-BODY-FLOW ANGLE WITH VERTICAL DISTANCE FOR B1+CT AT SURVEY POSITION A

HYDRONAUTICS, INCORPORATED

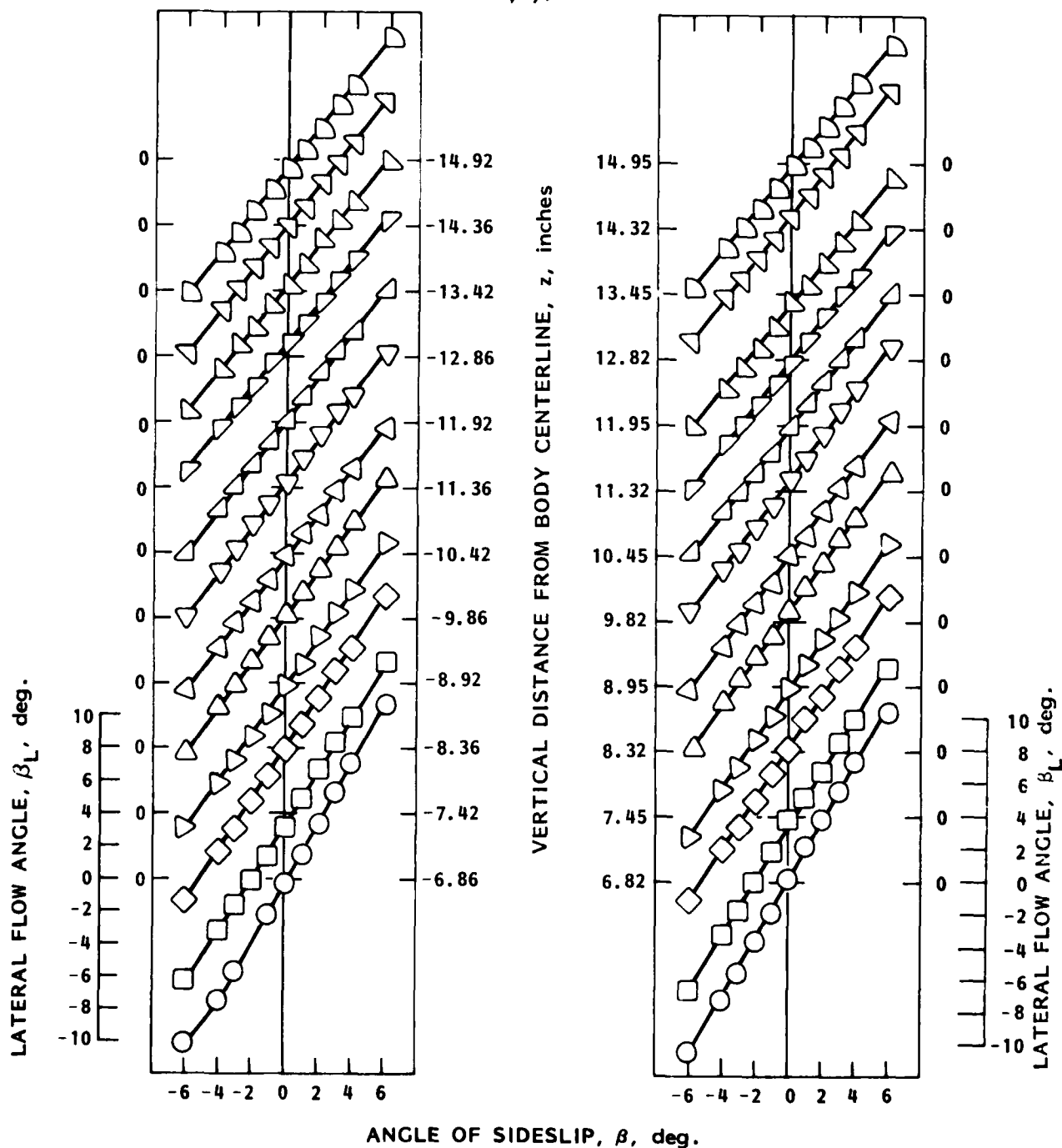
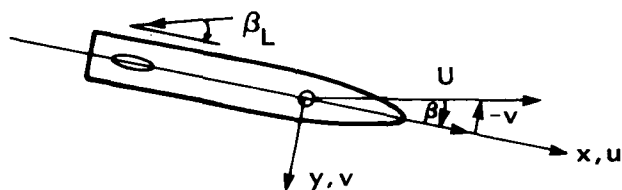


FIGURE B16 - VARIATION OF THE LATERAL-FLOW ANGLE WITH ANGLE OF SIDESLIP FOR BODY B3 AT SURVEY POSITION B

HYDRONAUTICS, INCORPORATED

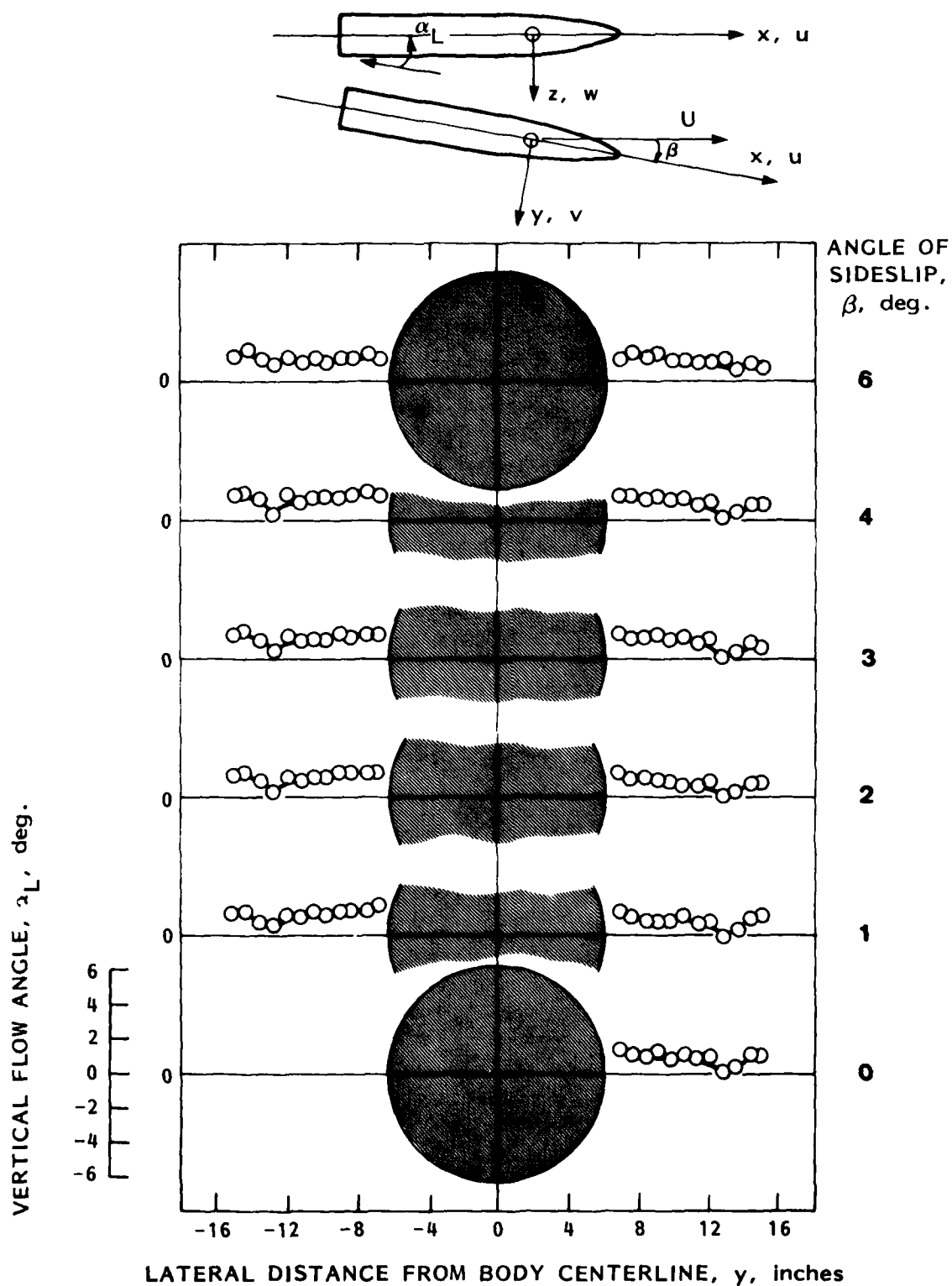


FIGURE B17 - VARIATION OF THE VERTICAL-FLOW ANGLE WITH LATERAL DISTANCE FOR BODY B3 AT SURVEY POSITION B

HYDRONAUTICS, INCORPORATED

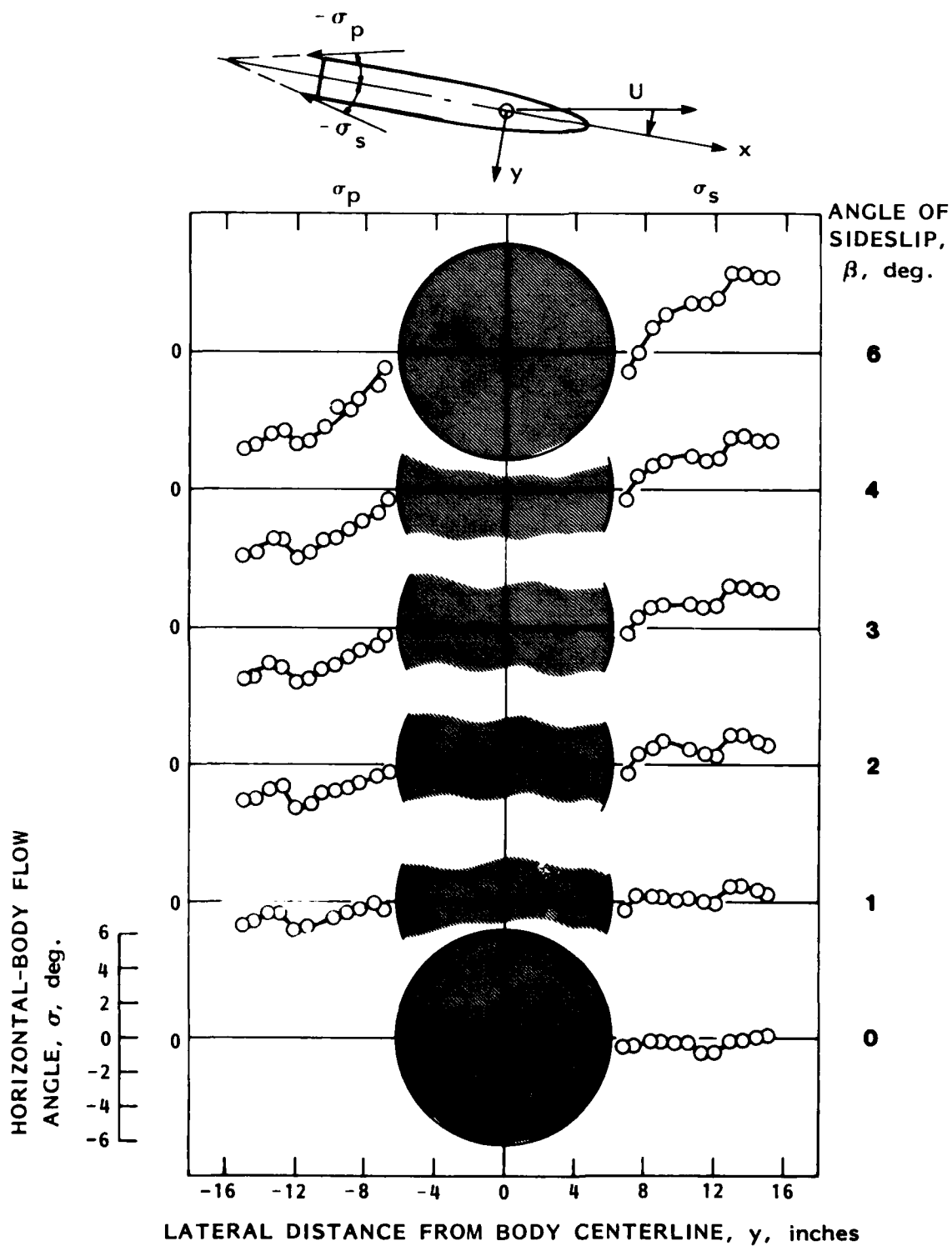


FIGURE B18 - VARIATION OF HORIZONTAL-BODY-FLOW ANGLE WITH LATERAL DISTANCE FOR BODY B3 AT SURVEY POSITION B

HYDRONAUTICS, INCORPORATED

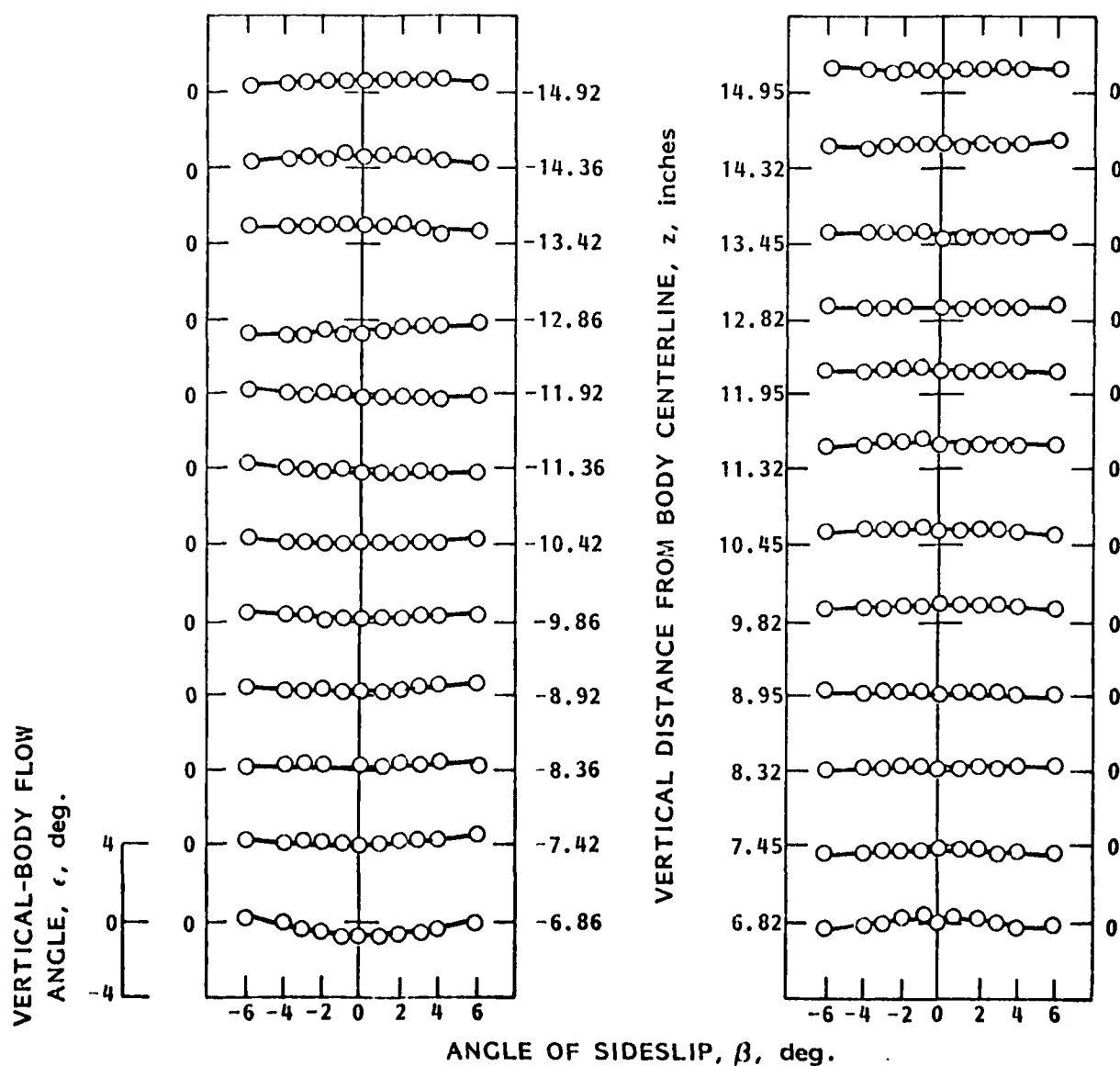
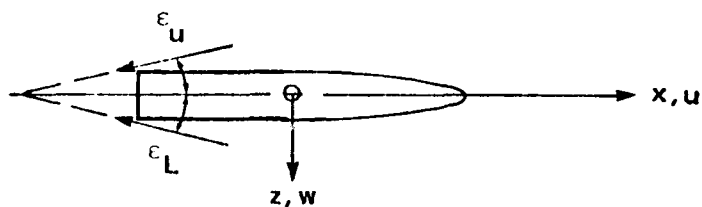


FIGURE B19 - VARIATION OF VERTICAL-BODY-FLOW ANGLE WITH VERTICAL DISTANCE FOR BODY B3 AT SURVEY POSITION B

HYDRONAUTICS, Incorporated

APPENDIX C

PITOT-STATIC YAWHEAD RAKE
ASSEMBLY DETAILS, ANALYSIS,
AND CALIBRATION

HYDRONAUTICS, Incorporated

-C1-

PITOT-STATIC YAWHEAD RAKE ASSEMBLY DETAILS, ANALYSIS, AND CALIBRATION

This appendix describes the pitot-static yawhead rake that was specifically designed, fabricated, and calibrated for the present investigation. The rake provided the ability to simultaneously measure the velocity and flow angularity at the aft end of the body in the vicinity of the fins.

Pitot-Static Yawhead Rake

The pitot-static yawhead rake is made up of six Prandtl-type pitot-static tubes equipped with four additional orifices in the hemispherical head as shown in Figure Cla. The additional orifices are used for measuring the angles of pitch and sideslip of the flow relative to the tube axis. As shown in Figure Cla, each of the four orifices is located on a line passing through the center of the hemispherical head at an angle of 45-degrees to the axis of the tube. The diagonals through these orifices are mutually perpendicular. Six yawhead tubes are fastened in a cylindrical holder as shown in Figure Clb so that the pitch and sideslip axes of the tubes are accurately aligned with respect to each other. The length of the tubes (distance from head to holder) and the tube spacing was established on the basis of the data presented in References C1 and C2.

Calibration Equipment

The rake assembly was calibrated in the TMB 24- x 48-inch Low Turbulence Wind Tunnel. The calibration equipment installation is shown in Figure C2. Special wall plates were designed

HYDRONAUTICS, Incorporated

-C2-

to support the rake in the tunnel. These plates provided the remotely operated angle indexing feature shown in Figure C2. The center of rotation of the indexing system was the heads of the tubes. The rake assembly could be rotated about its center support to allow for calibration of both the pitch and sideslip angles or combinations of these angles. The rake was connected to a multi-tube-inclined-alcohol manometer board shown in Figure C3. A typical manometer board hookup for one yawhead tube is shown in Figure C4. All readings were recorded by hand on standard data sheets prepared for the calibration tests.

Calibration Tests

The yawhead rake was calibrated over a range of pitch angles of ± 30 degrees at a zero sideslip angle, and over a range of sideslip angles of ± 30 degrees at a zero pitch angle. Tests were performed for dynamic pressures of from 8 to 25 psf. All tests were conducted with the yawhead rake in both erect and inverted positions to determine the asymmetrical characteristics of the yawhead tubes. The reason for this procedure is discussed in the following section.

Methods of Analysis for Yawhead

The effects of yawhead tube imperfections, or misalignment relative to the holder on the resultant calibrations are illustrated in Figure C5 for several cases. The symbols used in this section are defined at the end of the appendix and in Figure C6.

(a) Perfect Tube

Consider a perfect yawhead tube initially at zero flow angles and not rotated in the holder as shown in Figure C5a. A

perfect head is herein defined as one which gives the same readings erect and inverted. The effect of a perfect head can be achieved by using the mean curve between the results for the head erect and inverted. The form of the resultant curves of $\Delta P/(q_c)_y$ versus angle of pitch ϵ and angle of sideslip σ are presented in Figure C5a.

The sensitivities of the yawhead for the linear range can be expressed as follows

Since $k_3 = k_4 = 0$, over the linear portion of the curves:

$$\frac{P_1 - P_2}{(q_c)_y} = k_1 \epsilon \quad \text{or} \quad \epsilon = \left(\frac{P_1 - P_2}{(q_c)_y} \right) / k_1 \quad [1]$$

and

$$\frac{P_3 - P_4}{(q_c)_y} = k_2 \sigma \quad \text{or} \quad \sigma = \left(\frac{P_3 - P_4}{(q_c)_y} \right) / k_2 \quad [2]$$

(b) Perfect Tube Rotated in Holder

Consider a perfect yawhead initially at zero flow angles but rotated in the holder as illustrated in Figure C5b. The form of the resultant curves are shown in Figure C5b and the sensitivities of the yawhead for the linear range can be expressed as,

$$\frac{P_1 - P_2}{(q_c)_y} = k_1 \epsilon + k_3 \sigma \quad [3]$$

and

$$\frac{P_3 - P_4}{(q_c)_y} = k_2 \sigma + k_4 \epsilon \quad [4]$$

solving simultaneously for ϵ and σ

$$\epsilon = \frac{\left[\frac{P_1 - P_2}{(q_c)_y} - \frac{k_3}{k_4} \left(\frac{P_3 - P_4}{(q_c)_y} \right) \right]}{\left[k_1 - \frac{k_3 k_4}{k_2} \right]} \quad [5]$$

and

$$\sigma = \frac{1}{k_2} \left[\frac{P_3 - P_4}{(q_c)_y} - k_4 \epsilon \right] \quad [6]$$

(c) Imperfect Tube Rotated in Holder

Consider an imperfect yawhead initially at zero flow angles but rotated in the holder as illustrated in Figure C5c. The form of the resultant curves are shown in Figure C5c. The solid lines are for the imperfect tube in the erect position, dashed curves are for the perfect tube or the mean curve between the erect and inverted positions. The sensitivities of the yawhead for the linear range can be expressed as,

$$\frac{P_1 - P_2}{(q_c)_y} = k_1 \epsilon + k_3 \sigma + c_1 + c_3 \quad [7]$$

and

$$\frac{P_3 - P_4}{(q_c)_y} = k_2 \sigma + k_4 \epsilon + c_2 + c_4 \quad [8]$$

solving simultaneously for ϵ and σ

$$\epsilon = \frac{\left[\left(\frac{P_1 - P_2}{(q_c)_y} \right) - \frac{k_3}{k_2} \left(\frac{P_3 - P_4}{(q_c)_y} \right) + \frac{k_3}{k_2} (c_2 + c_4) - c_1 - c_3 \right]}{\left[k_1 - \frac{k_3 k_4}{k_2} \right]} \quad [9]$$

$$\sigma = \frac{1}{k_2} \left[\left(\frac{P_3 - P_4}{(q_c)_y} \right) - k_4 \epsilon - c_2 - c_4 \right] \quad [10]$$

Calibration Results

The results of the calibration of the yawhead rake are presented for each tube in Figures C7 through C13. The sensitivities for each tube are listed on the respective figure. The variation of the sensitivities (slopes of the calibration curves) with dynamic pressure was small. The results of tests to determine the effects of tube angle on the dynamic pressure ratio measured by each tube is presented in Figure C13. Average values of the ratio for ± 30 degrees are shown. It should be noted that the dynamic pressure ratio is very close to 1.0 for tube angles up to about 12 to 14 degrees. (See Figure C13.)

The use of Equations [9] and [10] to determine the airstream angles is a rather laborious process and furthermore is only suitable over the linear range of the airstream angles

against the yawhead factors. A graphical solution for determining the stream angles from the yawhead factors is contained in Figure C14. This type of plot was made by first plotting the yawhead factors against the true angles of the airstream and picking off values of the yawhead factors from Figures C7 to C12 for every one-degree increment of ϵ at $\sigma = 0$ and for σ at $\epsilon = 0$.

The values of the yawhead factors were then plotted on the grid of the paper (see Figure C14) and the points formed the master coordinates for the grid of the airstream angles. The grid of the airstream angles was confined to small angles of sideslip at large angles of pitch and vice versa because the calibration was made through the pitch range at zero sideslip only and through the sideslip range at zero pitch only, and a linear extrapolation of the curves to large angles of both pitch and sideslip would be erroneous.

Use of Calibration Charts

It is assumed that it is desired to know the angle of pitch, angle of sideslip and dynamic pressure at several points. Readings should be taken of H_y , P_y , P_1 , P_2 , P_3 , P_4 , and manometer fluid temperature for each tube. Using Figure C14, determine the point of common intersection of the yawhead factors on the grid of the paper and from this point interpolate between the superimposed grid to determine the angles of pitch and sideslip, ϵ and σ , respectively. The value of $H_y - P_y$ is equal to the dynamic pressure and is proportional to $\left(\frac{u}{U}\right)^2$. Using this technique, angles can be measured to an accuracy of about ± 0.1 degree.

HYDRONAUTICS, Incorporated

-C7-

Present day data acquisition and digital computer technology can provide a much more efficient means of data acquisition and data reduction (solution of Equations [9] and [10].) These techniques also permit the using of the nonlinear range of the tube calibration results.

SYMBOLS

The symbols used in this appendix are defined as follows:

ϵ	angle of pitch of airstream with respect to the axis of the tube, positive when airstream is rising with respect to the axis of the tube
σ	angle of sideslip of the airstream with respect to the axis of the tube, positive when airstream is approaching from right of the axis of the tube
i_{ϵ}	angle of incidence of tube in pitch measured with respect to tunnel axis, positive when head of tube is up with respect to the tunnel axis
i_{σ}	angle of incidence of tube in sideslip measured with respect to tunnel axis, positive when head of tube is to the left of the tunnel axis looking upstream
q_c	true impact pressure, $H - P$
$(q_c)_y$	impact pressure measured by yawhead tube, $H_y - P_y$
H	absolute total head
H_y	absolute total head measured by yawhead tube
P	absolute static pressure
P_y	absolute static pressure measured by yawhead tube
P_1	bottom orifice on yawhead
P_2	top orifice on yawhead
P_3	right orifice on yawhead looking upstream
P_4	left orifice on yawhead looking upstream
ΔP	$P_1 - P_2$ or $P_3 - P_4$

$$\left. \begin{array}{l} (P_1 - P_2)/(q_c)_y \\ (P_3 - P_4)/(q_c)_y \\ \Delta P/(q_c)_y \end{array} \right\} \text{ yawhead factors}$$

$$(q_c)_y/q_c \quad \text{impact pressure calibration factor}$$

$$\left. \begin{array}{l} k_1 = \left[\frac{\partial \left(\frac{P_1 - P_2}{(q_c)_y} \right)}{\partial \epsilon} \right]_{\sigma} \\ k_2 = \left[\frac{\partial \left(\frac{P_3 - P_4}{(q_c)_y} \right)}{\partial \sigma} \right]_{\epsilon} \\ k_3 = \left[\frac{\partial \left(\frac{P_1 - P_2}{(q_c)_y} \right)}{\partial \sigma} \right]_{\epsilon} \\ k_4 = \left[\frac{\partial \left(\frac{P_3 - P_4}{(q_c)_y} \right)}{\partial \epsilon} \right]_{\sigma} \end{array} \right\} \text{ yaw-head slopes}$$

HYDRONAUTICS, Incorporated

-C10-

c_1 } yawhead constants or differences between the average
 c_2 } yawhead factors and yawhead factor with the tube erect,
 c_3 } see Figure C5c for designations.

REFERENCES

- C1 - Krause, Lloyd N., "Effects of Pressure-Rake Design Parameters on Static-Pressure Measurement for Rakes Used in Subsonic Free Jets," NACA TN 2520, 1951.
- C2 - Schulze, Wallace M., Ashby, George C., Jr., and Erwin, John R., "Several Combination Probes for Surveying Static and Total Pressure and Flow Direction," NACA TN 2830, 1952.

HYDRONAUTICS, INCORPORATED

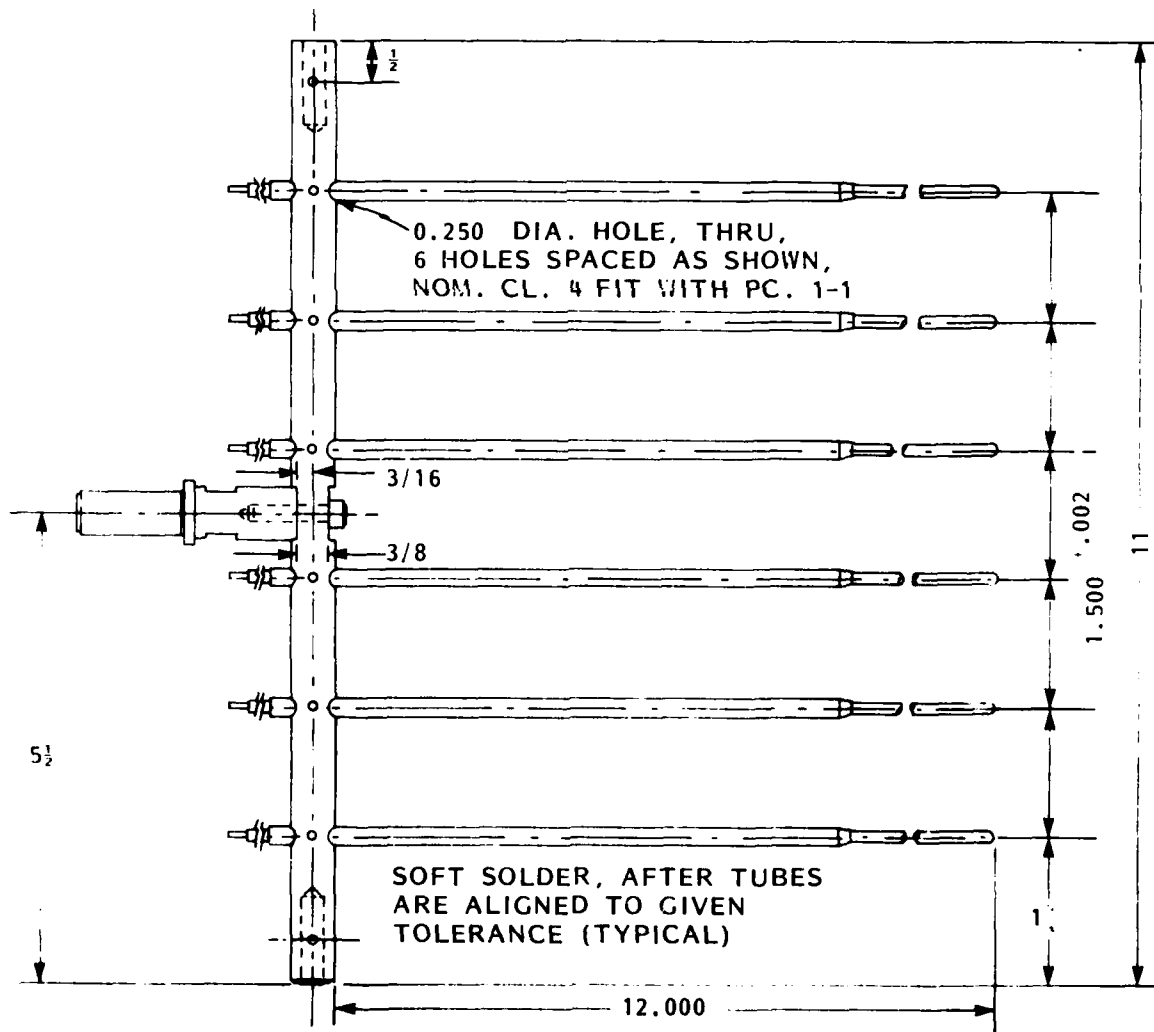
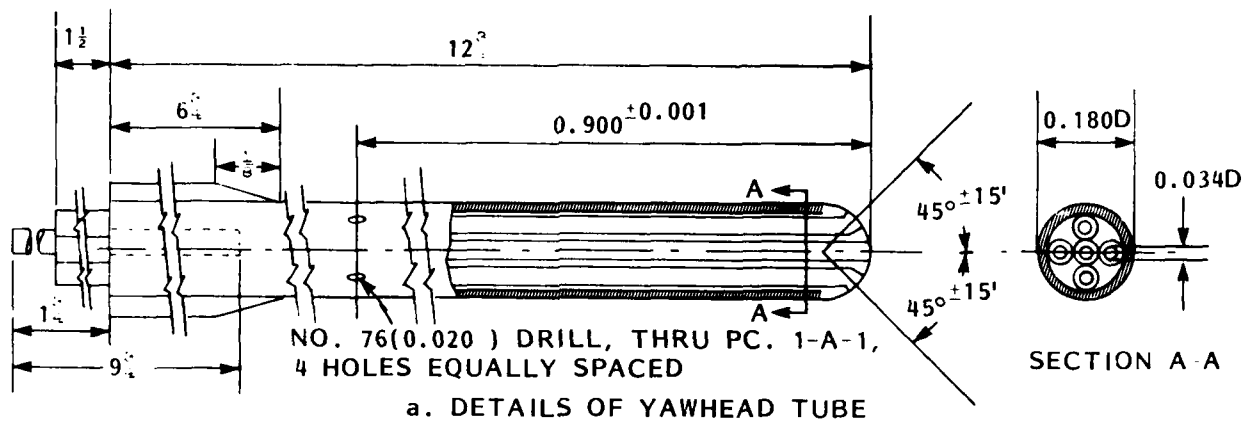


FIGURE C1 - PITOT-STATIC YAWHEAD RAKE ASSEMBLY
(ALL DIMENSIONS IN INCHES)

HYDRONAUTICS, INCORPORATED

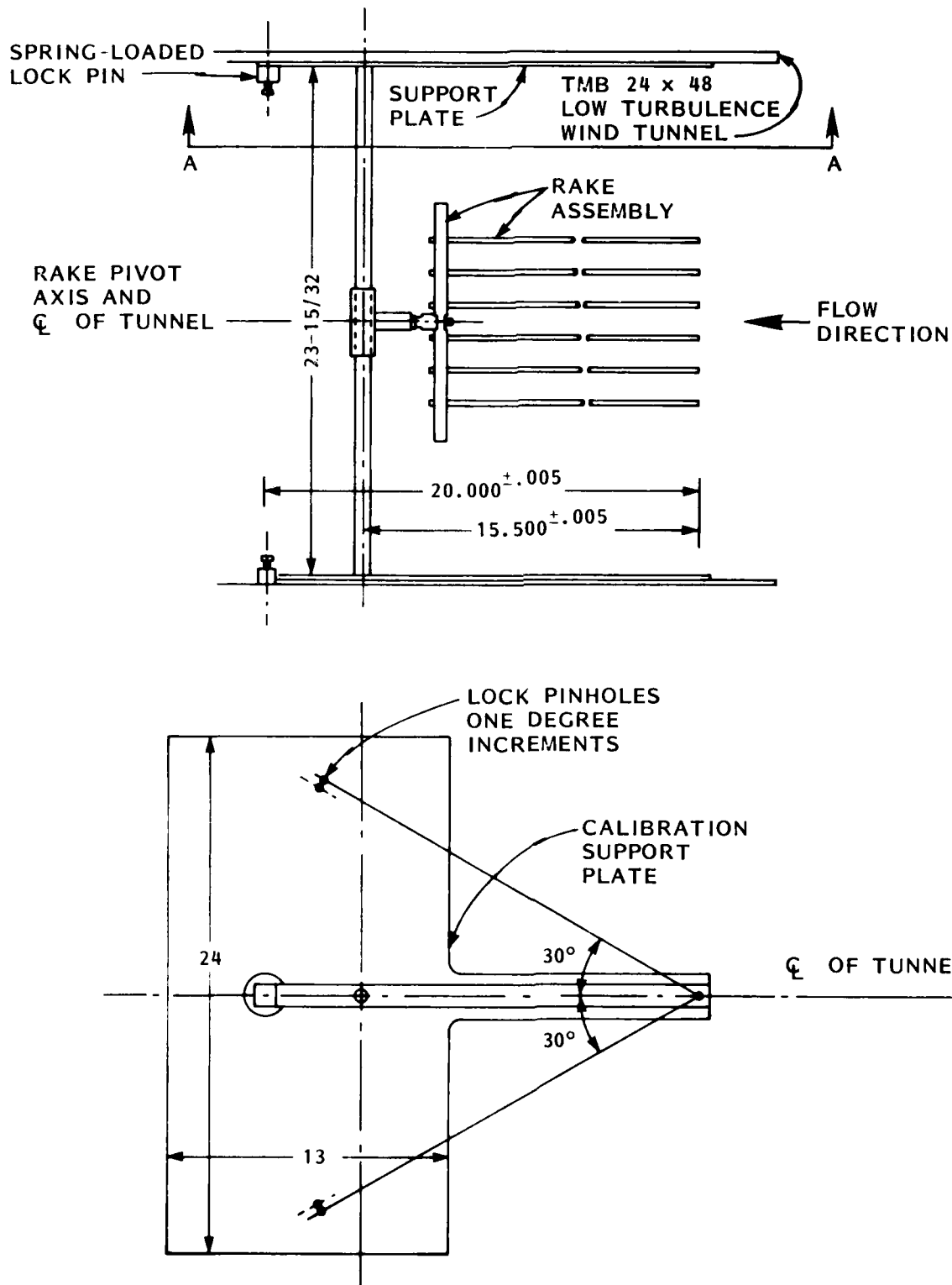


FIGURE C2 - SKETCH SHOWING ARRANGEMENT FOR CALIBRATION OF PITOT-STATIC-YAWHEAD RAKE ASSEMBLY IN TMB 24 x 48 LOW-TURBULENCE WIND TUNNEL (ALL DIMENSIONS IN INCHES)

HYDRONAUTICS, INCORPORATED

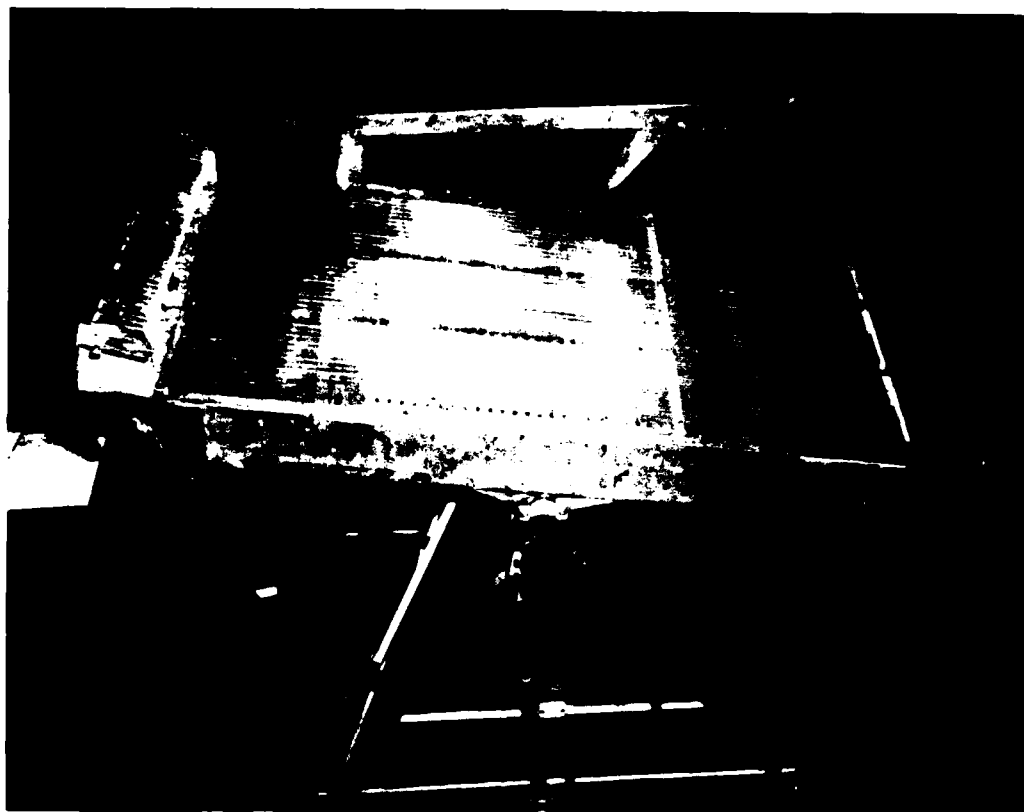


FIGURE C3 - INCLINED MANOMETER BOARD USED FOR CALIBRATION

HYDRONAUTICS, INCORPORATED

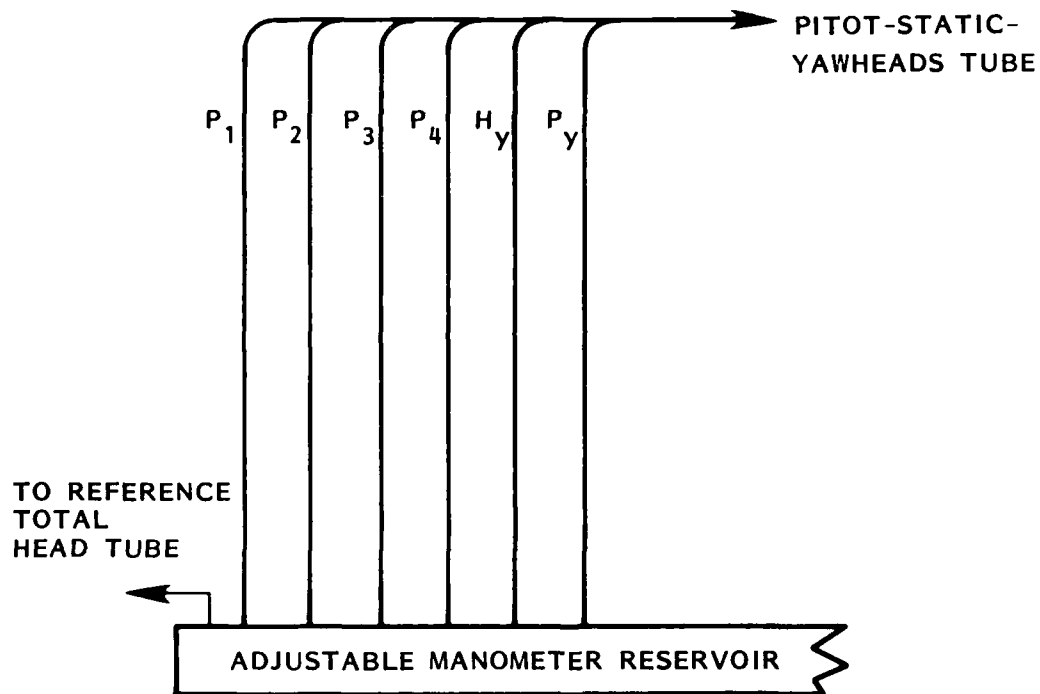


FIGURE C4 - TYPICAL MANOMETER BOARD HOOKUP FOR ONE
PITOT-STATIC-YAWHEAD TUBE
(36-TUBE ALCOHOL MANOMETER INCLINED
AT 5 TO 1)

HYDRONAUTICS, INCORPORATED

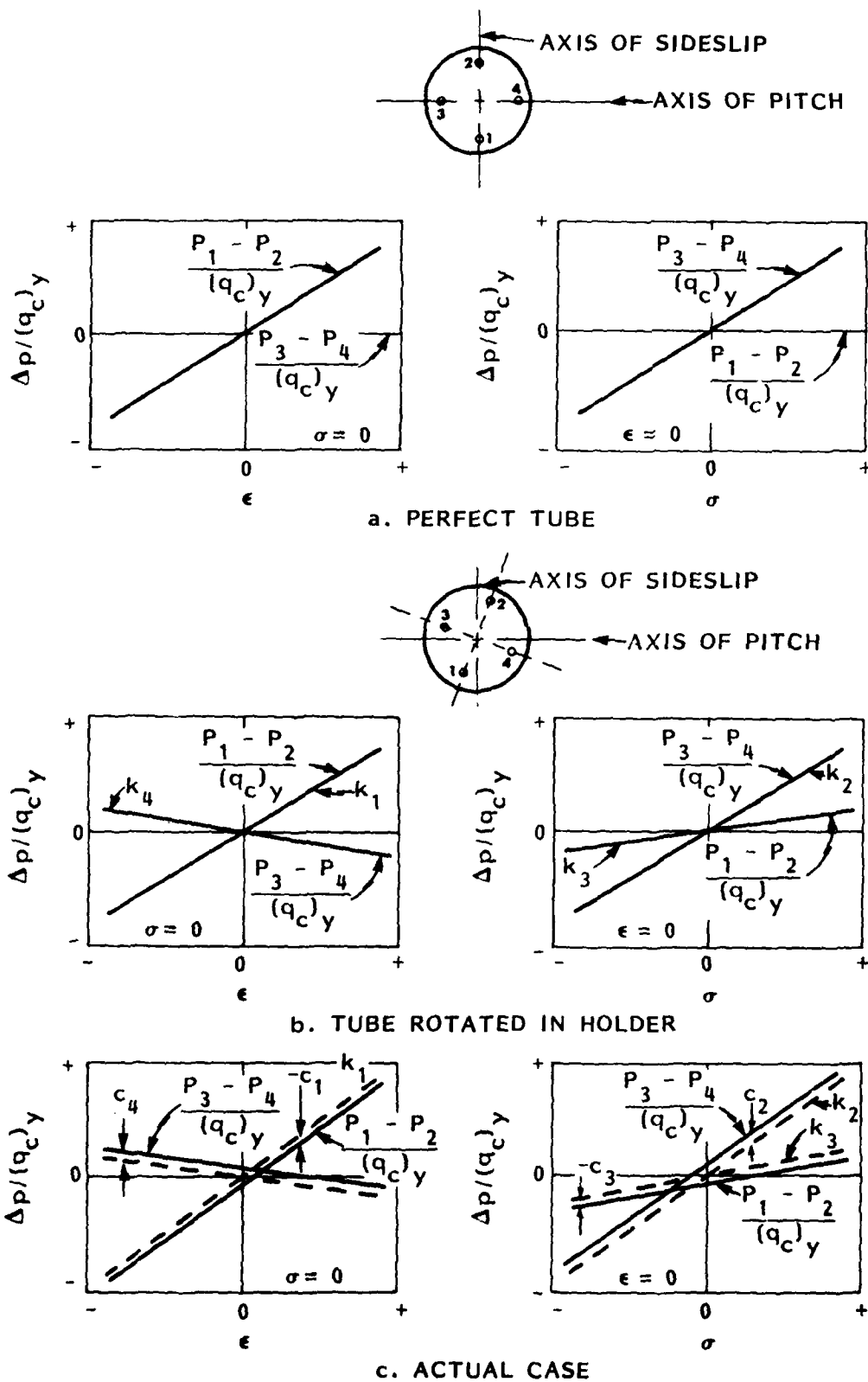


FIGURE C5 - SKETCHES SHOWING EFFECTS OF YAWHEAD TUBE IMPERFECTIONS ON CALIBRATION CURVES

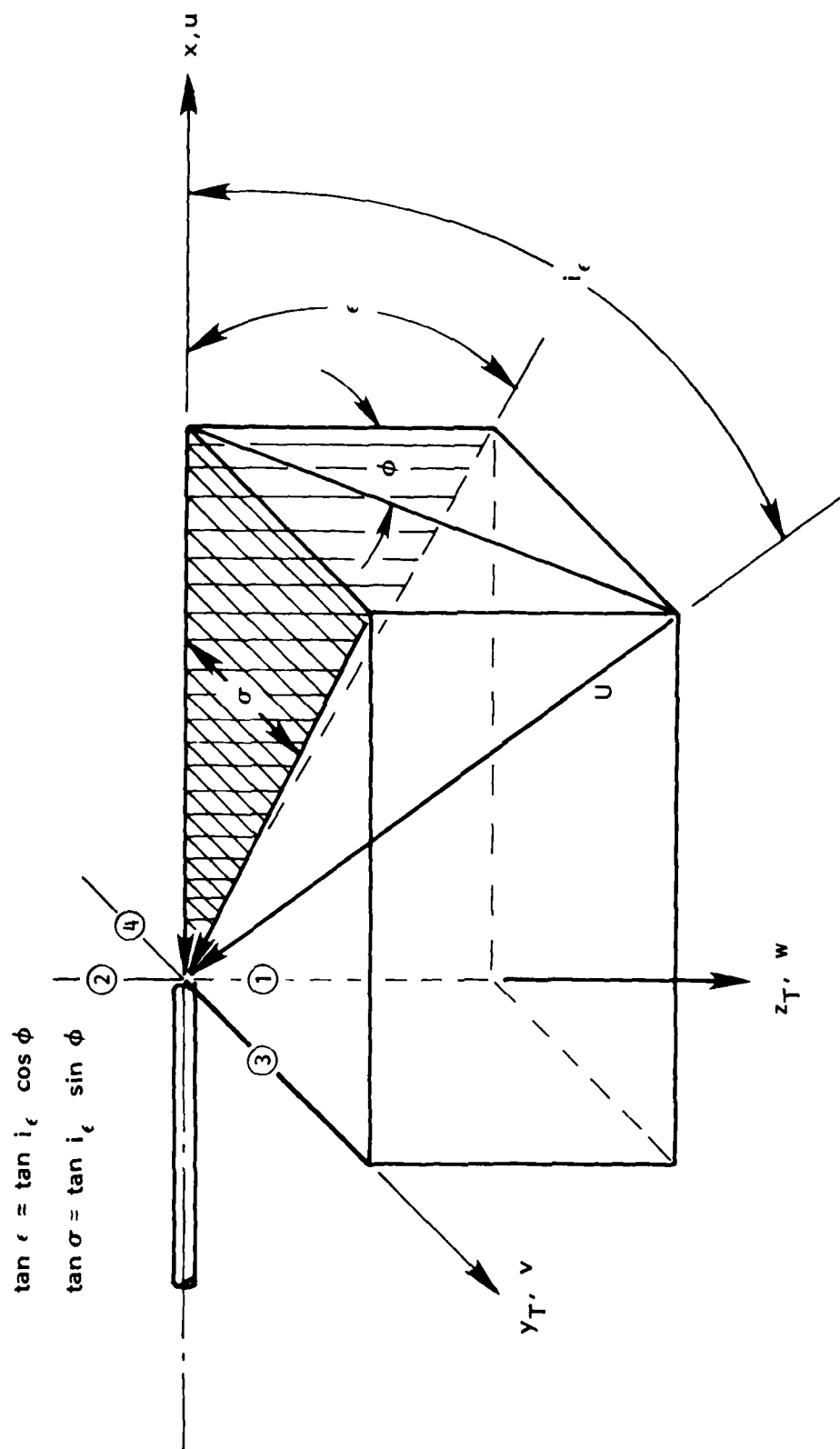
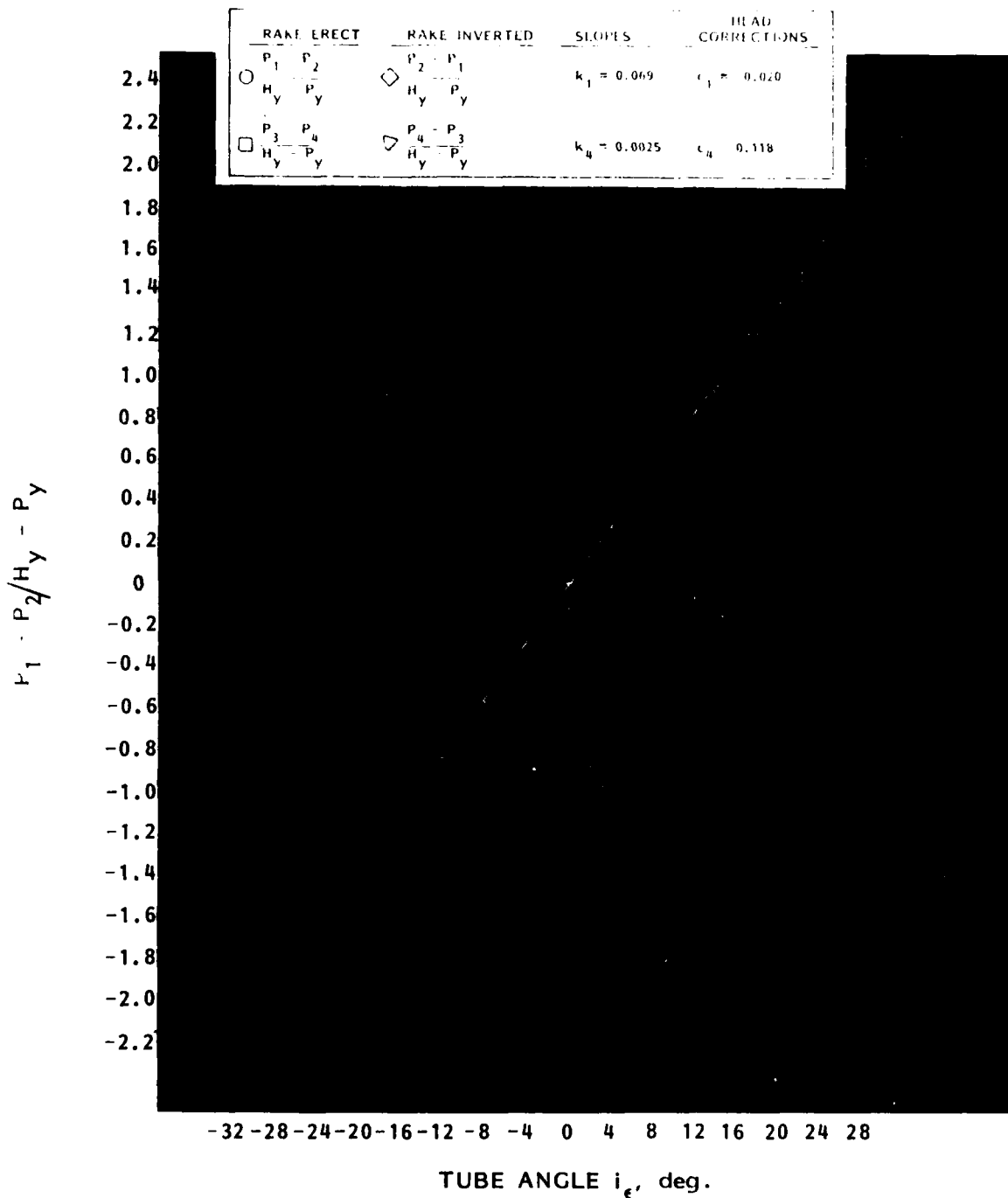


FIGURE C6 - SKETCH DEFINING ANGLES MEASURED BY PITOT-STATIC-YAWHEAD TUBE

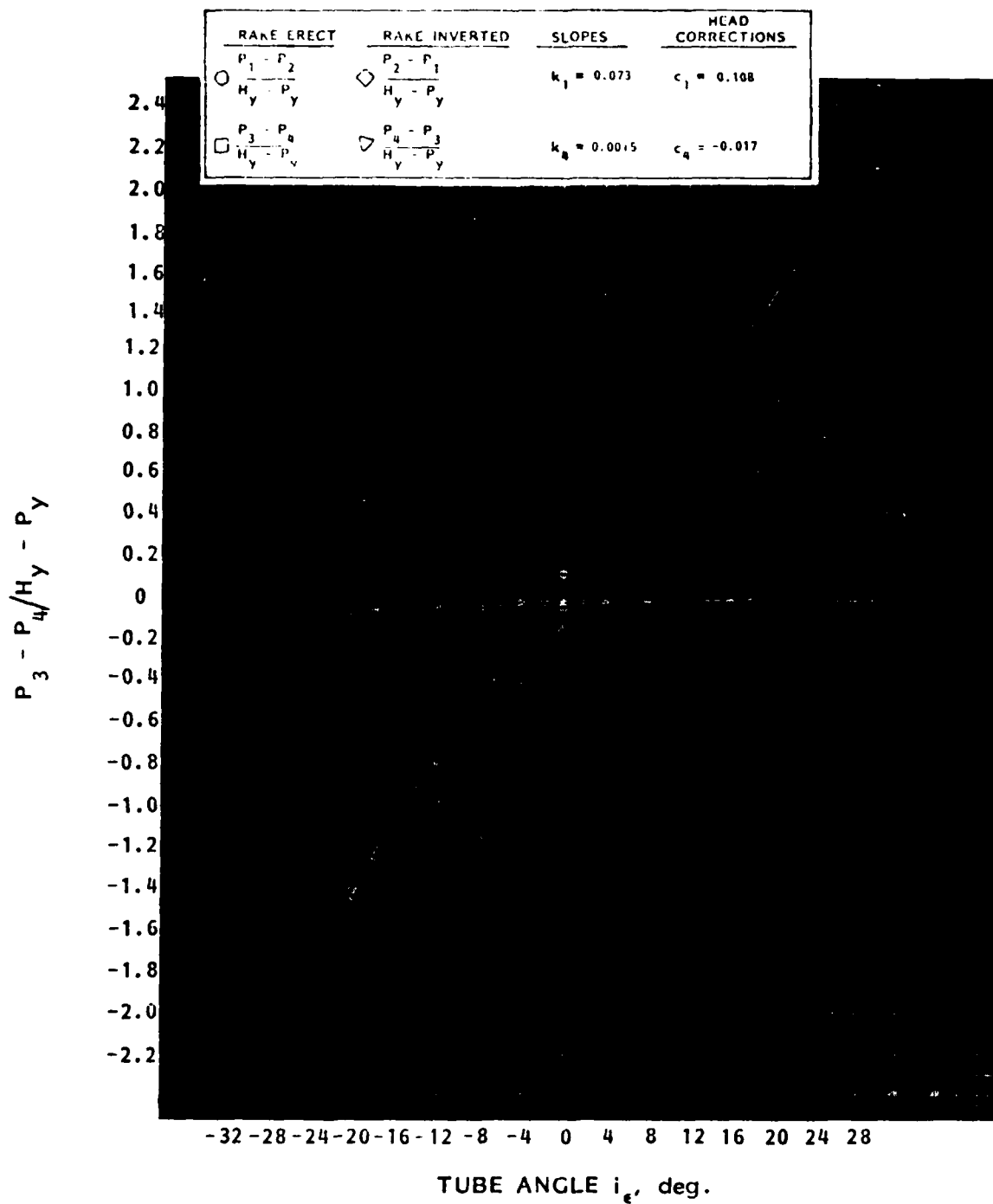
HYDRONAUTICS, INCORPORATED



a. PITCH ANGLE VARIATION

FIGURE C7 - VARIATION OF YAWHEAD PARAMETERS WITH ANGLE OF INCIDENCE OF THE TUBE NO. 1

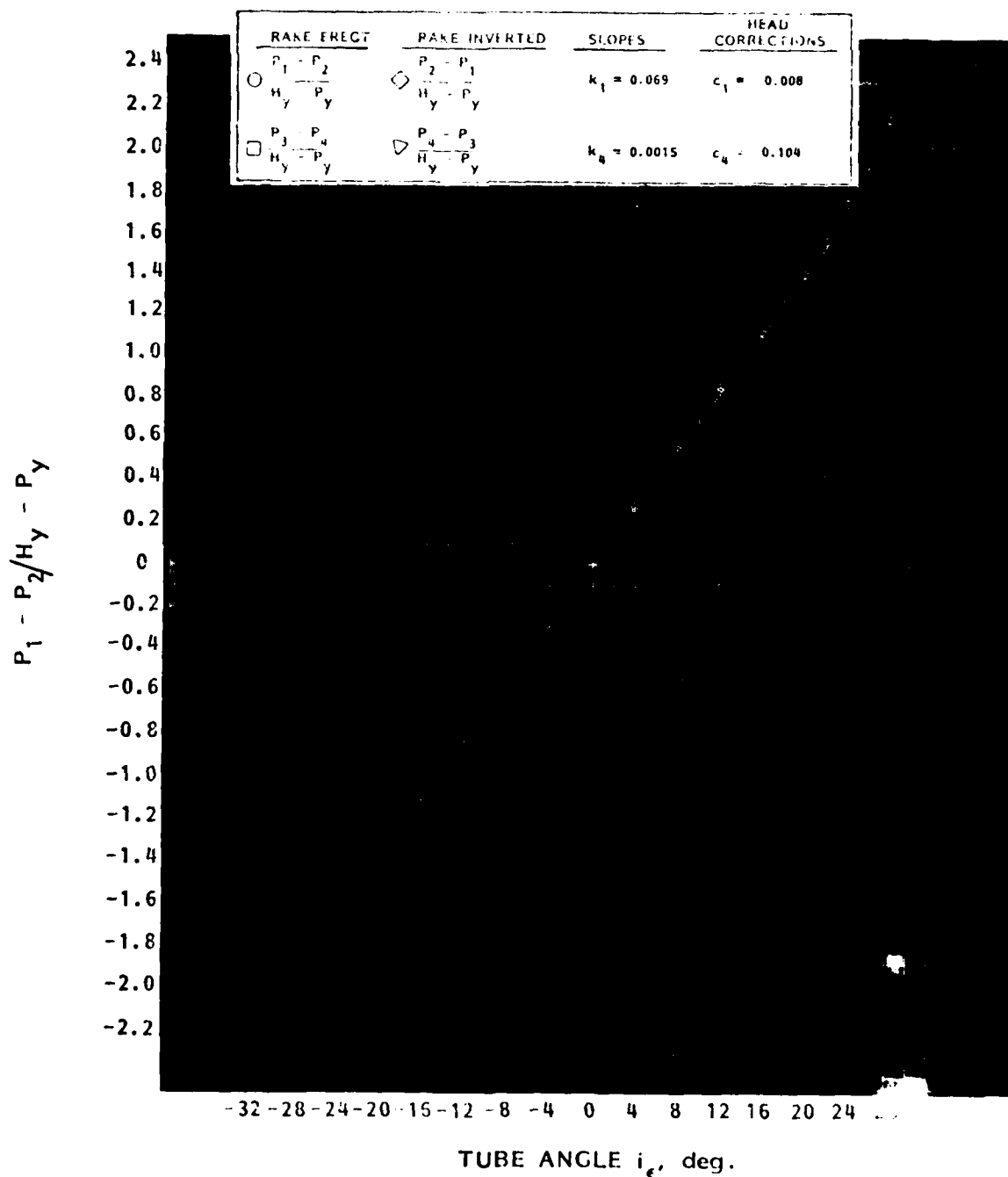
HYDRONAUTICS, INCORPORATED



b. SIDESLIP ANGLE VARIATION

FIGURE C7 - CONCLUDED

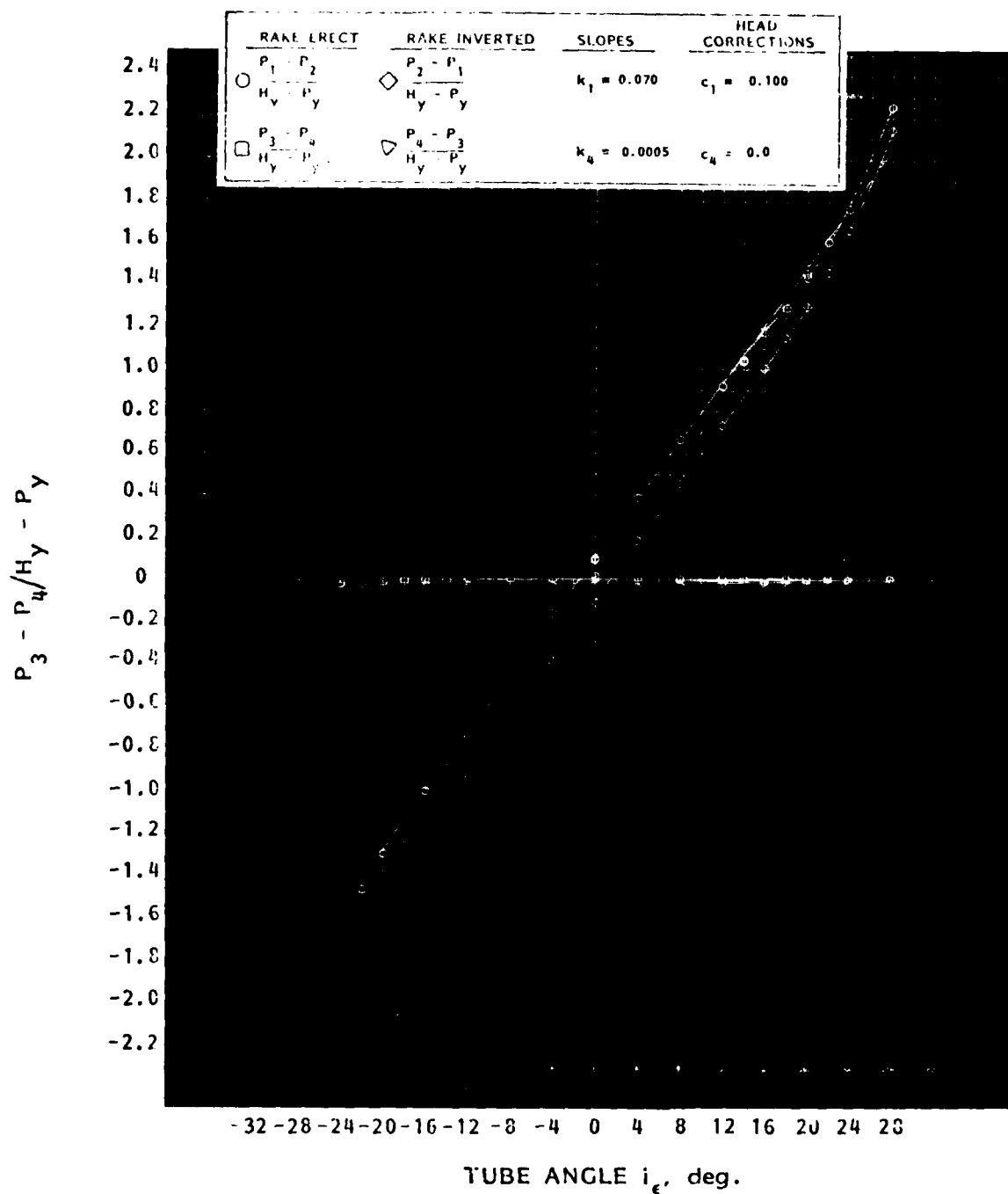
HYDRONAUTICS, INCORPORATED



a. PITCH ANGLE VARIATION

FIGURE C8 - VARIATION OF YAWHEAD PARAMETERS WITH ANGLE OF INCIDENCE OF THE TUBE NO. 2

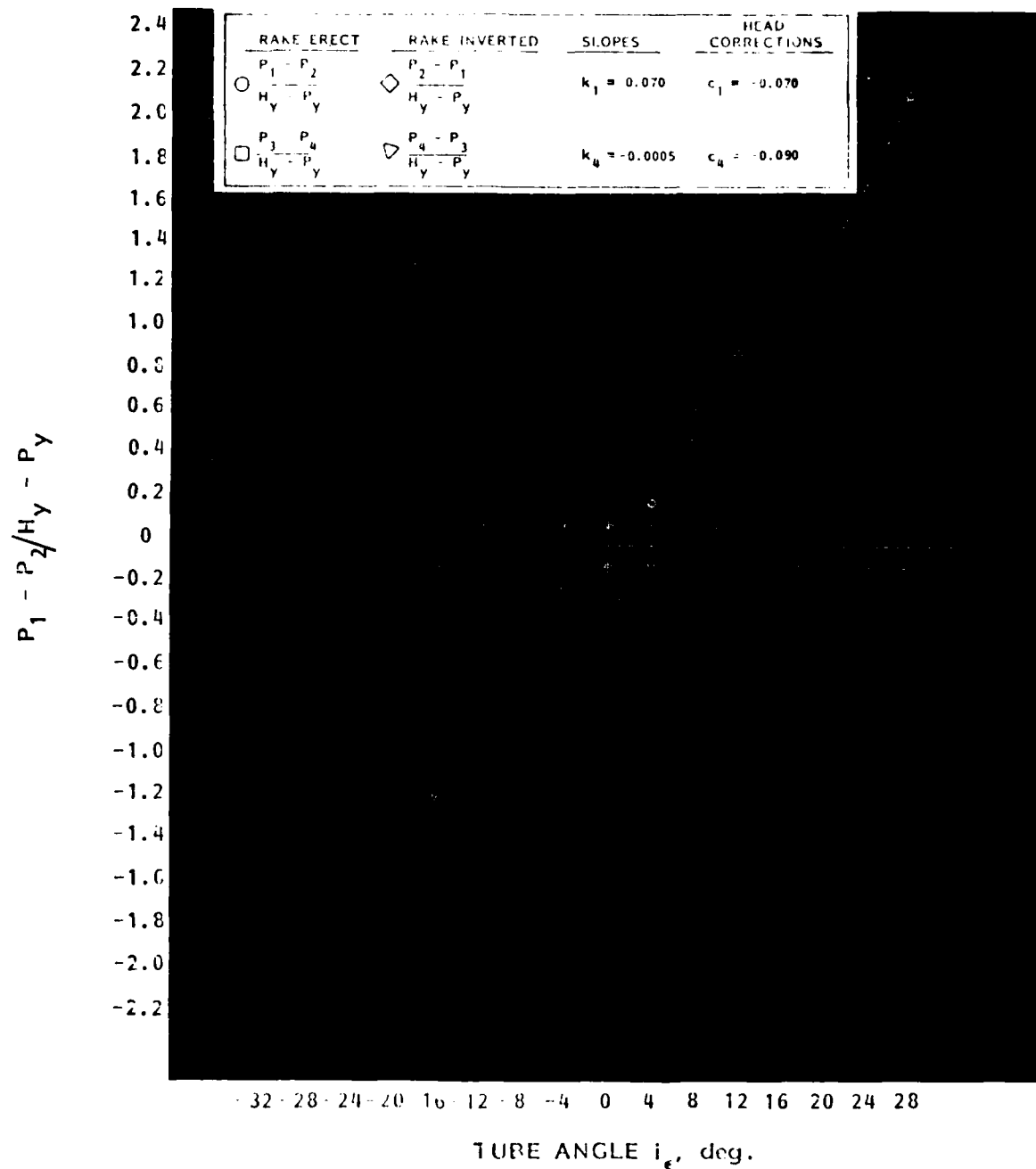
HYDRONAUTICS, INCORPORATED



b. SIDESLIP ANGLE VARIATION

FIGURE 8 - CONCLUDED

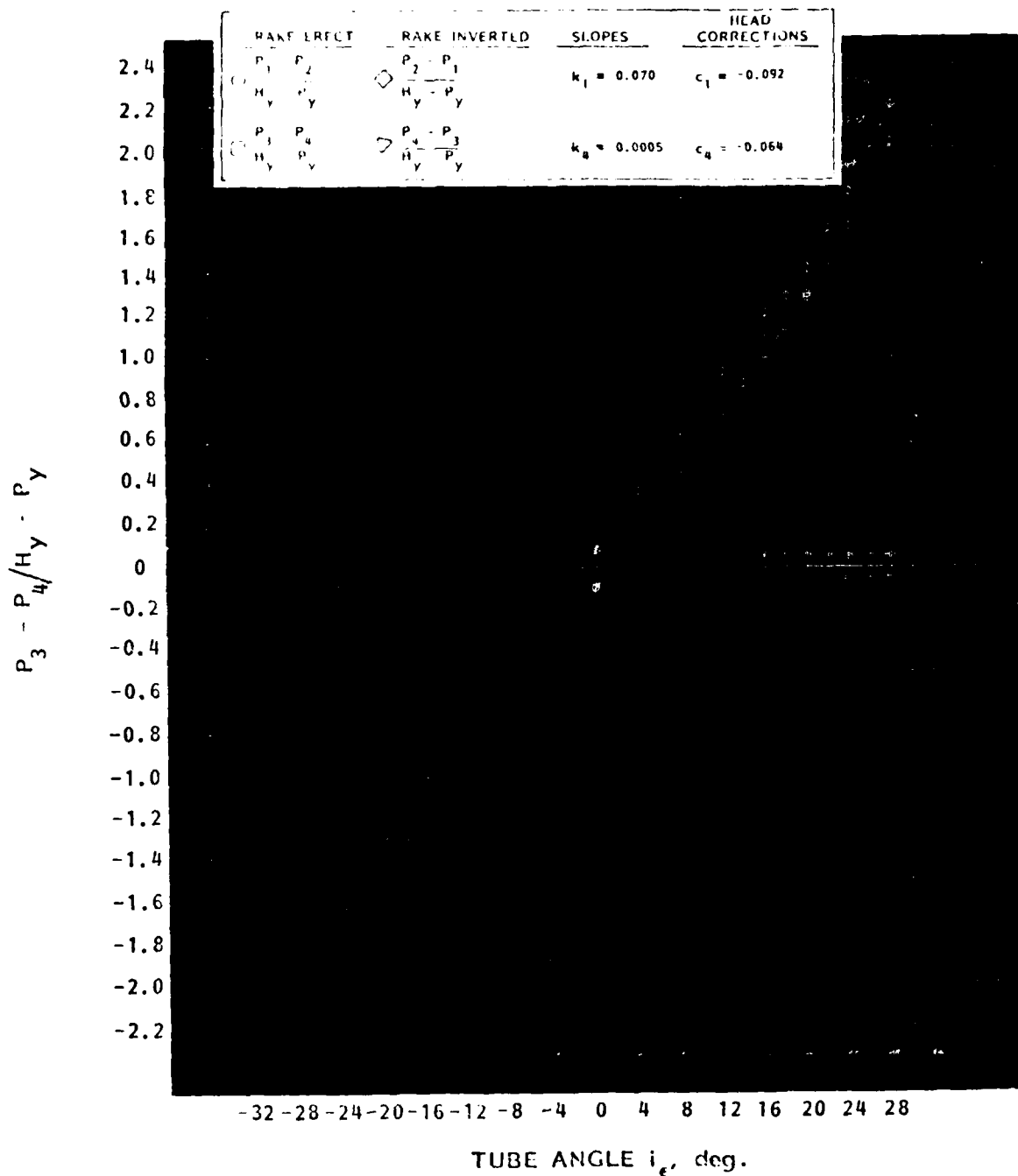
HYDRONAUTICS, INCORPORATED



a. PITCH ANGLE VARIATION

FIGURE C9 - VARIATION OF YAWHEAD PARAMETERS WITH ANGLE OF INCIDENCE OF THE TUBE NO. 3

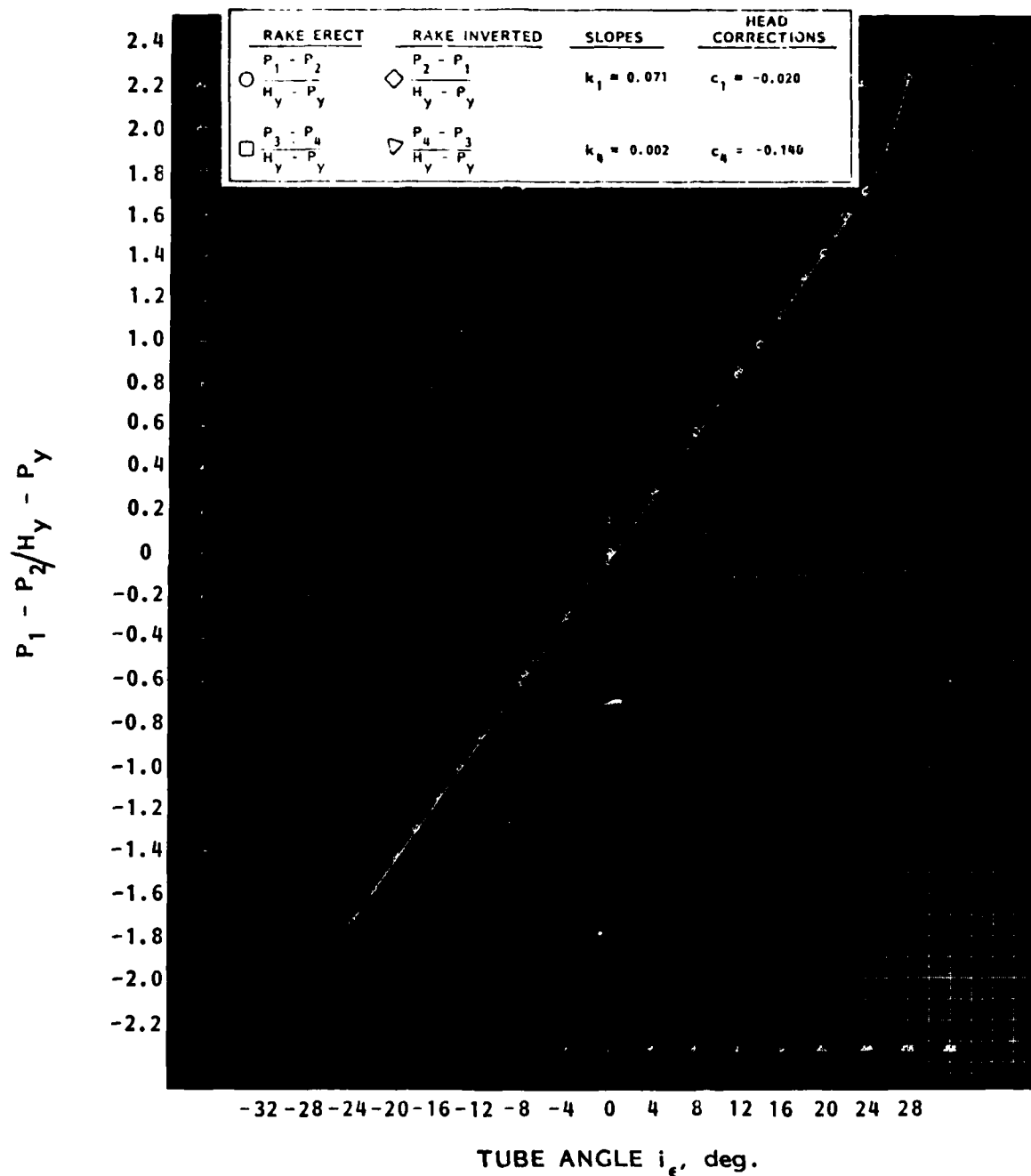
HYDRONAUTICS, INCORPORATED



b. SIDESLIP ANGLE VARIATION

FIGURE 9 - CONCLUDED

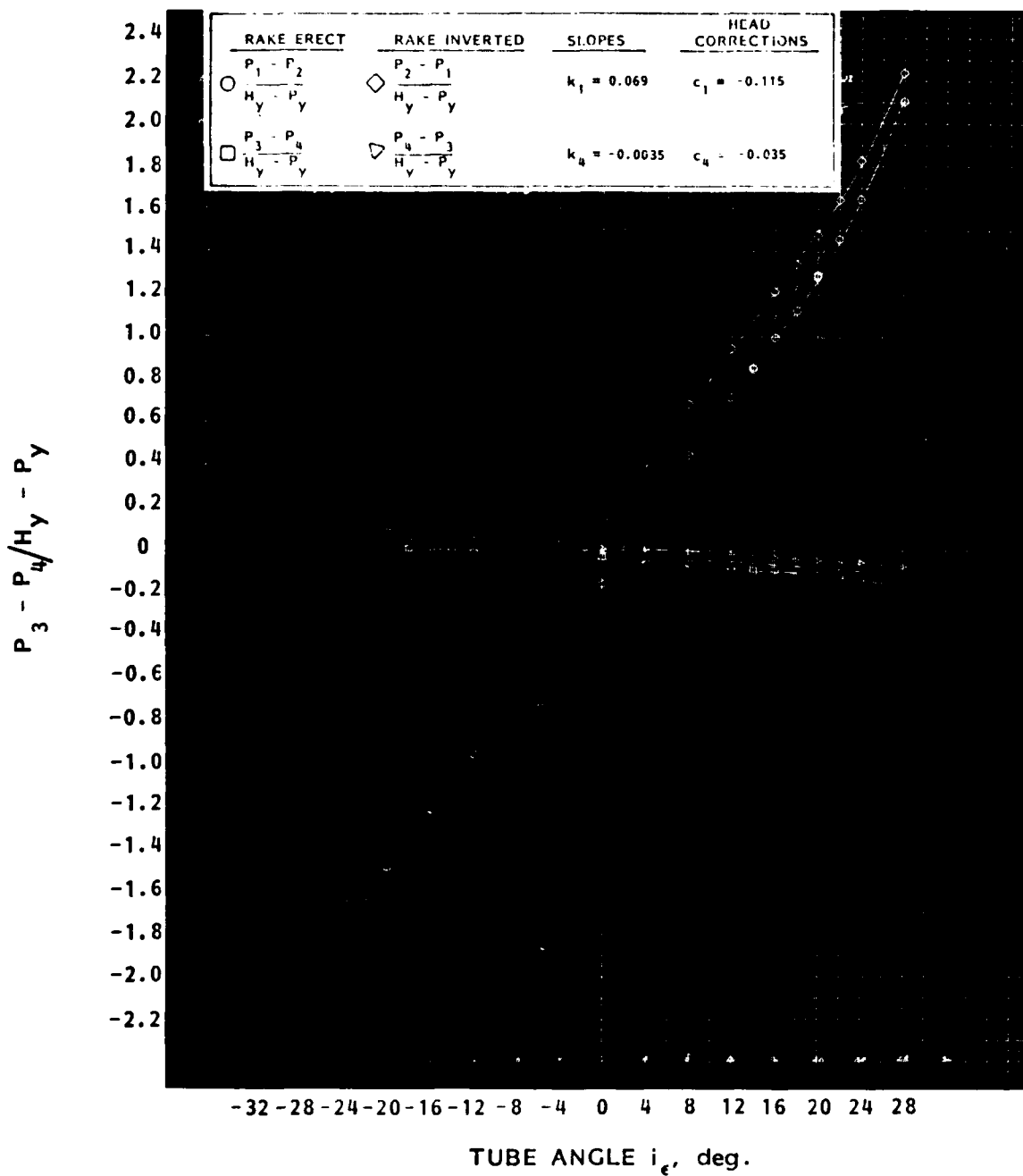
HYDRONAUTICS, INCORPORATED



a. PITCH ANGLE VARIATION

FIGURE C10 - VARIATION OF YAWHEAD PARAMETERS WITH ANGLE OF INCIDENCE OF THE TUBE NO. 4

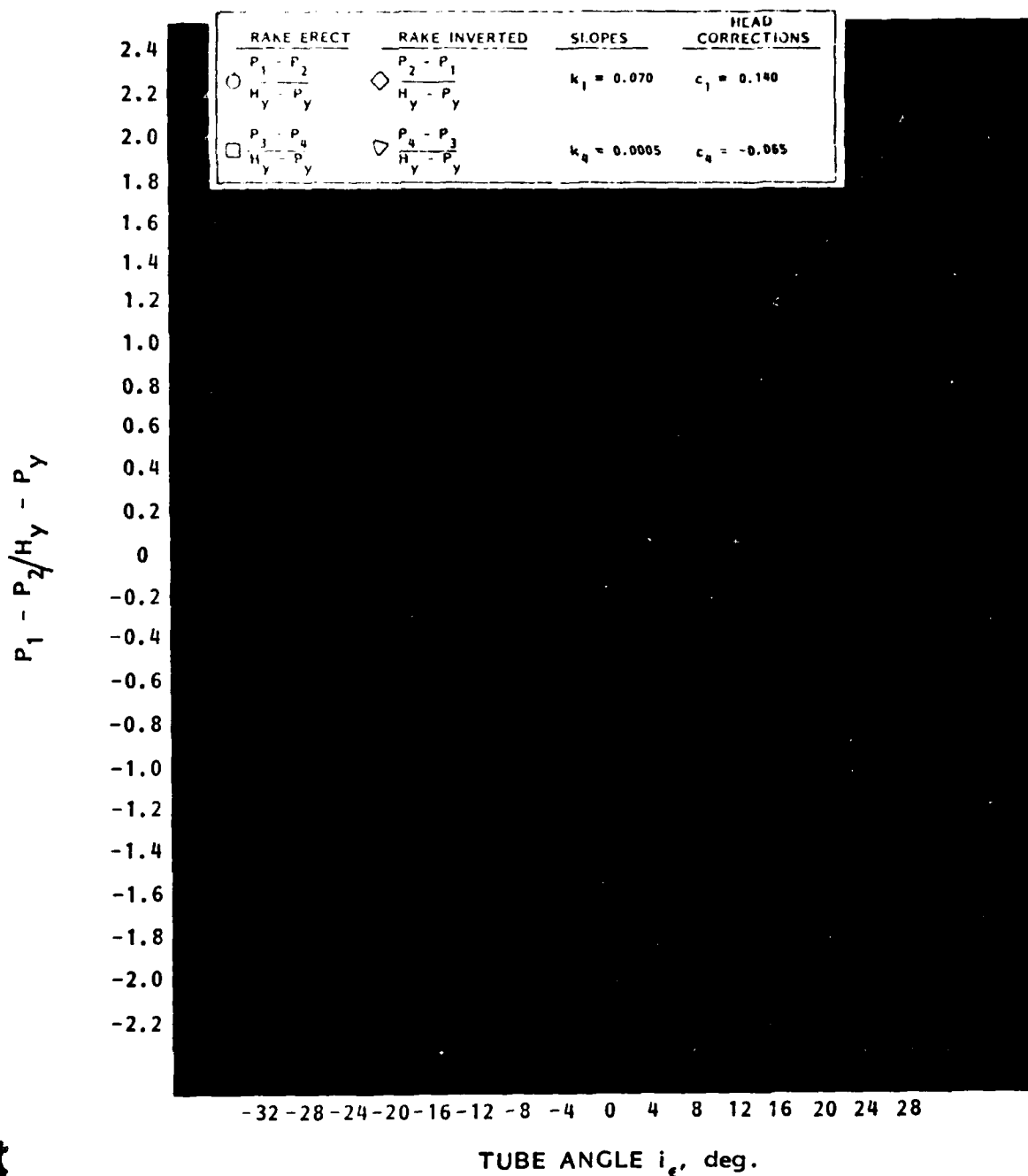
HYDRONAUTICS, INCORPORATED



b. SIDESLIP ANGLE VARIATION

FIGURE C10 - CONCLUDED

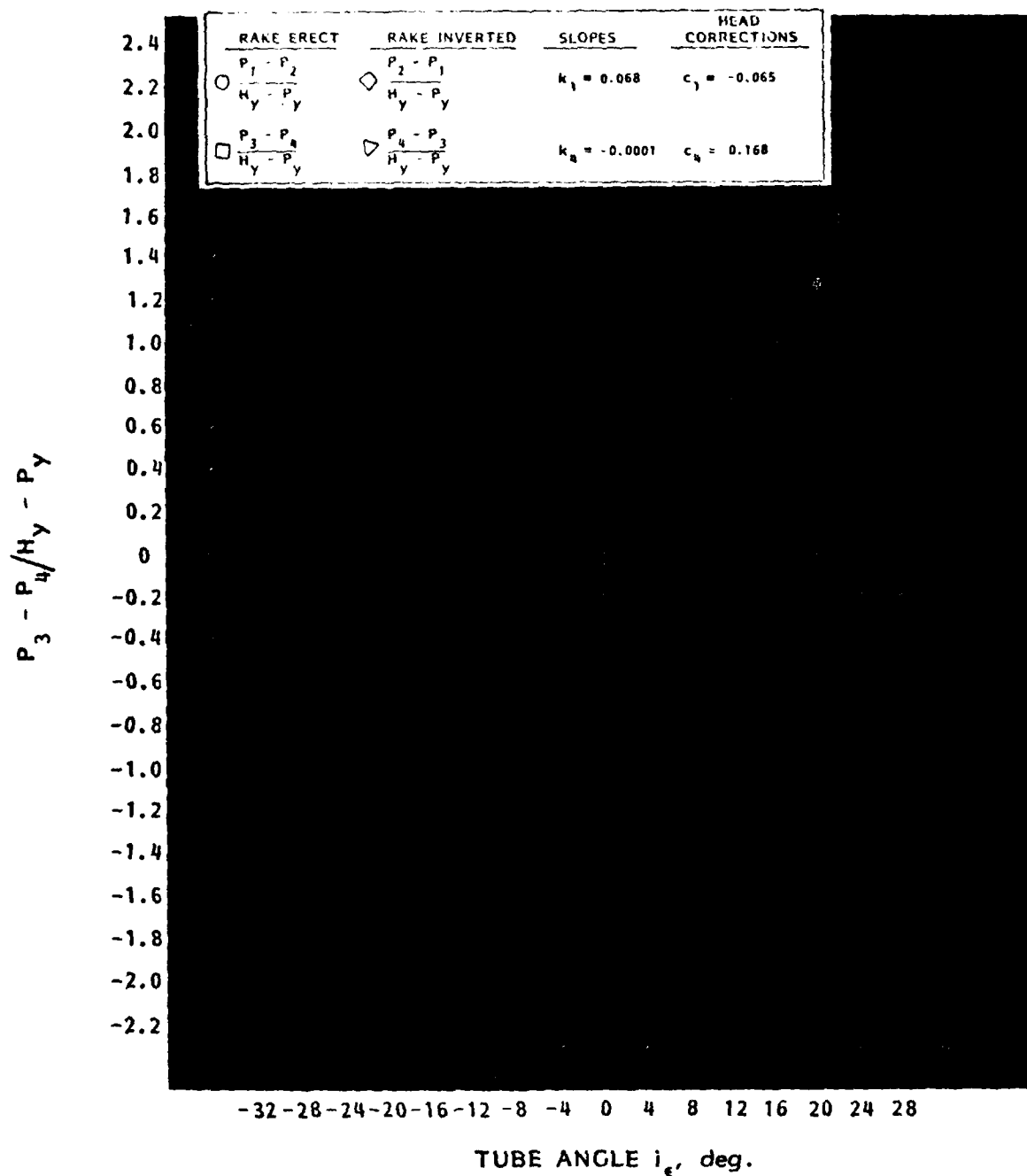
HYDRONAUTICS, INCORPORATED



a. PITCH ANGLE VARIATION

FIGURE C11 - VARIATION OF YAWHEAD PARAMETERS WITH ANGLE OF INCIDENCE OF THE TUBE NO. 5

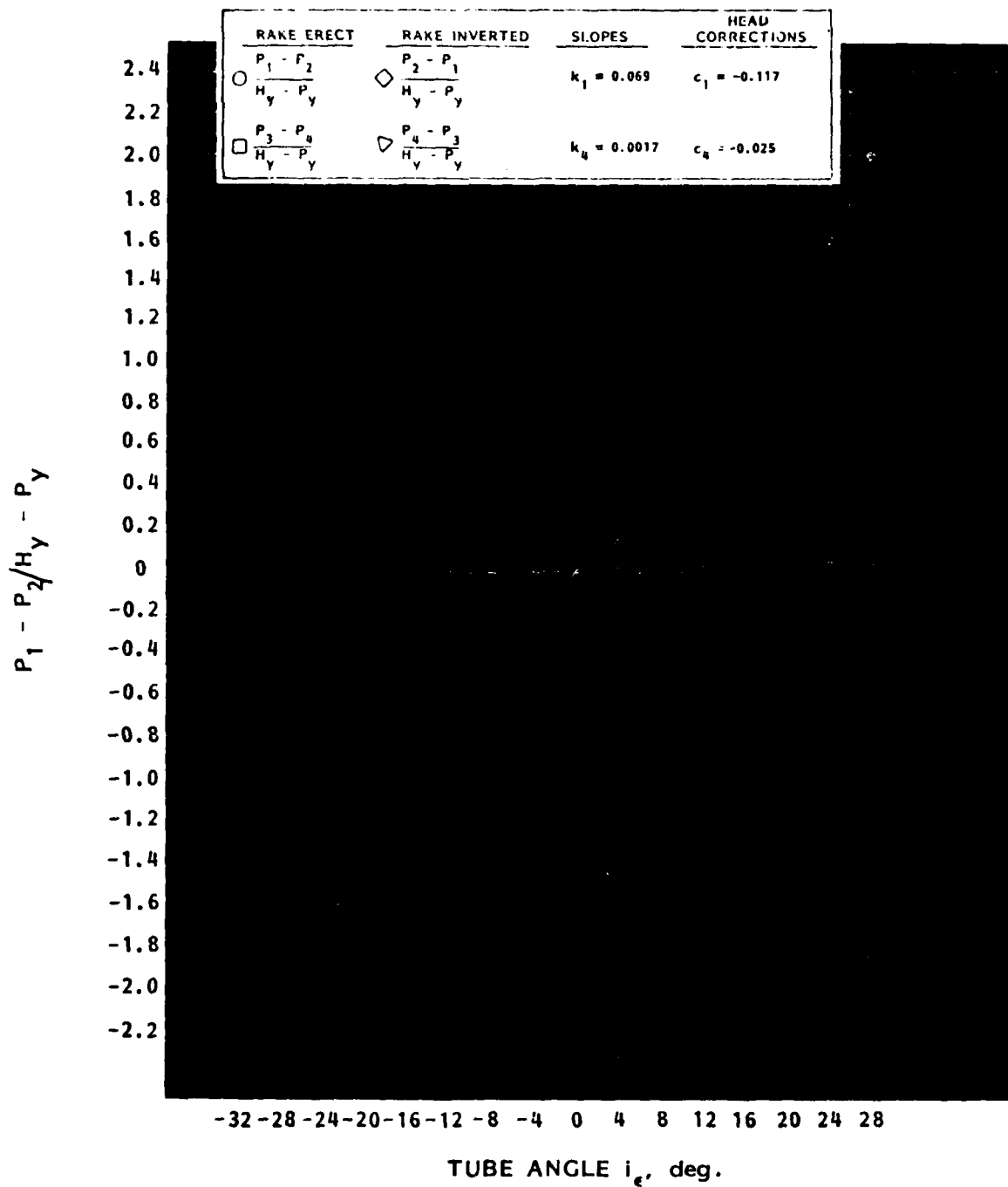
HYDRONAUTICS, INCORPORATED



b. SIDESLIP ANGLE VARIATION

FIGURE C11 - CONCLUDED

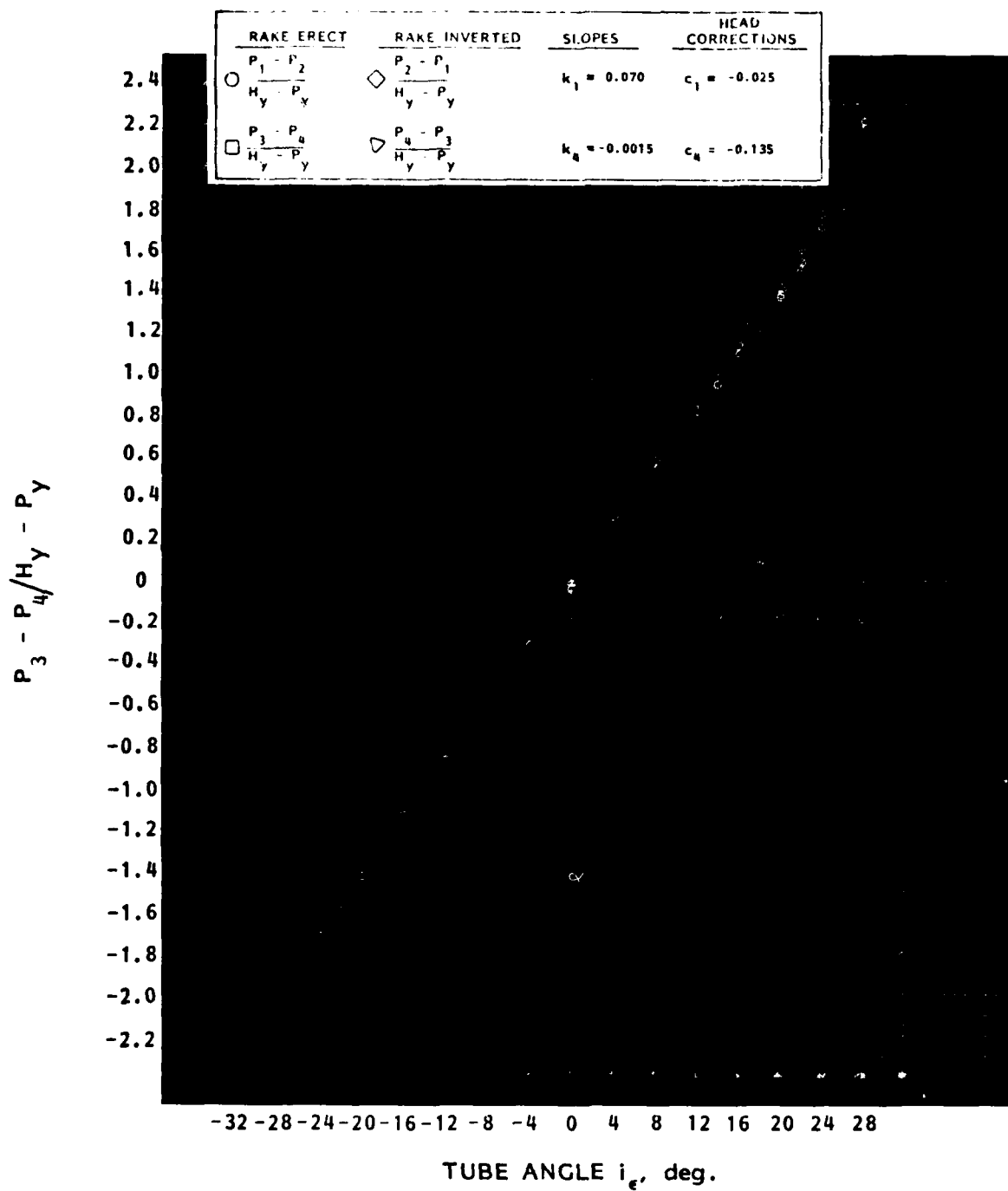
HYDRONAUTICS, INCORPORATED



a. PITCH ANGLE VARIATION

FIGURE C12 - VARIATION OF YAWHEAD PARAMETERS WITH ANGLE OF INCIDENCE OF THE TUBE NO. 6

HYDRONAUTICS, INCORPORATED



b. SIDESLIP ANGLE VARIATION

FIGURE C12 - CONCLUDED

HYDRONAUTICS, INCORPORATED

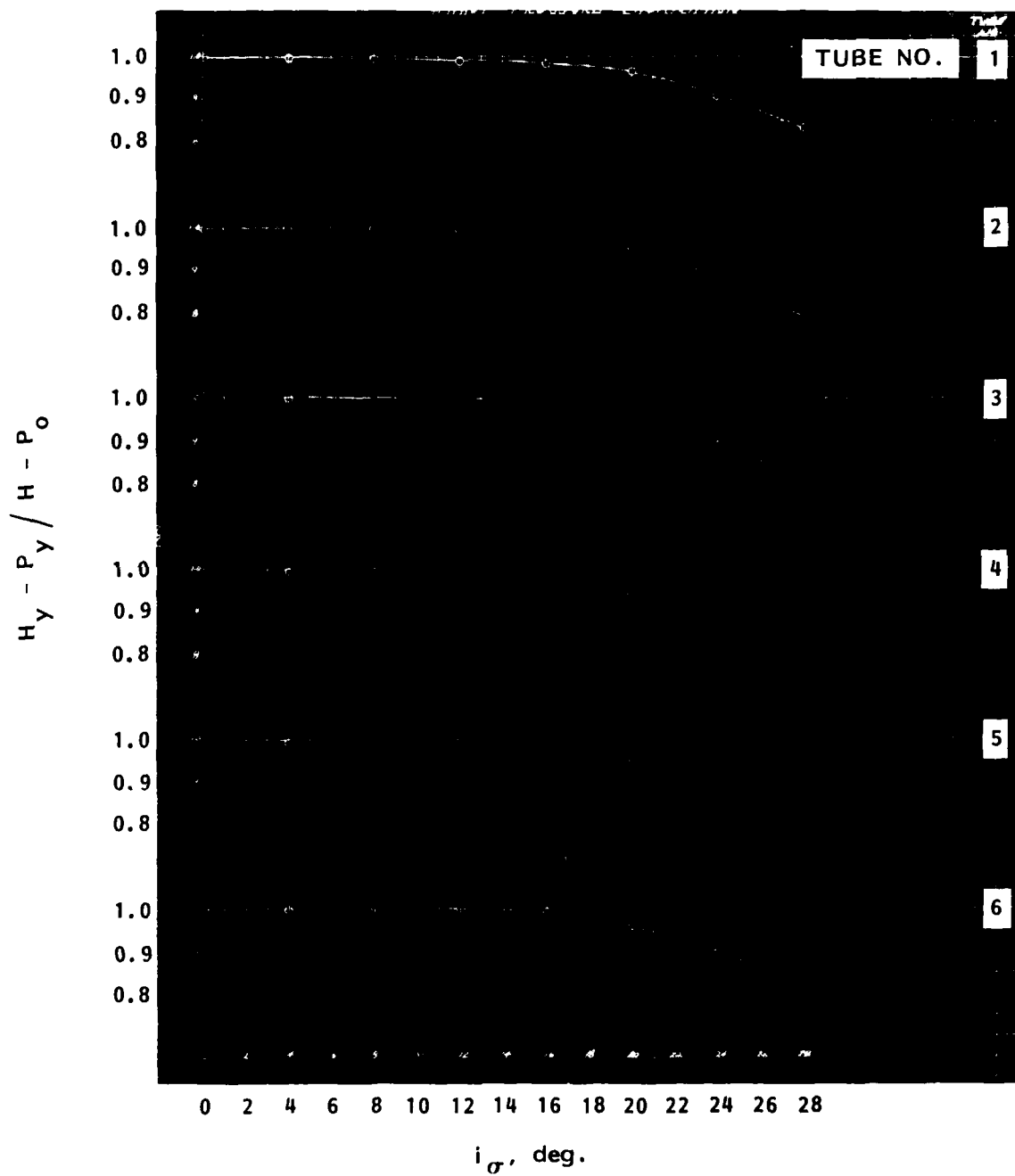
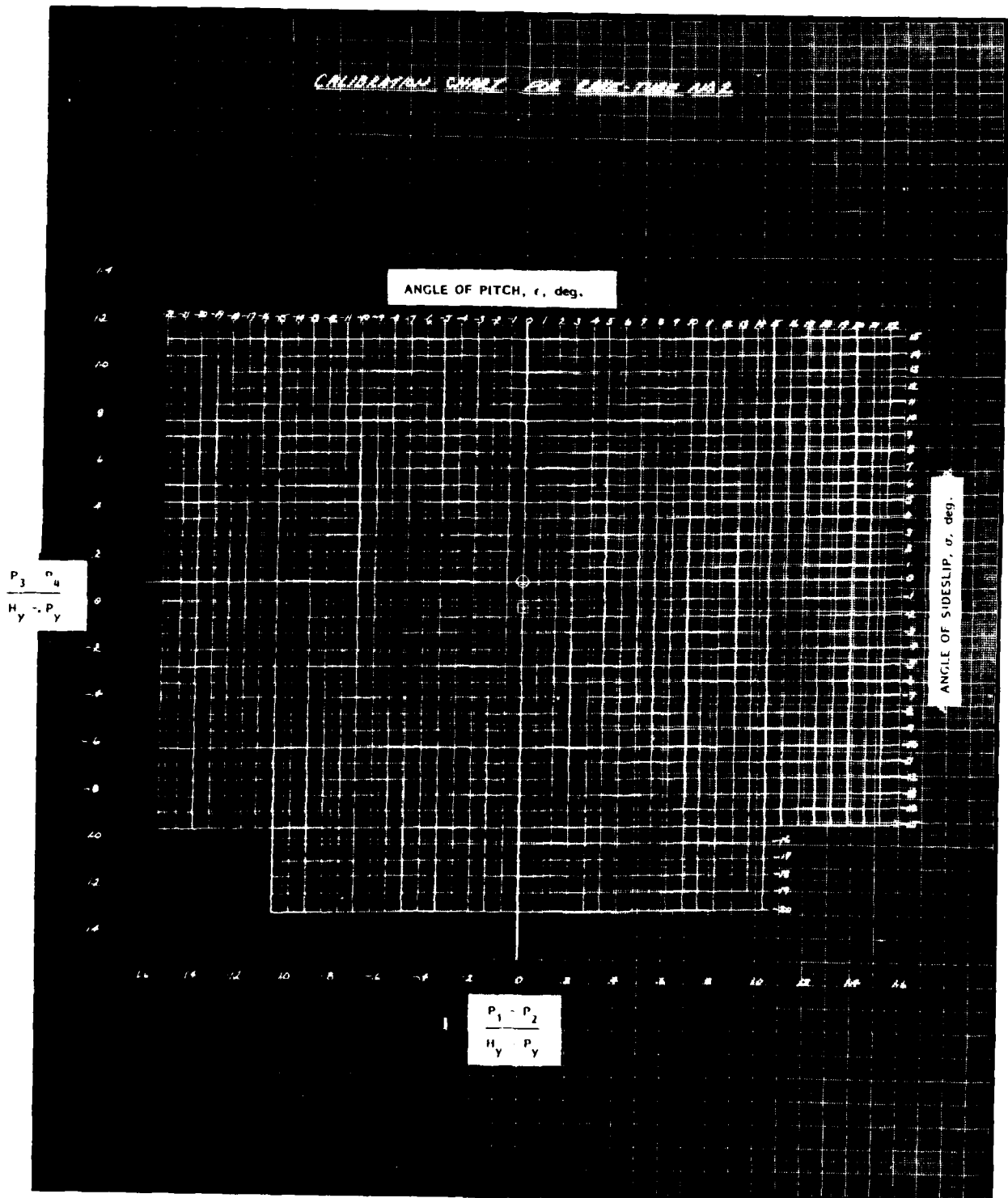


FIGURE C13 - VARIATION OF DYNAMIC PRESSURE RATIO WITH ANGLE OF INCIDENCE OF THE TUBE

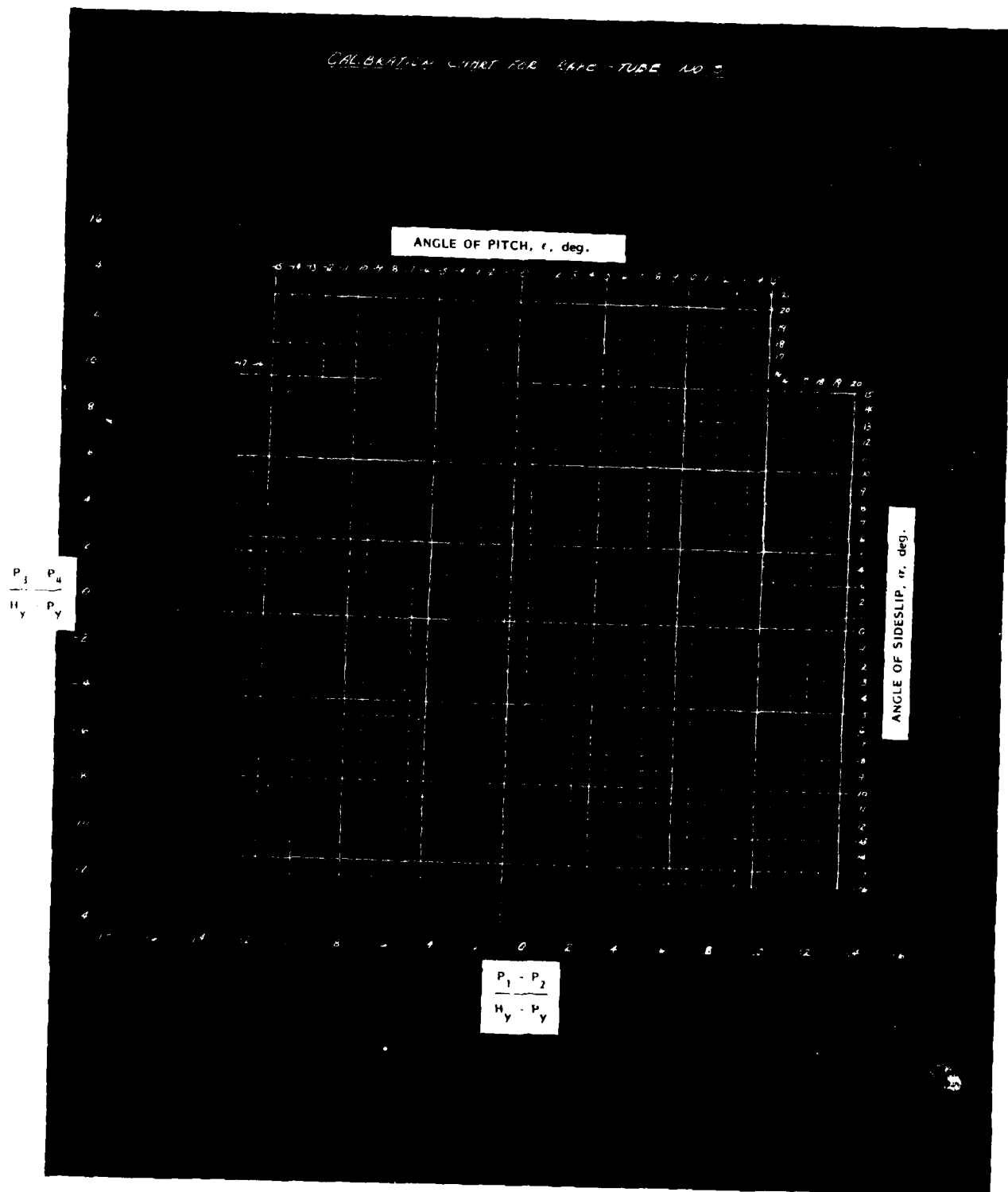
HYDRONAUTICS, INCORPORATED



a. TUBE NO. 2

FIGURE C14 - CHARTS FOR DETERMINING THE FLOW ANGLES FROM THE YAWHEAD PARAMETERS

HYDRONAUTICS, INCORPORATED



b. TUBE NO. 3

FIGURE C14 - CONTINUED

HYDRONAUTICS, INCORPORATED

CALIBRATION CHART FOR RAKE-TUBE NO. 1

ANGLE OF PITCH, ϵ , deg.

ANGLE OF SIDESLIP, σ , deg.

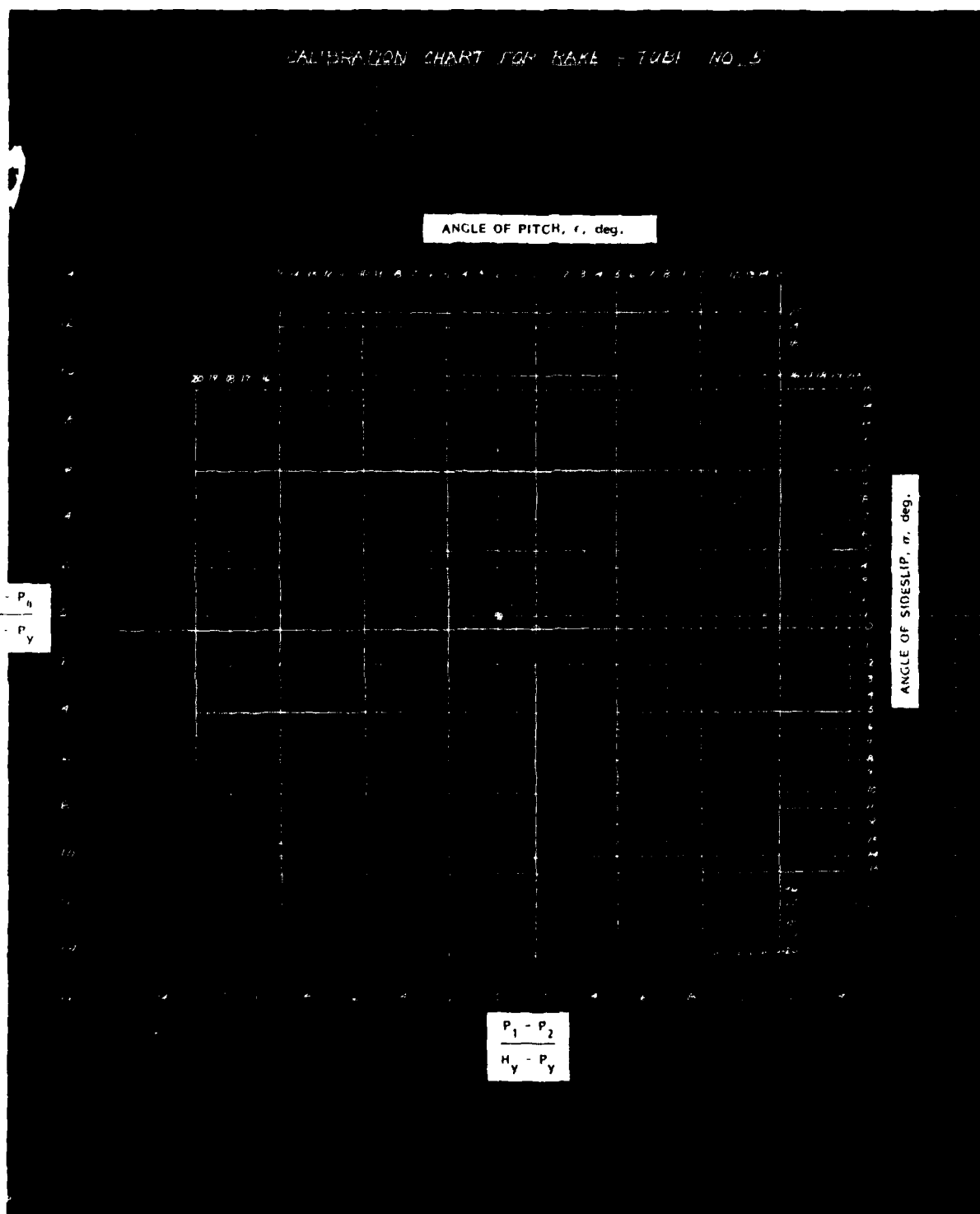
$\frac{P_1}{H_Y} - \frac{P_2}{P_Y}$

$\frac{P_1 - P_2}{H_Y - P_Y}$

c. TUBE NO. 4

FIGURE C14 - CONTINUED

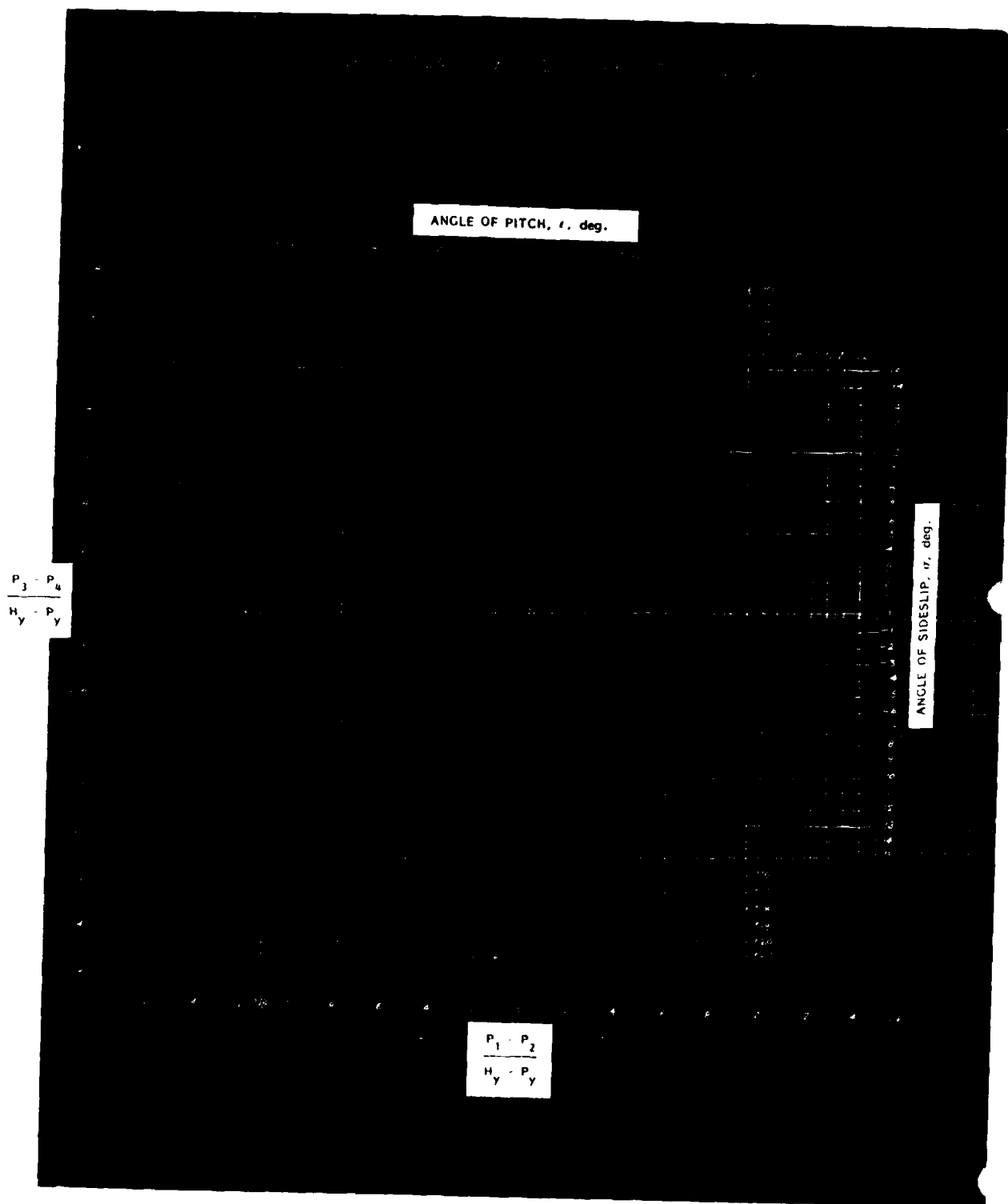
HYDRONAUTICS, INCORPORATED



d. TUBE NO. 5

FIGURE C14 - CONTINUED

HYDRONAUTICS, INCORPORATED



e. TUBE NO. 6

FIGURE C14 - CONCLUDED

HYDRONAUTICS, Incorporated

APPENDIX D

DESCRIPTION OF THE MODIFIED-LIFTING
SURFACE METHOD USED IN THEORETICAL CALCULATIONS

DESCRIPTION OF THE MODIFIED-LIFTING SURFACE
METHOD USED IN THEORETICAL CALCULATIONS

This appendix presents a review of several methods for calculating the lift curve slope of wings or fins alone as well as in the presence of a body. Specifically, a detailed description of a finite-step or modified-lifting surface method will be described and illustrated.

Fin Alone

Lifting-line and lifting-surface theories have been developed for the prediction of the lift characteristics of wings alone having various aspect ratios and sweep angles. Some of these theories are compared with experimental results in References D1 and D2. A semi-empirical expression developed in Reference D1 for lift-curve slope is

$$C_{L_\alpha} = \frac{a_o a}{\frac{57.4 a_o}{\pi} + \cos \Lambda \sqrt{\frac{a^2}{\cos^4 \Lambda} + 4}} \quad [1]$$

where

- C_{L_α} is the slope of the lift coefficient of the wing with respect to the angle of attack α in degrees at $\alpha = 0$,
- a is the effective aspect ratio,
- a_o is the section lift curve slope, equal to about $0.9 \left(\frac{2\pi}{57.3} \right)$ per degree to account for thickness

The lifting surface method of Weissinger developed in Reference D3 provides the results which have been reproduced in Figure D1. Estimates of C_{L_α} based on the results of Figure D1 is preferred to Equation [1] since it accounts for the effects of taper ratio and is also less time consuming to use.

Lifting surface methods employing a vortex-lattice technique are presented in References D4 and D5. In the method described in Reference D5 and illustrated in Figure D2 for a wing alone a finite number of horseshoe vortices are distributed along the quarter-chord line of the lifting surface. The downwash induced at the center of each horseshoe vortex along the three-quarter-chord line (control point) is equated to the component of the velocity normal to the chord of the lifting surface at each control point. Satisfying the boundary condition at each control point means that there is no flow through the lifting surface (see Reference D3). Also, calculating the downwash along the three-quarter-chord line instead of the quarter-chord line (as in the case of lifting-line theory) produces results which are in excellent agreement with experimental data. In addition, as illustrated in Figure D3, a section lift curve slope of 2π is obtained using the aforementioned conditions. Applying these steps results in a set of simultaneous equations which relates the strength of each horseshoe vortex to the angle of attack at each control point located along the three-quarter-chord line. Solution of the resulting set of simultaneous equations provides the span-load distribution, lift-curve slope, center of pressure and root-bending moments (if loading is asymmetrical).

HYDRONAUTICS, Incorporated

-D3-

Briefly, the downwash velocity at any point in the plane of the horseshoe vortex can be expressed as,

$$w(X,Y) = \frac{\Gamma_n}{4\pi s} F(X,Y) \quad [2]$$

From the Biot-Savart law, expressed in Reference D6 (Chapter XII), $F(X,Y)$ is the sum of terms having the form:

$$\begin{aligned} F(X,Y) = & -\frac{1}{X} \left[\frac{(Y+1)}{\sqrt{X^2 + (Y+1)^2}} - \frac{(Y-1)}{\sqrt{X^2 + (Y-1)^2}} \right] \\ & - \frac{1}{(Y-1)} \left[1 - \frac{X}{\sqrt{X^2 + (Y-1)^2}} \right] \\ & + \frac{1}{(Y+1)} \left[1 - \frac{X}{\sqrt{X^2 + (Y+1)^2}} \right] \end{aligned} \quad [3]$$

and the distances X and Y are nondimensionalized by the horseshoe semispan, s . Solutions to Equation [3] for various values of X and Y are tabulated in Reference D7. As shown in Figure D2, ten horseshoe vortices are used for the example. Based on the foregoing, this would imply a set of ten simultaneous equations. However, if the span-load distribution is symmetrical only five simultaneous equations are required.

HYDRONAUTICS, Incorporated

-D4-

Equation [2] can be rewritten as follows,

$$w(X, Y) = U\alpha = \frac{N}{4\pi} \sum_{n=1}^N \frac{2\Gamma_n}{b} F(X, Y) \quad [4]$$

Dividing both sides by $U\alpha$

$$\frac{w(X, Y)}{U\alpha} = \frac{N}{4\pi} \sum_{n=1}^N \frac{2\Gamma_n}{bU\alpha} F(X, Y) \quad [5]$$

where,

N is the number of horseshoe vortices ($\frac{b}{2s}$),

a is the aspect ratio $\frac{b^2}{A}$,

A is the total planform area,

s is the horseshoe semispan, and

b is the wing span

The lift per unit span can be expressed as (see Reference D6)

$$L = \rho U^2 s \quad [6]$$

and the lift coefficient can be written as

$$C_L = \frac{a}{N} \sum_{n=1}^N \frac{2\Gamma_n}{bU} \quad [7]$$

Differentiating Equation [7] with respect to α results in the expression for lift curve slope,

$$C_{L_\alpha} = \frac{a}{N} \sum_{n=1}^N \frac{2\Gamma_n}{bU\alpha} \quad [8]$$

which for a symmetrical loading becomes

$$C_{L_\alpha} = \frac{2a}{N} \sum_{n=1}^{N/2} \frac{2\Gamma_n}{bU\alpha} \quad [9]$$

If the matrix is solved without modification of the velocity term $\frac{w}{U\alpha}$ by the factor $\frac{4\pi}{N}$ (see Equation [5]), then Equation [9] can be written as

$$C_{L_\alpha} = \frac{a}{2\pi} \sum_{n=1}^{N/2} \frac{2\Gamma_n}{bU\alpha} \quad [10]$$

It should be noted that a section lift-curve slope of 2π is assumed in the derivation of Equation [11]. However, the effects of airfoil thickness on the section-lift curve slope can be accounted for by using measured section-lift curve slope data from Reference D8 as shown in Equation [12].

$$C_{L_\alpha} = \left(\frac{a_0}{2\pi} \right) \frac{a}{2\pi} \sum_{n=1}^{N/2} \frac{2\Gamma_n}{bU\alpha} \quad [11]$$

Values of $\Gamma'_n = \frac{2\Gamma_n}{b U_\alpha}$ for Equation [11] are obtained from the simultaneous solution of the equations resulting from Equation [5] using the CROUT method described in Reference D9 or present day digital computer techniques.

Fin-Body Interference

The mutual interference of wings and bodies was first studied by Lennertz (see References D10 and D11). Lennertz calculated the lateral and longitudinal lift distribution on the body of an idealized wing-body combination in which the body is represented by an infinite circular cylinder and the wing by a horseshoe vortex having a constant spanwise circulation. The vortices trailing from the wing tips have images inside the cylinder, and the bound vortex is extended inside the cylinder to join the trailing image vortices. With this configuration, the boundary condition of zero velocity normal to the surface of the cylinder is satisfied only at infinity and in the plane normal to the cylinder axis which passes through the vortex, so that it is necessary to superimpose an additional potential, which is calculated in Reference D10. For this case the lateral lift distribution is obtained by considering the momentum change in a vertical plane infinitely far behind the wing, and the longitudinal lift distribution is obtained by the use of Bernoulli's equation. The expression for lift coefficient derived in Reference D10, expressed in the notation of the present paper, can be written as

$$C_{L_\alpha} = 8a \left(\frac{\Gamma}{b_F U_\alpha} \right) \left[\left(1 + \frac{d}{2b_F} \right) \left(1 - \frac{\left(\frac{d}{2b_F} \right)^2}{\left(1 + \frac{d}{2b_F} \right)^2} \right) \right] \quad [12]$$

The work of Reference D10 and D11 have been extended and refined in References D12 and D13. The method used in Reference D13 combines the methods of Reference D10 and the horse-shoe-vortex method of Reference D5 described herein for the fin alone case. The modified-lifting surface method described and illustrated herein for the fin-body case, is similar to that used in Reference D13 except that in the present calculations no corrections are made for finite-body length or for rigorously satisfying the body-boundary conditions. In the present method, illustrated in Figure D4a, the fins are represented by a horse-shoe-vortex system with images situated inside the cylinder at the proper locations. The location of the images inside the cylinder is obtained as shown in Figure D4b. The velocities induced at the three-quarter-chord points of the fins by the vortex system and the image-vortex system are set equal to the velocity distribution on the fins due to sideslip angle and the influence of the body. For the case of no boundary, the velocity distribution is depicted in Figure 4c (see Reference D6, page 30). Solution of the set of simultaneous equations gives the vortex strengths and thus the forces on the fins and the induced loads on the body. Figure D4d illustrates a typical span-load distribution that results from the calculations. The procedure of Reference D12 is used to determine the load distribution induced on the body. An illustrative example for a typical fin-body combination is presented in Figure D5 and Table D1. The case presented in Table D1 uses the results of the velocity surveys presented in Figures B1 and B10. Using these results the velocity normal to the fin can be expressed as,

TABLE D1
ILLUSTRATIVE EXAMPLE OF MODIFIED-LIFTING SURFACE METHOD

$$a = 2.0 \quad d_F/2b_F = 0.52$$

Control Point n	Γ_1'	Γ_2'	Γ_3'	Γ_4'	Γ_5'	Γ_6'	$\frac{v_n}{U\beta} = \frac{u_n}{U} \left(\frac{\partial \Gamma}{\partial \beta} \right)$
1	4.048	-1.284	-0.232	-0.091	-0.047	-0.043	1.25
2	-1.296	4.042	-1.296	-0.238	-0.105	-0.072	1.30
3	-0.244	-1.305	4.031	-1.315	-0.259	-0.138	1.39
4	-0.100	-0.248	-1.321	4.007	-1.342	-0.329	1.55
5	-0.053	-0.113	-0.270	-1.349	3.953	-1.526	1.57
6	-0.052	-0.082	-0.149	-0.341	-1.523	2.822	0.48

$$\sum_{n=1}^6 \Gamma_n' = 8.216$$

$$C_{L_\alpha} = \frac{a}{2\pi} \sum_{n=1}^6 \Gamma_n' \quad (\text{see Equation [11]})$$

$$\Gamma_n' = \frac{2\Gamma_n}{b_F U \beta}$$

$$\Gamma_1' = 0.885$$

$$\Gamma_2' = 1.233$$

$$\Gamma_3' = 1.481$$

$$\Gamma_4' = 1.634$$

$$\Gamma_5' = 1.635$$

$$\Gamma_6' = 1.380$$

$$= 2.615 \text{ per radian}$$

$$= 0.0456 \text{ per degree}$$

HYDRONAUTICS, Incorporated

-D9-

$$\frac{v_n}{u_n} = \tan \beta_L \approx \beta_L \quad [13]$$

$$\frac{v_n}{U\beta} = \left(\frac{u_n}{U}\right) \frac{\partial \beta_L}{\partial \beta} \quad [14]$$

For the case without boundary layer, Equation [14] becomes in accordance with Reference D6,

$$\frac{v_n}{U\beta} = 1 + \left(\frac{R}{z}\right)^2 \quad [15]$$

The lift induced on the body by the fin can be expressed as (see Reference D12),

$$(L_B)_i = \rho U \sum_{n=1}^N (\Gamma_n')_B 2s_n' \quad [16]$$

where

$$(\Gamma_n')_B = \Gamma_n'$$

$$s_n' \neq s \neq \text{constant}$$

Nondimensionalizing Equation [16] and differentiating with respect to α ,

$$(C_{L_{\alpha B}})_i = 2a \sum_{n=1}^{N/2} \frac{2(\Gamma_n')_B}{b_F U \alpha} \frac{s_n'}{b_F} \quad [17]$$

The ratio of the lift induced on the body to the lift induced on the fin can be obtained by dividing Equation [17] by Equation [9].

$$\frac{\left(C_{L_{\alpha B}}\right)_F}{\left(C_{L_{\alpha F}}\right)_B} = \frac{\sum_{n=1}^{N/2} \Gamma_n' \frac{s_n'}{b_F}}{\frac{s_n}{b_F} \sum_{n=1}^{N/2} \Gamma_n'} \quad [18]$$

The modified lifting surface method has been used to calculate the lift on fins in the presence of a body as well as the lift induced on the body by the fins for a range of fin aspect ratios and diameter-span ratios for the case of no boundary layer. The results of these calculations (30 cases) are summarized in Figures D6, D7, and D8. The method has also been used to calculate the effects of gap ratio for fins in proximity to both a reflection plane and a cylindrical body. The results for the fin-reflection plane case are compared in Figure D9 with the experimental results of Reference D14. The comparison is quite good. The calculated spanwise loading distribution as a function of gap ratio is presented in Figure D10. Similar calculations which show the effects of gap ratio for fin-body combination are presented in Figures D11 and D12 and compared with the theory of References D15 and D16.

AD-A108 429

HYDRONAUTICS INC LAUREL MD

EXPERIMENTAL AND THEORETICAL INVESTIGATION OF FACTORS AFFECTING--ETC(U)

AUG 80 A GOODMAN

N00167-79-C-0093

NL

UNCLASSIFIED

TR-7927-1

3 4 3

000000



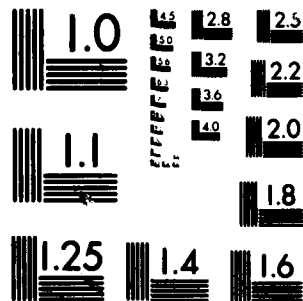
END

DATE

FILED

1 4 2

DTIC



MICROCOPY RESOLUTION TEST CHART
NATIONAL BUREAU OF STANDARDS-1963-A

Effects of Rolling Angular Velocity

The lateral force and rolling moment coefficients due to rolling have been calculated using the modified lifting surface method for a range of span-diameter ratios typical of submarine fairwater-hull combinations. The calculations were performed for an aspect ratio of 0.8. Calculations were made for a range fairwater aspect ratios of from 0.4 to 1.0. The results of these calculations did not include the induced load on the body. However, the results indicate that the effects of aspect ratio on Y_p' and K_p' are small.

The boundary condition for the rolling case to be satisfied at each control point along the three-quarter chord line can be expressed as,

$$\frac{v_n}{U} = \frac{P_n}{U} \left[\frac{d}{2} + b_F \left(\frac{13 - 2N}{12} \right) \right] \quad [19]$$

Equation [19] assumes that six horseshoe vortices are distributed along the fairwater span ($N = 6$).

The results of the calculations are presented in Figure D13 as plots of $(Y_p') \left(\frac{l}{d} \right)^3$ and $(K_p') \left(\frac{l}{d} \right)^4$ versus the span-diameter ratio $\frac{b_{FW}}{d}$.

HYDRONAUTICS, Incorporated

-D12-

REFERENCES

- D1 - Polhamus, Edward C., "A Simple Method of Estimating the Subsonic Lift and Damping in Roll of Sweptback Wings," NACA TN 1862, 1949.
- D2 - Whicker, L. Folger and Fehlner, Leo F., "Free-Stream Characteristics of a Family of Low-Aspect-Ratio, All-Movable Control Surfaces for Application to Ship Design," DTMB Report 933 Revised Edition, December 1958.
- D3 - De Young, John and Harper, Charles, W., "Theoretical Symmetric Span Loading at Subsonic Speeds for Wings Having Arbitrary Plan Form," NACA Rept. 921, 1948.
- D4 - Falkner, V. M., "The Solution of Lifting Plane Problems by Vortex Lattice Theory," Rept. No. 10, 895, British A.R.C., September 29, 1947.
- D5 - Campbell, George S., "A Finite-Step Method for the Calculation of Span Loadings of Unusual Plan Forms," NACA RML50L13, July 16, 1951.
- D6 - Glauert, H., "The Elements of Aerofoil and Airscrew Theory," Second Edition, Cambridge University Press, 1948.
- D7 - Staff of the Mathematics Division, "Tables of Complete Downwash Due to a Rectangular Vortex," Reports and Memoranda No. 2461, July 21, 1947.
- D8 - Abbott, Ira H., Von Doenhoff, Albert E., and Stevens, Louis S., Jr., "Summary of Airfoil Data," NACA Rept. 824, 1945.
- D9 - Crout, Prescott D., "A Short Method for Evaluating Determinants and Solving Systems of Linear Equations with Real or Complex Coefficients," Trans. AIEE, Vol. 60, 1941, pp. 1235-1241.
- D10 - Lennertz, J., "Beitrag zur Theoretischen Behandlung des Gegenseitigen Einflusses von Trafläche und Rumpf," Z.f.a.M.M., Bd. 7, August 1927, pp. 249-276.

HYDRONAUTICS, Incorporated

-D13-

- D11 - Lennertz, J., "Influence of the Airplane Body on the Wings," Aerodynamic Theory, W. F. Durand, Editor, Durand Reprinting Committee, Vol. IV, 1943, pp. 152-158.
- D12 - Robinson, Samuel W., Jr. and Zlotnick, Martin, "A Method for Calculating the Aerodynamic Loading on Wing-Tip-Tank Combinations in Subsonic Flow," NACA RM L53B18, 1953.
- D13 - Zlotnik, M. and Robinson, S. W., Jr., "A Simplified Mathematical Model for Calculating Aerodynamic Loading and Downwash for Wing-Fuselage Combinations with Wings of Arbitrary Plan Form," NACA Technical Note 3057, January 1954.
- D14 - Darnell, R. C., "Hydrodynamic Characteristics of Twelve Symmetrical Hydrofoils," DTMB Report 341, November 1932.
- D15 - Mirels, H., "Gap Effect on Slender Wing-Body Interference," Readers Forum, Journal of Aeronautical Science, Volume 20, No. 8, August 1955.
- D16 - Dugan, Duane W. and Hikido, Katsumi, "Theoretical Investigation of the Effects Upon Lift of a Gap Between Wings and Body of a Slender Wing-Body Combination," NACA TN 3224, August 1954.

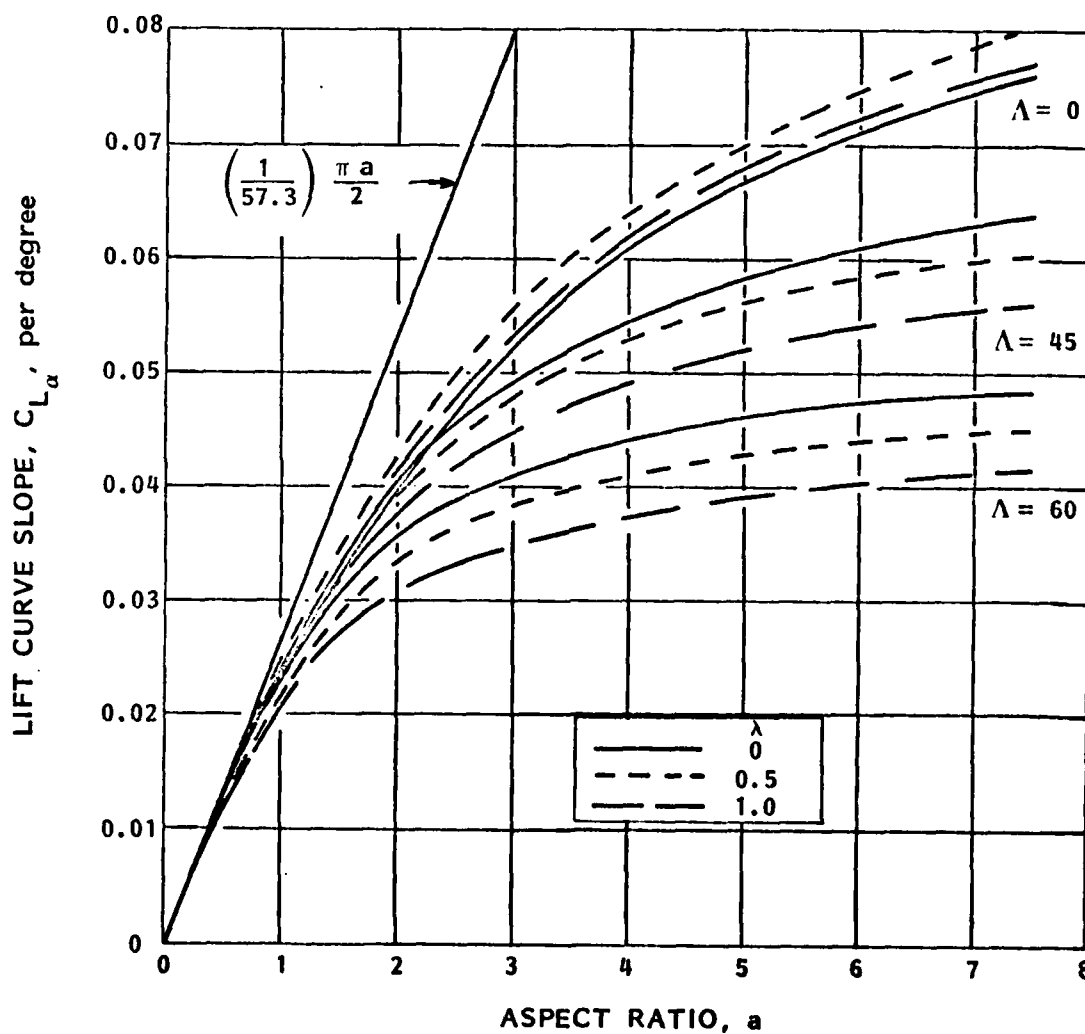


FIGURE D1 - VARIATION OF LIFT CURVE SLOPE WITH ASPECT RATIO FOR VARIOUS VALUES SWEEP AND TAPER RATIO

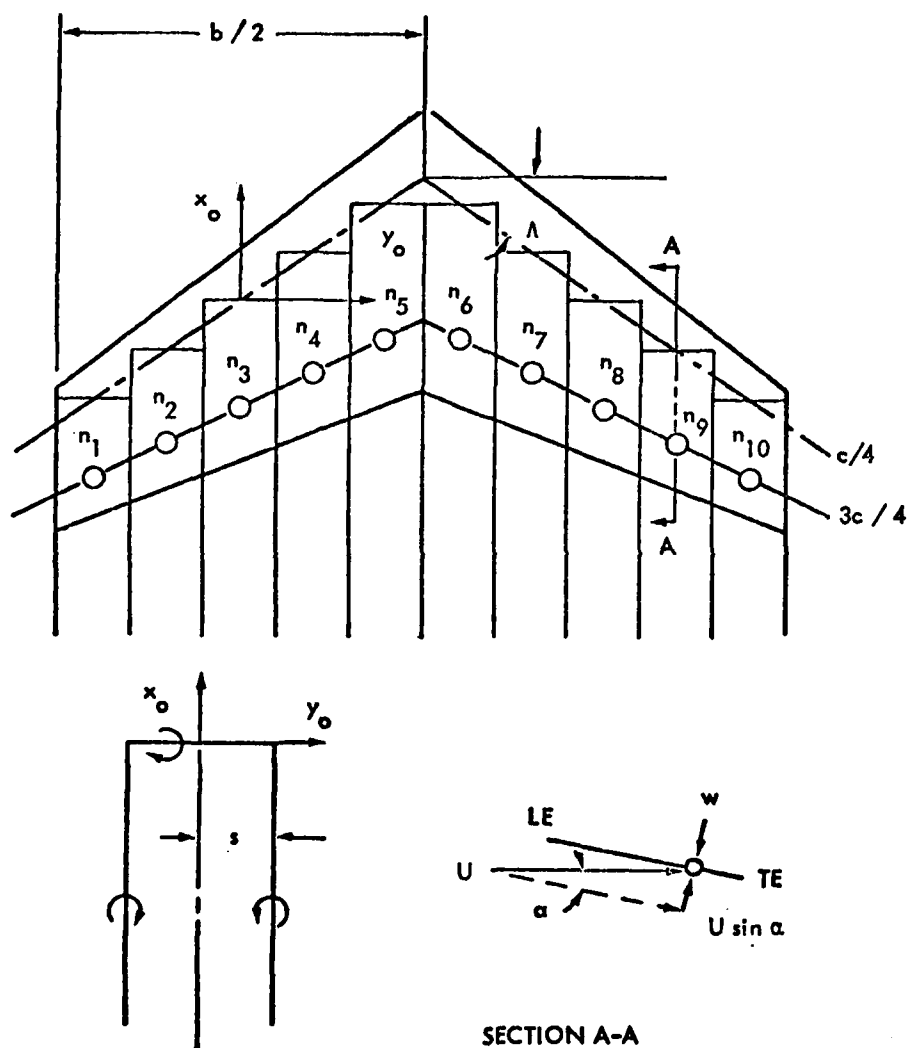
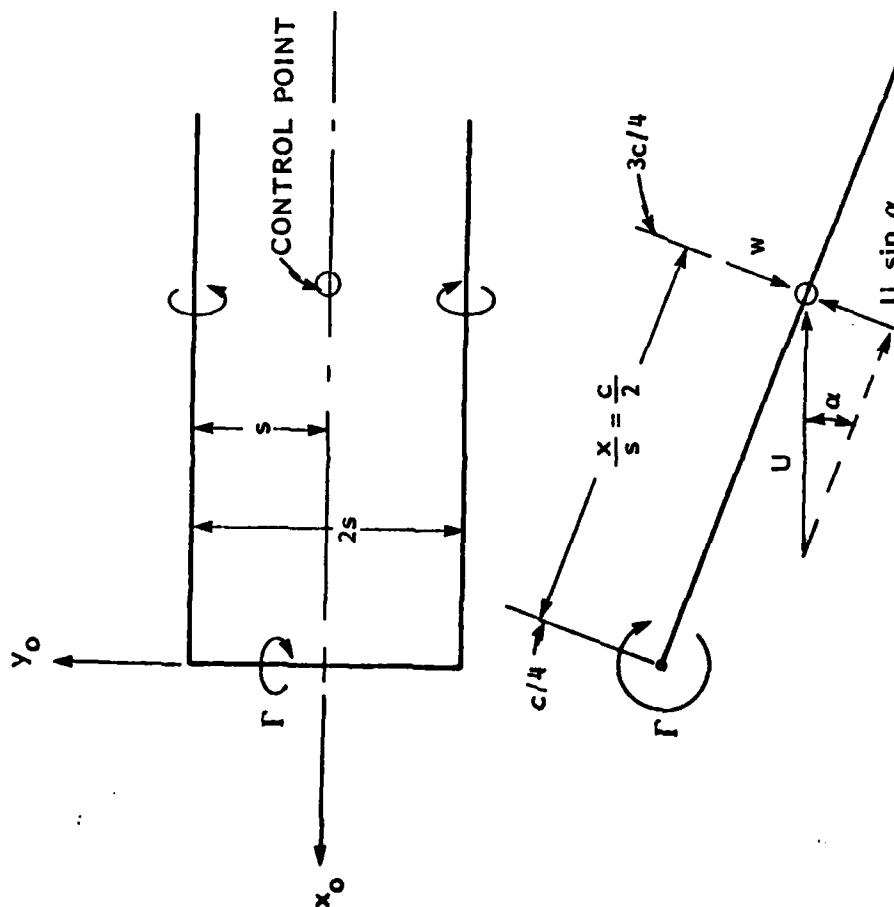


FIGURE D2 - VORTEX PATTERN, SYSTEM OF AXES, AND SUBSCRIPTS USED IN CALCULATION OF SPAN LOADINGS BY MODIFIED-LIFTING-SURFACE METHOD

HYDRONAUTICS, INCORPORATED



$$w = \frac{\Gamma}{2\pi(c/2)}$$

$$l = \rho U \Gamma \text{ (SECTION LIFT)}$$

$$= \rho U 2\pi(c/2) w$$

$$c_l = \frac{\rho U \pi c w}{\rho/2 U^2 c}$$

$$= 2\pi\alpha$$

$$c_{l\alpha} = 2\pi \text{ (THEORETICAL SECTION LIFT-CURVE SLOPE)}$$

FIGURE D3 - ANALYSIS OF SINGLE HORSESHOE VORTEX

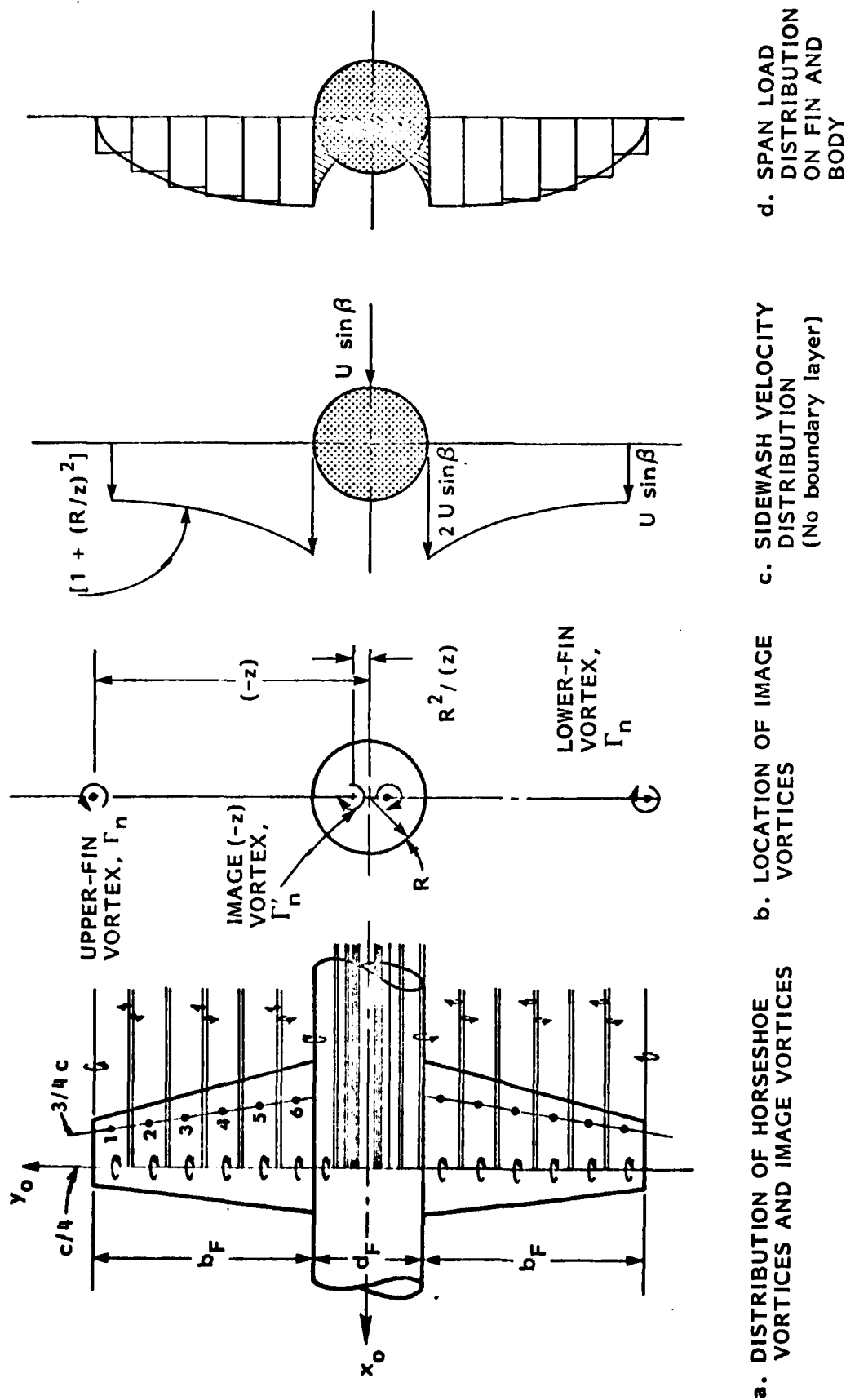


FIGURE D4 - PICTORIAL DESCRIPTION OF THE MODIFIED-LIFTING SURFACE METHOD USED TO CALCULATE INTERFERENCE EFFECTS OF FINS IN THE PRESENCE OF A BODY

HYDRONAUTICS, INCORPORATED

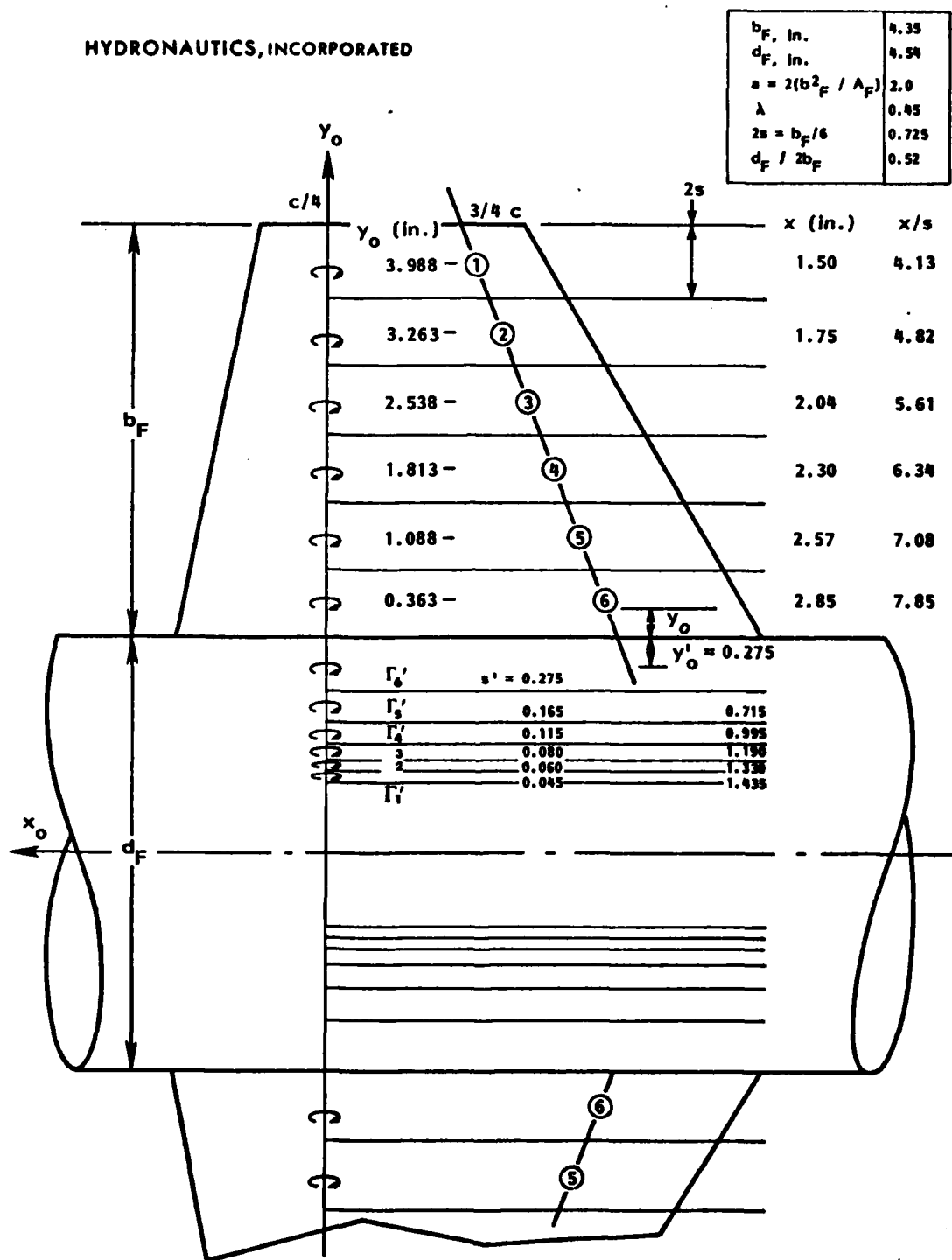


FIGURE D5 - SKETCH OF FIN-BODY CONFIGURATION AND VORTEX-IMAGE SYSTEM USED IN THE CALCULATION OF SPAN LOADINGS BY THE MODIFIED-LIFTING SURFACE METHOD

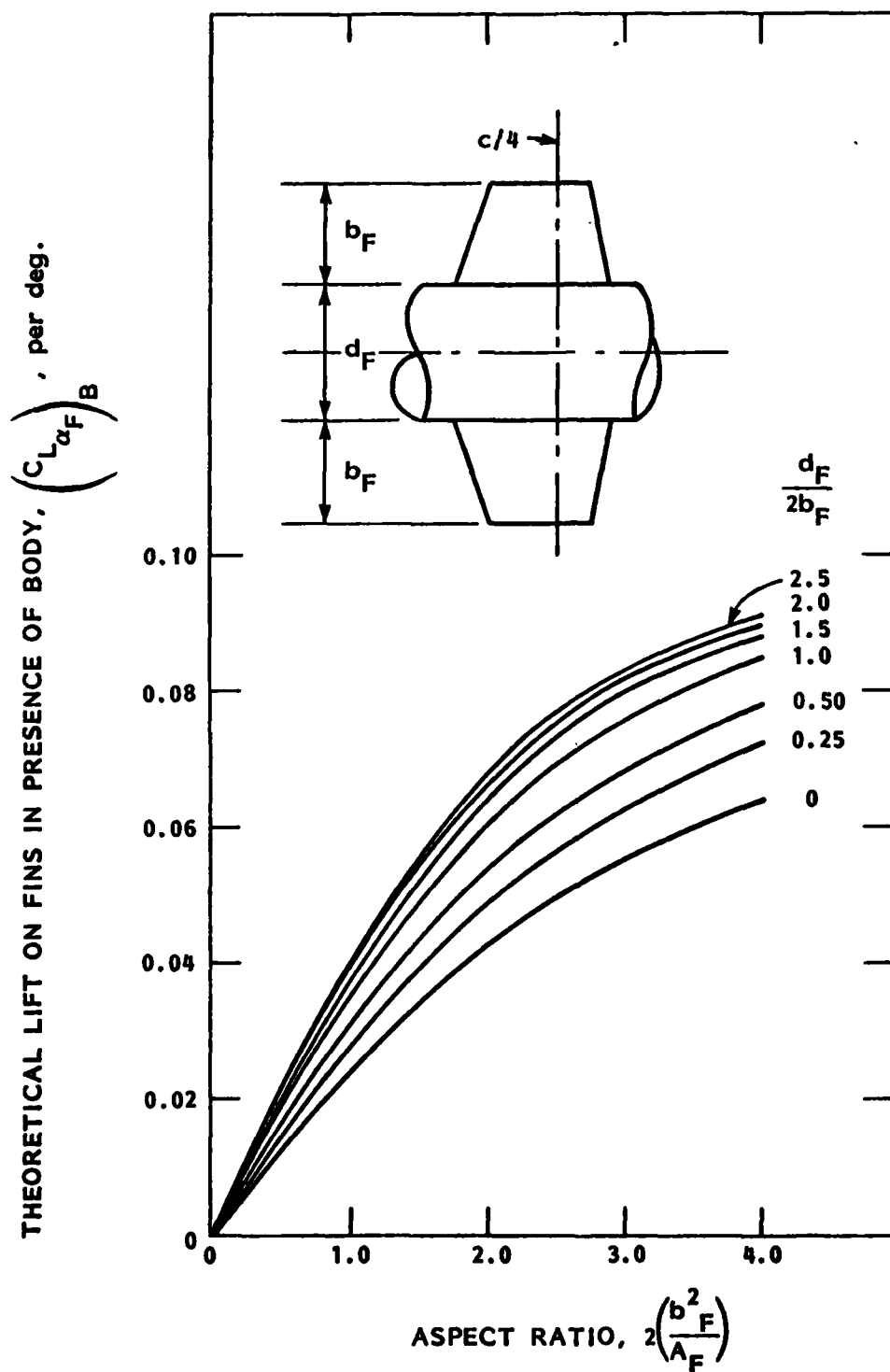


FIGURE D6 - VARIATION OF THEORETICAL LIFT ON FINS IN PRESENCE OF BODY WITH ASPECT RATIO FOR VARIOUS DIAMETER-SPAN RATIOS

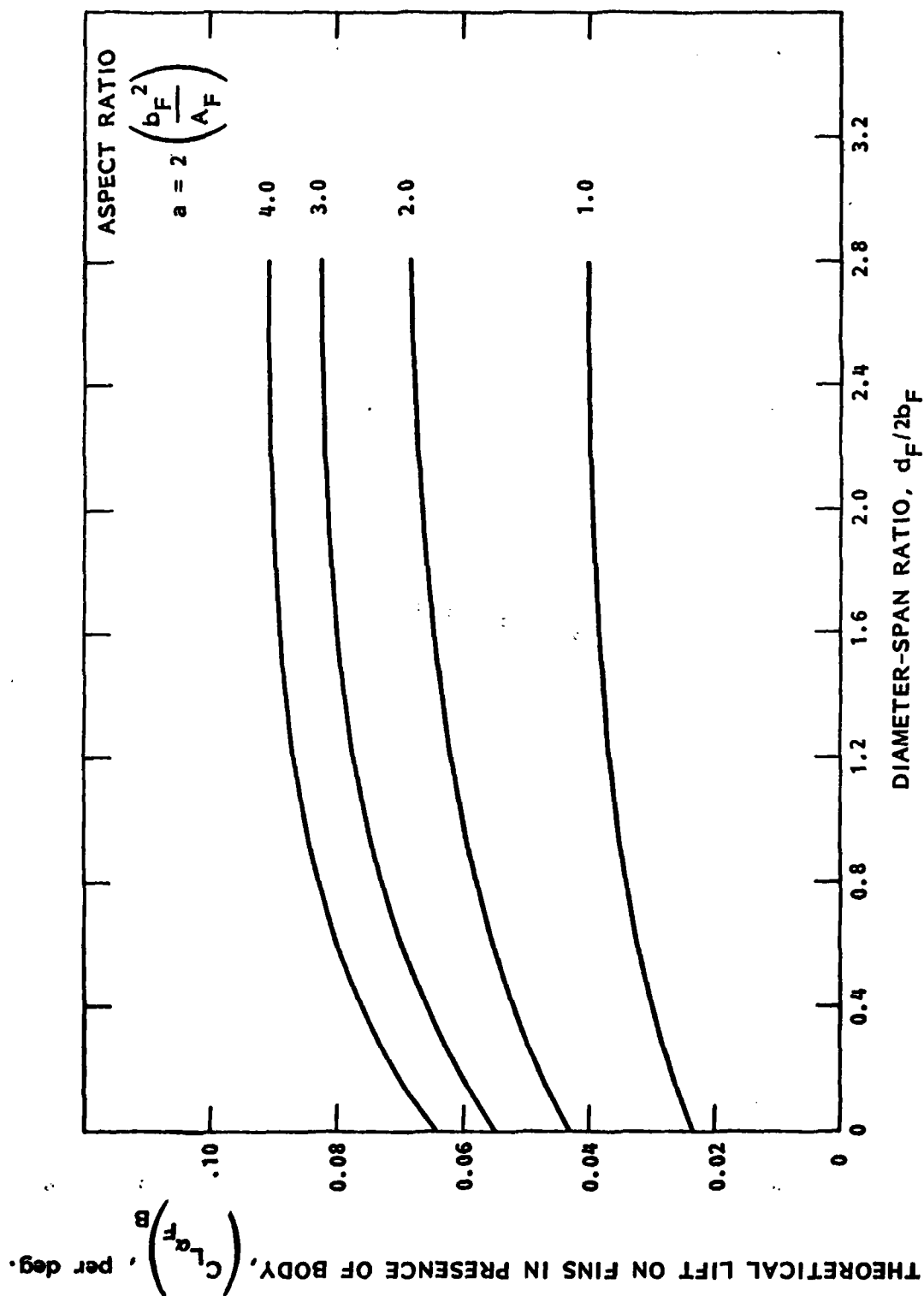


FIGURE D7 - VARIATION OF THEORETICAL LIFT ON FINS IN PRESENCE OF BODY WITH DIAMETER-SPAN RATIO FOR SEVERAL ASPECT RATIOS

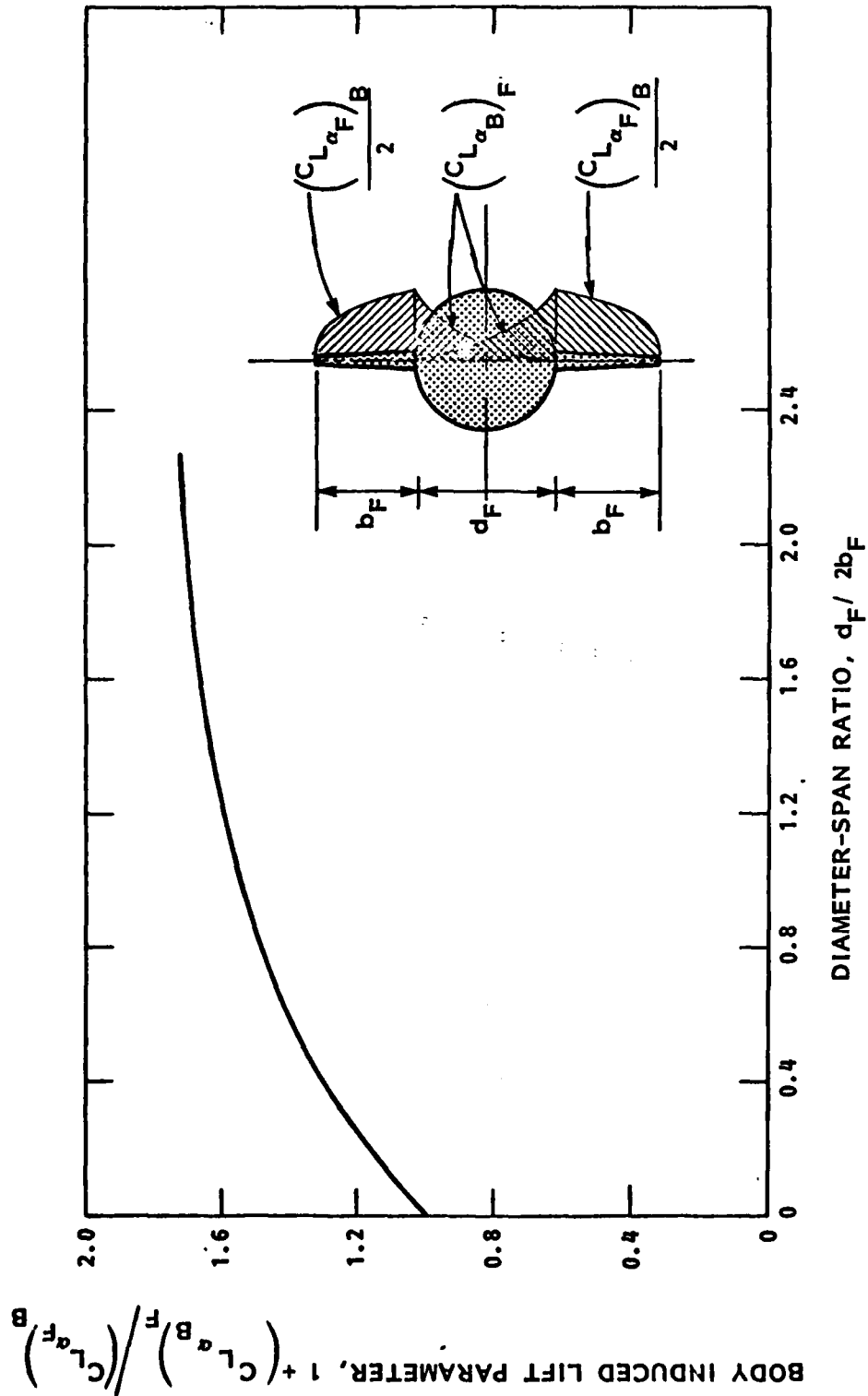


FIGURE D8 - VARIATION OF THEORETICAL BODY-INDUCED LIFT PARAMETER WITH DIAMETER-SPAN RATIO

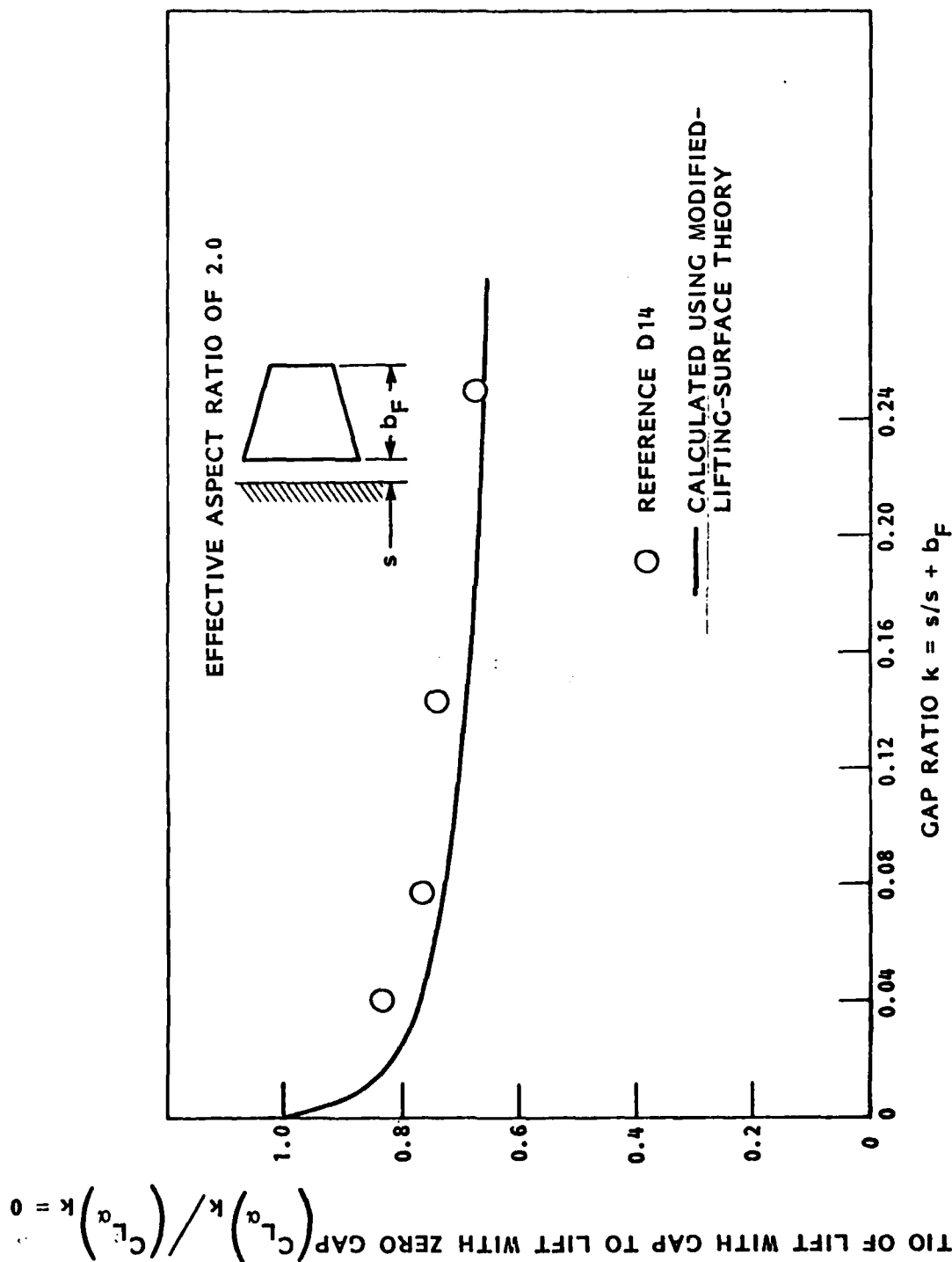


FIGURE D9 - EFFECT OF GAP SIZE ON FIN LIFT IN PRESENCE OF A REFLECTION PLANE

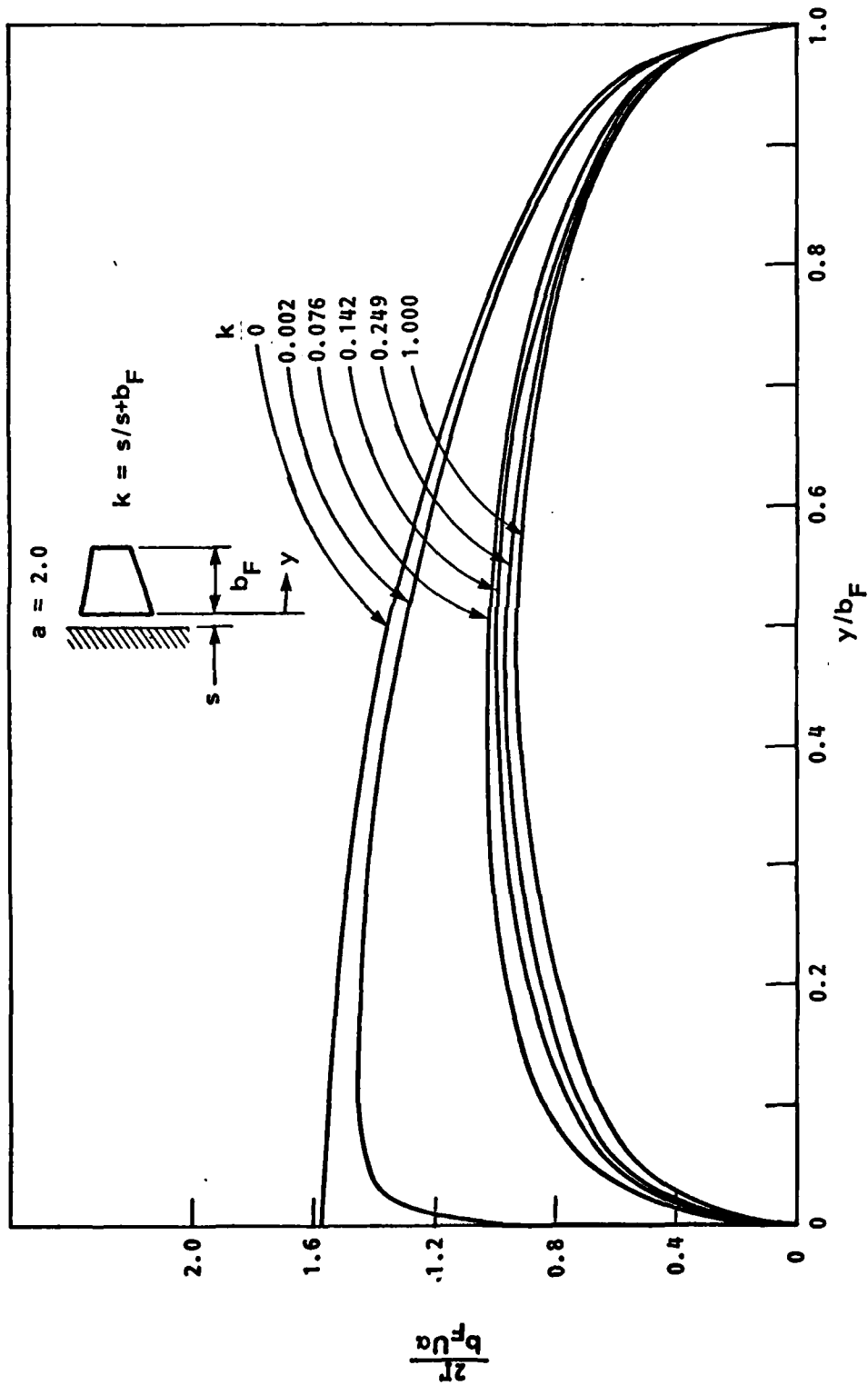
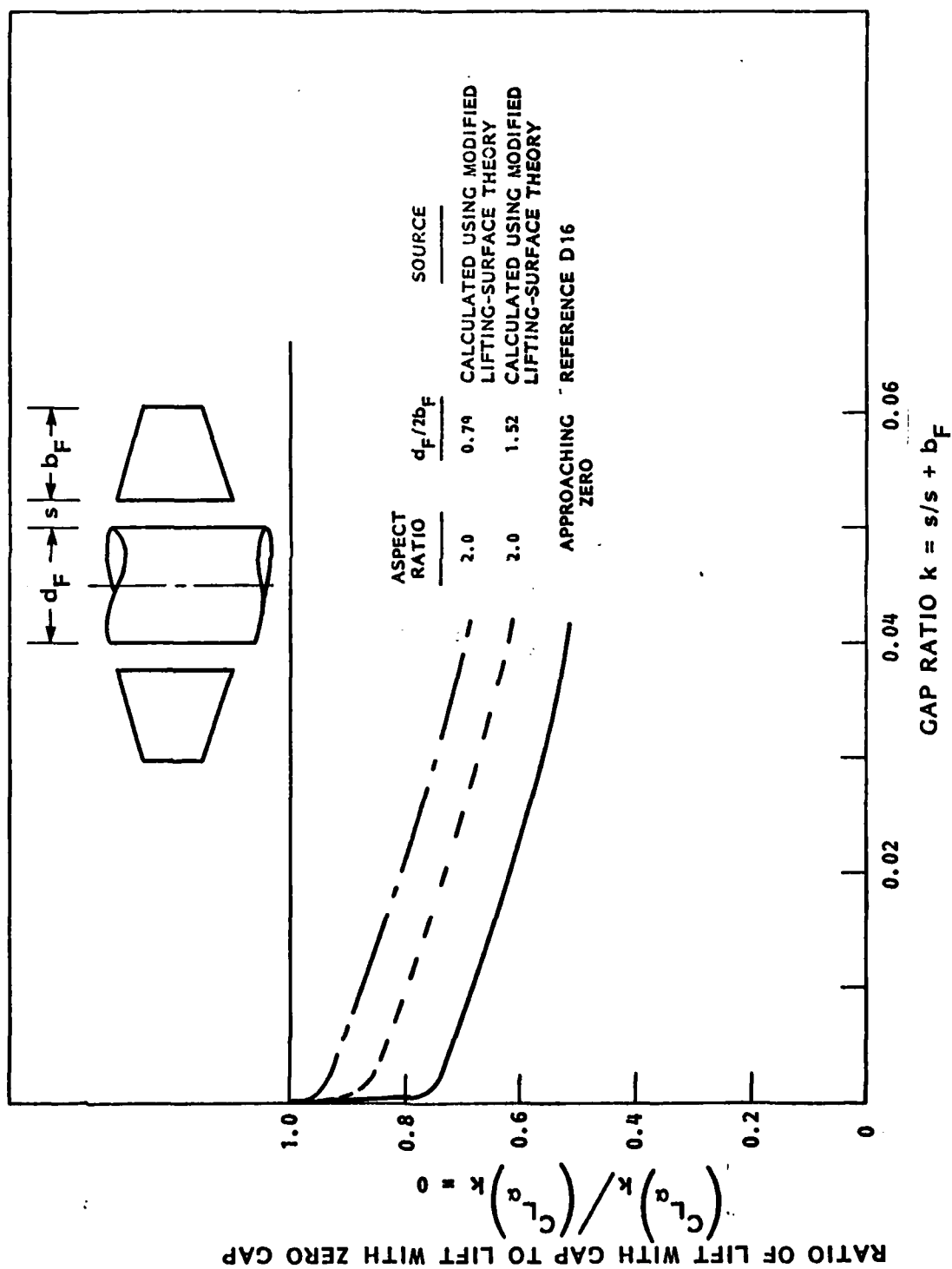


FIGURE D10 - EFFECT OF GAP SIZE ON FIN LOAD DISTRIBUTION IN PRESENCE OF A REFLECTION PLANE



FIGURED11 - EFFECT OF GAP SIZE ON FIN LIFT IN PRESENCE OF BODY

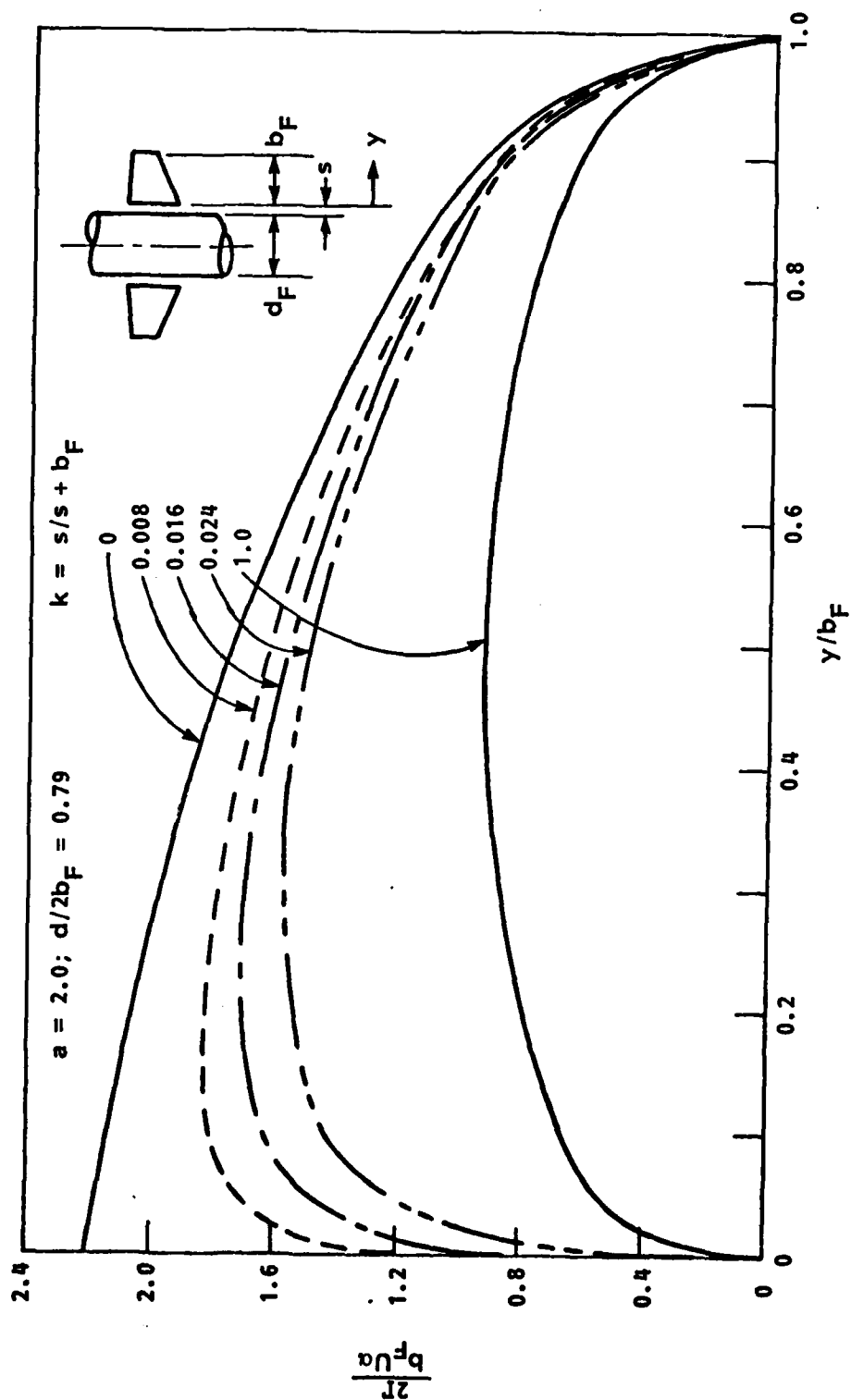


FIGURE D12 - EFFECT OF GAP ON FIN LOAD DISTRIBUTION PRESENCE OF A BODY

HYDRONAUTICS, INCORPORATED

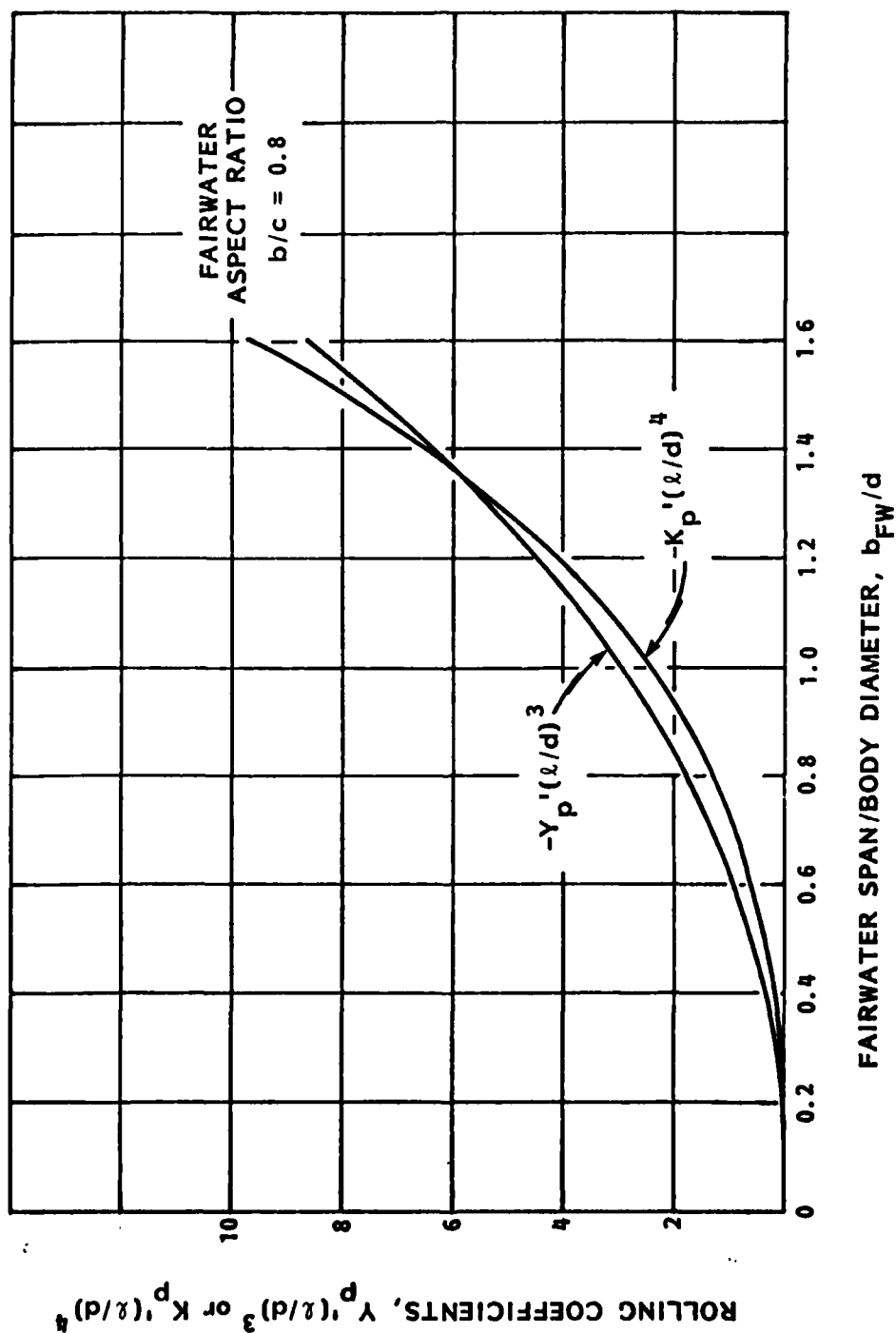


FIGURE D13 - CALCULATED VALUES OF THE FORCE AND MOMENT COEFFICIENTS DUE TO ROLLING FOR VARIOUS FAIRWATER SPAN-BODY DIAMETER RATIOS

END

DATE
FILMED

1-82

DTIC